Investigations on Intelligent Control Techniques for Efficient Frequency Support in Interconnected Power Systems Integrated with Renewable Energy Sources

THESIS

Submitted in partial fulfillment of the requirements for the degree of

DOCTOR OF PHILOSOPHY

by

AKHILESH KUMAR MISHRA
ID No. 2017PHXF0426P

Under the Supervision of

Dr. PUNEET MISHRA

and Under the Co-supervision of

PROF. HITESH DATT MATHUR

BITS Pilani
Pilani | Dubai | Goa | Hyderabad

BIRLA INSTITUTE OF TECHNOLOGY & SCIENCE,
PILANI
2023

BIRLA INSTITUTE OF TECHNOLOGY AND SCIENCE PILANI – 333031 (RAJASTHAN), INDIA

CERTIFICATE

This is to certify that the thesis entitled **"Investigations on Intelligent Control Techniques for Efficient Frequency Support in Interconnected Power Systems Integrated with Renewable Energy Sources"** submitted by **Mr. Akhilesh Kumar Mishra,** ID No. **2017PHXF0426P** for the award of Ph.D. degree of the Institute embodies original work done by him under our supervision.

Signature of the Supervisor	Signature of the Co-Supervisor
Name: **DR. PUNEET MISHRA**	Name: **PROF. HITESH DATT MATHUR**
Designation: **Assistant Professor**	Designation: **Professor**

Date:

Acknowledgments

I feel it is a great privilege to express my deepest and most sincere gratitude to my supervisor, Dr. Puneet Mishra, for his suggestions, constant encouragement, and support during the course of the thesis work.

I also express my deep gratitude to Prof. Hitesh Datt Mathur, who has guided me in the critical phases of this work and encouraged me in all stages. I appreciate his consistent peaceful, and jolly nature.

The time spent at BITS-Pilani was very enjoyable and inspiring. I wish to thank all my colleagues for creating a great working environment for in-depth technical discussions and valuable suggestions to cope with all sorts of difficulties. I owe a debt of gratitude to my Doctoral Advisory Committee members, Dr. Sujan Yenuganti and Dr. Bijoy Krishna Mukherjee, whose well-versed comments have shed new light on several aspects and feedback in stratifying the research work. I heartily thank Prof. Surekha Bhanot for unveiling the meaning of life with positive reflections at every juncture. I owe my sincere gratitude to HoD Prof. Navneet Gupta and Ex HoD Prof. Vinod Kumar Chubey for providing me the requisite facility to carry out my doctoral research. I would like to express my gratitude to Prof. Praveen Kumar A.V., convener of the Doctoral Research Committee, for all their support and useful suggestions.

I wish to thank Vice-Chancellor Prof. V. Ramgopal Rao, Ex Vice-Chancellor Prof. Souvik Bhattacharyya, Director Prof. Sudhir Kumar Barai, Dean of Academic Graduate Studies and Research Division (AGSRD) Prof. M.B Srinivas, Dean Administration Prof. S. K. Verma, Associate Dean, AGSRD Prof. Shamik Chakraborty and Registrar Col Soumyabrata Chakraborty (Retd) for giving me an opportunity to do the research in the area of my interest.

I am also grateful to my seniors, friends, and colleagues Dr. Ravinder Kumar, Dr. Dhananjay Kumar, Dr. Heema Dave, Dr. Prashant Upadhyay, Dr. Krishna Veer Singh, Mr. Anukaran Khanna, Mr. Sisir Yadav, Ms. Pavitra Sharma, and Mr. Krishna Kumar Saini who kept me inspiring and helped in difficult times.

I express my deep sense of gratitude and respect to my beloved mother, Smt. Shashi Kala Mishra and father Late Sri. Rama Shanker Mishra. My father is the person in my life who inspires me, motivates me, and helps me. And the most important things are that he always stands with me in every good or bad situation. I know you are with me all the time. You are present everywhere in my mind, in my heart. I would like to thank my dear brother Arvind Kumar Mishra. His unwavering support and encouragement have motivated me during both the highs and lows of this undertaking. Next, I extend my heartfelt appreciation to my loving wife Shweta Mishra. Her patience, understanding, and unwavering support have been my pillar of strength. Her belief in me and countless sacrifices made during this time have enabled me to focus on my work with utmost dedication and determination. I am truly grateful for her love and encouragement throughout this challenging process. I am also indebted to my beloved son Sankalp Mishra, whose innocence and infectious laughter brought light into my life even during the most demanding phases of Ph.D.

During my teaching assistantship, I got unflinching support from Mr. Ravindra Kumar, Mr. Ashok Saini, Mr. Tulsiram Sharma, Mr. Mahesh Chandra, and Mr. Manoj Jangir for the successful course delivery. I extend my sincere gratitude to Mr. Yogesh and Mr. Sanjay Bhargava for dealing with all the documentation required for a research scholar. They always made cumbersome processes trouble-free.

It is a great pleasure for me to acknowledge and express my appreciation throughout my research work to all my good wishers for their understanding, relentless support, and encouragement. Last but not least, I would like to express my sincere gratitude to all those who helped me directly or indirectly at different stages of this work.

I would like to thank all my peers and seniors for their support and inspiration during the gamut of adverse times and for helping me to overcome such impasses. I would cherish happy moments spent with my friends at the BITS Pilani campus for my whole life.

Akhilesh Kumar Mishra

Abstract

Future sustainable development tends to rely on how we achieve sustainable energy goals, requiring quick and comprehensive adjustments throughout the energy system. The globe has been pushed to include renewable energy sources (RESs) for energy production because of concerns about global warming and the depletion of fossil fuel sources. Solar and wind power plants have been utilized to fulfill the energy needs of remote locations due to the difficulty in transporting electrical power during the early stages of electrification. Integrating renewable energy sources into the existing power system is exceedingly difficult because of their unpredictable energy generation pattern.

The load frequency control structure has undergone various changes from its inception to cope with alternations made in the power system due to increasing power demand for sustainable growth of the world. Further, meeting the exponential energy demand and integrating renewable energy sources makes the load frequency control problem highly complex. Integrating wind energy units with existing interconnected power systems (IPS) has enormous advantages, but certain complications must be addressed sensibly.

The traditional load frequency control approaches are insufficient to address issues caused due to increased complexity of the power system and integration of renewable energy sources. Hence, intelligent control strategies should be implemented to address the power system's inherent nonlinearities and unmodeled system dynamics. This thesis investigates a self-tuned fractional order fuzzy PID (STFOFPID) controller for effective load frequency control in a multi-area power system. The investigated control structure efficacy has been evaluated under different scenarios, including parametric system variation and random step load perturbation. The OPAL-RT 4510, based on the Xilinx Kintex-7 FPGA board with an INTEL multi-core processor as a real-time digital platform, has been used for evaluating investigated controller performance.

Further, with the integration of wind power plants (WPPs) into the existing power system grid, the inertia of a power system significantly reduces. Inherently WPPs do not participate in frequency regulation as they are decoupled from the grid frequency through power electronics-based interfacing devices. In this thesis, the inertial and

deloading methodology has been explored for frequency support from WPP. When there is an increase in load demand, the system frequency accordingly decreases and is responsible for activating the inertial control scheme as it utilizes the deviation in frequency as the input signal. The controller provides a control signal, which in turn is going to increase the reference power setting or increase in reference torque setting of WPP. To compensate, the required torque setting speed of the rotor eventually starts decreasing with the release of stored kinetic energy in the rotating mass of WPP. The inertial control scheme has been employed with a dual-layered tilt-integral control structure as a secondary control structure. The inertial control scheme can provide frequency support for the short-term duration from the WPP and enhances the load frequency control performance.

Moreover, the deloaded or derated operation of a wind turbine generator (WTG) can provide a power margin, which can be utilized during power system contingency events for long-term frequency support. During deloading operation, a WTG is operated lower than its maximum power operating point at overspeeding conditions. Linear and quadratic deloading are the existing methods for long-term frequency support from WTG. The wind turbine generator has nonlinear power versus speed characteristics. Hence, in order to generate accurate reference active power, a higher-order Newton's interpolation polynomial (HNIP) based nonlinear deloading approach for WTG has been proposed in this thesis. Also, the advancements in neural networks for time-series effective data prediction techniques open the opportunity for accurate prediction of intermittent wind speed. These prediction approaches can be utilized to improve the overall performance of the power system.

Further, to improve the deloading performance, an adaptive nonlinear deloading strategy has been implemented. The deloading amount adaptation has been performed according to wind speed between 0 to 20%. The wind speed is required in advance to implement the adaptive nonlinear deloading. Hence, a recently devised forecasting methodology based on deep learning has been utilized to predict the wind. The deep learning assisted nonlinear adaptive deloading (DL-AND) strategy has been proposed for IPS and its performance has been investigated under nominal and parametric variations. The proposed DL-AND strategy provides improved dynamic performance and has superior frequency regulation.

Table of Contents

List of Figures

List of Tables

List of Abbreviations and Symbols

ACE	Area control error
AGC	Automatic generation control
ANFIS	Adaptive neuro-fuzzy interface system
ANN	Artificial neural network
BESS	Battery energy storage system
BFOA	Bacterial foraging optimization algorithm
CES	Capacitive energy storage
DFIG	Doubly fed induction generator
DG	Distributed Generation
DLTFCS	Dual-layered tilt fuzzy control structure
DL-AND	Deep learning assisted adaptive nonlinear deloading
FFOPID	Fuzzy FOPID
FOPID	Fractional order PID
FIS	Fuzzy inference system
FTIDN	Fuzzy tilt integral derivate with filter
GA	Genetic Algorithm
GDB	Governor deadband
GRC	Generation rate constraint
GTTP	Geo-thermal power plant
GSC	Grid side converter
HNIP	Higher order Newton's interpolating polynomial
IPS	Interconnected power system
ITAE	Integral time absolute error
IRNEA	International renewable energy agency
LFC	Load frequency control
LSTM	Long short-term memory
MPPT	Maximum power point tracking
NRTPU	Non reheated thermal power unit
OM	Oscillatory measure
PFC	Primary frequency control

pu	Per unit
puMW	Per unit Megawatt
PMSG	Permanent magnet synchronous generator
PSO	Particle swarm algorithm
RDSP	Real-time digital simulator
RES	Renewable energy resources
RFB	Redox flow battery
RNN	Recurrent neural network
RSC	Rotor side converter
RSLP	Random step load perturbation
RTTP	Reheated Solar-thermal power plant
SIL	Software in loop
SMES	Superconducting magnetic energy storage
SSA	Salp swarm algorithm
STFOFPID	Self-tuned fractional order fuzzy PID
SWP	Step wind profile
TIDN	Tilt integral derivative with filter
VSWT	Variable speed wind turbine
WPP	Wind power plant
WTG	Wind turbine generator
a	Control area capacity ratio
A	Swept area
B	Frequency bias constant
C_p	Power coefficient for wind energy
D	Load frequency constant
Δf	Deviation in frequency
J	Performance index or Objective function
H	Inertia Constant
K_{PS}	Power system gain
K_r	Reheater gain for reheated thermal power unit
K_{st}	Gain for solar thermal field power unit
K_{RFB}	Gain of redox flow battery

K_{Pf}	Proportional gain of inertial PD controller
K_{Df}	Derivative gain of inertial PD controller
ΔP_{tie}	Deviation in tie-line power
ΔP_G	Deviation in generated power
ΔP_m	Deviation in mechanical power
ΔP_D	Deviation in the load
P_r	Rating of an area (MW)
Pm	Mechanical power developed by wind turbine generator
R	Speed frequency regulation constant
$R_{\omega t}$	Rotor radius of turbine
T_G	Governor Time constant
T_T	Turbine time constant
T_{PS}	Power system time constant
T_{ji}	Synchronizing power coefficient of tie-line
T_{grt}	Governor time constant for reheated thermal power unit
T_{trt}	Turbine time constant for reheated thermal power unit
T_r	Reheater time constant for reheated thermal power unit
T_{gst}	Governor time constant for solar thermal power unit
T_{tst}	Turbine time constant for solar thermal power unit
T_{st}	Time constant for solar thermal field power unit
T_{ggt}	Governor time constant for geothermal power unit
T_{tgt}	Governor time constant for geothermal power unit
T_{RFB}	Time constant of redox flow battery
T_W	Time constant for washout filter
ΔX_G	Governor Valve displacement
λ_t	Tip speed ratio
β	Pitch angle
λ_c	Tip speed constant
v	Wind speed
ρ	Air density
σ	Variance

Chapter 1: Introduction

1.1 Background:

The energy demand is increasing exponentially to achieve future goals for industrial development and domestic needs. As we know, a major part of electrical energy is generated through conventional sources, i.e., fossil fuels. Fossil fuel-based sources of electrical energy generation are primarily responsible for greenhouse gas production and global temperature increase. Even though the 1.8^0 Fahrenheit rise in the world's average surface temperature from the pre-industrial era (1880-1900) may not seem like much, however it represents a huge increase in the amount of heat accumulated. The sea level is increasing by 3.3 millimeters per year while the mass of the polar ice sheets is decreasing by 413 gigatons annually. Moreover, the arctic ice is disappearing quickly, with 12.8% each decade [1-3].

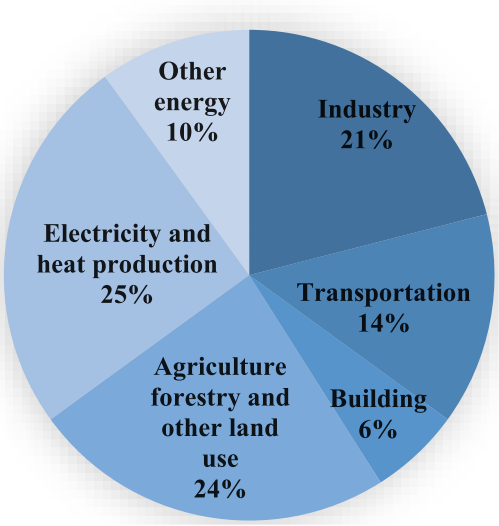

Fig. 1.1 *Greenhouse gases stake in economic activities*

Figure 1.1 shows the greenhouse gases share according to different economic activities and electrical energy generation has a significant amount. Hence it is a need of the hour to replace fossil fuel based electrical energy generation with renewable energy sources (i.e., wind, solar, geothermal, and others) to address the issues regarding global climate change. In November 2022, at the 27th Climate change conference (COP27) summit in Egypt, India committed to reduce its projected total carbon emissions by 2.5-3 billion

tonnes by 2030, to reduce the country's economy carbon intensity to less than 45% by the end of the decade, and to achieve net-zero carbon emissions by 2070 [4].

Henceforth, several renewable energy sources have been introduced into the existing grid. The global renewable sources installed capacity has increased by 122.6% within a decade from 2011 to 2021, as shown in Fig 1.2. It can be observed that wind and solar renewable energy sources have been widely used and show a growth of three times and ten times, respectively, in the previous decade. Figure 1.3 represents the top ten countries' renewable energy sources installed capacity, and India stands fourth with 151.907 GW installed capacity [5].

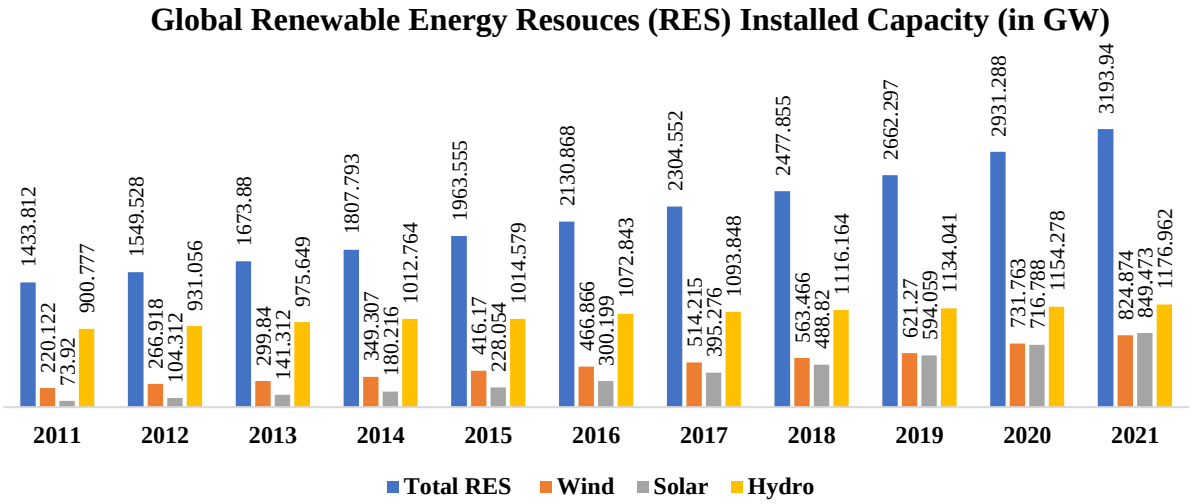

Fig. 1.2 *Expansion of global installed capacity of renewable energy sources in a decade*

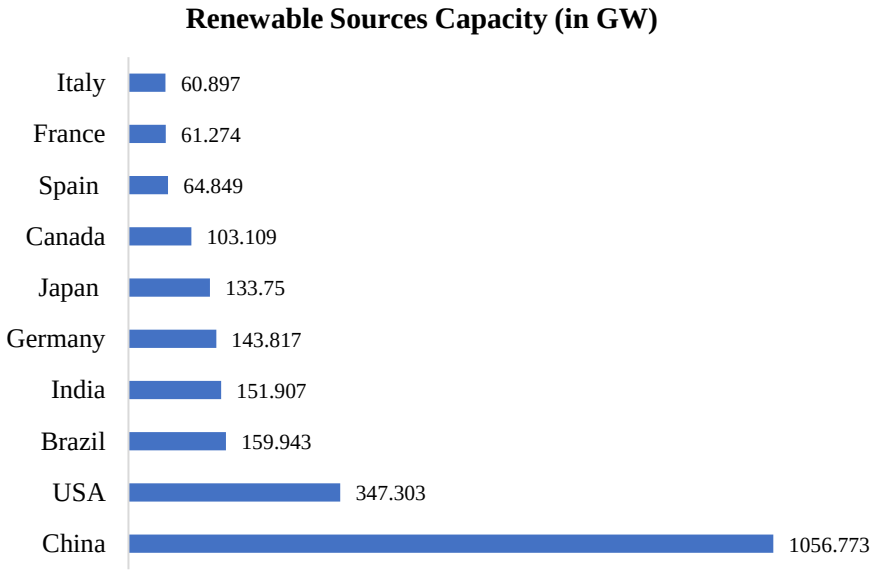

Fig. 1.3 *Top ten countries according to renewable energy sources installed capacity*

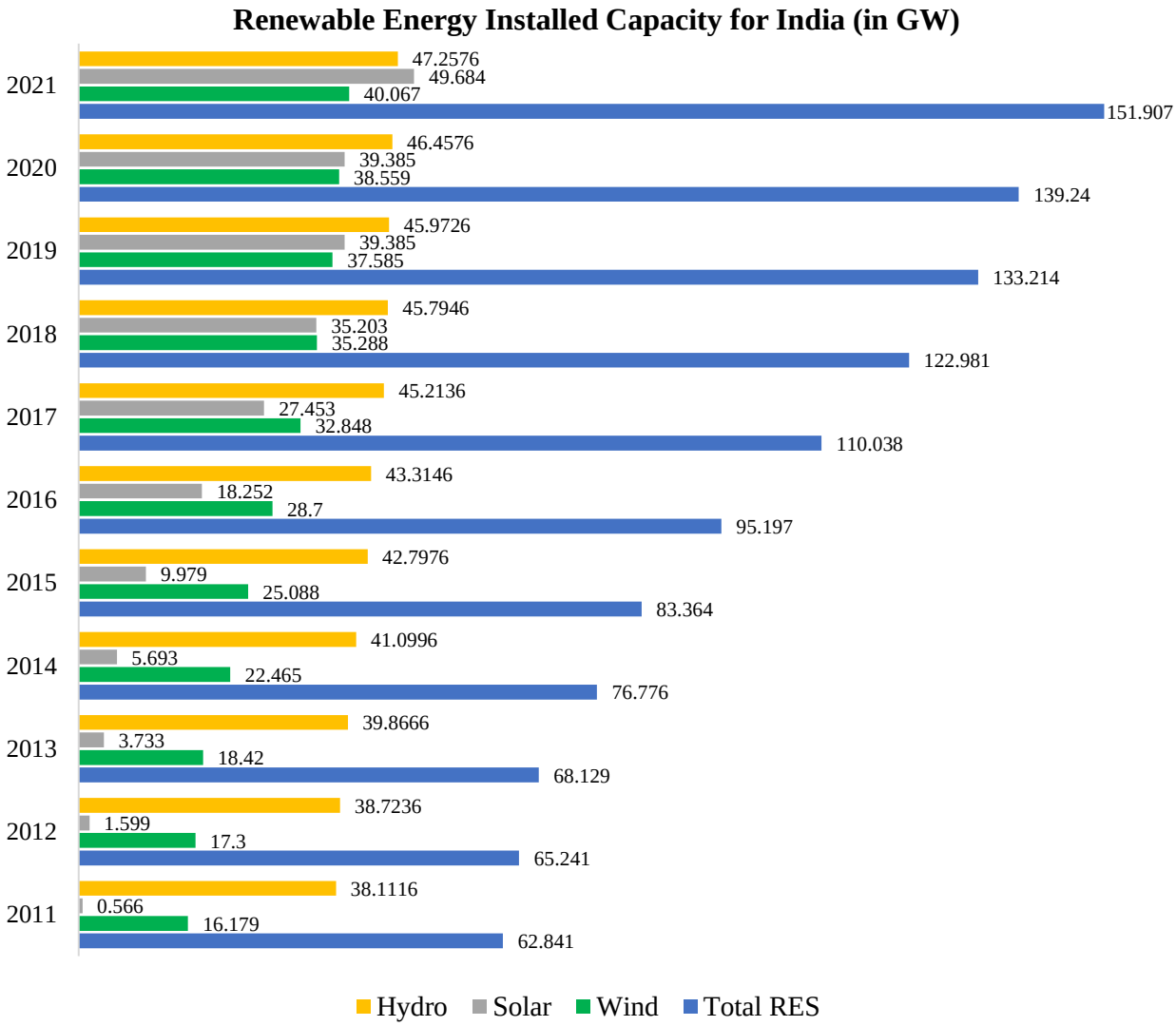

Fig. 1.4 *Expansion of Indian renewable installed capacity of renewable energy sources in a decade*

Further, the installed capacity of RESs has increased from 62.841 GW to 151.907 GW in the last decade (2011-2021) [6]. India has increased its wind installed capacity from 16.179 GW to 40.067 GW in the same duration as presented in Fig. 1.4. It is needed to mention here that the wind energy installed capacity is close to the solar during the previous decade. The above presentation shows that electrical energy generation is shifting from fossil fuel to renewable energy sources to address the global climate change issue. Wind energy is one of the prominent options for clean electrical energy generation; hence, it should be integrated with the existing power system for its reliable operation. The subsequent subsection briefly presents the interconnected power system configuration for the integration perspective of RESs.

1.1.1 Interconnected power system:

During the early stage of the power system, different power generation units are operated independently without inter-connection with other power generating units. The association of generating unit, control unit, and connected load forms a control area that independently operates to fulfill its area load demand in real-time by altering the generation or curtailing the load. However, the independent operation of different control areas in an electrical power system has various issues which the interconnection of different control areas can address through tie-line. In the case of independent control area operation, a sufficient stand by capacity generation unit must be present to handle any power system contingency scenario. The reserve plant capacity decreases significantly by interconnecting the various control areas through a tie-line. The two or more isolated control areas must be interconnected through tie-lines to enhance their intended operations' reliability and continuity.

A typical interconnected multi-area power system has been represented in Fig. 1.5, where 'H_i', 'D_i', 'T_{Gi}', 'T_{Ti}', 'R_i', 'B_i', and 'P_{ri}' are inertia constant, load frequency constant, governor time constant, turbine time constant, speed frequency regulation constant, frequency bias constant and MW rating of 'i^{th}' control area respectively [7][8]. Further, 'Δf_i', 'ΔP_{tie}', 'ΔP_{Gi}', and 'ΔP_{Di}' are the frequency deviation, tie-line power deviation, generator power deviation, and Load deviation in 'i^{th}' control area, respectively.

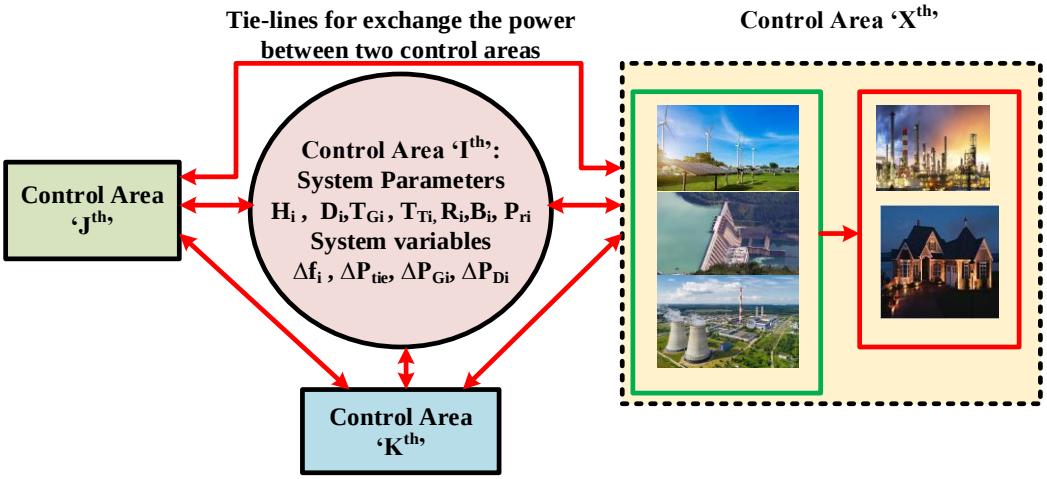

Fig. 1.5 *Multi-area interconnected power system*

The electrical power system consisting of different generating and load units with speed governor mechanisms to synchronize the generation and load demand is commonly referred to as the control area. Further, if the peak load demand exceeds the capacity of the control area, then it can be fulfilled by another control area in an interconnected power system. An interconnected power system needs to have an efficient load frequency control structure to maintain the system's stability and economical operation. Further, the global climate is adversely changing due to the increase in the production of greenhouse gases to meet the goals of world economic growth. Hence, electrical power systems should also participate in resolving climate change issues by integrating clean energy generation strategies. The integration of renewable energy resources, i.e., wind energy, has enormous potential to meet our ever-increasing global energy demand without producing greenhouse gases. However, many difficulties are involved in integrating RESs with existing interconnected power systems. The subsequent subsection presents the challenges faced while integrating RESs into the existing grid.

1.1.2 Challenges in the integration of RESs:

The usage of RESs is subject to several restrictions and constraints in addition to all their benefits and global accessibility. Different renewable energy sources' inherent characteristics are responsible for the slowdown in the growth of their integration with the grid. Natural topographical restrictions on the production of geothermal energy and hydropower exist throughout the planet. For storage, biomass needs a lot of natural resources. Under these restrictions, installing solar and wind power systems is a superior option. These sources, however, are sporadic in nature. The kind of turbine, wind density, and wind speed affect how much electricity can be produced by wind. If the wind speed is too high (>25 m/s), turbines must be shut down for safety reasons. If the wind speed is too low (2.5 m/s), it cannot generate power. Contrarily, solar PV output relies on the local light level, which changes from hour to hour, season to season, and is influenced by clouds.

One can use either the wind or the solar power plant, depending on their location and energy requirements. Making the wrong decision based on location can cause a huge financial loss. Experts in the field of renewable energy can offer assistance in

assessing the situation and guidance on the best form of renewable energy to use. One may perform better than the other in some circumstances. Approximately 48,704 solar panels can produce the same power per kWh as a wind turbine. It may be erected on already-existing ranches or farms. Since it only consumes a small portion of the land, it has little impact on the farmers. The ability to convert sunshine into useful power determines how effective solar panels and wind turbines are. Only approximately 22% of the energy captured from sunshine is converted into electrical energy by solar panels, even the most effective ones. Wind turbines have the capacity to transform up to 60% of wind energy into useful electrical energy. The main advantage of wind power plants is that they can produce electricity for the whole day, while solar power plants operate only during day sunshine [9][10].

When solar PV systems are connected to the grid naturally, they do not offer any inertia. Furthermore, power electronic converters connect variable wind turbines, which decouples the wind turbines from the grid frequency. Therefore, the equivalent power system's inertia is reduced by replacing traditional power plants with RESs. The United Kingdom's power system inertia would decrease by up to 70%, as estimated for 2014 to 2034 [11]. Due to their modest inertia constants, the primary technical problems with these new RESs are frequency and overall power system stability.

Given its abundant availability and ease of use, generation entities worldwide consider wind energy a prominent choice for electricity production. Wind power plants also offer lower maintenance costs than other renewable energy sources. Since established and well-understood techniques are often used to harness the electrical energy from the wind, such as doubly-fed induction generators (DFIGs) or permanent magnet synchronous generators (PMSGs). The energy sector has adopted DFIG-based wind turbine generators to produce clean electricity [12] [13]. However, its integration with the existing grid has serious issues, which should be addressed to operate the electrical power system efficiently and economically.

1.2 Motivation:

Wind energy has become an essential part of electrical power systems due to excessive investment by numerous countries that invested heavily in reducing the carbon footprint. Conventionally the inertia of an electrical power system is calculated

by taking all the rotating mass connected directly to the electric grid. Electrical power system dynamic characteristics have changed significantly during the past twenty years due to the integration of renewable energy sources, particularly solar and wind power plants. The inertia of the existing grid tends to reduce with the integration of renewable energy resources. The fundamental cause of the reduction in the inertia of the power system is that most renewable energy sources have power electronics devices involved at the grid interface. Integrating such a huge amount of renewable energy into the existing grid without any prior arrangement of frequency support strategy can hamper the reliability and stability of the electrical power system. If the reduction in system inertia is significant, then sudden alteration in operating conditions of the power system can even cause a system failure.

The load frequency control mechanism is used to maintain the synchronism of load demand and power generation in real-time for stable operation of the electrical power system. In the presence of renewable energy sources inertia of the power system gets reduced, and it is difficult to maintain the synchronism in load demand and corresponding generation. Renewable energy sources, i.e., wind power plant, does not alter their generation with change in the system frequency, unlike the conventional generating unit due to the involvement of power electronics devices with its grid interface. The doubly-fed induction generator (DFIG) has been utilized as a wind energy conversion system to reduce the carbon footprint in electrical power systems. Integrating the wind power plant with the existing power grid has certain challenges, i.e., power system stability due to its inability to inherently participate in frequency regulation.

Further, the electrical power system has benefited from advancements in soft computing and artificial neural network-based prediction approaches. The performance and reliability of power systems have been significantly enhanced by including these approaches with extreme accuracy in forecasting various quantities of intermittent renewable energy resources, i.e., wind and solar.

1.3 Problem description:

The load frequency control must take place as quickly as feasible for the power frequency balance. The generation within each control area must be managed to sustain

planned power exchange in an interconnected power system. Two control loops for primary and secondary control are present in the control systems. The power system uses a turbine-governor system to implement the primary control action. The steady-state frequency error can still be present with primary control action. Consequently, this basic level of control is insufficient for interconnected power systems. The second level of generation control, also known as secondary or supplemental control, is offered, consisting of two or more control areas.

Central and local load frequency controllers are used to control active power through the tie line connected between different control areas. The complexity of the secondary control structure increases with the integration of renewable energy sources, such as wind power plants, due to their intermittent power production. Further control problem becomes complex due to their inherent noncooperation in the frequency support mechanism. Hence, it is essential to have a frequency support mechanism for such sources before integrating them into the grid. Figure 1.6 shows the frequency control hierarchy for an interconnected power system in the presence of a renewable energy source. It is evident that the frequency nadir can be significantly reduced with the employment of frequency support mechanisms in renewable energy sources [11].

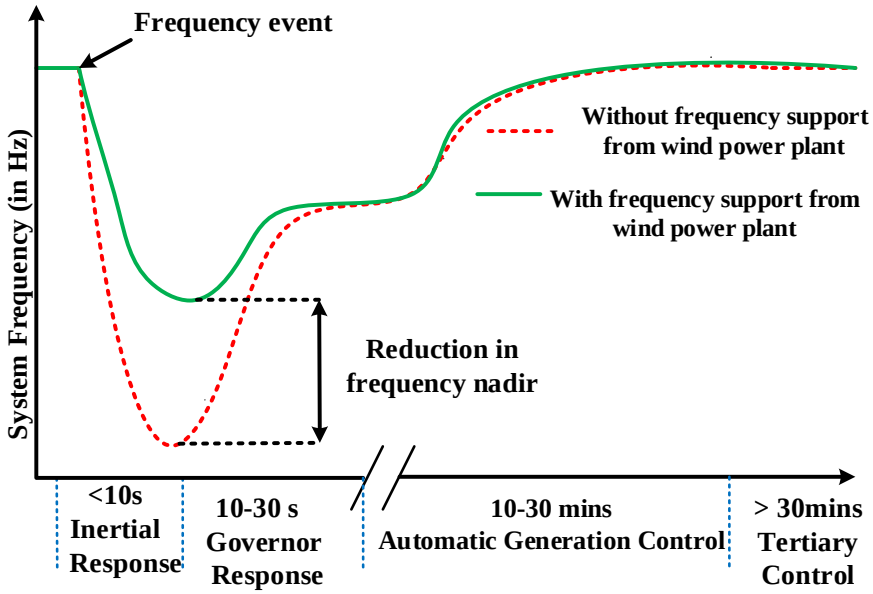

Fig. 1.6 *Frequency control types and corresponding time frames in the interconnected power system in the presence of renewable energy sources* [14]

The equivalent inertia of the power system can be significantly reduced in the presence of renewable energy sources and cause a sharp change in the system frequency corresponding to a sudden load alteration. If load demand and generation synchronism fail to occur within the prescribed time frame, it can result in a blackout for the system due to the operation of protective devices.

The reserve capacity of a power system can be increased by interconnecting several isolated power systems into a common grid. However, as the penetration from renewable energy sources significantly increases, the reserve capacity is also hampered due to the sporadic nature of their generation, even in interconnected power systems. Renewable energy sources have the tendency to operate their maximum generation capacity with the help of power electronics devices. Such operation mechanism restricts them from participating in frequency regulation like conventional energy sources under power system contingencies [15][16]. Hence, for stable and reliable power system operation, renewable energy sources must be equipped with frequency support strategies. The frequency support mechanism can create a reserve power margin, which can be utilized during sudden load mitigation and enhancement of the overall system performance. A few works regarding short-term frequency support from the wind power system have been reported. However, long-term frequency support is required from such sources for the reliability of the overall power system, and the same can be achieved through the deloaded operation of the wind power system. It is necessary to mention that very little work has been reported for frequency support from wind power systems through deloading. Linear and quadratic deloading has been proposed and found suitable for frequency support in microgrid scenarios [17][18]. However, a nonlinear deloading methodology can be a candidate solution due to the nonlinear behavior of wind turbine generators to precisely implement the deloading.

The constant deloading factor is utilized for previously proposed linear and quadratic deloading approaches, in which the deloading factor has been kept constant irrespective of wind speed. It is evident that for the lower wind speed, the operation of the WTG can be uneconomic due to its overutilization in the frequency support scheme. On the other hand, at higher wind speeds, the ability of the wind to support the grid under any contingency event can be underutilized. These snags of the constant deloading approach can be addressed effectively by varying the deloading factor in

accordance with the wind speed to optimize the effective available power margin. Wind energy is intermittent in nature; hence, the amount of electrical power that can be harnessed from a wind turbine generator has sporadic behavior. The forecasting techniques can play an important role in ensuring the real time synchronism of generation and load with effective load frequency control implementation.

Further, the traditional load frequency control approaches are insufficient to address issues caused due to increased complexity of the power system and integration of renewable energy sources. Hence, intelligent control strategies should be implemented to address the power system's inherent nonlinearities and unmodeled system dynamics. The wind based electrical power generating units do not participate in frequency regulation when operated under nominal condition and reduces power system inertia. Hence, frequency support strategies must be developed for such sources for efficient integration with the grid.

1.4 Objectives of proposed research:

The objectives of the proposed research project work are as follows:

- ✓ Design of an intelligent load frequency control configuration for a nonlinear multi-area interconnected power system utilizing energy storage elements.
- ✓ Investigating short-term frequency support through wind turbine generators in interconnected power system with an efficient supplementary control design.
- ✓ Development of advanced and effective nonlinear deloading technique to realize frequency regulation through wind power plant.
- ✓ Hybridizing deep learning-based forecast scheme with nonlinear deloading approach for efficient operation of wind turbine generators.

1.5 Thesis organization:

The organization of the thesis is as follows:

Chapter-1 describes the introduction, background, motivation, and objectives of the research carried out in the thesis.

Chapter-2 describes an exhaustive literature review of state-of-art load frequency control techniques and integration of renewable energy sources and identifies research gaps.

Chapter-3 utilizes a self-tuning fractional order fuzzy control structure as a load frequency controller for a three-area interconnected power system. The presented control structure performance has been evaluated under system parametric variation and random step load perturbation. Further, this chapter also presents the real-time validation on a real-time simulator 'OPAL-RT 4510' for the presented scheme.

Chapter-4 presents the integration of DFIG based wind power plant with a two-area interconnected power system and studies the impact of an inertial frequency scheme with varying wind penetration levels.

Chapter-5 proposes a nonlinear deloading strategy for implementing the frequency support from the DFIG-based wind power plant in a two-area interconnected power system.

Chapter-6 presents the deep leaning assisted nonlinear adaptive deloading for enhancement of frequency support from the DFIG-based wind power plant in a two-area interconnected power system.

Chapter-7 concludes the research work by outlining its contributions and future scope for research.

References:

[1] NASA Climate Change, "Vital signs of the planet," 2019. [Online]. Available: url: https://climate. nasa. gov/vital-signs/global-temperature.

[2] H. O. Pörtner et al., "Climate change 2022: Impacts, adaptation and vulnerability," IPCC Geneva, The Netherlands, 2022.

[3] Z. Occhipinti and R. Verona, "Kyoto Protocol (KP)," Clim. Action, pp. 605–617, 2020.

[4] S. Mukherjee, "Exploring a Design of Carbon Tax for Coal-and Lignite-Based Thermal Power Sector in India," Rev. Mark. Integr., p. 09749292221103916, 2022.

[5] IRENA, "Renewable Energy Capacity Highlights," International Renewable Energy Agency, 2021. https://www.irena.org/publications/2021/March/Renewable-Capacity-Statistics-2021.

[6] Ministry of New and Renewable Energy, "Overview | Ministry of New and Renewable Energy, Government of India," Wind Energy, Government of India website, 2021. https://mnre.gov.in/wind/current-status/.

[7] C. E. Fosha and O. I. Elgerd, “The megawatt-frequency control problem: A new approach via optimal control theory,” IEEE Trans. Power Appar. Syst., vol. 4, pp. 563–577, 1970.

[8] A. Ibraheem, P. Kumar, and D. P. Kothari, “Recent philosophies of automatic generation control strategies in power systems,” IEEE Trans. Power Syst., vol. 20, no. 1, pp. 346–357, 2005, doi: 10.1109/TPWRS.2004.840438.

[9] R. M. Elavarasan et al., “A comprehensive review on renewable energy development, challenges, and policies of leading Indian states with an international perspective,” IEEE Access, vol. 8, pp. 74432–74457, 2020.

[10] A. Ahmed, T. Ge, J. Peng, W.-C. Yan, B. T. Tee, and S. You, “Assessment of the renewable energy generation towards net-zero energy buildings: a review,” Energy Build., vol. 256, p. 111755, 2022.

[11] M. A. Basit, S. Dilshad, R. Badar, and S. M. Sami ur Rehman, “Limitations, challenges, and solution approaches in grid-connected renewable energy systems,” Int. J. Energy Res., vol. 44, no. 6, pp. 4132–4162, 2020.

[12] M. Dreidy, H. Mokhlis, and S. Mekhilef, “Inertia response and frequency control techniques for renewable energy sources: A review,” Renew. Sustain. Energy Rev., vol. 69, November 2015, pp. 144–155, 2017, doi: 10.1016/j.rser.2016.11.170.

[13] E. J. Novaes Menezes, A. M. Araújo, and N. S. Bouchonneau da Silva, “A review on wind turbine control and its associated methods,” J. Clean. Prod., vol. 174, pp. 945–953, 2018, doi: 10.1016/j.jclepro.2017.10.297.

[14] G. V. B. Kumar, R. K. Sarojini, K. Palanisamy, S. Padmanaban, and J. B. Holm-Nielsen, “Large scale renewable energy integration: Issues and solutions,” Energies, vol. 12, no. 10, p. 1996, 2019.

[15] A. Fernández-Guillamón, E. Gómez-Lázaro, E. Muljadi, and Á. Molina-García, “Power systems with high renewable energy sources: A review of inertia and frequency control strategies over time,” Renew. Sustain. Energy Rev., vol. 115, p. 109369, 2019.

[16] M. Ranjan and R. Shankar, “A literature survey on load frequency control considering renewable energy integration in power system: Recent trends and future prospects,” J. Energy Storage, vol. 45, p. 103717, 2022.

[17] K. V. Vidyanandan and N. Senroy, “Primary frequency regulation by deloaded wind turbines using variable droop,” in IEEE Transactions on Power Systems, vol. 28, no. 2, pp. 837-846, May 2013, doi: 10.1109/TPWRS.2012.2208233.

[18] D. Kumar, P. Sharma, H. D. Mathur, S. Bhanot, and R. C. Bansal, “Modified Deloading Strategy of Wind Turbine Generators for Primary Frequency Regulation in Micro-Grid,” Technol. Econ. Smart Grids Sustain. Energy, vol. 5, no. 1, 2020, doi: 10.1007/s40866-020-00083-7.

Chapter 2: Literature Review

2.1 Introduction:

The independent operation of different control areas in an electrical power system has various limitations, which can be addressed by the interconnection of different control areas through the tie-line. In the case of independent operation, a sufficient stand by generation capacity must be present to handle any power system contingency scenario. In contrast, the reserve plant capacity can be significantly reduced by interconnecting the various control area through the tie-line. Further, if the peak load demand exceeds that of the capacity of the specified control area, then it can be fulfilled by other control areas in an interconnected power system.

The frequency of the electrical power system is primarily influenced by variations in loads. However, reactive power, associated with voltage magnitude, is less susceptible to variations in frequency. For this reason, active and reactive powers are managed independently. Active power and frequency management are more important for the stable and economical operation of the power system. The disparity in generation and load demand results in a grid frequency variation from its nominal value, which can be eliminated by enabling coordinated control of participating active elements in the different control areas along with exchangeable tie-line power in a multi-area system [1][2]. As a power system's frequency is associated with the synchronous generators' rotation speed, frequency stability is strongly tied to the generating unit's rotor speed regulation.

If sustained frequency oscillation in the power system is not addressed, it can lead to system deterioration, unacceptable relay functioning, and system blackout in the worst-case scenario. Several grid blackouts have occurred, including those in Brazil on March 11, 1999; Iran in the springs of 2001 and 2002; North American blackout on August 14, 2003; Switzerland and Italy on September 28, 2003; north-eastern India on July 30, 2012; Bangladesh on November 1, 2014; and Venezuela on March 7, 2019 (the world's longest blackout) [3]. Hence, a governor mechanism can be included to address this issue, which feedbacks the generator speed and adjusts the actuator input to modify the output power to follow the load fluctuation and improve the power system stability. The speed governor mechanism used in the power system for mitigating the frequency

and tie-line power exchange deviations by regulating the generator output is not an infallible solution. A speed governor mechanism in coordination with a supplementary controller, known as automatic generation control (AGC) or load frequency control (LFC), can offer constant frequency and constant tie-line power exchange and must be used to improve the dynamic performance of an interconnected electrical power system. An IEEE working group described the fundamental purpose of LFC as automatic tie-line power and frequency control. In [4][5], the first optimum controller synthesis for megawatt frequency (popularly known as load frequency regulation) regulation in multi-area power grids was published, which included two identical generation units with non-reheat thermal turbines.

Increasingly distributed generations (DGs) integrated through power electronics devices to meet the load demand cause new problems for frequency stability and power system management in today's power networks. Such integration of renewable energy resources by replacing the synchronous generators causes a significant reduction in the power system's rotational inertia. The grid frequency response and the efficacy of traditional load frequency control mechanisms may be adversely impacted by decreasing rotational inertia in a power system with increasing penetration of RESs. The existing approaches for load frequency control can result in frequency instability, load shedding, and possibly major frequency fluctuations. Load-power balancing and frequency management are exceedingly difficult due to the power grid's decreasing inertia caused by the large penetration of DGs with power electronic interfaces. This issue is greatly exacerbated by the unpredictability of renewable energy supply.

Further, this chapter provides a literature review with an emphasis on load frequency control structures in detail for interconnected power systems, as well as difficulties that occur during the integration of renewable energy resources into the existing system. The remaining chapter has been organized as follows; Section 2.2 reviews the traditional interconnected power system, the integration of renewable energy sources with the existing power system, and the associated impact of the integration of renewable energy resources. Section 2.3, the load frequency control strategies have been elaborated briefly along with various metaheuristic optimization algorithms. This

section also presents frequency support schemes for wind power plants. Finally, section 2.4 discusses the identified research gaps based on the extensive literature review.

2.2 Interconnected power system:

In traditional interconnected power systems (IPS), domination by a single utility company for electrical power generation, transmission, and distribution, affects its reliability and economic operation. To deal with these issues, the power sector has adopted various changes from its inception, and deregulation is one of them. In recent years, the power system has shifted from a vertically oppressive to a reformed, autonomous, and competitive paradigm.

A competitive environment in the power sector was created by deregulation in 1995 with a Notice of Proposed Rulemaking (NOPR) by the Federal Energy Regulatory Commission (FERC) [6]. The FERC designated various ancillary services for the power system's smooth operation in a deregulated scenario, where electrical power generation and consumption occur simultaneously. This condition can be balanced with one of the essential ancillary services designated by FREC, i.e., automatic generation control or load frequency control (LFC) [6]. Sweden and Norway were the first to adopt power sector restructuring. Customers should have a wider range of options, reasonable prices, and a superior level of quality are the key motivation behind the implementation of the deregulation in modern electrical power systems. The global population and associated electricity demand to fulfill day-to-day needs require an exponential increase in electricity generation with various power sources available.

The primary sources of electricity production use fossil fuels, which are responsible for the increase in greenhouse gases and adverse effects on the climate. Climate change and continuously decaying fossil fuels are the main push for the wider deployment of renewable energy technology. Concerns about climate change, which first surfaced in the late 1980s, have given a clean, low-carbon energy technologies, such as incorporating renewable energy into the current power generating system. Natural resources, including sunshine, wind, water, hydropower, biomass, geothermal resources, biofuels, and hydrogen, are used to generate renewable energy [7]. These sources do not produce greenhouse gases which are mainly responsible for increasing global warming.

Moreover, increasing the production of electricity from renewable sources can ease the burden on the current fossil fuel-based power generation. Governments all around the world are investing in infrastructure to create Micro-Grids that can deliver effective, affordable, and clean power to sparsely connected regions. Electricity is a basic requirement for social welfare and economic prosperity. In the majority of cases, the conventional power system offers dependable electricity. However, blackouts may be devastating and expensive when the grid is threatened by natural catastrophes or security breaches. A microgrid can effectively address the potential solution for combating electricity crises in rural and remote areas.

It can be referred from the above presentation that the penetration of renewable energy resources has significantly increased and have the tendency to increase its share in electrical energy generation in an exponential manner to meet the global energy requirement. Typically, a major portion of renewable energy resources available does not have inherent inertia or very lesser inertia as compared with traditional power generating sources. Hence, we must understand the possible adverse effect and associated solutions before integrating such sources of electricity production. Further, the subsequent subsection presents the different renewable energy resources and their integration impact on the existing grid.

2.2.1 Integration of RESs with IPS and associated impact:

As conventional energy sources are the dominant source of electrical power generation; nevertheless, these sources are rapidly diminishing and contributing to global climate change. According to a recent assessment by the International Renewable Energy Agency (IRENA), conventional energy sources now meet a considerable amount (nearly 75 percent) of the world's electrical energy demand [8]. It is evident that such sources have a significant role in increasing carbon footprint and, as a result, global warming. For decades, it has been well-known that using renewable energy has benefits for the environment, including lower carbon emissions and less air pollution. However, the numerous socio-economic benefits of renewable energy technologies have been experienced due to their widespread adoption.

The number of people without access to electricity exceeds one billion, and the number of people with intermittent power is approximately more than one billion in the

present global scenario. Stand-alone and mini-grid renewable power options are now financially feasible for the 80% of people without access to rural areas or modest developing island nations because of increased dependability, rapidly declining technological prices, and supporting policies [8][9]. Off-grid solutions' decentralization and the fact that project development activities take place locally encourage local employment creation, which is one of their strongest justifications. Air pollution is minimal or absent when using wind, sun, and hydropower. While a worldwide energy transition is in place, more effort is required to cut carbon emissions and lessen the consequences of climate change.

In comparison to most conventional fuels, renewable energy sources, including geothermal and biomass, create very less air pollutants. As 2.9 billion people still use wood, coal, and charcoal for cooking and house heating in many developing nations, air pollution has emerged as a major problem [10-13]. Cleaner alternatives, such as wind and solar technology, can be useful in this context. Renewable energy sources, without question, have shown enormous promise in combating these issues. Furthermore, current concerns about an impending global energy crisis and a push to combat climate change have resulted in a rise in the use of RESs that are naturally sustainable. Literature indicates that their contribution to fulfilling the world's electrical energy requirements has significantly boosted in the last two decades, contributing almost 25% of overall generation capacities. In 2021, India added 15.4 GW of new renewable power capacity, placing third behind China (136 GW) and the US (43 GW). India's installed renewable energy capacity was fourth in the world in 2021, and its installed wind and solar capacity were fourth and fifth, respectively [8]. Wind energy has shown great potential as a renewable energy source for electricity production, and India has also gained momentum.

The international energy agency believes that offshore wind has the potential to generate more than 420,000 TWh per year, which is around eighteen times the current world power consumption, making the market for offshore wind extremely lucrative. The total worldwide wind power capacity expanded fivefold between 2008 and 2018. The growth of wind energy in India has increased from 16.18GW to 40.067GW in a decade and is comparable with aggregate renewable energy source increment from 62.84Gw to 151.907 same time span (2011-2021) as presented in Fig.2.1[13]. The

government promotes wind power as clean energy and has identified various spots in India for wind farm installment purposes.

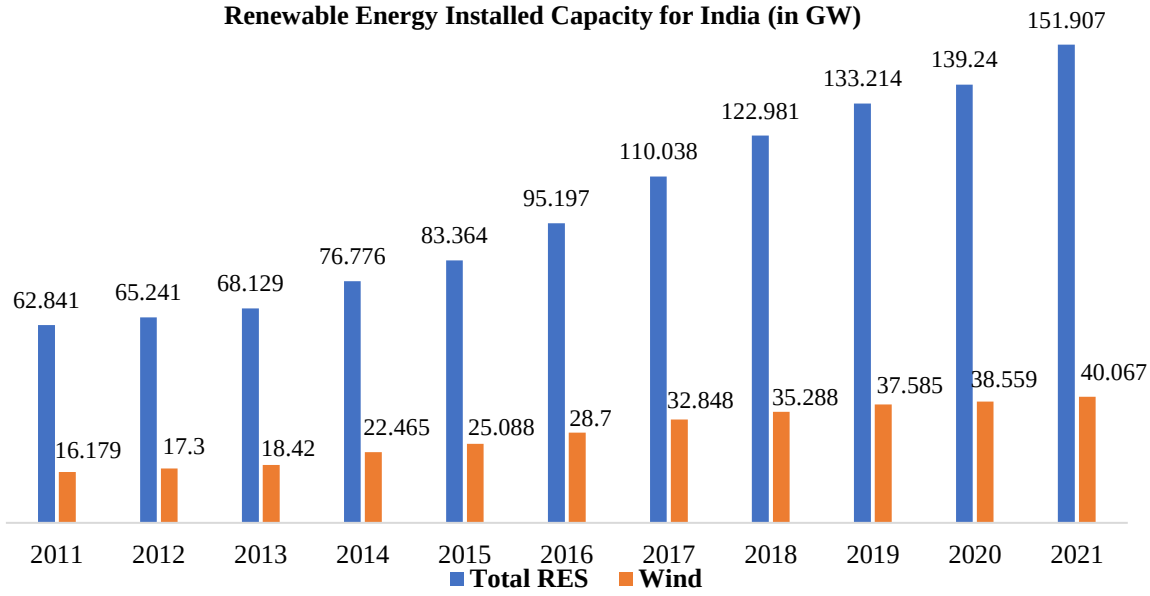

Fig. 2.1 *Expansion of India's installed capacity of renewable energy sources in a decade*

Figure 2.2 shows the wind potential of different states at 100 and 120-meter heights. The total wind potential in India is approximately 695 GW and 302 GW at 100m and 120m heights. Gujrat has enormous wind potential, as presented in Fig.2.2, with 84.43 GW and 142.56 GW at 100m and 120m, respectively, which is around six times of current installed wind energy capacity of India [13]. Wind energy can be converted to electricity by two popular mechanisms: permanent magnet synchronous generator (PMSG) and doubly fed induction generator (DFIG); later, one has an edge in terms of cost and operation.

Given the advantages of wind energy sources, integrating DFIG-based wind turbines with existing IPS is an increasing global trend [14]; however, this can cause a significant behavioral change in the IPS operation. The growing integration of power electronics-based distributed generators and loads poses new problems to frequency stability and regulation in today's power networks. As power electronics-based DGs and RESs rapidly replace synchronous generators, the major issues are caused by a reduction in system rotational inertia.

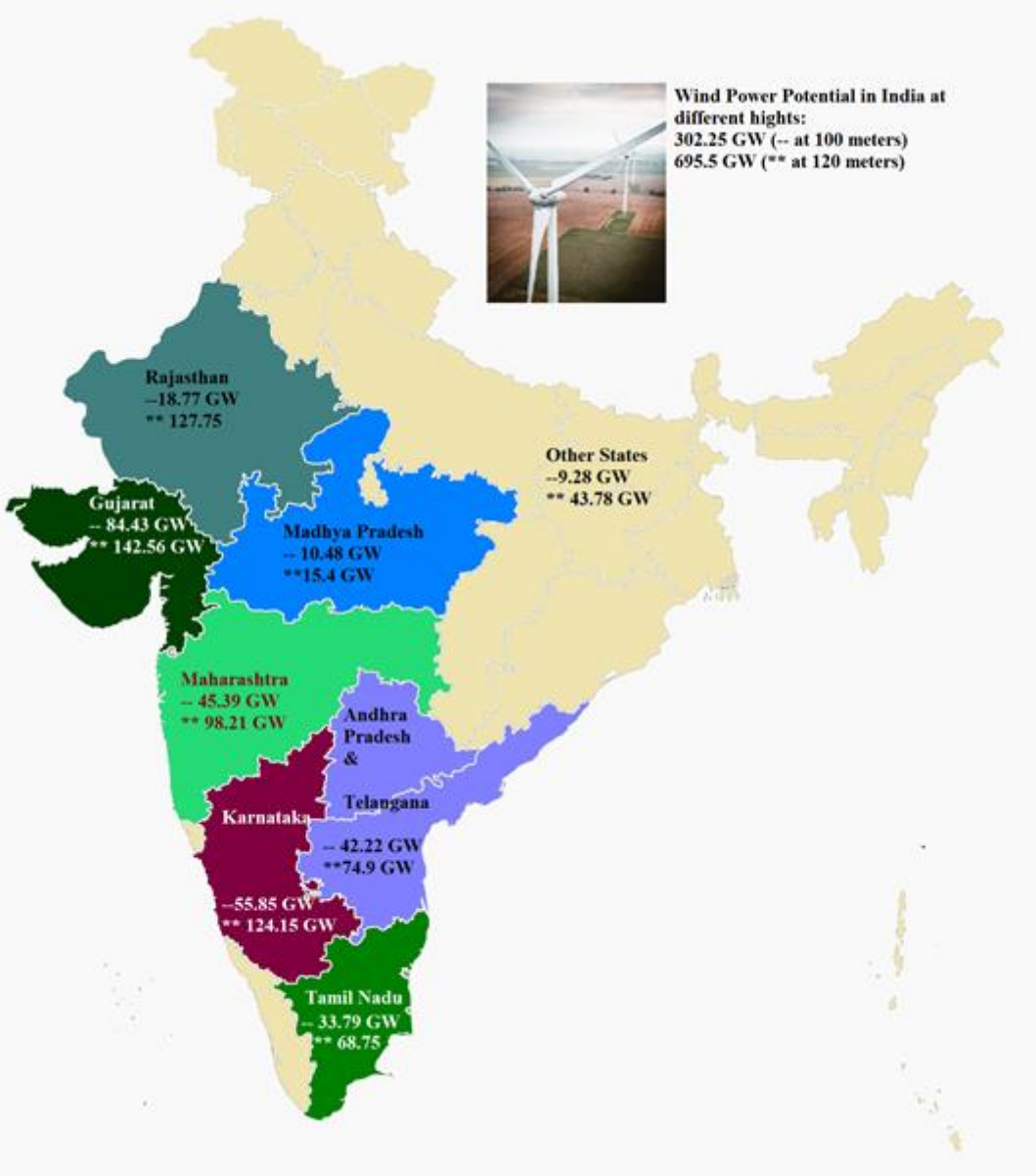

Fig. 2.2 *Wind power potential at 100 and 120m in different states of India [13]*

Reduced rotational inertia in a power system can have a detrimental impact on grid frequency response and diminish traditional frequency control capability and performance. Various research works have been reported lately, which study the impact of the integration of DFIG-based wind turbines with IPS. These unanimously suggest that variable speed wind turbine (VSWT) does not contribute towards load frequency restoration when IPS is subjected to load disturbances, primarily due to the presence of power electronics converters [15][16]. It has also been noted that increased penetration from DFIG-based wind power plants (WPP) reduces the equivalent inertia of the IPS

and hinders achieving optimal load frequency regulation [17]. Load-power balancing and frequency regulation are becoming increasingly difficult as power grid inertia decreases owing to the widespread use of power electronic interfaced DGs. This clearly points to a conclusion that the integration of DFIG-based wind energy conversion systems with existing IPS have enormous advantages but have certain complications as well, which must be addressed sensibly. It is evident from the above discussion that an optimal load frequency control structure is required for the efficient operation of the overall electrical power system with consideration of the system's inherent nonlinearities and intermittency of generation in the presence of renewable sources. Hence, the detailed load frequency control structure review has been presented in the subsequent section.

2.3 Load frequency control:

The power system is a dynamic system where various active elements are connected via power lines, commonly referred to as tie lines. Its goal is to deliver power to a variable load or ensemble of consumers, which is one of its critical parts. The frequency of the electrical power system is primarily affected by changes in loads (active power). At the same time, the reactive power is controlled by voltage magnitude and is less susceptible to variations in frequency. The frequency control and voltage control do not interact with each other, and hence both can be managed independently. Here we can focus on frequency control through active power management of the electrical power system. One of the key actions for the effective management of any electrical system is automatic generation control (AGC), also known as load frequency control (LFC). LFC's objective is to provide signals for controlling the load frequency controller and the active power output of various generating units within the boundaries of the prescribed control area in response to changes in system frequency and tie-line power [4]. It also assists in maintaining the scheduled system frequency and establishing interaction with other areas.

Further, the electrical power system considered for the LFC will usually be subjected to small changes in load demand. Hence, it is usually linearized around the operating point and appropriately represented by the linear model. A multi-area power system can be constituted by interconnecting individual control areas through tie lines. Every

individual control area of the power system is essentially equipped with a speed governing mechanism, turbine, and generator. The block diagram of any control area, for example, 'j^{th}' area of an interconnected multi-area power system, is shown in Fig. 2.3.

Where 'R_j', 'B_j', 'T_{Gj}', 'T_{Tj}', 'T_{PSj}', and 'K_{PSj}' is the governor speed regulation or droop constant, frequency bias constant, time constant of speed governor control mechanism, time constant for non-reheated steam turbine, time constant of generator and load system and generator and load system gain of area 'j^{th}' respectively. Further, 'Δf_j', 'ΔP_{Dj}', 'ΔP_{mj}', and 'ΔX_{Gj}' is the frequency deviation, step load perturbation, mechanical power deviation, and governor valve displacement of area 'j^{th}'. The ΔP_{tie-ji}, 'a_{ji}' and 'T_{ji}' are tie-line power deviations, the negative ratio between rated megawatts, and synchronizing power coefficients of tie-line connected between area 'j^{th}' and 'i^{th}', respectively. The control signal, which drives the load frequency controller to maintain the balance between generation and load demand in real time is known as the area control error. From Fig. 2.3, the area control error (ACE) for 'j^{th}' area can be given by Eq. (2.1)

$$ACE_j = B_j * \Delta f_j + \Delta P_{tie-ji} \tag{2.1}$$

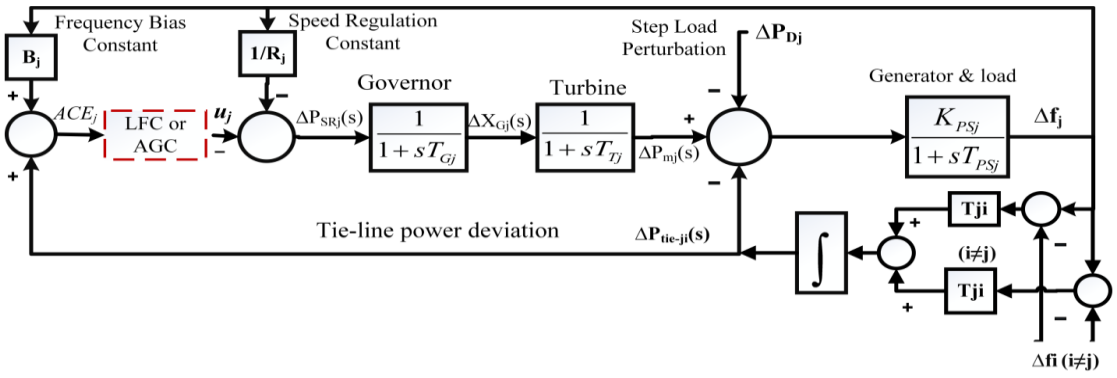

Fig. 2.3 *Interconnected power system with load frequency control (LFC) or automatic generation control*

A step load perturbation applied to any control area causes the mismatch between the active power generation and load demand plus losses. Due to a mismatch in active power, the frequency can deviate from its nominal value. Frequency deviation causes a change in the scheduled power transfer between control areas. Load frequency controllers are designed to restore frequency and tie-line power to their nominal values.

The area control error can act as an input signal for load frequency control purposes and produces corresponding controller output.

The goals of LFC are to guarantee that the frequency variation returns to zero with minimum deviations in the tie-line power flows, which are used as the control variables. The tie-line power flow out of each area should be maintained at the anticipated value using a control system technique that retains the frequency at the nominal level. The control action should be applied in such a manner so that under steady state conditions individual control area should be capable of fulfilling its area load demand. In this regard, numerous control structure has been designed and implemented for effective load frequency control. The load frequency control structure has gone through various changes from its inception to cope up with alternations made in the power system due to increasing power demand for sustainable growth of a country and world. Further, meeting the exponential energy demand and integrating renewable energy sources makes the load frequency control problem highly complex. A brief literature survey of load frequency control structures from the early stage to the current complex structure of the electrical power system has been presented in the subsequent subsection. The review for load frequency control structure has been primarily divided into two parts, i.e., for traditional electrical power systems and electrical power systems after the integration of renewable energy sources.

2.3.1 Control structure for traditional electrical power system:

2.3.1.1 Classical control structure:

In order to reduce the area control error (ACE) in power systems and improve the frequency response, conventional control techniques often apply classical controllers to the governor mechanism of generating unit respective control area. In practice, many electric power systems use the classical control methodologies for LFC since they have been thoroughly studied for LFC in power systems. A number of traditional control techniques have been put out in the past for the effective operation of the power system [9], [18-22]. Customary control structures employed for LFC are based on integer order (IO) controllers, which are typically used to regulate the governor and reduce the area control error of the electrical power system to enhance

frequency regulation. In both conventional and microgrid environments, several studies demonstrated the LFC technique employing I/PI/PID controllers [23-26].

Anwar and Pan propose a direct synthesis design of a novel PID controller as an LFC structure [27]. The effectiveness of the proportional plus integral and double derivative (PIDD) control structure has been demonstrated through comparisons between the performance of numerous classical controllers, including the I/PI/PID and integral plus double derivative (IDD) controllers [28].

The GDB and GRC can cause a significant deterioration in power system performance due to sustained oscillation and increased settling time of frequency and tie-line power exchange responses. To address such issues, Tripathy *et al.* [29] used the Lyapunov method to optimize the integral gain and tie-line coefficient of a two-area power system with GDB. In contrast, Gozde and Taplamacioglu [30] used the multi-objective evolution algorithm and the swarm optimization (PSO) algorithm to optimize the proportional-integral (PI)-type LFC controller. The design process for the traditional solutions to the LFC problem is simple, easy to understand, and suitable for real-world application. However, the analyses carried out using these methods show that they have poor dynamic performance, especially in the presence of additional destabilizing influences, such as parameter fluctuations and nonlinearities [31][32]. Hence, the subsequent subsection presents the optimal control approaches utilized as load frequency control structures.

2.3.1.2 Optimal control techniques:

The heuristic-based parameter modifications have been employed in the majority of traditional LFC techniques. As a result, they are not suitable for offering adequate dynamical performance under a variety of operating situations. The optimal control strategy requires the state space model of the system under consideration for its control and achieves the desired control objective through the minimization of the prescribed function. Further, an optimal control approach can be employed for such a system in which every state variable is available for measurement. The design of load frequency controllers that can optimally regulate both frequency and tie-line power variations has been done during the past four decades using contemporary optimum control theory [5], [33-36]. Moreover, for an interconnected power system having non-

reheated thermal generating units, Fosha and Elgerd proposed a novel feedback control scheme using a state variable model for load frequency control using optimal control approach [5]. Suboptimal automatic generation control regulator designs were taken into consideration in order to overcome the practical restrictions on the implementation of regulators based on full order state feedback [37-39]. The optimal control approach for the load frequency control implementation is not feasible for grid connected power systems, which can have a commonly large number of state variables. Further, the subsequent section explores the adaptive control schemes for load frequency control applications for the electrical power system.

2.3.1.3 Adaptive control techniques:

For more than three and half decades, adaptive control has been a subject of study. Self-tuning regulators and model reference control systems are the two broad groups into which adaptive control systems fall. The objective of the adaptive control approach is to reduce the sensitivity of the controlled process to changes in plant parameters and nonlinear plant dynamics. The system's operation point changes and the performance of the frequency controller could not be as good as it might be. Thus, to improve control performance, it would be desirable to update the settings in accordance with the operating point. To deal with changes in plant parameters, a variety of adaptive control methods were suggested for the implementation of LFC [40-43]. Vajk *et al.* [40] have implemented and examined an adaptive LFC approach to the Hungarian power system. To satisfy the criteria of the hyper stability condition while taking plant parameter changes into account, Pan and Liaw [41] devised an adaptive controller adopting a proportional integral adaptation.

The self-tuning control strategy for load frequency control has been presented in [44-46]. According to Lee *et al.* [44], a self-tuning method for solving the LFC problem of interconnected power systems offers the optimum control performance under a variety of operating circumstances. For the purpose of designing load frequency controllers, several researchers in [45-48] used the variable structure system (VSS) control approach. It should be emphasized that by carefully choosing the controller parameter, the VSS controllers may significantly enhance transient reactions resulting from load disturbances in the power system. These controllers may not have been completely

recognized in LFC tasks, nevertheless, because of the intricacy of VSS and the accompanying chattering problem.

Furthermore, controllers based on the linearized model's state equation can need estimations of inaccessible state variables. It is possible to construct observers for this scenario, but doing so would increase costs due to the added expense of data telemetry. The next subsection represents the robust control approaches efficiently dealing with the load frequency control problem.

2.3.1.4 Robust control techniques:

Each control region in a power system is subject to a variety of uncertainties and disruptions imposed by changes in the system's parameters and characteristics, variations in the load, errors made during the modeling and linearization processes, and external factors. During a daily cycle, a power system's operational parameters may alter arbitrarily. Therefore, an optimum LFC regulator design based on nominal system parameter values is undoubtedly inappropriate for the LFC issue, and consequently, the application of these regulators on the system may not be sufficient to achieve the required system functioning. A system's dynamic performance may suffer as a result, and occasionally system stability may also be lost. As a result, significant efforts have been made to devise LFC controllers with improved performance to handle changes in system parameters [49-57]. It should be highlighted that the control objectives for the robust control techniques are to build load frequency controllers that not only fulfill the requirements for nominal stability and performance but also ensure robust stability and robust performance in power systems with effectively handling the LFC problem. In order to solve the LFC problem, Wang *et al.* have suggested a robust controller based on the Riccati equation technique [49]. To handle small and large parametric uncertainties, the robust control approach and the adaptive control methodology were combined and used as effective solution load frequency problems in [50].

In order to construct a robust LFC while taking into account allowable parametric uncertainties, Shayeghi *et al.* [57] employed mu-synthesis and the analytical approach. Azzam and Mohamed suggested a robust controller for load frequency control based on the Q-parameterization theory [53]. This method has a number of benefits, including the fact that a stable controller is always present, closed loop poles can be placed in a

specific area to achieve the desired transient response, and the resulting controller order is lower than that of comparable robust controllers, i.e., H_∞, linear quadratic regulator (LQG), and mu-synthesis.

In a multi-area power system, Bevrani *et al.* [56] provided a methodical approach for reliable sequential decentralized load frequency controllers utilizing mu-synthesis. However, the complex organizational structure of power systems prevents the direct application of the typical robust control approaches due to the extremely large model order, ambiguous connections between subsystems, and wide parameter changes. Further, to deal with such challenges, intelligent control strategies, i.e., fuzzy logic and artificial neural network (ANN), have been presented in a subsequent subsection.

2.3.1.5 Intelligent Control approaches:

Classical and non-flexible LFC systems do not provide adequate solutions because to the complexity and multi-variable characteristics of the power system. Therefore, a flexible technique was devised to assess the effectiveness of such systems. The challenges listed above have been greatly alleviated in recent years by developing contemporary intelligent methods like ANNs, fuzzy logic, and GAs.

Researchers have been inspired to model controls on human neural network systems by the capacity of humans to regulate sophisticated plants. ANNs are presently being employed in the field of nonlinear control issues, especially when the system is operating throughout the nonlinear range, because of their huge parallelism and capacity to learn any form of nonlinearities. The use of ANNs to solve the LFC problem is documented in Refs. [58-63]. Multi-layer nonlinear networks that were trained using a back propagation over time technique were proposed for system management by Franoise *et al.* [58].

The ANN methodology based on reliable control techniques for resolving the LFC issue in an interconnected power system has been documented in the literature [60-62]. Shayeghi and Shayanfar employed the concept of mu-synthesis control approaches to training an ANN-based LFC controller [61]. These methods combined the strengths of neural networks with robust control strategies to deliver the needed degree of robust performance under high parametric uncertainty and produced a versatile controller with a comparatively straightforward structure like PID. The H_∞, robust control approach

was utilized in [63] along with radial basis function neural networks to enhance the performance of the proposed controller under changing network circumstances.

The power system's control-related issues have seen an extensive application of fuzzy logic. The fuzzy control approach seeks to construct the controller directly from domain experts or operators who are effectively running the plant manually, in contrast to standard control theory, which is mostly based on mathematical models of the investigated systems. Numerous research has been documented in the literature for developing a fuzzy logic-based LFC regulator to take into account various features of the power system [64-70]. The fuzzy PI controller is more practical and easier to use to eliminate steady error, according to studies on the LFC problem [66-68]. Chia and Chun [69] utilized a GA-based fuzzy gain scheduling for load frequency control for a two-area thermal power system.

Pappachen and Fatima proposed a North America electric reliability corporation (NERC) standard-based adaptive neuro-fuzzy interface system (ANFIS) controller for an interconnected four-area power system under a deregulated scenario. It was claimed that their proposed control scheme provides fewer variations in the speed governor compared to the conventional control approach, which reduces wear and tear in the system [70]. Also, since fuzzy logic controllers are considered more robust for handling imprecise information, adaptive controller realization based on the fuzzy logic scheme is being explored for effective frequency regulation in power systems [71-75]. This aspect of fuzzy controllers is also discussed in detail through a rigorous study in [76][77], where different fuzzy logic control structures, such as self-tuning, stable adaptive, and single-input fuzzy logic control structures, are reviewed in depth. Multi-stage fuzzy PID and Fuzzy PI/PID control structures have also been utilized in IPS for LFC [71-73], and their application is extended to a nonlinear deregulated power system. Moreover, it is essential to obtain the optimal control parameters for the efficient operation of the load frequency controller in order to have a stable and economical operation of the electrical power system. The subsequent subsection presents the soft computing-based control structure and optimization strategies.

2.3.1.6 Soft computing-based control structure and Optimization strategies:

The structure and complexity of the electrical power system evolve when renewable energy sources are added to the system. As a result, there can be significant system disruptions. In this scenario, the conventional LFC may not be feasible in the current convoluted framework. In order to overcome this challenge, researchers are looking at using soft computing approaches, including the genetic algorithm (GA), the bacterial foraging optimization algorithm (BFOA), the swarm optimization (PSO) algorithm, and the firefly algorithm.

Darwin's principle of natural selection and survival of the fittest is the foundation for GA. The GA is frequently used for various electrical power system issues such as optimal power flow, a study of system topologies, power distribution system design, and economic dispatch due to its appealing properties such as robustness and simplicity. To achieve higher optimal performance, Ghoshal *et al.* [78] calculated GA based optimal gains for linked power systems. AGC was also studied using the Sugeno fuzzy logic approach for online adaptive integral gain scheduling. Ghoshal [25] investigated GA and hybrid genetic algorithm-simulated annealing strategies to generate optimal integral gains for integral controllers and PID controller gains for interconnected power systems.

Further, the BFOA approach is based on Escherichia coli's social foraging behavior. Chemotaxis, swarming, reproduction, elimination, and dispersion are the four primary processes of E. coli's foraging strategy. In [79], the BFOA approach is used to tune the control parameters of fractional-order PID controllers and regular integer order controllers for LFC. In [80], the BFOA approach is utilized to optimize the integral gains and speed regulation parameters for a three-area system.

The birds swarming social behavior was the foundation for another optimization algorithm, i.e., the PSO algorithm. This is a population-based stochastic nature-inspired optimization strategy for finding optimal solutions. Authors in [81] present the PSO-based LFC applications in deregulated electricity systems. Sharifi *et al.* [82] developed a multi-objective PID controller for AGC for a two-area interconnected power system with swarm optimization. Peak overshoot/Frequency nadir, as well as settling time, were employed as objective functions for multi-objective optimization in this method. Moreover, various optimization algorithms have been proposed and utilized for load

frequency control structure optimal parameter calculations, which include Firefly Algorithm, quasi-oppositional harmony search, Big Bang Big Crunch, Craziness-based swarm optimization, artificial cuckoo search algorithm, quasi-oppositional grey wolf optimization algorithm, ant lion optimizer algorithm and gravitational search algorithm [83-89].

Further, an efficient optimization technique, i.e., the salp swarm algorithm (SSA), has been proposed by S. Mirjalili *et al.* for engineering problem optimization purposes [90]. The SSA is a swarm-based meta-heuristic optimization algorithm motivated by the foraging behavior of salps found in the Deep Ocean. Salps have barrel-shaped bodies like jellyfish and belong to the family of Salpidae. Due to its presence in the Deep Ocean, very little literature is available about its swarming behavior. Further, SSA has been recently used in many applications, including load frequency control problems [91] [92]. The various optimization algorithms presented here can be utilized for obtaining the optimal controller parameters depending on the complexity of the system under investigation and the number of controller parameters to be calculated.

However, integration of renewable energy based electrical generation units into existing power systems should be an additional control mechanism for providing frequency support to the grid. Hence subsequent subsection presents the control strategies for renewable energy resources to participate in frequency support.

2.3.2 Control strategies for RESs to participate in frequency support:

The system frequency is around 50 Hz or 60 Hz under nominal operating conditions. However, the system frequency begins to decrease with frequency rates when a generation-demand imbalance event occurs, based on the total system inertia and the quantity of imbalanced power, as determined by the swing equation.

$$\frac{df}{dt} = \frac{f_0}{2S_{sys}H_{sys}}(P_m - P_e) \tag{2.2}$$

Where, ‘df/dt’ is the rate of change of frequency, ‘S_{sys}’ and ‘H_{sys}’ is the power rating and inertia of equivalent power system, respectively, and ‘f_0’ is the system nominal frequency. The ‘Pm’ and ‘Pe’ are the mechanical and electrical power of the system, respectively [93] [94].

Inertia and primary response are the two important reactions of conventional generators to frequency fluctuations, as shown in Fig. 2.4. The mechanical speed of the

turbine-generator combination immediately decreases because of the inertia, a natural response to abrupt dips in system frequency. By responding in this way, the rotating components of the turbine and generator release their stored kinetic energy. For the WTG speed to settle at a new, slower synchronous speed, kinetic energy must be drained in order to enhance the generator's mechanical output power and maintain the balance between electricity demand and mechanical output. But the deceleration, or kinetic energy extraction, has a threshold that depends on the generator's inertia constant and the normal frequency of the grid.

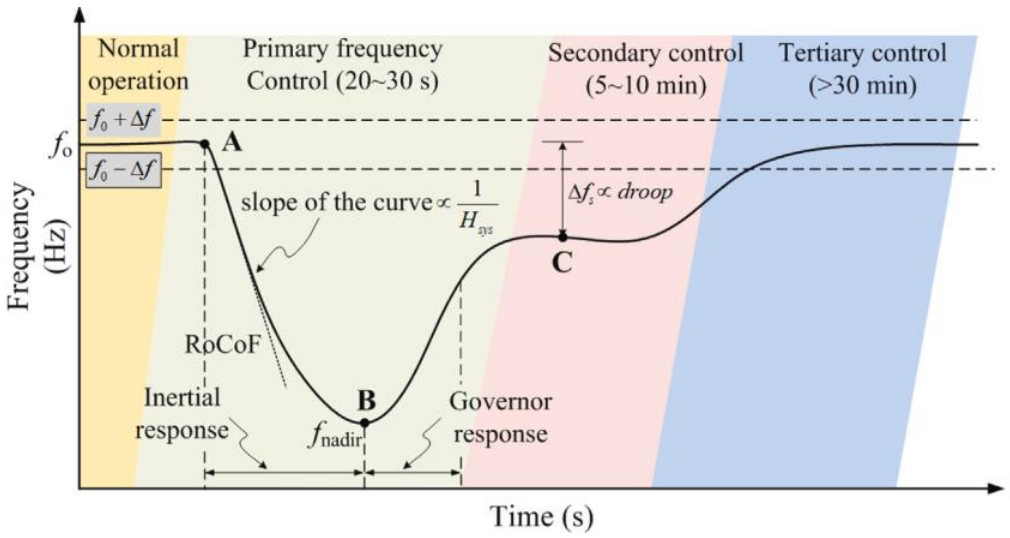

Fig. 2.4 *Graphical depiction of the time frame and frequency response of a system [93]*

The principal reaction is proportional to the incidence frequency drop based on the chosen droop value, which is generally 4–12%. In order to restore the frequency to the safe deadband, the secondary response, which comes after the inertia and primary reactions, balances generation and demand completely.

The governor of the primary frequency control (PFC), which operates on a timeframe of up to a few low tens of seconds, adjusts the mechanical power input around a predetermined set-point in response to the local frequency variation. Numerous contemporary wind turbine systems employ variable speed machines in order to extract the most energy possible from the wind resource. The doubly fed induction generator (DFIG) or a multi-pole permanent magnet synchronous generator (PMSG) is frequently used to connect wind turbines for variable speed operation. For the purpose of connecting the above energy conversion devices with the power system,

power electronic converters are needed because the power output of these wind turbine generators (WTGs) won't be at the nominal frequency. PMSGs employ full scale power electronic converters in their stator circuit for grid connection. These machines offer a wide range of speed control capabilities, and the turbines may be directly connected to the electric generators due to the full-scale converters. However, the PMSGs is quite costly since they require 100% capacity power electronic converters. The filter design becomes complicated and expensive since the electromagnetic interface, and inverter output filters are rated for 100% output power. Additionally, across the full operating range, converter efficiency plays a significant impact on overall system efficiency. Due to the high number of poles, direct drive PMSG-WTGs frequently have very large dimensions [95-97]. These devices are not frequently utilized because permanent magnets are expensive as raw materials and because a small air gap is necessary, which complicates the pole assembly.

However, the rotor circuit of DFIGs uses partial scale power electronic converters (20–30% of full rating), while the stator is directly linked to the power grid. Compared to fixed speed generators, wind turbines utilizing DFIGs have several benefits, such as enhanced energy conversion efficiency, the ability to produce both active and reactive power, and speed control within a certain range. In both sub-synchronous and super-synchronous areas, the torque profile of DFIGs may be altered by altering the rotor current. However, a gearbox is required in the drive train since the DFIG speed control range is insufficient to achieve the typical wind turbine generator speed of 20 to 30 rpm.

The DFIG-based WTGs have recently drawn more attention among the two variable speed technologies, i.e., the PMSG and DFIG-based WTGs. Hence the frequency support strategies for RESs have been presented in considering DFIG-based wind turbine generators. It is a common practice to use an energy storage unit to provide quicker responses under any system contingency. The subsequent subsection reviews the energy storage devices used for improving the load frequency controller performance.

2.3.2.1 Energy Storage:

A significantly quicker response by the system is required during a sudden load change for satisfactory LFC performance in the presence of higher penetration from renewable energy sources. To achieve this, various energy storage devices such as battery energy storage systems (BESS), Superconducting Magnetic Energy Storage (SMES), Capacitive Energy Storage (CES), and Redox Flow battery (RFB) have been investigated by researchers. A BESS unit was included in certain studies [98-100], which explored LFC performance enhancement of power systems. A fast-acting BESS efficiently dampens electromechanical oscillations in a power system by providing storage space in addition to the kinetic energy of the generator rotor, which may share abrupt variations in the power demand. H. Shayeghi *et al.* performed a maiden application of SMES to improve dynamic performance in a deregulated power system [101]. Using ANN and fuzzy logic-based supplementary controllers, Demiroren [102][103] has observed the SMES unit performance to tackle the LFC problem. The findings demonstrate that the addition of SMES to each control area is successful in lowering the peak deviations of frequency and tie-line power flow and in enhancing transient system response.

CES can be an economical option and has a similar dynamic performance compared to SMES shown in [104]. However, SMES and CES can be replaced with RFB because of their long life, quick response (equivalent to SMES), and superior overload handling capability. For a short duration of charging and discharging, RFB has proved itself as efficient and supports the LFC implementation by maintaining the power quality of distributed energy sources in an IPS [105]. However, energy storage units are the temporary solution in order to provide instant frequency support. It is needed to mention here that energy storage units have higher capital and maintenance costs, which affects the overall economic operation of the power system. Hence the cost-effective strategies should be developed for WTGs for short-term and long-term frequency support to the connected power system. Further, the upcoming subsection explores the various strategies for DFIG-based wind turbine generators proposed in order to participate in frequency regulation process.

2.3.2.2 Frequency support strategies from WTGs:

Figure 2.5 presents an approach for frequency support from variable speed wind turbines to the electrical power system during power system contingencies. These approaches are classified into three groups, i.e., droop control, inertial control, and deloaded operation. Further, all three strategies have been reviewed in brief.

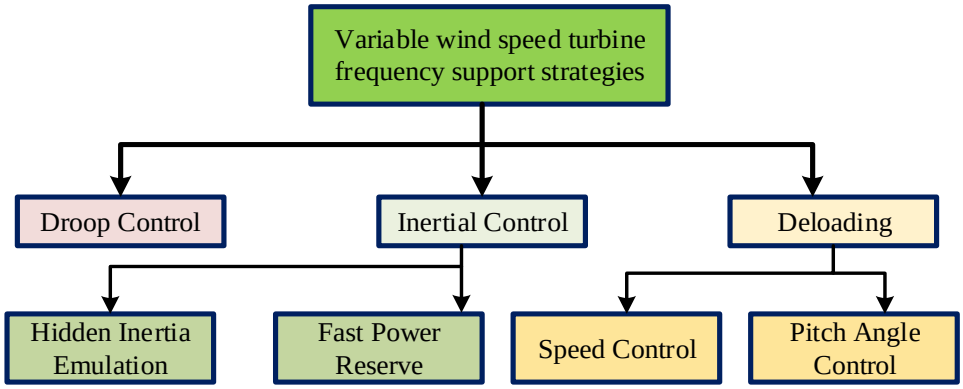

Fig. 2.5 *Frequency support schemes for variable speed WTGs*

(a) Droop control:

The wind turbine's active power output is regulated by the droop control method in accordance with changes in frequency. The frequency nadir and the procedure of frequency recovery after disturbances are both significantly enhanced by the droop control approach. The active power support can be provided as presented by equation 2.3 and regulated in accordance with linear characteristics as described in [106][107].

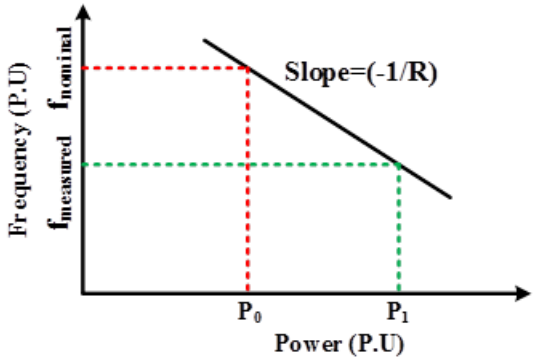

Fig. 2.6 *DFIG-based wind turbine generator droop characteristics*

$$P_0 = \frac{f_{measured} - f_{nominal}}{R} \tag{2.3}$$

Where, 'P_0' and '$f_{nominal}$' is the active power and frequency under nominal operating conditions, while 'P_1' and '$f_{measured}$' is the active power and frequency under new operating conditions with speed regulation constant or droop constant (R).

Fig. 2.6 shows the linear relationship between frequency and the wind turbine's active power [108]. The wind turbine raises power production from P_o to P_1 to compensate for frequency variations as the frequency decreases from '$f_{nominal}$' to '$f_{measured}$'. Further, the next subsection presents the second scheme, known as inertia response control for frequency support from WTG to the integrated grid.

(b) Inertia response control:

Wind turbines lack the capability to immediately release the kinetic energy contained in revolving blades as conventional generators, which can do so because of their rotating mass. The ability of variable speed wind turbines to release the kinetic energy contained in their revolving blades is made possible using a power electronic converter in conjunction with an appropriate controller. Typically, inertia emulation and fast power reserve are the two control strategies that deal with the inertial response. The first method, inertia emulation, suggests the deployment of control loops for releasing the kinetic energy trapped in a wind turbine's moving blades. The second method, fast power reserve, can also prevent frequency variation. This method, however, reacts to frequency variations by releasing continuous power for a predetermined period [109-111]. The two different control loops are considered for the inertia emulation frequency support strategy. One-loop inertial response and two-loop inertial response are the two main forms of inertial response. In the former, a single loop control based on the rate of change of frequency is used to release the kinetic energy contained in the revolving blades, whereas the latter employs two loops based on the rate of change of frequency and frequency deviations [111-113]. To make the wind turbine responsive to the rate of change in frequency, the authors used the one-loop inertia response for the swiftness of the control system. These control loops, known as inertia emulation, precisely replicate the inertia response of traditional power plants [113]. The definition of the fast power reserve is a persistent 10% of the nominal active power for a few seconds, regardless of the wind speed [114][115]. Further, long-

term frequency support can be provided with the help of a third strategy known as deloading, which has been presented in the subsequent subsection in detail.

(c) Deloading control:

It is customary to run a DFIG-based variable speed wind turbine generator in the maximum power point tracking mode to capture the maximum energy from the wind. However, under such operating mode, WTGs fail to respond to any system frequency change due to a lack of reserve power. In the event of sudden load alteration or generation loss, a significant fluctuation in tie-line power flow along with frequency deviation is observed [116][117]. Few control schemes, such as in [118], have been proposed to address this issue, which enables DFIG-based WTGs to operate dynamically in two different modes, viz. frequency support mode and maximum power point tracking mode, to handle any power system contingencies.

Bao and Li presented various deloading approaches for variable speed wind turbines by rotor speed control by operating the WTGs below the MPPT to provide frequency support by considering a distinct output power set point curve [119]. In [120], the authors proposed a control strategy for WTGs to participate in frequency regulation by derating them in consideration of overspeeding characteristics of wind turbines in the presence of flywheel. Such operation of WTGs is commonly referred to as the deloading of wind turbines, which can make the WTGs participate in frequency regulation effectively [121].

Further, the power versus rotor speed characteristics of WTG plays a significant role during the implementation of the deloading operation. The relation of power versus rotor speed is nonlinear in nature, as shown in Eq. (3). The mechanical power developed by a WTG can be given as;

$$P_m = \frac{1}{2}\rho A C_P(\lambda_t, \beta) v^3 \tag{2.4}$$

Where, $\lambda_t = \frac{\omega_r * R_{\omega t}}{v}$, and $C_P(\lambda_t, \beta) = \frac{1}{2}\left[\left(\frac{116}{\lambda_c}\right) - 0.4\beta - 5\right] e^{-21/\lambda_c}$ (2.5)

$$\lambda_c = \left[\left(\frac{1}{\lambda_t + 0.08\beta}\right) - \left(\frac{0.035}{\beta^3 + 1}\right)\right]^{-1} \tag{2.6}$$

Where 'v' is the wind speed in m/s, 'ρ' is the air density in Kg/m^3, 'A' is the area swept by the turbine blades in square meters, 'β' is the turbine blade pitch angle in degree, 'λ_t' is the tip speed ratio, 'λ_c' is the tip speed constant, 'ω_r' is the wind turbine rotor

speed in rpm, '$R_{\omega t}$' is the rotor radius of the turbine in meters, *'C_P'* is known as the power coefficient.

It is obvious from Eq. (2.5), however, that the tip speed ratio (λ_t) and pitch angle (β) affect the wind turbine's output power. The rotor speed control approach has been mainly used for performing the deloaded operation of WTG.

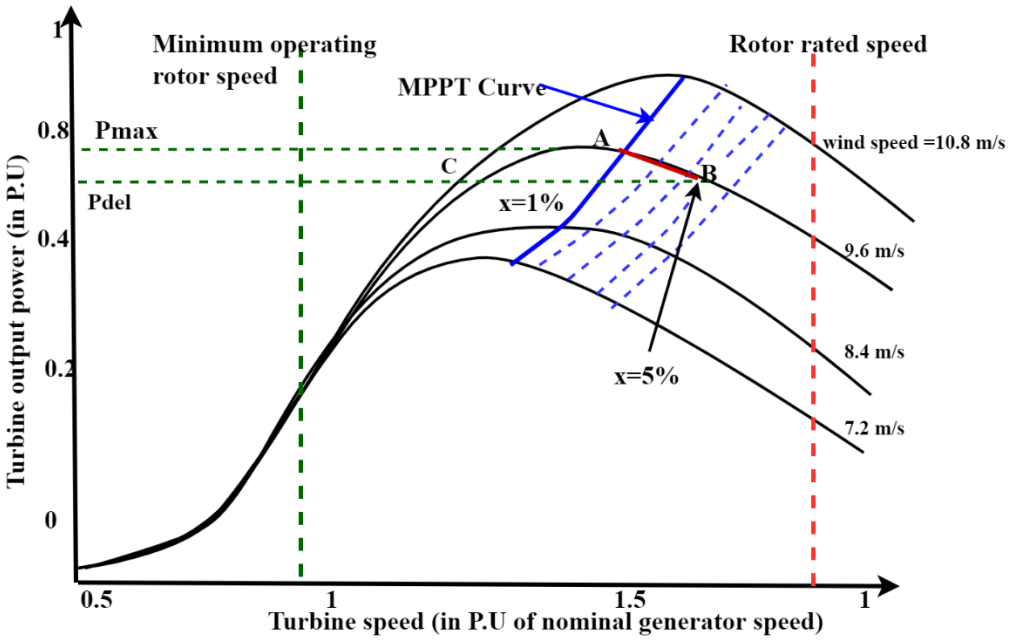

Fig. 2.7 *MPPT and deloaded power curves of DFIG-based WTG [121]*

By moving the operating point to the left or right of the maximum power point (A), speed control is advised to alter the value of the tip speed ratio as presented in Fig. 2.7. The deloading function of a DFIG-based wind turbine is depicted in this diagram as (1-x) of the maximum power at a specific wind velocity. Here 'x' indicates the percentage of deloading from the maximum power point operation. The under speed or over speed control has the ability to deload the wind turbine operating at maximum power point 'A'. In the case of under-speed control, the operating point of the wind turbine travels in the direction of point 'C', whereas in the case of an over speed control, it goes in the direction of point 'B'. Over speed control for deloading operation is preferred in comparison to speed control due to the enhanced stability of the power system [120][121].

A specific quantity of active power proportional to frequency variation is released by the wind turbine when the system frequency falls, as presented in Fig. 2.8. The operational point can thus be situated with P_{ref} between 'A' and 'B', as indicated by

$$P_{ref} = P_{del} + (P_{max} - P_{del}) \left[\frac{\omega_{del} - \omega_m}{\omega_{del} - \omega_{max}}\right] \quad (2.7)$$

Where 'ω_{max}' is the rotor speed at maximum power, 'ω_{del}' is the rotor speed at deloaded power, 'ω_m' is the rotor speed corresponding to reference power, 'P_{max}' is the maximum power (pu), 'P_{del}' is the deloaded power (pu), and 'P_{ref}' is the deloaded reference power (pu). In general, medium wind speeds are optimal for deloading with over-speed control. Further, the subsequent section presents the research gaps based on the exhaustive literature review.

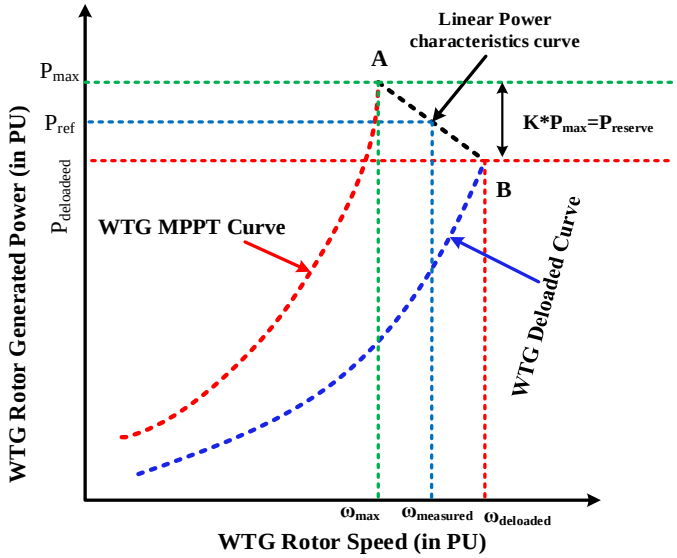

Fig. 2.8 *Reference power calculation of deloaded WTG*

2.4 Research Gaps:

To fulfill the increasing energy demand for the sustainable economic and industrial growth of the world and individual country, renewable energy sources has been extensively integrated with the existing power system. Integration of such sources can decrease the power system inertia significantly. The reason behind such a reduction in power system inertia is that power electronics devices must be employed for interfacing such energy sources with the grid. In the near future, this tendency can rapidly increase, and power system inertia can decrease accordingly. Then, these gaps are addressed in this thesis, and subsequent chapters give a detailed explanation.

- The complexity of the power system has been increased by manifolds from its inception. Further, to address the increasing global power demand and climate change issues, RES's penetration has also increased in existing power systems. Hence, an intelligent control approach must be employed to design an effective load frequency control structure.
- WPP integration with existing IPS performance can be significantly hampered due to their inherent non-participation in the frequency regulation process. Hence frequency support scheme must be explored with an efficient load frequency control structure.
- Inertial, droop, and deloading strategies must be explored for providing frequency support from DFIG based wind power plants. Such frequency support strategies can address the problem arising from reduced inertia of power systems with highly penetrated renewable energy sources.
- Renewable energy sources have sporadic nature in power generation, and forecasting techniques can be utilized for enhancing the performance of frequency support schemes such as the deloading of wind power plants. Further, the adaptive deloading technique can be explored for superior performance of electrical power systems in the presence of renewable energy sources under system contingencies.

Further, the subsequent chapter represents the design and implementation of an efficient load frequency control structure for a realistic power system operating in a deregulated mode in the presence of an energy storage unit.

References:

[1] P. S. Kundur and O. P. Malik, Power system stability and control. McGraw-Hill Education, 2022.

[2] O. P. Malik, A. Kumar, and G. S. Hope, "A load frequency control algorithm based on a generalized approach," IEEE Trans. Power Syst., vol. 3, pp. 375–382, 1988, doi: 10.1109/59.192887.

[3] T. Yang, S. Cai, P. Yan, W. Li, and A. Y. Zomaya, "Saturation Defense Method of a Power Cyber-physical System Based on Active Cut Set," IEEE Trans. Smart Grid, 2022.

[4] Elgerd O.I. and Fosha Charles, "Optimum Megawatt-Frequency Control of Multiarea Electric Energy Systems," IEEE Trans. Power Appar. Syst., vol. 4, pp. 556–563, 1970.

[5] C. E. Fosha and O. I. Elgerd, "The megawatt-frequency control problem: A new approach via optimal control theory," IEEE Trans. Power Appar. Syst., vol. 4, pp. 563–577, 1970.

[6] R. D. Christie Member and A. B. Fellow, "Load frequency control issues in power system operations after deregulation," IEEE Trans. Power Syst., vol. 11, pp. 1191–1200, 1996, doi: 10.1109/59.535590.

[7] K. Solaun and E. Cerdá, "Climate change impacts on renewable energy generation. A review of quantitative projections," Renew. Sustain. Energy Rev., vol. 116, p. 109415, 2019, doi: https://doi.org/10.1016/j.rser.2019.109415.

[8] IRENA, "Renewable Energy Capacity Highlights," International Renewable Energy Agency, 2021. https://www.irena.org/publications/2021/March/Renewable-Capacity-Statistics-2021.

[9] S. K. Pandey, S. R. Mohanty, and N. Kishor, "A literature survey on load-frequency control for conventional and distribution generation power systems," Renew. Sustain. Energy Rev., vol. 25, pp. 318–334, 2013, doi: 10.1016/j.rser.2013.04.029.

[10] International Renewable Energy Agency, "Renewable energy status," 2021. https://www.irena.org/benefits.

[11] The World Bank, "Access to Energy is at the Heart of Development," World Bank Group, 2018.

[12] K. R. S. (United S. José Goldemberg (Brazil), Amulya K.N. Reddy (India), "Rural Energy in Developing Countries," New York City. [Online]. Available: https://www.undp.org/content/dam/undp/library/Environment and Energy/Sustainable Energy/wea 2000/chapter10.pdf.

[13] Ministry of New and Renewable Energy, "Overview | Ministry of New and Renewable Energy, Government of India," Wind Energy, Government of India website, 2021. https://mnre.gov.in/wind/current-status/.

[14] P. Bhatt, S. P. Ghoshal, and R. Roy, "Coordinated control of TCPS and SMES for frequency regulation of interconnected restructured power systems with dynamic participation from DFIG based wind farm," Renew. Energy, vol. 40, pp. 40–50, 2012, doi: 10.1016/j.renene.2011.08.035.

[15] S. Xie, X. Wang, C. Qu, X. Wang, and J. Guo, "Impacts of different wind speed simulation methods on conditional reliability indices," Int. Trans. Electr. energy Syst., vol. 20, pp. 1–6, 2013, doi: 10.1002/etep.

[16] T. H. Mohamed, J. Morel, H. Bevrani, and T. Hiyama, "Model predictive based load frequency control-design concerning wind turbines," Int. J. Electr. Power Energy Syst., vol. 43, pp. 859–867, 2012, doi: 10.1016/j.ijepes.2012.06.032.

[17] S. Chaine, M. Tripathy, and S. Satpathy, "NSGA-II based optimal control scheme of wind thermal power system for improvement of frequency regulation characteristics," Ain Shams Eng. J., vol. 6, pp. 851–863, 2015, doi: 10.1016/j.asej.2015.01.011.

[18] W. Tan, "Unified Tuning of PID Load Frequency Controller for Power Systems via IMC," IEEE Trans. Power Syst., vol. 25, pp. 341–350, 2010, doi: 10.1109/TPWRS.2009.2036463.

[19] K. Chatterjee, "Design of Dual Mode PI Controller for Load Frequency Control," Int. J. Emerg. Electr. Power Syst., vol. 11, 2010, doi: doi:10.2202/1553-779X.2452.

[20] J. Nanda, S. Mishra, P. G. Mishra, and K. V Sajith, "A novel classical controller for automatic generation control in thermal and hydrothermal systems," in 2010 Joint International Conference on Power Electronics, Drives and Energy Systems & 2010 Power India, 2010, pp. 1–6, doi: 10.1109/PEDES.2010.5712439.

[21] M. Farahani, S. Ganjefar, and M. Alizadeh, "PID controller adjustment using chaotic optimisation algorithm for multi-area load frequency control," IET Control Theory Appl., vol. 6, pp. 1984–1992, 2012.

[22] E. J. Oliveira, L. M. Honório, A. H. Anzai, L. W. Oliveira, and E. B. Costa, "Optimal transient droop compensator and PID tuning for load frequency control in hydro power systems," Int. J. Electr. Power Energy Syst., vol. 68, pp. 345–355, 2015.

[23] J. Nanda, S. Mishra, and L. C. Saikia, "Maiden application of bacterial foraging-based optimization technique in multiarea automatic generation control," IEEE Trans. Power Syst., vol. 24, no. 2, pp. 602–609, 2009, doi: 10.1109/TPWRS.2009.2016588.

[24] W. Tan, H. Zhang, and M. Yu, "Decentralized load frequency control in deregulated environments," Int. J. Electr. Power Energy Syst., vol. 41, pp. 16–26, 2012, doi: 10.1016/j.ijepes.2012.02.013.

[25] S. P. Ghoshal, "Application of GA/GA-SA based fuzzy automatic generation control of a multi-area thermal generating system," Electr. Power Syst. Res., vol. 70, pp. 115–127, 2004.

[26] S. D. Hanwate and Y. V Hote, "Optimal PID design for Load frequency control using QRAWCP approach," IFAC-PapersOnLine, vol. 51, pp. 651–656, 2018.

[27] M. N. Anwar and S. Pan, "A new PID load frequency controller design method in frequency domain through direct synthesis approach," Int. J. Electr. Power Energy Syst., vol. 67, pp. 560–569, 2015, doi: 10.1016/j.ijepes.2014.12.024.

[28] M. Hajiakbari Fini, G. R. Yousefi, and H. Haes Alhelou, "Comparative study on the performance of many-objective and single-objective optimisation algorithms in tuning load frequency controllers of multi-area power systems," IET Gener. Transm. Distrib., vol. 10, no. 12, pp. 2915–2923, 2016.

[29] S. C. Tripathy, G. S. Hope, and O. P. Malik, "Optimisation of Load-Frequency Control Parameters for Power Systems With Reheat Steam Turbines and Governor Deadband Nonlinearity.," IEE Proc. C Gener. Transm. Distrib., vol. 129, pp. 10–16, 1982, doi: 10.1049/ip-c.1982.0002.

[30] H. Gozde and M. C. Taplamacioglu, "Automatic generation control application with craziness based particle swarm optimization in a thermal power system," Int. J. Electr. Power Energy Syst., vol. 33, pp. 8–16, 2011.

[31] P. Kundur, Power System Stability and Control. New Delhi: Tata McGraw Hill, 2009.

[32] D. Das, J. Nanda, M. L. Kothari, and D. P. Kothari, "Automatic generation control of a hydrothermal system with new area control error considering generation rate constraint," Electr. Mach. Power Syst., vol. 18, pp. 461–471, 1990.

[33] A. Feliachi, "Load frequency control using reduced order models and local observers," Int. J. energy Syst., vol. 7, pp. 72–75, 1987.

[34] S. Velusami and K. Romar, “Design of observer-based decentralized load-frequency controllers for interconnected power systems,” Int. J. power energy Syst., vol. 17, pp. 152–160, 1997.

[35] E. V Bohn and S. M. Miniesy, “Optimum load-frequency sampled-data control with randomly varying system disturbances,” IEEE Trans. Power Appar. Syst., vol. 5, pp. 1916–1923, 1972.

[36] K. Yamashita and T. Taniguchi, “Optimal observer design for load-frequency control,” Int. J. Electr. Power Energy Syst., vol. 8, pp. 93–100, 1986.

[37] V. R. Moorthi and R. P. Aggarwal, “Suboptimal and near-optimal control of a load-frequency-control system,” in Proceedings of the Institution of Electrical Engineers, 1972, vol. 119, pp. 1653–1660.

[38] M. Aldeen and H. Trinh, “Load-frequency control of interconnected power systems via constrained feedback control schemes,” Comput. Electr. Eng., vol. 20, pp. 71–88, 1994.

[39] M. Aldeen and H. Trinh, “Combined modal and singular perturbation approach to decentralized control,” Int. J. Syst. Sci., vol. 23, pp. 741–764, 1992.

[40] I. Vajk, M. Vajta, L. Keviczky, R. Haber, J. Hetthéssy, and K. Kovacs, “Adaptive load-frequency control of the hungarian power system,” Automatica, vol. 21, pp. 129–137, 1985.

[41] C.-T. Pan and C.-M. Liaw, “An adaptive controller for power system load-frequency control,” IEEE Trans. Power Syst., vol. 4, pp. 122–128, 1989.

[42] C. M. Liaw, “Design of a reduced-order adaptive load-frequency controller for an interconnected hydrothermal power system,” Int. J. Control, vol. 60, pp. 1051–1063, 1994.

[43] R. R. Shoults and J. A. J. Ibarra, “Multi-area adaptive LFC developed for a comprehensive AGC simulator,” IEEE Trans. Power Syst., vol. 8, pp. 541–547, 1993.

[44] K. A. Lee, H. Yee, and C. Y. Teo, “Self-tuning algorithm for automatic generation control in an interconnected power system,” Electr. Power Syst. Res., vol. 20, no. 2, pp. 157–165, 1991.

[45] M. A. Sheirah and M. M. Abd-El-Fattah, “Improved load-frequency self-tuning regulator,” Int. J. Control, vol. 39, pp. 143–158, 1984.

[46] K. Yamashita and H. Miyagi, “Load frequency self-tuning regulator for interconnected power systems with unknown deterministic load disturbances,” Int. J. Control, vol. 49, pp. 1555–1568, 1989.

[47] A. Y. Sivaramakrlshnan, M. V Hariharan, and M. C. Srisailam, “Design of variable-structure load-frequency controller using pole assignment technique,” Int. J. Control, vol. 40, pp. 487–498, 1984.

[48] A. Kumar, O. P. Malik, and G. S. Hope, “Discrete variable structure controller for load frequency control of multiarea interconnected power systems,” IEE Proc. Gener. Transm. Distrib. [see also IEE Proceedings-Generation, Transm. Distrib., vol. 2, pp. 116–122, 1987.

[49] Y. Wang, R. Zhou, and C. Wen, “Robust load-frequency controller design for power systems,” in IEE proceedings C (generation, transmission and distribution), 1993, vol. 140, pp. 11–16.

[50] Y. Wang, R. Zhou, and C. Wen, “New robust adaptive load-frequency control with system parametric uncertainties,” IEE Proceedings-Generation, Transm. Distrib., vol. 141, pp. 184–190, 1994.

[51] A. M. Stankovic, G. Tadmor, and T. A. Sakharuk, “On robust control analysis and design for load frequency regulation,” IEEE Trans. Power Syst., vol. 13, pp. 449–455, 1998.

[52] M. Azzam and Y. S. Mohamed, “Robust controller design for automatic generation control based on Q-parameterization,” Energy Convers. Manag., vol. 43, pp. 1663–1673, 2002, doi: https://doi.org/10.1016/S0196-8904(01)00118-2.

[53] G. Ray, A. N. Prasad, and G. D. Prasad, “A new approach to the design of robust load-frequency controller for large scale power systems,” Electr. power Syst. Res., vol. 51, pp. 13–22, 1999.

[54] K. Y. Lim, Y. Wang, and R. Zhou, “Robust decentralised load–frequency control of multi-area power systems,” IEE Proceedings-Generation, Transm. Distrib., vol. 143, pp. 377–386, 1996.

[55] T. Ishii, G. Shirai, and G. Fujita, “Decentralized load frequency based on H∞ control,” Electr. Eng. Japan, vol. 136, pp. 28–38, 2001.

[56] H. Bevrani, Y. Mitani, and K. Tsuji, "Sequential design of decentralized load frequency controllers using μ synthesis and analysis," Energy Convers. Manag., vol. 45, pp. 865–881, 2004.

[57] H. Shayeghil, M. Karrari, and M. B. Menhaj, "Theory of mu-Synthesis for Single Machine Powerer Systems Load Frequency Control," J. Electr. Eng., vol. 51, pp. 258–263, 2000.

[58] F. Beaufays, Y. Abdel-Magid, and B. Widrow, "Application of neural networks to load-frequency control in power systems," Neural Networks, vol. 7, pp. 183–194, 1994.

[59] D. K. Chaturvedi, P. S. Satsangi, and P. K. Kalra, "Load frequency control: a generalised neural network approach," Int. J. Electr. Power Energy Syst., vol. 21, pp. 405–415, 1999.

[60] N. S. S. Demiroren H. Lale Zeynelgil, Aysen, "Automatic generation control by using ANN technique," Electr. Power Components Syst., vol. 29, pp. 883–896, 2001.

[61] H. Shayeghi and H. A. Shayanfar, "Application of ANN technique based on μ-synthesis to load frequency control of interconnected power system," Int. J. Electr. Power Energy Syst., vol. 28, pp. 503–511, 2006.

[62] H. L. Zeynelgil, A. Demiroren, and N. S. Sengor, "The application of ANN technique to automatic generation control for multi-area power system," Int. J. Electr. power energy Syst., vol. 24, pp. 345–354, 2002.

[63] T. P. I. Ahamed, P. S. N. Rao, and P. S. Sastry, "A reinforcement learning approach to automatic generation control," Electr. power Syst. Res., vol. 63, pp. 9–26, 2002.

[64] J. Talaq and F. Al-Basri, "Adaptive fuzzy gain scheduling for load frequency control," IEEE Trans. power Syst., vol. 14, pp. 145–150, 1999.

[65] C. S. Indulkar and B. Raj, "Application of fuzzy controller to automatic generation control," Electr. Mach. power Syst., vol. 23, pp. 209–220, 1995.

[66] C. S. Chang and W. Fu, "Area load frequency control using fuzzy gain scheduling of PI controllers," Electr. Power Syst. Res., vol. 42, pp. 145–152, 1997.

[67] D. Revathi and G. Mohan Kumar, "Analysis of LFC in PV-thermal-thermal interconnected power system using fuzzy gain scheduling," Int. Trans. Electr. Energy Syst., vol. 30, p. e12336, 2020.

[68] E. Çam and I. Kocaarslan, "Load frequency control in two area power systems using fuzzy logic controller," Energy Convers. Manag., vol. 46, pp. 233–243, 2005.

[69] C. Juang and C. Lu, "Power system load frequency control by genetic fuzzy gain scheduling controller," J. Chinese Inst. Eng., vol. 28, pp. 1013–1018, 2005.

[70] A. Pappachen and A. Peer Fathima, "Critical research areas on load frequency control issues in a deregulated power system: A state-of-the-art-of-review," Renew. Sustain. Energy Rev., vol. 72, pp. 163–177, 2017, doi: 10.1016/j.rser.2017.01.053.

[71] H. Shayeghi, H. A. Shayanfar, and A. Jalili, "Multi-stage fuzzy PID power system automatic generation controller in deregulated environments," Energy Convers. Manag., vol. 47, pp. 2829–2845, 2006, doi: 10.1016/j.enconman.2006.03.031.

[72] Y. Arya and N. Kumar, "Design and analysis of BFOA-optimized fuzzy PI/PID controller for AGC of multi-area traditional/restructured electrical power systems," Soft Comput., vol. 21, no. 21, pp. 6435–6452, 2017, doi: 10.1007/s00500-016-2202-2.

[73] N. Nayak, S. Mishra, D. Sharma, and B. K. Sahu, "Application of modified sine cosine algorithm to optimally design PID/fuzzy-PID controllers to deal with AGC issues in deregulated power system," IET Gener. Transm. Distrib., vol. 13, pp. 2474–2487, 2019, doi: 10.1049/iet-gtd.2018.6489.

[74] Y. Arya, "AGC performance enrichment of multi-source hydrothermal gas power systems using new optimized FOFPID controller and redox flow batteries," Energy, vol. 127, pp. 704–715, 2017.

[75] K. Nithilasaravanan, N. Thakwani, P. Mishra, V. Kumar, and K. P. S. Rana, "Efficient control of integrated power system using self-tuned fractional-order fuzzy PID controller," Neural Comput. Appl., vol. 31, pp. 4137–4155, 2019, doi: 10.1007/s00521-017-3309-9.

[76] P. Sreenivas, V. S. Srinivasa Murthy, S. Vijaya Kumar, and U. Pradeep Kumar, "Design and analysis of new pitch angle controller for enhancing the performance of wind turbine coupled with PMSG," Mater. Today Proc., 2021, doi: 10.1016/j.matpr.2021.11.195.

[77] V. Kumar, K. P. S. Rana, and D. Kler, "Efficient control of a 3-link planar rigid manipulator using self-regulated fractional-order fuzzy PID controller," Appl. Soft Comput. J., vol. 82, p. 105531, 2019, doi: 10.1016/j.asoc.2019.105531.

[78] S. P. Ghoshal and S. K. Goswami, "Application of GA based optimal integral gains in fuzzy based active power-frequency control of non-reheat and reheat thermal generating systems," Electr. Power Syst. Res., vol. 67, pp. 79–88, 2003.

[79] S. Debbarma, L. C. Saikia, and N. Sinha, "AGC of a multi-area thermal system under deregulated environment using a non-integer controller," Electr. Power Syst. Res., vol. 95, pp. 175–183, 2013, doi: 10.1016/j.epsr.2012.09.008.

[80] S. S. Dhillon, J. S. Lather, and S. Marwaha, "Multi objective load frequency control using hybrid bacterial foraging and particle swarm optimized PI controller," Int. J. Electr. Power Energy Syst., vol. 79, pp. 196–209, 2016.

[81] H. Shayeghi, H. A. Shayanfar, and A. Jalili, "LFC design of a deregulated power system with TCPS using PSO," Int. J. Electr. Comput. Eng., vol. 3, pp. 691–699, 2009.

[82] A. Sharifi, K. Sabahi, M. A. Shoorehdeli, M. A. Nekoui, and M. Teshnehlab, "Load frequency control in interconnected power system using multi-objective PID controller," in 2008 IEEE Conference on Soft Computing in Industrial Applications, 2008, pp. 217–221.

[83] P. C. Pradhan, R. K. Sahu, and S. Panda, "Firefly algorithm optimized fuzzy PID controller for AGC of multi-area multi-source power systems with UPFC and SMES," Eng. Sci. Technol. an Int. J., vol. 19, pp. 338–354, 2016.

[84] C. K. Shiva and V. Mukherjee, "A novel quasi-oppositional harmony search algorithm for AGC optimization of three-area multi-unit power system after deregulation," Eng. Sci. Technol. an Int. J., vol. 19, pp. 395–420, 2016.

[85] B. Mohanty and P. K. Hota, "Comparative performance analysis of fruit fly optimisation algorithm for multi-area multi-source automatic generation control under deregulated environment," IET Gener. Transm. Distrib., vol. 9, pp. 1845–1855, 2015.

[86] A. Y. Abdelaziz and E. S. Ali, "Load frequency controller design via artificial cuckoo search algorithm," Electr. Power Components Syst., vol. 44, pp. 90–98, 2016.

[87] D. Guha, P. K. Roy, and S. Banerjee, "Load frequency control of large scale power system using quasi-oppositional grey wolf optimization algorithm," Eng. Sci. Technol. an Int. J., vol. 19, pp. 1693–1713, 2016.

[88] W. Tasnin, L. C. Saikia, and M. Raju, "Deregulated AGC of multi-area system incorporating dish-Stirling solar thermal and geothermal power plants using fractional order cascade controller," Int. J. Electr. Power Energy Syst., vol. 101, pp. 60–74, 2018, doi: 10.1016/j.ijepes.2018.03.015.

[89] M. Packiasudha, S. Suja, and J. Jerome, "A new Cumulative Gravitational Search algorithm for optimal placement of FACT device to minimize system loss in the deregulated electrical power environment," Int. J. Electr. Power Energy Syst., vol. 84, pp. 34–46, 2017.

[90] S. Mirjalili, A. H. Gandomi, S. Z. Mirjalili, S. Saremi, H. Faris, and S. M. Mirjalili, "Salp Swarm Algorithm: A bio-inspired optimizer for engineering design problems," Adv. Eng. Softw., vol. 114, pp. 163–191, 2017, doi: 10.1016/j.advengsoft.2017.07.002.

[91] H. M. Hasanien and A. A. El-Fergany, "Salp swarm algorithm-based optimal load frequency control of hybrid renewable power systems with communication delay and excitation cross-coupling effect," Electr. Power Syst. Res., vol. 176, p. 105938, 2019, doi: 10.1016/j.epsr.2019.105938.

[92] D. Guha, P. K. Roy, and S. Banerjee, "Maiden application of SSA-optimised CC-TID controller for load frequency control of power systems," IET Gener. Transm. Distrib., vol. 13, pp. 1110–1120, 2019, doi: 10.1049/iet-gtd.2018.6100.

[93] P. S. Kundur, N. J. Balu, and M. G. Lauby, "Power system dynamics and stability," Power Syst. Stab. Control, vol. 3, 2017.

[94] F. Díaz-González, M. Hau, A. Sumper, and O. Gomis-Bellmunt, "Participation of wind power plants in system frequency control: Review of grid code requirements and control methods," Renew. Sustain. Energy Rev., vol. 34, pp. 551–564, 2014.

[95] M. Dreidy, H. Mokhlis, and S. Mekhilef, "Inertia response and frequency control techniques for renewable energy sources: A review," Renew. Sustain. Energy Rev., vol. 69, no. November 2016, pp. 144–155, 2017, doi: 10.1016/j.rser.2016.11.170.

[96] X. Yingcheng and T. Nengling, "Review of contribution to frequency control through variable speed wind turbine," Renew. Energy, vol. 36, pp. 1671–1677, 2011, doi: 10.1016/j.renene.2010.11.009.

[97] E. J. Novaes Menezes, A. M. Araújo, and N. S. Bouchonneau da Silva, "A review on wind turbine control and its associated methods," J. Clean. Prod., vol. 174, pp. 945–953, 2018, doi: 10.1016/j.jclepro.2017.10.297.

[98] H.-J. Kunisch, K. G. Kramer, and H. Dominik, "Battery energy storage another option for load-frequency-control and instantaneous reserve," IEEE Trans. Energy Convers., pp. 41–46, 1986.

[99] S. K. Aditya and D. Das, "Battery energy storage for load frequency control of an interconnected power system," Electr. power Syst. Res., vol. 58, pp. 179–185, 2001.

[100] C.-F. Lu, C.-C. Liu, and C.-J. Wu, "Effect of battery energy storage system on load frequency control considering governor deadband and generation rate constraint," IEEE Trans. Energy Convers., vol. 10, pp. 555–561, 1995.

[101] H. Shayeghi, A. Jalili, and H. A. Shayanfar, "A robust mixed H2/H∞ based LFC of a deregulated power system including SMES," Energy Convers. Manag., vol. 49, pp. 2656–2668, 2008, doi: 10.1016/j.enconman.2008.04.006.

[102] A. Demiroren, "Automatic generation control using ANN technique for multi-area power system with SMES units," Electr. Power Components Syst., vol. 32, pp. 193–213, 2004.

[103] A. Demiroren and E. Yesil, "Automatic generation control with fuzzy logic controllers in the power system including SMES units," Int. J. Electr. power energy Syst., vol. 26, pp. 291–305, 2004.

[104] H. Shayeghi, H. A. Shayanfar, and A. Jalili, "Load frequency control strategies: A state-of-the-art survey for the researcher," Energy Convers. Manag., vol. 50, pp. 344–353, 2009, doi: 10.1016/j.enconman.2008.09.014.

[105] A. Saha and L. C. Saikia, "Load frequency control of a wind-thermal-split shaft gas turbine-based restructured power system integrating FACTS and energy storage devices," Int. Trans. Electr. Energy Syst., vol. 29, pp. 1–19, 2019, doi: 10.1002/etep.2756.

[106] R. L. Josephine and S. Suja, "Estimating PMSG wind turbines by inertia and droop control schemes with intelligent fuzzy controller in Indian development," J. Electr. Eng. Technol., vol. 9, pp. 1196–1201, 2014.

[107] W. Yao and K. Y. Lee, "A control configuration of wind farm for load-following and frequency support by considering the inertia issue," in 2011 IEEE Power and Energy Society General Meeting, 2011, pp. 1–6.

[108] B. M. Eid, N. Abd Rahim, J. Selvaraj, and A. H. El Khateb, "Control methods and objectives for electronically coupled distributed energy resources in microgrids: A review," IEEE Syst. J., vol. 10, pp. 446–458, 2014.

[109] P. Li, W. Hu, R. Hu, and Z. Chen, "The Primary Frequency Control Method of Tidal Turbine Based on Pitch Control," in Energy Procedia, 2018, vol. 145, pp. 199–204, doi: 10.1016/j.egypro.2018.04.035.

[110] F. Gonzalez-Longatt, "Frequency control and inertial response schemes for the future power networks," in Large scale renewable power generation, Springer, 2014, pp. 193–231.

[111] H. Knudsen and J. N. Nielsen, "Introduction to the modelling of wind turbines," Wind power power Syst., pp. 767–797, 2012.

[112] Z.-S. Zhang, Y.-Z. Sun, J. Lin, and G.-J. Li, "Coordinated frequency regulation by doubly fed induction generator-based wind power plants," IET Renew. Power Gener., vol. 6, pp. 38–47, 2012.

[113] L. Holdsworth, J. B. Ekanayake, and N. Jenkins, "Power system frequency response from fixed speed and doubly fed induction generator-based wind turbines," Wind Energy, vol. 7, pp. 21–35, Jan. 2004, doi: 10.1002/we.105.

[114] S. Wachtel and A. Beekmann, "Contribution of wind energy converters with inertia emulation to frequency control and frequency stability in power systems," 2009.

[115] P.-K. Keung, P. Li, H. Banakar, and B. T. Ooi, "Kinetic energy of wind-turbine generators for system frequency support," IEEE Trans. power Syst., vol. 24, pp. 279–287, 2008.

[116] P. Sonkar and O. P. Rahi, "Contribution of wind power plants in grid frequency regulation: Current perspective and future challenges," Wind Eng., vol. 45, pp. 442–456, 2021, doi: 10.1177/0309524X19892899.

[117] M. Debouza and A. Al-Durra, "Grid ancillary services from doubly fed induction generator-based wind energy conversion system: A review," IEEE Access, vol. 7, pp. 7067–7081, 2018.

[118] R. Ahmadi, A. Sheikholeslami, A. Nabavi Niaki, and A. Ranjbar, "Dynamic participation of doubly fed induction generators in multi-control area load frequency control," Int. Trans. Electr. energy Syst., vol. 20, pp. 1–6, 2014, doi: 10.1002/etep.1891.

[119] Y. Bao and Y. Li, "On deloading control strategies of wind generators for system frequency regulation," Int. Trans. Electr. energy Syst., vol. 20, no. January 2014, pp. 1–6, 2013, doi: 10.1002/etep.

[120] F. Díaz-González, M. Hau, A. Sumper, and O. Gomis-Bellmunt, "Coordinated operation of wind turbines and flywheel storage for primary frequency control support," Int. J. Electr. Power Energy Syst., vol. 68, pp. 313–326, 2015, doi: 10.1016/j.ijepes.2014.12.062.

[121] R. Prasad and N. P. Padhy, "Coordinated Frequency Controller Operation for DFIG based Wind Turbine Generator Control using Combination Selection Scheme," 2020 IEEE Int. Conf. Power Electron. Smart Grid Renew. Energy, PESGRE 2020, pp. 1–6, 2020, doi: 10.1109/PESGRE45664.2020.9070477.

Chapter 3: LFC of Interconnected Power System Utilizing a Redox Flow Battery with Fractional Order Fuzzy Control Structure

3.1 Introduction:

In traditional interconnected power systems (IPS), domination by a single utility company for electrical power generation, transmission, and distribution affects its reliability and economical operation. The literature survey focuses on the need for a load frequency control structure that effectively copes with the complexity of interconnected power systems. To deal with issues in vertical structure of electrical power system, the power sector has adopted various changes from its inception, and deregulation is one of them. A competitive environment in the power sector was created by deregulation in 1995 with a notice of proposed rulemaking (NOPR) by the Federal energy regulatory commission (FERC) [1-3].

The restructured or deregulated electricity system is dominated by companies such as generating companies (GENCOs), transmission companies (TRANSCOs), distribution companies (DISCOs), and independent service providers (ISOs). In an open power market scenario, a DISCO from any control area has the flexibility to enter into a contract with any GENCO from any control area for the purchase of power at a competitive price. To overcome the load frequency control problem in deregulated power system scenario, Donde *et al.* proposed the DISCO participation matrix (DPM). The elements of DPMs are referred to as contract participation factors (cpf) [4]. ISO works as a supervisor for reliable power system operation with maintaining power transactions among various GENCOs and DISCOs in accordance with area participation factor (apf) and DPM.

Conventional energy sources are the dominant source of electrical power generation; nevertheless, these sources are rapidly diminishing and contributing to global climate change. It should be noted that including renewable energy sources in an IPS can improve the dynamic performance of frequency regulation for an IPS. However, in the case where a larger contribution from renewable energy sources is included in an IPS, this benefit may be lost due to a decrease in power system inertia due to the increased use of associated power electronics devices in such policies. Compared to traditional power sources, such integration may result in greater voltage

and frequency fluctuations. Hence, a significantly quicker response by the system is required during a sudden load change for satisfactory LFC performance in the presence of higher penetration from renewable energy sources. A Rechargeable Redox Flow battery (RFB) can be explored to achieve the same. For a short duration of charging and discharging, RFB has proven to be more efficient and supports the LFC by maintaining the power of distributed energy sources in an IPS [5][6]. In the presence of continuous load variations, modelling errors in the practical power system, and changing power system configurations, which are bound to occur to compensate for ever increasing load demands, control techniques based on a fixed gain nature may fail to provide satisfactory LFC performance. Adaptive controllers are intended to solve the limitations of fixed gain controllers, and cognitive algorithms are usually utilized to achieve efficient adaptive controllers. Efforts are ongoing to build adaptive load frequency controllers that can effectively manage system parametric fluctuations, modelling errors, and continuous load variations in an IPS structure.

A three-area integrated power system containing a geothermal power plant (GTPP), solar-thermal power plant (STPP), and wind turbine power plant (WPP) has been considered in the deregulated scenario for investigating the load frequency control structure performance, i.e., fuzzy based intelligent controller [7][8]. To deal with the issues of uncertainties and incorporating adaptation capabilities in the control structure, a self-tuned fractional order fuzzy PID (STFOFPID) controller has been investigated, and extensive simulation studies have been carried out on the considered IPS in the deregulated mode of operation [8]. Apart from this, the advantages of using a recently devised energy storage device, i.e., Redox flow Battery, have also been investigated, and shown that the frequency regulation can be significantly improved by incorporating RFBs in the investigated power system. In this chapter, thorough comparative studies with conventional PID and fractional order PID (FOPID) controllers are also presented for the investigated STFOFPID control structure performance evaluation. In order to effectively design the investigated controller and to present a fair comparative study, all the considered controllers are tuned using two bio-inspired optimization algorithms, i.e., Genetic Algorithm (GA) and Salp-Swam algorithm (SSA) [9][10].

Further, this chapter is organized into five sections. Following a detailed introduction in section 3.1, section 3.2 presents the mathematical model description of

the interconnected three-area power system under investigation. The investigated load frequency control scheme, i.e., self-tuned fractional order fuzzy PID (STFOFPID), has been presented in detail in section 3.3. Section 3.4 presents the optimal controller parameter through a recently devised optimization algorithm, i.e., SSA. Further, extensive simulation studies considered three areas of IPS, and their comparative analyses are presented in section 3.5. Finally, section 3.6 presents the summary of the chapter.

3.2 Description of the interconnected power system (IPS):

The schematic block diagram of the system under investigation for the present study is shown in Fig.3.1. Considered IPS has three areas with unequal capacity, i.e., 2000MW:4000MW:8000MW, GTPP, STPP and WPP in area-1, area-2, and area-3 along with reheated thermal power plant (RTPP) acting as a traditional power source. The mathematical model of various plants considered for IPS in this work has been adapted from [5] [7] [11], and their nominal parameter values are provided in Appendix-I. Along with this, the inclusion of RFB is also considered in each area to deal with sizeable sudden power requirements. Further, a detailed description of individual subsystems is presented in the subsequent section.

3.2.1 Reheated-thermal power plant (RTPP):

The conventional power generating unit, i.e., RTTP, is employed in each area and other renewable energy sources, as shown in Fig. 3.1. A detailed block diagram depicting the implementation of RTTP is shown in Fig. 3.2(a), which consists of a speed governor mechanism, boiler, and a turbine with a re-heater. It needs to be emphasized here that the nonlinearities associated with speed governor and turbine, i.e., Governor deadband (GDB) and generation rate constraint (GRC), have also been considered for simulating RTTP in this study, and their nominal values are considered as 0.06 pu and 0.0005 puMW/sec, respectively [5]. Further, the speed governing mechanism and reheated turbine transfer function model have been adapted from [5][7]and presented as,

$$G_{GRT}(s) = \frac{1}{1+sT_{grt}} \text{ and } G_{TRT}(s) = \left(\frac{1}{1+sT_{trt}}\right)\left(\frac{1+sK_rT_r}{1+sT_r}\right) \quad (3.1)$$

Where T_{grt} and T_{trt} are the time constants of the governor and turbine, respectively, while K_r and T_r are re-heater gain and time constant of the reheated thermal power

plant.

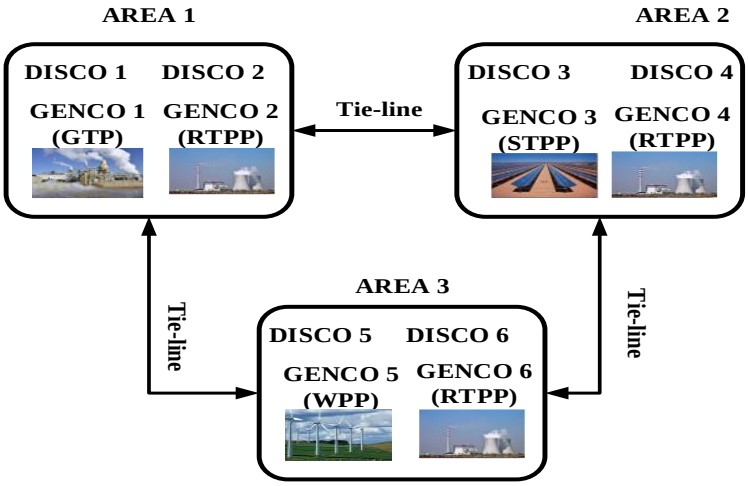

Fig. 3.1 *Schematic block diagram of three areas interconnected power system with renewable energy sources*

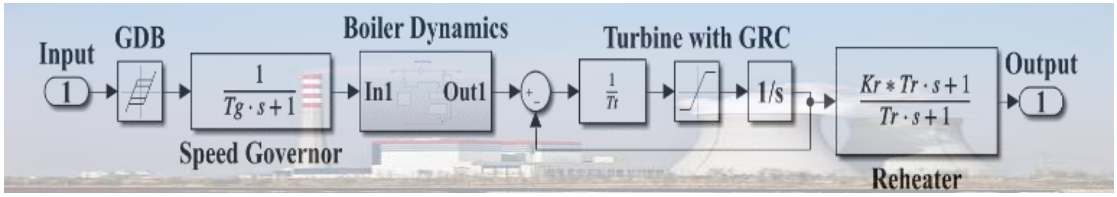

(a)

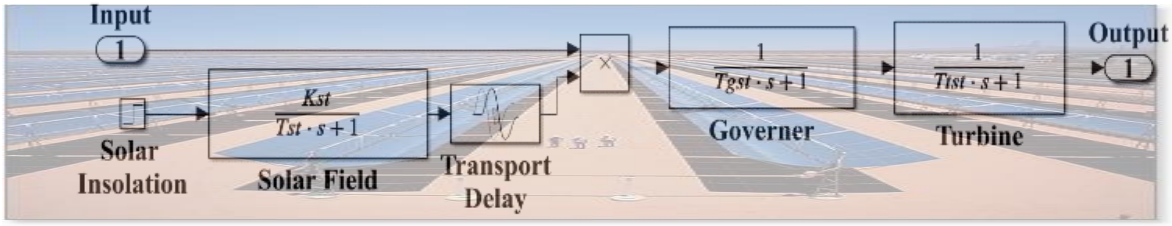

(b)

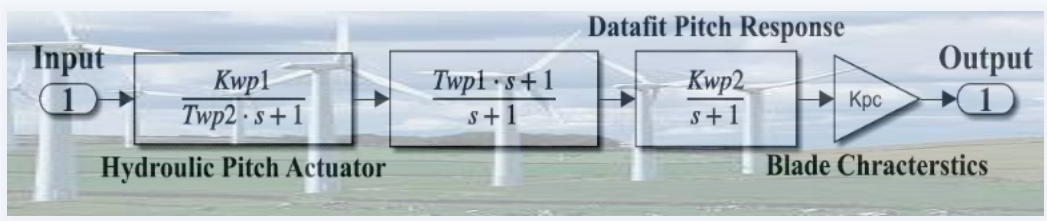

(c)

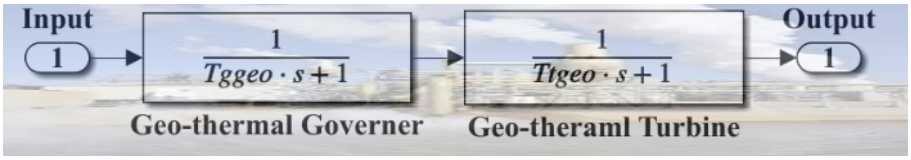

(d)

Fig. 3.2 *Block diagram of* ***(a)*** *Reheated thermal power plant* ***(b)*** *Solar Thermal Power Plant* ***(c)*** *Wind Power Plant* ***(d)*** *Geothermal Power Plant*

3.2.2 Solar-thermal power plant (STPP):

The STPP utilizes solar energy radiated from the sun to excite the speed governor mechanism and turbine to produce electric power. Solar irradiance focuses on the pipes which carry the water or molten salt as a useful fluid through a flat plate or parabolic trough collector. The transfer function model of the governor, turbine, and solar field has been adapted from [7] and presented as,

$$G_{GST}(s) = \frac{1}{1+sT_{gst}},\ G_{TST}(s) = \frac{1}{1+sT_{tst}} \text{ and } G_{ST}(s) = \frac{K_{st}}{1+sT_{st}} e^{-sT_D} \quad (3.2)$$

T_{gst} and T_{tst} are the governor and turbine time constants, respectively, of the solar thermal power plant. The K_{st}, $T_{st,}$ and T_D are the gain, time constant, and transport delay of the solar field, respectively, which excites the governor and turbine. The block diagram implementation for STPP is presented in Fig. 3.2(b).

3.2.3 Wind power plant (WPP):

The wind power plant's mathematical model implementation consists of a hydraulic pitch actuator, data fit pitch response, and blade characteristics presented in Fig. 3.2(c). The pitch angle control system maintains the pitch angle at the desired value corresponding to wind speed. Thus, wind turbine output can be regulated by controlling the pitch angle irrespective of wind speed. The mathematical modeling of the wind power plant has been adapted from [12] and is given as follows,

$$G_{GST}(s) = \frac{K_{WP1}\,(sT_{WP1}+1)}{(sT_{WP2}+1)(s+1)} \text{ and } G_{GDT}(s) = \frac{K_{WP2}}{s+1} \quad (3.3)$$

Where $K_{wp1,}$ $T_{wp1,}$ and T_{wp2} are the gain and time constants for the hydraulic pitch actuation system. The K_{wp2} and K_{pc} are the gain for data fit pitch response and pitch characteristics system, respectively.

3.2.4 Geothermal power plant (GTPP):

Geothermal energy is one of the promising sources of energy to fulfill the need for increasing future energy demand. It belongs to the thermal energy category and can be taken directly from the earth's crust. Its electrical energy conversion is similar to non-reheated thermal power plants, as steam can be taken directly from the earth's crust at high pressure and temperatures. The mathematical model of a geothermal power plant has been adapted from [11] and can be given as a transfer function as follows,

$$G_{GGT}(s) = \frac{1}{1+sT_{ggeo}} \text{ and } G_{TGT}(s) = \frac{1}{1+sT_{tgeo}} \quad (3.4)$$

Where, T_{ggeo} and T_{tgeo} are the time constants of the governor and turbine of geothermal power plants, respectively, the block diagram implementation for the same is shown in Fig. 3.2(d).

3.2.5 Redox flow battery (RFB):

RFBs are rechargeable electrochemical energy storage devices that can be used as an add-on solution for the LFC problem during abrupt mismatches in generation and consumption in an interconnected power system. RFB can be used as energy storage devices for LFC problems like SMES, but with faster response, better power capacity, and longer life. It stores the electrical energy in chemical form and generates electrical energy in a controlled manner through the reduction-oxidation (REDOX) reaction process. The RFB incorporated in the power system to improve the load frequency control performance is presented in Fig. 3.3.

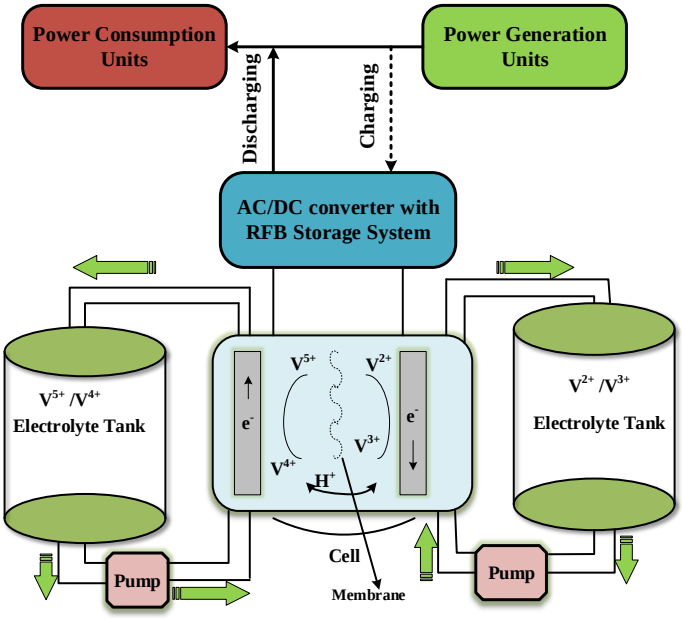

Fig. 3.3 *Power system with Redox Flow Battery (RFB)*

The RFB configuration has the advantage of having separate battery output (cell section) and battery energy storage (cell capacity) units, enabling the user to optimize the utilization of available physical space. A pair of centrifugal pumps circulate the positive and negative electrolyte (solution of sulphuric acid with vanadium ion) to the battery cell. In normal operations, RFB, while getting charged, acts as a minimal load and stores electrical energy in chemical energy. It can deliver electrical energy during any abrupt mismatch of generated and consumed power [5]. The mathematical model

of RFB can be represented as in Eq. 3.5, where the input to the transfer function is a deviation in frequency. The K_{RFB} and T_{RFB} are the gain and time constant for the RFB mathematical model. The mathematical model for RFB has been adapted from [5] and can be represented as follows

$$\mathrm{RFB(s)} = \frac{\mathrm{K_{RFB}}}{1+\mathrm{sT_{RFB}}} \tag{3.5}$$

3.2.6 IPS under deregulated scenario:

Figure 3.4 represents the detailed simulation model of considered IPS. It consists of three parts: (a) restructured interconnected three-area power system, (b) a distribution participation matrix employed with cpf, and (c) scheduled tie-line power.

$$DPM = \begin{bmatrix} cpf_{11} & cpf_{12} & cpf_{13} & cpf_{14} & cpf_{15} & cpf_{16} \\ cpf_{21} & cpf_{22} & cpf_{23} & cpf_{24} & cpf_{25} & cpf_{26} \\ cpf_{31} & cpf_{32} & cpf_{33} & cpf_{34} & cpf_{35} & cpf_{36} \\ cpf_{41} & cpf_{42} & cpf_{43} & cpf_{44} & cpf_{45} & cpf_{46} \\ cpf_{51} & cpf_{52} & cpf_{53} & cpf_{54} & cpf_{55} & cpf_{56} \\ cpf_{61} & cpf_{62} & cpf_{63} & cpf_{64} & cpf_{65} & cpf_{66} \end{bmatrix} \tag{3.6}$$

Where cpf_{mn} is the factor of the total power demand (contract) by m^{th} DISCO with n^{th} GENCO. In this work, three contract schemes, viz. Poolco transactions, bilateral transactions, and contract violation, have been investigated for considering three-area IPS under the deregulated scenario. It may be noted that, in a deregulated scenario, the elements of the DPM matrix change in accordance with the contract, and for the system under investigation, the DPM is taken as in Eq. 3.6.

3.2.6.1 Poolco-based contract:

In this work, the Poolco contract has been considered only for control area-1 for better understanding. Therefore, DISCO1 and DISCO2 have a contract with GENCO1 and GENCO2 only. As other DISCOs do not participate in the contract, they do not require power from any other GENCO; hence their cpfs are zero in the DPM. In this case, the load demand from DISCO1 and DISCO2 has been considered as 0.01 puMW [5]. Further, the area participation factor (apf) for GENCO1, GENCO3, GENCO5 and GENCO2, GENCO4, GENCO6 has been considered as 0.4 and 0.6, respectively. It should be noted here that the 0.01 puMW load demanded from the DISCO1 can be shared by GENCO1 and GENCO2 according to their area participation factor, i.e., 0.004 and 0.006 puMW, respectively.

Further, $cpf_{11} = \frac{power\ provided\ to\ \ DISCO1\ form\ GENCO1}{Total\ power\ demand\ of\ \ DISCO\ 1} = \frac{0.004}{0.01} = 0.4$, and similarly, other elements of DPM can be calculated. Therefore, DPM is given by Eq. 3.7 can represent this case.

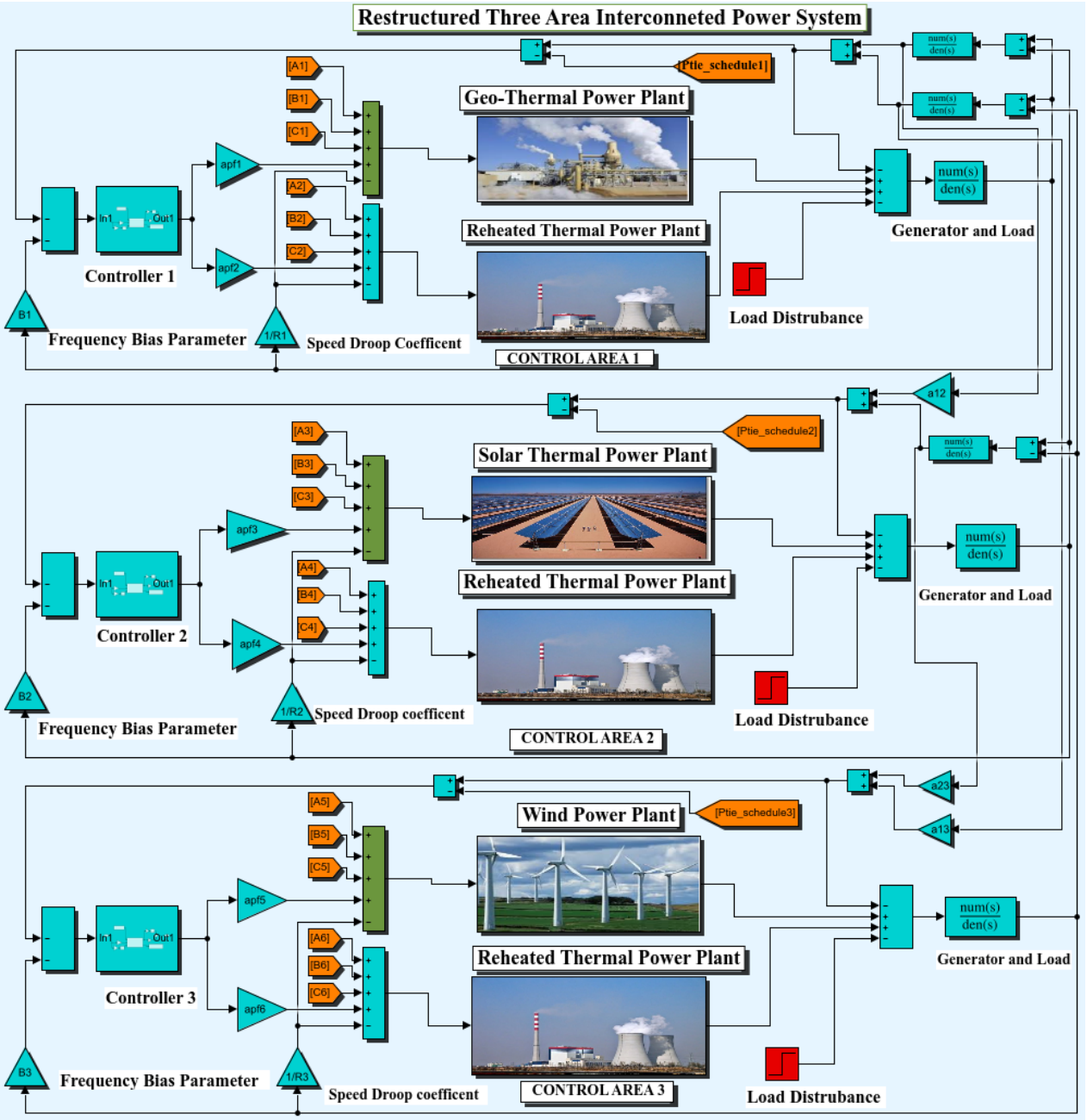

(a)

Fig. 3.4 (a) *Simulation model of an interconnected three-area deregulated power system with renewable energy sources*

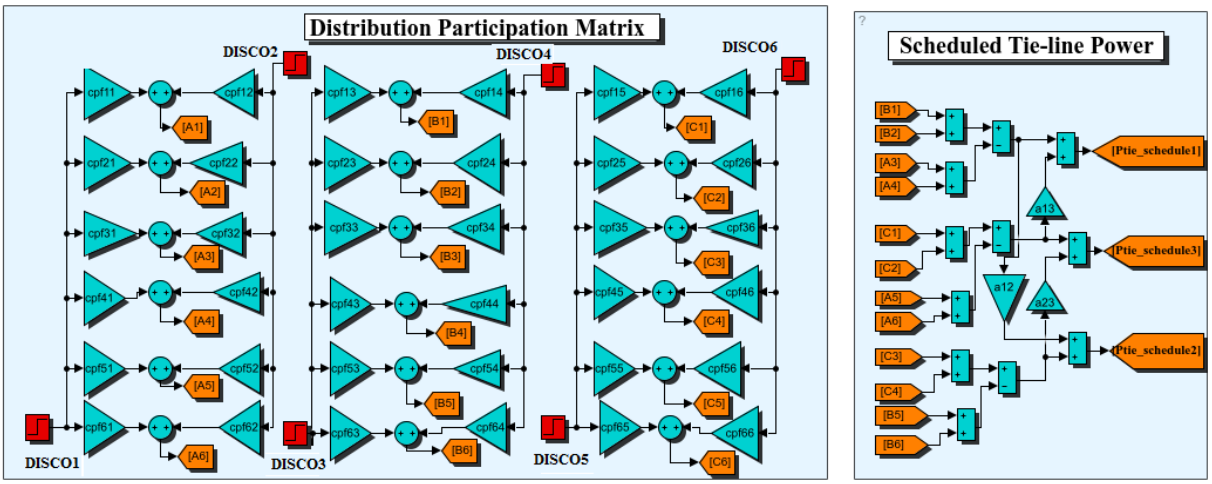

(b) **(c)**

Fig. 3.4 (b) *Distribution participation matrix* **(c)** *Schedule tie-line power for simulation model*

The scheduled generation by different GENCOs can be calculated with the help of cpfs, and DISCO load demand can be calculated as,

$GENCO1_{scheduled}$ = [0.4 + 0.4 + 0 + 0 + 0 + 0]×0.01=0.008 puMW

$GENCO2_{scheduled}$ = [0.6 + 0.6 + 0 + 0 + 0 + 0]×0.01=0.012 puMW; other GENCOs have zero scheduled generation as they do not have any contracts.

$$DPM_{Poolco} = \begin{bmatrix} 0.4 & 0.4 & 0 & 0 & 0 & 0 \\ 0.6 & 0.6 & 0 & 0 & 0 & 0 \\ 0 & 0 & 0 & 0 & 0 & 0 \\ 0 & 0 & 0 & 0 & 0 & 0 \\ 0 & 0 & 0 & 0 & 0 & 0 \\ 0 & 0 & 0 & 0 & 0 & 0 \end{bmatrix} \quad (3.7)$$

3.2.6.2 Bilateral and Contract-violation based transactions:

For the Bilateral contract-based operation, the DISCOs have the freedom to contract with GENCOs of their own area and other areas' GENCOs. Further, the change in demand from each DISCO has been considered as 0.01 puMW, and hence change in load demand for each area is 0.02 puMW. The apfs for GENCO1, GENCO2, GENCO3, GENCO4, GENCO5, and GENCO6 can be calculated as in the case of Poolco-based transactions and given by 0.4, 0.6, 0.4, 0.6, 0.4, and 0.6 respectively with the help of $DPM_{Bilateral}$ [7].

$\Delta P_{schedule12}$ =[Power demand by DISCOs in area-2 from GENCOs in area-1] - [Power demand by DISCOs in area-1 from GENCOs in area-2] (3.8)

Hence the area-1, area-2, and area-3 scheduled tie-line exchange power can be given as

$\Delta P_{schedule1}=\Delta P_{schedule12} + a_{13}\times\Delta P_{schedule13}$ (3.9)

$\Delta P_{schedule2}=\Delta P_{schedule23} + a_{12}\times\Delta P_{schedule12}$ (3.10)

$\Delta P_{schedule3}=\Delta P_{schedule13} + a_{23}\times\Delta P_{schedule23}$ (3.11)

Where a_{12}, a_{23}, and a_{13} are the area capacity ratio between area1-2, area2-3, and area1-3, respectively. The error in the tie-line power exchange at any instant for any given control area can be provided by

$\Delta P_{tie\text{-}error\text{-}i} =\Delta P_{actual\text{-}i} -\Delta P_{schedule\text{-}i}$ (3.12)

Where, i=1,2,3 for area-1, area-2 and area-3 respectively. The area control error (ACE) signal acts as the input for the controller, which is defined for control area 'i' and given as,

$$ACE_i = (\Delta f_i \times B_i) + (\Delta P_{tie-error-i}) \quad (3.13)$$

Where, 'B' and 'Δf' is the frequency bias constant and deviation, respectively. The DPM for the bilateral contract scenario has been presented by Eq. 3.14.

$$DPM_{Bilateral} = \begin{bmatrix} 0.2 & 0.2 & 0.1 & 0.1 & 0.1 & 0.1 \\ 0.4 & 0.2 & 0.1 & 0.3 & 0.1 & 0.1 \\ 0.1 & 0.1 & 0.1 & 0.1 & 0.2 & 0.2 \\ 0.1 & 0.2 & 0.3 & 0.1 & 0.1 & 0.1 \\ 0.1 & 0.1 & 0.1 & 0.1 & 0.2 & 0.2 \\ 0.1 & 0.2 & 0.3 & 0.1 & 0.1 & 0.1 \end{bmatrix} \quad (3.14)$$

Further, the bilateral mode DPM is considered for the contract violation scenario, where DISCO1 is assumed to be violating the contract. The contract violation condition is simulated by demanding an excess power of 0.01 puMW by DISCO1, which will be supplied by only area-1 GENCOs. Hence the change in load demand in area-1 can be given by,

$$\Delta P_{LD1} = [0.01 + 0.01] + [0.01] = 0.03 \text{ puMW} \quad (3.15)$$

It may be noted that the secondary or supplementary control loop must be incorporated to achieve satisfactory LFC dynamic response for each considered contract scenario, i.e., Poolco, Bilateral, and Contract-violation. In the study, a conventional PID, a FOPID, and a self-tuned fractional order fuzzy PID (STFOFPID) controller are investigated for said LFC problem. The next section presents a detailed description of the considered control scheme, along with its implementation aspect.

3.3 The control scheme for load frequency control:

As indicated in the previous section, three different controllers are considered in this work; this section deals with a detailed discussion on used control structures. Since conventional parallel PID and FOPID controllers have well-established control structures, their description is omitted here for brevity. This section primarily focuses on the STFOFPID control structure and its implementation for effective LFC in deregulated IPS. Further, to obtain optimal control performance, a global optimization algorithm, i.e., SSA, has been used and briefly discussed in this section.

3.3.1 Self-tuning fractional order fuzzy PID controller:

The STFOFPID controller is a fuzzy logic-based controller that adapts its gain in run time according to the combination of error and the rate of error change. This is a direct adaptive control scheme based on dedicated formula-based outputs for different input combination regions. Another notable feature of STFOFPID is that its implementation is independent of estimating plant parameters, unlike indirect adaptive control schemes. A unique feature of STFOFPID is its ease of implementation since only two membership functions for input linguistic variables are considered, which substantially reduces the number of rules. In this study, the input linguistic variables are considered as scaled versions of area control error (ACE) and its fractional order derivative, as shown in Fig. 3.7. The STFOFPID controller output generates a self-tuning PID action by aggregating the output of an *input combination based fuzzy controller* (ICFC) [8] [13], where the output of ICFC is considered as a PD action in position form and a PI action in velocity form. A detailed description of ICFC is presented in the subsequent section. It may be noted that the fractional order calculus operators are utilized at both, i.e., input and output sides of the STFOFPID controller.

3.3.2 Input combination-based fuzzy controller (ICFC):

It is worth mentioning here that the ICFC is the backbone of the STFOFPID controller responsible for generating primary control action for STFOFPID. This control action is generated with various input combination regions created by two input linguistic variables based on their membership functions. The input linguistic variables, i.e., scaled ACE ($\tilde{e}(nT)$) and fractional rate of change of ACE ($\tilde{r}(nT)$) are defined using two membership functions, viz. negative (N) and positive (P), in the entire

universe of discourse, as shown in Fig. 3.5(a). It may be noted that scaling factors are utilized to map input linguistic variables in the range of -1 to 1. Further, three singleton output membership functions are considered in the ICFC structure, located symmetrically at about zero at a distance 'u_α' from each other, as shown in Fig. 3.5 (b).

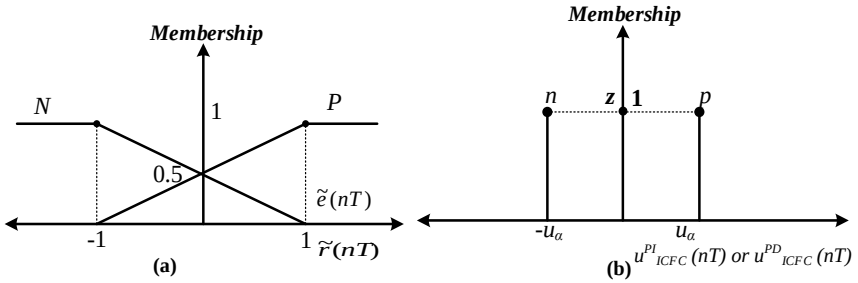

Fig. 3.5 *Membership functions for* **(a)** *Input* **(b)** *Output*

For ICFC output generation, a fuzzy rule base has been decided based on the LFC problem for considered IPS. The input to the controller is $\tilde{e}(nT)$ and $\tilde{r}(nT)$ and the equivalent controller output is u_{ICFC}, which is considered as, u^{PI}_{ICFC} or u^{PD}_{ICFC}. It needs a mention here that u^{PI}_{ICFC} and u^{PD}_{ICFC}, correspond to self-tuning PI action in velocity form and self-tuning PD action in position form, respectively.

Also, corresponding to two membership functions defined on each linguistic variable, four rules have been designed, which are as follows,

R^1: If $\tilde{e}(nT)$ is **'N'** and $\tilde{r}(nT)$ is **'N'**, Then $u_{ICFC}(nT)$ is **'p'**
R^2: If $\tilde{e}(nT)$ is **'N'** and $\tilde{r}(nT)$ is **'P'**, Then $u_{ICFC}(nT)$ is **'z'**
R^3: If $\tilde{e}(nT)$ is **'P'** and $\tilde{r}(nT)$ is **'N'**, Then $u_{ICFC}(nT)$is **'z'**
R^4: If $\tilde{e}(nT)$ is **'P'** and $\tilde{r}(nT)$ is **'P'**, Then $u_{ICFC}(nT)$ is **'n'**

Further, the center of gravity approach for defuzzification has been used, and the final output of ICFC is calculated as,

$$u_{ICFC} = \frac{\sum_i^4 \left[u^i_{ICFC} \times \mu^i_{ICFC}\right]}{\sum_i^4 \mu^i_{ICFC}} \tag{3.16}$$

Where μ^i_{ICFC} is the strength of i^{th} rule and u^i_{ICFC} are the singleton output of i^{th} rule. Though, u_{ICFC} calculation can be done using Eq. 3.16; however, the strength of each rule using min T-norm has to be calculated using each input linguistic variable's membership value. This process can further be simplified by defining various input combination (IC) regions on '$\tilde{e}(nT)$' and '$\tilde{r}(nT)$' and then defining output for each IC region. For the present structure of ICFC, the two-dimensional input space comprising of '$\tilde{e}(nT)$' and '$\tilde{r}(nT)$' is divided into twelve input-combination regions, as shown in Fig. 3.6(a).

The analytical formula for controller output u_{ICFC} is obtained with defuzzification as given by Eq. 3.16, which is presented in tabular form as in Table 3.1. The three-dimensional control surface with the input and output variables has been presented in Fig. 3.6(b). It may be noted that the structure of ICFC can be considered either a velocity form self-tuning fractional-order PI or a position form self-tuning fractional-order PD controller. But, in order to generate self-tuning fractional order PID action, the structure of Fig. 3.7 can be considered, which is named as STFOFPID controller in this work.

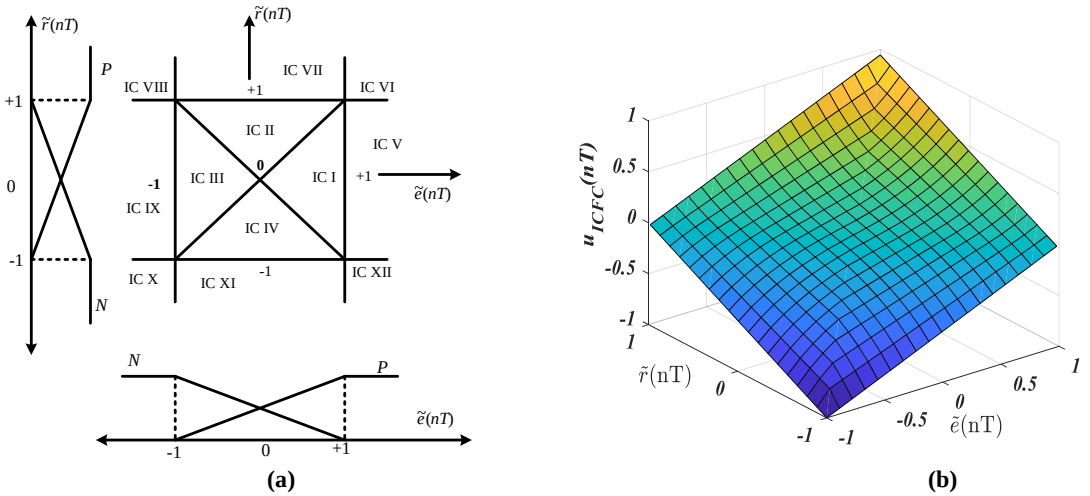

(a) **(b)**

Fig. 3.6 ***(a)*** *STFOFPI and STFOFPD input-combination (IC) regions [8]* ***(b)*** *Three-dimensional surface for ICFC output*

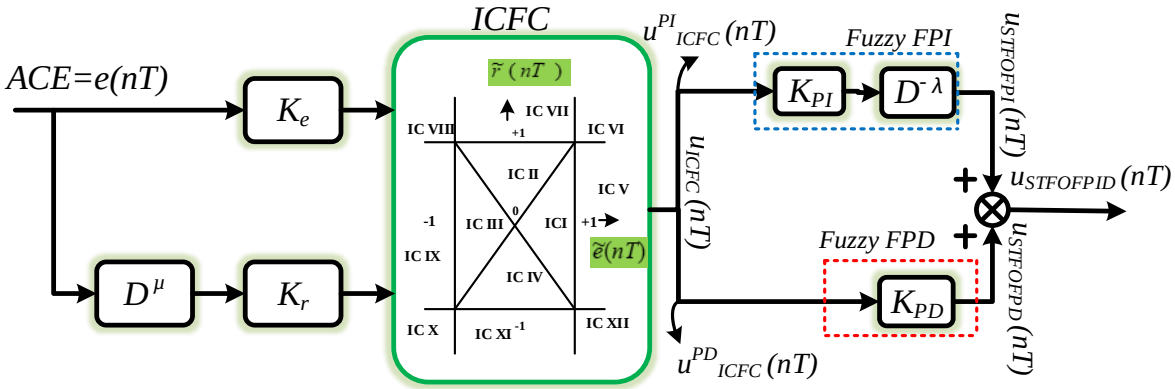

Fig.3.7 *Detailed configuration of STFOFPID controller*

To understand this aspect in detail about the generation of self-tuning PID control action using ICFC, consider the following scenario. The rule base of the ICFC indicates the realization of a self-tuning fuzzy PD control action; however, the same control structure of the ICFC may provide both fuzzy PD and fuzzy PI control action. If we simply consider the output of ICFC to be in position form, i.e., the output of control

law represents the instantaneous control action, then it can be considered as fuzzy PD control action, and if we consider it to be in velocity form (i.e., integration is required to generate the instantaneous control output), then it can be a fuzzy PI control output.

Table 3.1 *Values of u_{ICFC} ($u^{PI}{}_{ICFC}$ or $u^{PD}{}_{ICFC}$) for different input-combination (IC) regions*

Input-combination (IC) region	$\mathbf{u_{ICFC}^{PI}(nT)}$ **or** $\mathbf{u_{ICFC}^{PD}(nT)}$
IC-I & IC-III	$\frac{u_\alpha}{2[2-\lvert\tilde{e}(nT)\rvert]}[\tilde{e}(nT)+\tilde{r}(nT)]$
IC-II & IC-IV	$\frac{u_\alpha}{2[2-\lvert\tilde{r}(nT\rvert)]}[\tilde{e}(nT)+\tilde{r}(nT)]$
IC-V	$\frac{\tilde{r}(nT)u_\alpha}{2}+\frac{u_\alpha}{2}$
IC-VI	u_α
IC-VII	$\frac{\tilde{e}(nT)u_\alpha}{2}+\frac{u_\alpha}{2}$
IC-IX	$\frac{\tilde{r}(nT)u_\alpha}{2}-\frac{u_\alpha}{2}$
IC-X	$-u_\alpha$
IC-XI	$\frac{\tilde{e}(nT)u_\alpha}{2}-\frac{u_\alpha}{2}$
IC-VIII & IC-XII	0

To generate the self-tuning fuzzy PID controller output, these actions must be manipulated in a certain way, which is explained as follows.

It may be noted that the structure of ICFC receives an error and fractional derivative of error as its inputs, and the ICFC output can be obtained by Eq. 3.17.

$$u_{ICFC}(nT) = f[\tilde{e}(nT), \tilde{r}(nT)] \tag{3.17}$$

Where, $f(e,r)$ is a fuzzy function representing ICFC structure and Table 3.1 can be used to find u_{ICFC}. Further, STFOFPID controller output can be calculated as,

$$u_{STFOFPID}(nT) = K_{PI}\left[\frac{d^{-\lambda}}{dt^{-\lambda}}(u_{ICFC}^{PI}(nT))\right] + K_{PD}\left(u_{ICFC}^{PD}(nT)\right) \tag{3.18}$$

Eq. 3.17 and 3.18 describe the STFOFPID control structure, and K_e, K_r, K_{PI}, and K_{PD} are the input and output gains of the STFOFPID controller, respectively. It is worth mentioning here that, numerically, $u_{ICFC}^{PI}(nT)$ and $u_{ICFC}^{PD}(nT)$ have the same values and are obtained from the output of ICFC, as shown in Fig. 3.7.

Further, it may be noted that the STFOFPID and FOPID controllers require fractional order differential and integral operators for their implementation. The fractional-order calculus provides the user liberty to implement the non-integer or differential order operator, which can have a superior level of performance in terms of

robustness compared to integer order. In this thesis, 'Oustaloup approximation' is used to approximate the non-integer order calculus because of its excellent fitting to non-integer order elements. This approach fits the approximation utilizing a higher-order filter having an order of '2N+1' inside a specified frequency bound [ω_L, ω_H].

The approximation of s^{λ} can be written as,

$$S^{\lambda} \approx G' \prod_{k=-N}^{k=N} \frac{s+\omega_{z_k}}{s+\omega_{p_k}} \tag{3.19}$$

Where G' is gain, ω_{z_k} and ω_{p_k} , characterizes as the zeros and poles of the analog filter, respectively, and can be represented as

$$\omega_{z_k} = \omega_L \left(\frac{\omega_H}{\omega_L}\right)^{\frac{k+N+0.5(1-\lambda)}{2N+1}}, \omega_{p_k} = \omega_L \left(\frac{\omega_H}{\omega_L}\right)^{\frac{k+N+0.5(1+\lambda)}{2N+1}} \text{ and } G' = (\omega_H)^{\lambda} \tag{3.20}$$

The effectiveness of fractional order approximation of this technique primarily depends upon the value of 'N'. With smaller values of 'N', it is easy to implement fractional-order operator approximation in hardware but deteriorates the approximation performance by producing the ripple in magnitude as well in phase response. The present chapter uses 'N' as 3, and the frequency bound of [ω_L, ω_H] is considered as [10^{-2}, 10^{-2} rad/s], which is suitable in the LFC application [13], [14].

3.4 Controller parameters optimization:

It is essential to optimize the controller parameters with a considered objective function to achieve the desired control performance. In this investigation, optimal parameters for considered controllers, i.e., PID, FOPID, and STFOFPID, have been obtained with a recently proposed bio-inspired optimization algorithm, i.e., salp swarm algorithm (SSA) and a well-established optimization technique, i.e., GA. A genetic algorithm is a type of heuristic search that draws inspiration from Charles Darwin's idea of natural evolution. The GA has been explored in many fields, including power systems for optimal controller parameter evaluation [15]. Further, the subsequent subsection presents the details of the newly devised optimization algorithm, i.e., SSA.

3.4.1 Salp swarm algorithm (SSA):

SSA is a swarm-based meta-heuristic optimization algorithm motivated by the foraging behavior of salps found in the deep ocean. Salps have barrel-shaped bodies like jellyfish and belong to the family of Salpidae. Due to its presence in the deep ocean, very little literature is available about its swarming behavior. S. Mirjalili *et al.* proposed

the salp swarm algorithms for engineering problem optimization purposes [9]. And recently been used in many applications, including the load frequency control problem [10] [16]. In SSA, the population is classified into two categories, i.e., leader salps and follower salps. The best solution obtained in each iteration is assigned as the food source variable (leader salps update their position according to the position of the food source variable). Even if the complete population deteriorates, this can provide the best optimal stored solution food source variables. In this algorithm, '*S*' is considered a food source in search space as the target of salp swarms. The flow chart of the SSA is given in Fig. 3.8.

The following equations are used for updating the swarm position in the search space.

$$x_i^1 = \begin{cases} S_i + A_1((ub_i - lb_i)A_2 + lb_i & \text{for } A_3 \geq 0.5 \\ S_i - A_1((ub_i - lb_i)A_2 + lb_i & \text{for } A_3 < 0.5 \end{cases} \tag{3.21}$$

$$A_1 = 2 * e^{-\{4*I/Max\_iter\}^2} \tag{3.22}$$

Where ' x_i^1', 'S_i,' 'ub_i', and 'lb_i' are the position of the leader (first salp), the position of the food source, upper limit, and lower limit in the i^{th} dimension, respectively. A_2 and A_3 are random numbers uniformly generated in the range of 0 and 1. *'I'* and *'Max_iter'* are the current and maximum iteration, respectively. The maximum number of iteration (Max_iter) is taken as 100 for simulations.

Newton's law of motion was used to update the position of the followers, which can be given as;

$$x_i^k = \frac{1}{2}at^2 + v_0 t \tag{3.23}$$

$$x_i^k = \frac{1}{2}\left(x_i^k - x_i^{k-1}\right) \tag{3.24}$$

Where, $k \geq 2$, x_i^k shows the position of k^{th} follower salp in i^{th} dimension, 't' is time or iteration, 'v_0' is the initial speed and $a = \frac{v_{final}}{v_o}$. Iteration is the time required to perform optimization, and the difference between iterations is unity, and considering $v_0 = 0$, the expression has been restructured in Eq. 3.24. Equations 3.23 and 3.24 can be utilized as a mathematical model for simulating the salp chain's behavior. To exploit the potential of SSA to optimize (by minimization) an objective function efficiently,

the thesis has adopted it to design LFC for interconnected power systems and presented it in the next subsection.

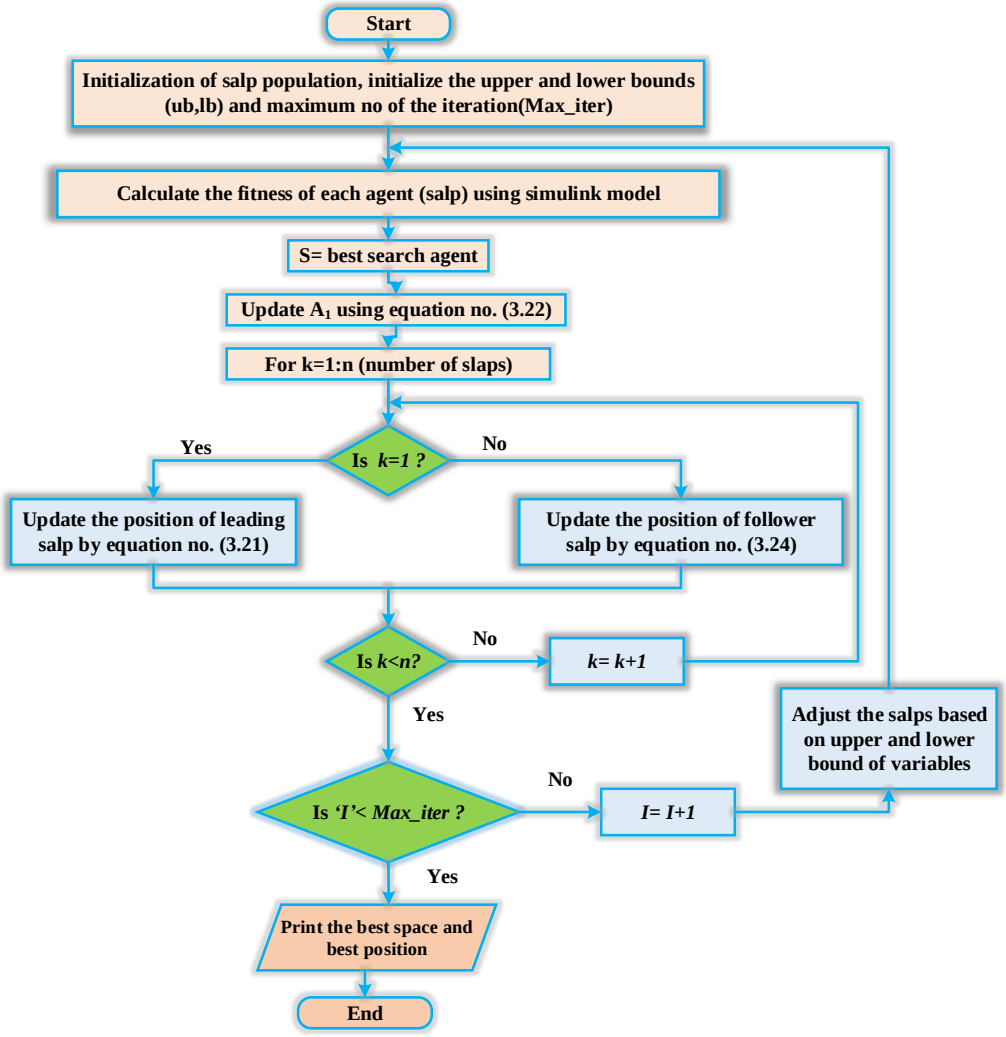

Fig. 3.8 *Flow chart of salp swarm algorithm (SSA)* [9]

3.4.2 Objective function and optimal controller parameter:

Further, to effectively tune the controllers, the objective function should be critically designed so that it essentially blends the required performance measures. For effective load frequency regulation in considered IPS, the current work proposes a hybrid objective function (Eq. 3.25) comprising a weighted combination of integral time-weighted absolute error (ITAE) and oscillatory measure (OM). The 'ITAE' component of the objective function is responsible for the betterment of dynamic performance as well as steady-state performance, whereas 'OM' take care of the oscillatory behavior of IPS produced due to inherent nonlinearities, i.e., GRC and GDB,

as the latter nonlinearity is the primary sources of sustained oscillations in various variables in IPS.

Objective function or Performance Index (J) = [w_1×ITAE + w_2×OM] (3.25)

$$ITAE = \int_0^{t_{final}} [|\Delta f_1| + |\Delta f_2| + |\Delta f_3| + |\Delta P_{tie-1}| + |\Delta P_{tie-2}| + |\Delta P_{tie-3}|] t \, dt \quad (3.26)$$

$$OM = \int_0^{t_{final}} \left\{ \left|\frac{d}{dt}(\Delta f_1)\right| + \left|\frac{d}{dt}(\Delta f_2)\right| + \left|\frac{d}{dt}(\Delta f_3)\right| + \left|\frac{d}{dt}(\Delta P_{tie-1})\right| + \left|\frac{d}{dt}(\Delta P_{tie-2})\right| + \left|\frac{d}{dt}(\Delta P_{tie-3})\right| \right\} t \, dt \quad (3.27)$$

Where 'Δf_1', 'Δf_2' and 'Δf_3' are the deviations in the frequency of area-1, area-2, and area-3, respectively while, 'ΔP_{tie-1}', 'ΔP_{tie-2}' and 'ΔP_{tie-3}' are the deviation in the tie-line power exchange between area1-2, area 2-3 and area1-3 respectively. The weighting factors w_1 and w_2 have been calculated using the analytical hierarchy process (AHP) technique and found to be 0.85 and 0.15, respectively [17]. Further, along with SSA, a genetic algorithm is adopted here for solving the controller parameter optimization problem, which serves as a basis for comparative analysis. The search space for various gains has been taken in the range of [-3, 3] for all the considered controllers. Further, the order of integral and differential operators, i.e., λ and μ, respectively, are bound in the range of [0, 2], wherever applicable. The range of 'u_α' in the case of STFOFPID is taken as [-10, 10]. The optimization procedure for both algorithms was run for 100 iterations with a population size of 50. It needs to a mention here that all the controllers were tuned for all the considered modes of operation, i.e., Poolco, Bilateral, and contract violation. The convergence curves for SSA and GA optimization algorithms for different controllers tuning under bilateral transactions are presented in Fig. 3.9.

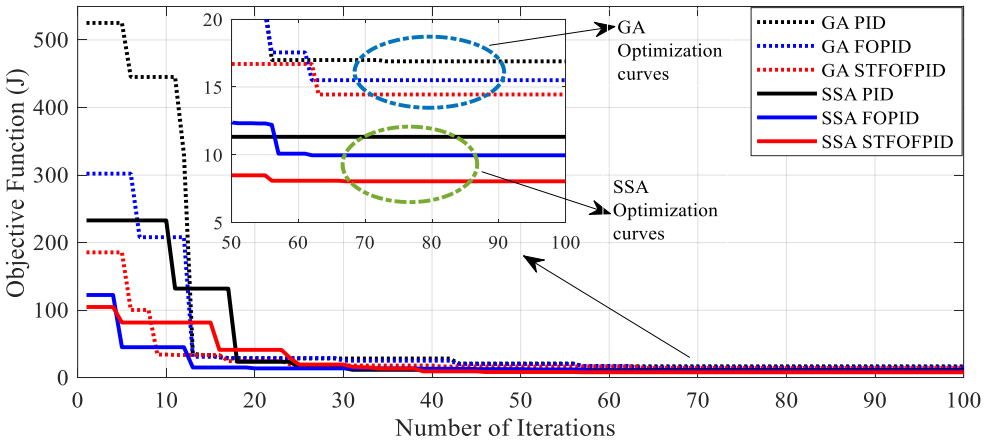

Fig. 3.9 *Convergence curve for different controllers using GA and SSA under Bilateral transaction*

Other convergence curves are omitted for the sake of brevity of the present study;

however, their gains are presented along with detailed simulation results. It is evident from Fig. 3.9 that SSA provides faster convergence irrespective of controller structures along with superior objective function values. The optimal controller parameters obtained with SSA and GA optimization techniques for PID, FOPID, and STFOFPID control structure under Poolco, Bilateral, and Contract-violation contracts are given in Tables 3.2 and 3.3. A detailed analysis of each controller's performance for all the considered modes of operation is presented in the subsequent section.

3.5 Simulation results and discussion:

The various systems utilized for investigation purpose in this thesis has been implemented on MATLAB/SIMULINK environment with version 2019b. In this study, extensive simulation studies have been carried out under various contract scenarios, i.e., Poolco, bilateral, and contract-violation, with optimal controller parameters obtained for PID, FOPID, and STFOFPID using GA and SSA. A thorough comparative analysis of LFC dynamic performance with different control schemes under all three contract scenarios with nominal system parameters is first presented. Further, detailed simulation studies have also been conducted, where RFB is included in each area to enhance the system's dynamic performance under investigation. Since, in an IPS, the load profile is uncertain, hence the performance of controllers for the two contract modes is carried out for random step load perturbation. In addition to this, robustness analysis for handling parametric variations in RTPP inherent non-linearities, i.e., GDB and GRC, has also been considered for all the contract modes, and detailed comparative studies are carried out for the same. It needs to a mention here that such comparative studies for a three-area hybrid IPS in a deregulated environment are carried out for the first time, which establishes the need and effectiveness of the STFOFPID controller for such scenarios.

3.5.1 LFC performance without energy storage unit:

The LFC performance investigation of considered IPS in deregulated mode with three contract scenarios viz Poolco, Bilateral, and Contract-violation using PID, FOPID, and STFOFID control structure optimized with GA and SSA with nominal system parameters is performed. The DPM and apfs for all three contracts have been taken as given in the system description section 3.2. The simulation has been performed

with optimized controller parameters, as provided in Tables 3.2 and 3.3, for three different contract scenarios.

Table 3.2 *GA and SSA optimized PID and FOPID controller's parameter under Poolco, Bilateral and Contract –violation*

Contract		Poolco				Bilateral				Contract violation			
Optimization		GA		SSA		GA		SSA		GA		SSA	
Controller Parameters		PID	FOPID	PID	FOPID	PID	FOPID	PID	FOPID	PID	FOPID	PID	FOPID
Control Area-1	K_{P1}	2.953	2.988	2.989	2.999	1.957	2.934	1.402	-2.596	2.968	2.386	0.443	-0.435
	K_{I1}	0.481	2.911	2.998	2.998	2.585	-1.001	1.334	1.625	2.501	2.829	2.880	2.076
	K_{D1}	2.666	2.887	1.984	1.561	1.313	-2.126	1.637	2.172	1.208	0.387	2.878	1.803
	λ_1	1	1.136	1	1.159	1	0.051	1	0.739	1	0.869	1	1.141
	μ_1	1	1.228	1	1.157	1	0.176	1	0.616	1	1.608	1	0.525
Control Area -2	K_{p2}	0.035	2.252	1.651	0.355	0.205	2.526	0.708	-2.533	0.748	1.174	0.589	1.287
	K_{I2}	2.997	2.471	0.003	-0.739	1.497	2.514	-.039	2.329	0.085	1.263	0.848	2.441
	K_{D2}	2.665	1.486	1.987	-0.735	1.326	2.038	-.831	0.085	0.81	-1.273	2.196	0.990
	λ_2	1	0.004	1	0.041	1	0.323	1	0.427	1	0.802	1	0.588
	μ_2	1	1.719	1	0.051	1	1.486	1	0.551	1	0.224	1	1.283
Control Area-3	K_{P3}	0.691	-1.229	1.723	1.322	1.573	2.624	1.425	2.826	0.307	1.242	2.032	-2.293
	K_{I3}	0.064	0.292	1.308	0.669	0.068	2.995	0.056	0.008	0.801	1.108	0.004	2.001
	K_{D3}	0.905	2.993	1.99	2.97	0.912	2.995	1.404	1.229	1.946	2.828	2.166	2.288
	λ_3	1	0.247	1	0.415	1	0.018	1	0.937	1	0.182	1	0.058
	μ_3	1	1.112	1	0.992	1	0.912	1	0.797	1	0.697	1	0.927

Table 3.3 *GA and SSA optimized STFOFPID controller parameters*

Contract		Poolco		Bilateral		Contract violation	
Optimization		GA	SSA	GA	SSA	GA	SSA
Control Area-1	$u_{\alpha 1}$	3.6171	6.5021	8.8884	2.8053	9.8004	0.9203
	K_{e1}	2.9989	-2.8547	-0.2207	1.5709	2.0239	1.7363
	K_{r1}	1.7314	-1.5730	-0.0271	1.7831	0.3784	1.2871
	K_{PI1}	-2.7277	2.9909	2.3259	-1.5254	-0.2405	-1.0601
	K_{PD1}	-0.3144	1.1993	2.9497	-0.8006	-1.0688	-0.72261
	λ_1	1.2227	1.1263	0.3014	0.7278	1.5824	0.87271
	μ_1	1.4245	1.1513	1.8709	1.541	1.8631	1.7636
Control Area-2	$u_{\alpha 2}$	8.5218	9.9900	4.5180	3.2291	9.8253	9.1716
	K_{e2}	0.9788	0.1082	-2.6218	-1.453	0.9418	1.6026
	K_{r2}	-0.7341	-0.6108	1.3746	-1.3531	1.4905	1.181
	K_{PI2}	0.7479	0.01748	2.5332	1.0575	0.7075	-0.58211
	K_{PD2}	-1.5233	0.7952	0.6412	0.5827	1.4382	-1.3866
	λ_2	0.1797	0.6819	0.6542	0.5943	0.3172	0.82338
	μ_2	1.3157	0.3028	0.8576	1.756	1.8462	1.6703
Control Area-3	$u_{\alpha 3}$	-7.5816	1.8763	-0.0380	7.1925	-4.1284	8.1566
	K_{e3}	2.2769	1.4389	2.7496	-1.468	-0.1959	1.7041
	K_{r3}	1.7739	-2.585	1.9582	-0.5729	0.7944	1.9249
	K_{PI3}	-1.9940	1.1201	2.7889	1.3361	1.0181	1.2307
	K_{PD3}	-2.0150	-2.6994	1.3847	1.8545	-0.1804	-1.9549
	λ_3	0.0298	0.2999	0.6214	0.03952	0.6028	0.023831
	μ_3	1.1619	0.6559	1.5286	1.1528	1.2956	0.79369

Figure 3.10 represents the objective function values (J) for considered contract

scenarios with a different controller optimized with GA and SSA. It may be readily inferred from Fig. 3.10(a) that SSA-optimized STFOFPID has the least value of the considered objective function for the Poolco transaction. The improvement achieved by SSA tuned STFOFPID controller stands at 67.42% and 41.87% in terms of 'J' compared to SSA tuned FOPID and GA tuned STFOFPID, respectively, which are its closest competitors in this analysis. Similarly, for Bilateral mode, the performance of SSA STFOFPID is 19.28% better than its closest competitor, i.e., SSA tuned FOPID, which provides a 'J' value of 9.956 as shown in Fig 3.10(b). Further, in this case, GA tuned PID performed worst and caused a 'J' value of 16.89, which suggests that conventional PID controllers are unsuitable for such complex control scenarios.

Further, in the case of the contract-violation scenario, the SSA STFOFPD controller performance in terms of 'J' has improved by 24.44% and 43.18% compared with SSA FOPID and GA STFOFPID controller, respectively, as represented in Fig. 3.10(c). The same is reflected in the 'OM' value for the SSA STFOFPID controller, which is 3.616, compared to SSA FOPID, which has its 'OM' value as 6.691. This is a considerable improvement of 45.95%, which can lead to a better life span of control components present in the control loop.

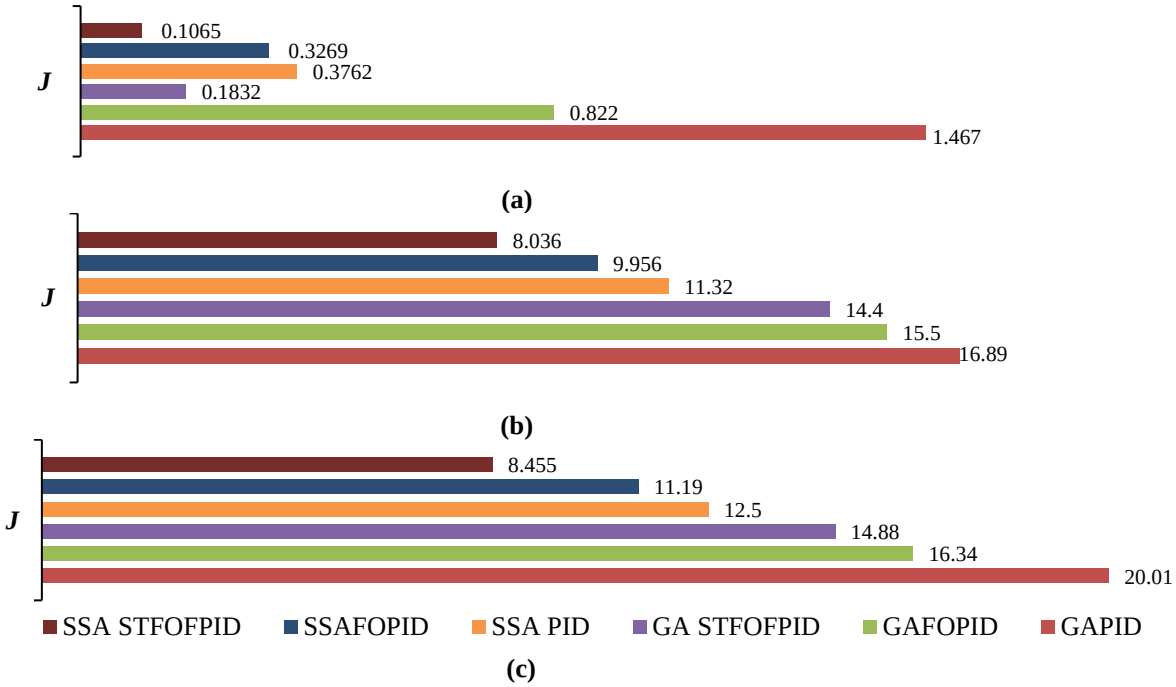

Fig. 3.10 *Objective function (J) values* ***(a)*** *Poolco transaction* ***(b)*** *Bilateral transaction* ***(c)*** *Contract-violation transaction with different controllers optimized with GA and SSA*

To provide detailed insight into various controllers optimized with GA and SSA, the

ITAE values in frequency deviations of all three control areas under Poolco, bilateral, and contract-violation transaction situations are presented in Table 3.4. It may be inferred from these results that the minimum improvement in ITAE value is 20.35% for Δf_3 in the case of a bilateral transaction, while the maximum improvement is 58.73% for Δf_3 in the case of the Poolco transaction with SSA STFOFPID controller with its closest competitor. The boldface values in Table 3.4 represent the best ITAE value obtained by controllers for the frequency deviation of different control areas under different contract scenarios, from where it may be noted again that the SSA STFOFPID controller proves to be best among all the applied controllers.

Table 3.4 *ITAE values for frequency deviation in area-1, 2 and 3 with different controller optimized by GA and SSA under different transactions*

Transaction	Poolco			Bilateral			Contract violation		
Controller	$ITAE_{\Delta f1}$	$ITAE_{\Delta f2}$	$ITAE_{\Delta f3}$	$ITAE_{\Delta f1}$	$ITAE_{\Delta f2}$	$ITAE_{\Delta f3}$	$ITAE_{\Delta f1}$	$ITAE_{\Delta f2}$	$ITAE_{\Delta f3}$
GAPID	0.2138	0.1924	0.1736	3.103	3.58	2.969	3.699	3.835	3.685
SSAPID	0.0757	0.0453	0.0419	1.440	1.802	1.427	1.967	2.058	1.872
GAFOPD	0.1959	0.1412	0.1434	3.311	1.963	1.556	3.502	3.502	3.374
SSAFOPID	0.0674	0.0390	0.0311	1.176	1.400	1.080	1.829	1.662	1.568
GASTFOFPID	0.0521	0.0269	0.0212	2.092	2.417	2.161	2.865	3.061	2.774
SSASTFOFPID	**0.0215**	**0.0178**	**0.0139**	**0.8857**	**0.9876**	**0.8602**	**0.9373**	**1.014**	**0.933**

From the above-detailed discussion of various control structures optimized with GA and SSA, it needs to a mention here that SSA tuned controllers performed better than GA tuned controllers, and STFOFPID controller performance is exceptionally outstanding in all three contract scenarios. Hence GA optimized controller results have been omitted. Further, for the brevity of the thesis, the responses of the Poolco transaction have been omitted.

For Bilateral transactions, the restrictions as present in the case of the Poolco scenario for power transactions among various GENCOs and DISCOs will be relaxed. The same is reflected by its DPM, as shown in Eq. 3.13. The frequency deviations in each area for this case are shown in Fig. 3.11(a), from where it may be inferred that the dynamic performance is best for SSA STFOFPID in terms of transient and steady-state response. The effects of nonlinearities, which mainly contribute to oscillations, are largely suppressed for SSA STFOFPID, as sustained oscillations are eliminated from all three areas.

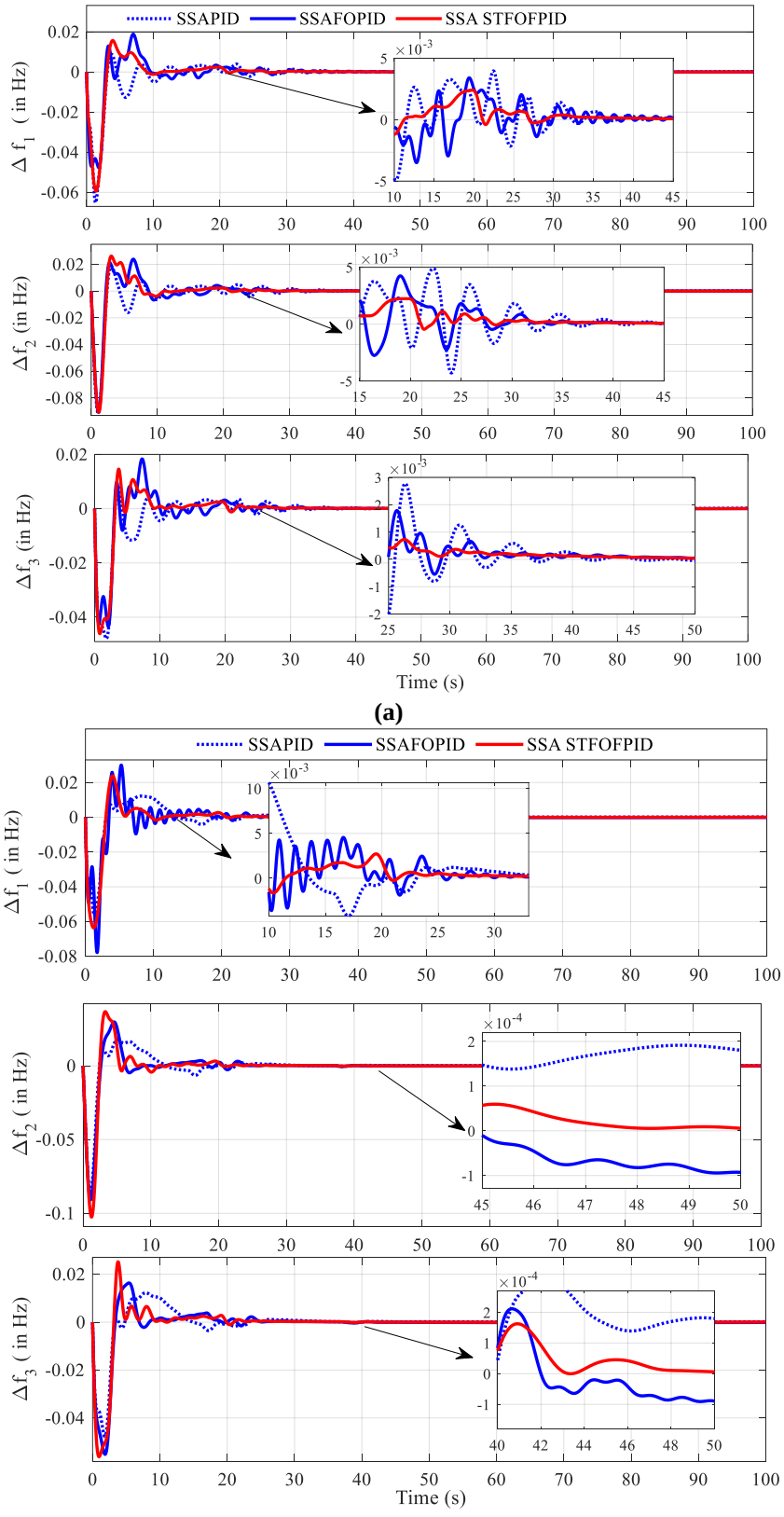

Fig. 3.11 *Frequency deviations in area-1, 2 and 3 with different SSA optimized controllers under **(a)** Bilateral transaction **(b)** Contract-violation without RFB*

Further, for simulating the contract-violation scenario, the same DPM, as in the case of the bilateral transaction, has been taken into consideration; however, DISCO1 violated the contract by excess power demand. The dynamic performance in terms of frequency deviations for all three control areas with SSA optimized controllers is presented in Fig. 3.11(b), from which it can be inferred that the SSA STFOFPID controller performs better as it contains the least oscillations as well as reaches to its desired values faster than its other competitors.

3.5.2 IPS with RFB under different contract scenarios:

Due to inherent nonlinearities (GDB and GRC) present in the interconnected power system, the deviations in frequency and tie-line power exchange can exist for a longer time, even with tuned controller parameters. To mitigate these deviations, a rapid response energy source is often required. RFB can be a suitable choice for this purpose due to its various advantages, as discussed previously in the system description section. This study employs an RFB in each area, as shown in Fig. 3.12, for improving the system's dynamic response under investigation, for which optimal control parameters have been obtained for considered power contract scenarios. The controller optimization procedure was needed again as the inclusion of RFB completely changed the power system's characteristics. Further, it is worth mentioning here that only SSA tuned STFOFPID controller is considered for this study since it proved to be best in all the previous studies presented.

Table 3.5 presents the optimal controller parameters and corresponding cost objective function value achieved with SSA for the STFOFPID control structure under various contract scenarios having the same parameters as discussed in the previous section. It may be noted that the objective function values achieved by SSA tuned STFOFPID for all the contract scenarios is better than SSA tuned STFOFPID for IPS without RFBs. A detailed comparative analysis is shown henceforth for this study under all the contract scenarios.

This betterment in control performance for various transactions is quantified with objective function values, as shown in Fig. 3.13 as a bar graph. The '*J'* values for this Poolco transaction scenario for the IPS having RFB came out to be 0.04365 compared to 0.1065 achieved by IPS without RFB. Similarly, for bilateral and contract-violation

scenarios, the SSA STFOFPID controller incorporating RFB in the power system has improved its '*J*' by 30.3% and 17.78% under bilateral and contract-violation scenarios, respectively, in comparison to the SSA STFOFPID controller without RFB.

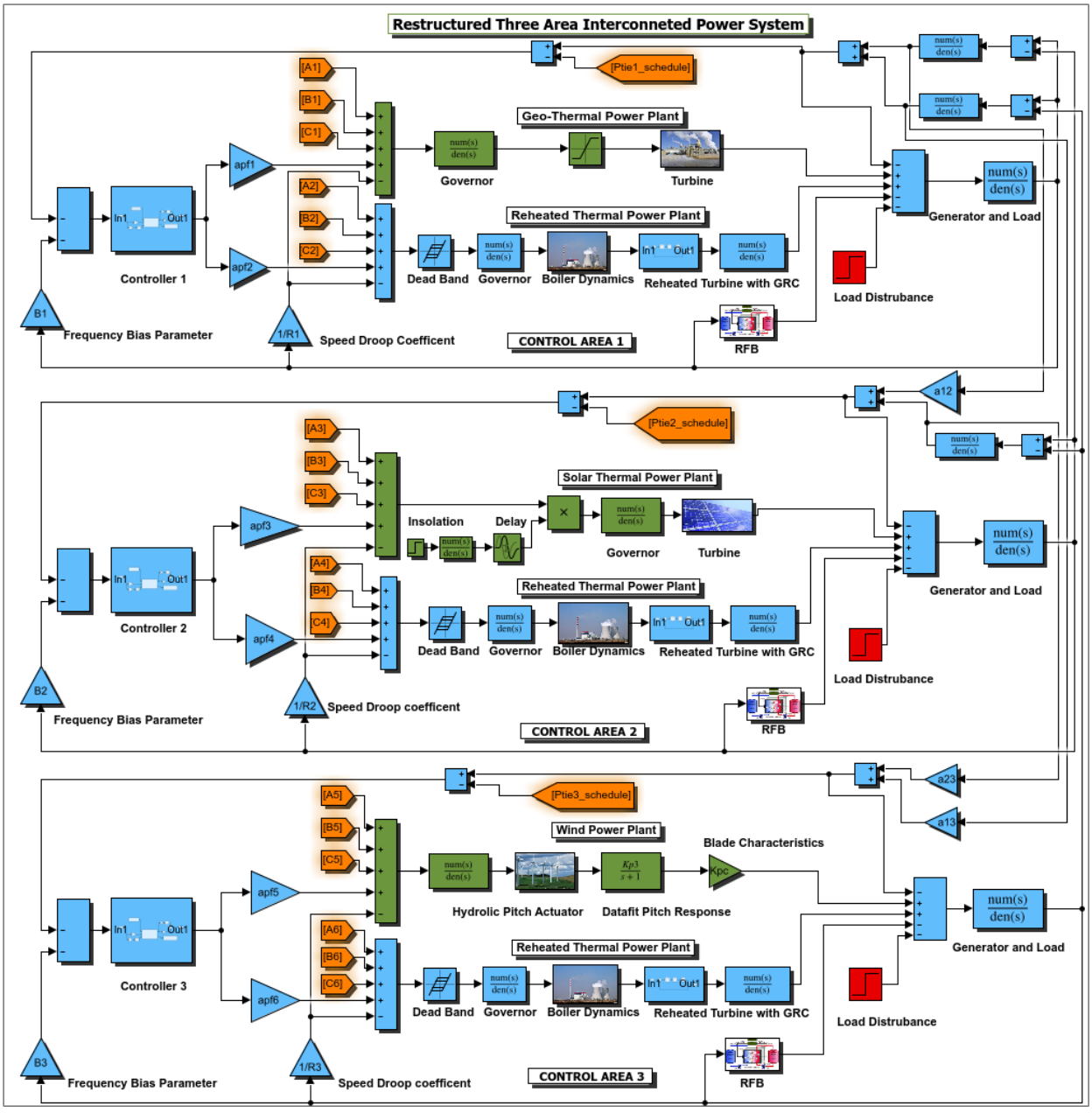

Fig. 3.12 *Restructured Three-area interconnected power system with RFB*

Further, the frequency responses under Bilateral and Contract-violation scenarios have been discussed in detail. The parameters and sudden load changes are considered as same as in the previous section for Bilateral and Contract-violation scenarios. Figure 3.14 shows the variations in frequency deviation in each control area for the bilateral transaction scenario.

Table 3.5 *SSA optimized STFOFPID controller parameters with RFB*

Contract		Poolco	Bilateral	Contract violation
Control Area-1	$u_{\alpha 1}$	-3.3258	6.0881	-5.9155
	K_{e1}	-2.99	-2.7801	1.1777
	K_{r1}	-2.3174	-2.1193	-0.3000
	K_{PI1}	-2.9905	0.44376	-2.7010
	K_{PD1}	-0.8266	1.2604	0.4992
	λ_1	1.2717	0.39837	0.8577
	μ_1	0.9484	0.09143	0.1515
Control Area-2	$u_{\alpha 2}$	-9.9996	4.2353	4.7898
	K_{e2}	-2.7575	1.3266	-2.5219
	K_{r2}	2.93	0.3944	2.5744
	K_{PI2}	-0.4781	-0.5128	1.2960
	K_{PD2}	0.02469	-2.0138	0.4651
	λ_2	0.0013	1.0098	0.5828
	μ_2	1.3427	0.36358	1.4417
Control Area-3	$u_{\alpha 3}$	-4.929	8.2427	1.9752
	K_{e3}	1.1655	0.96679	2.1703
	K_{r3}	-2.2924	2.1153	1.9036
	K_{PI3}	0.9125	1.0827	-2.7871
	K_{PD3}	0.7779	2.3484	-1.4587
	λ_3	0.0512	0.07093	0.0154
	μ_3	1.3e-07	0.31175	1.6664
J		0.04365	5.601	6.952

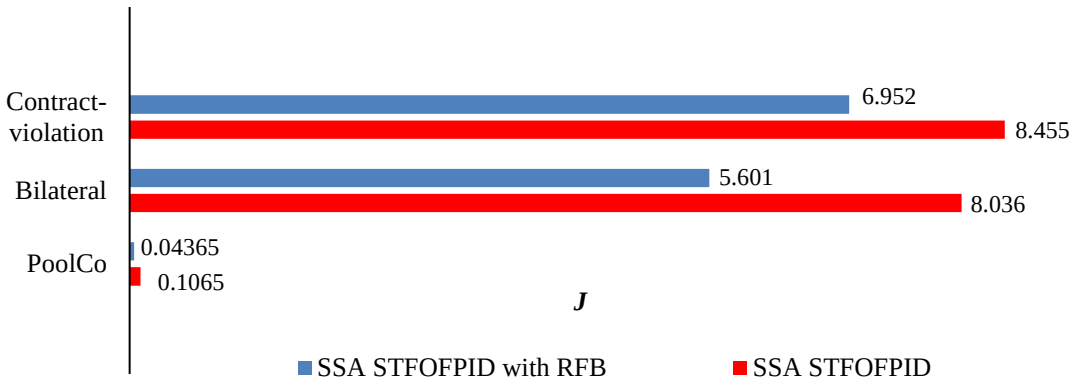

Fig. 3.13 *Objective function 'J' for SSA STFOFPID controllers under Bilateral and Contract violation*

Table 3.6 *ITAE values for frequency deviation with STFOFPID controller for different contract scenario with and without RFB*

Transaction	Poolco			Bilateral			Contract Violation		
Controller	$ITAE_{\Delta f1}$	$ITAE_{\Delta f2}$	$ITAE_{\Delta f3}$	$ITAE_{\Delta f1}$	$ITAE_{\Delta f2}$	$ITAE_{\Delta f3}$	$ITAE_{\Delta f1}$	$ITAE_{\Delta f2}$	$ITAE_{\Delta f3}$
SAA STFOFPID	0.0215	0.0178	0.0139	0.8857	0.9876	0.8602	0.9373	1.014	0.933
SSA STFOFPID with RFB	**0.0138**	**0.0022**	**0.00118**	**0.2782**	**0.2891**	**0.2644**	**0.6439**	**0.5917**	**0.443**

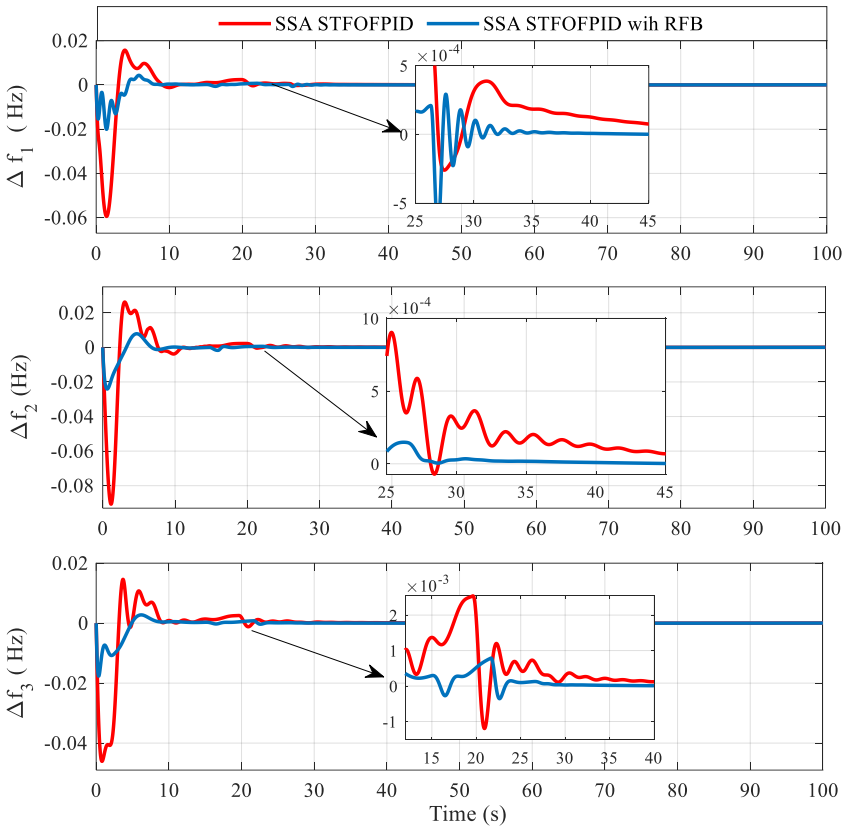

(a)

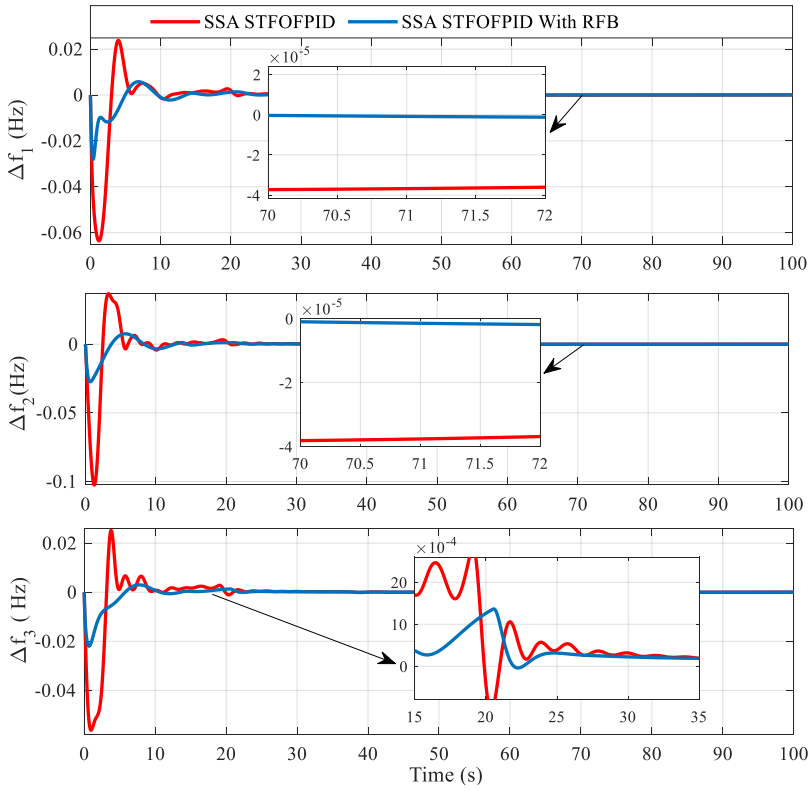

(b)

Fig. 3.14 *Frequency deviations with SSA STFOFPID controller with and without RFB under* ***(a)*** *Bilateral transaction* ***(b)*** *Contract-violation*

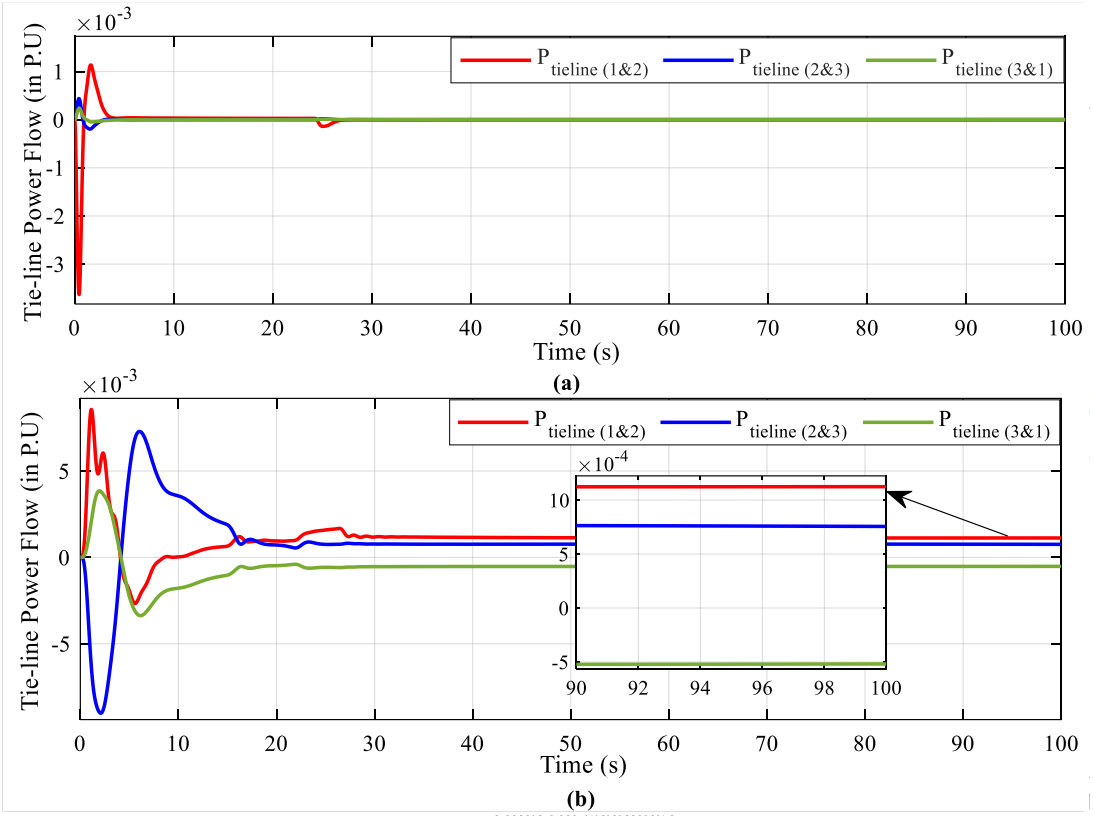

Fig. 3.15 *Tie-line power flow with SSA STFOFPID controller with RFB under* ***(a)*** *Poolco transaction* ***(b)*** *Bilateral transaction*

It may be noted from Fig. 3.14(a), that the maximum Frequency nadirs for all the control areas always remain less than 0.023 Hz, whereas this goes up to 0.09 Hz in the case of IPS, which is not supported by RFB. Whereas, Fig. 3.14(b) shows the frequency deviation variation for the contract violation mode of operation, which supports the finding that RFB can substantially improve the load frequency regulation even in critical control requirements. However, this issue can be handled by introducing RFB in conjunction with an adaptive control scheme. This effect can be easily noted from Fig. 3.14(b), that frequency deviations remain very minimal for IPS having RFB in it, where the maximum frequency deviation was found to be 0.0279 Hz, whereas the maximum frequency deviation for IPS without RFB was observed as 0.1025 Hz, for all the related control areas.

It may be noted that for a Poolco transaction scenario, the respective control area generating units are responsible for fulfilling the load requirements of the area. Whereas, in the case of bilateral contract scenario the distribution companies have the liberty to make contract for their load demand with generating units of other control

areas as well. Fig. 3.15 shows the tie line power flow variation among different control areas for poolco and bilateral transaction scenario. For the Poolco transaction, the tie line power flow settles to zero after transient condition, i.e., after the load demand for respective control area is fulfilled by its own generating units. It is evident from Fig. 3.15(a), that the power flow among different control areas is zero after transient condition. The power flow between different control areas in bilateral contract will be in accordance with distribution participation matrix (DPM) for bilateral contract as presented in section 3.2.6.2. The scheduled tie line power flow can be calculated in accordance with distribution participation matrix (DPM) and will be 0.001125 P.U., 0.00075 P.U. and -0.0005 P.U. respectively for control area1 & 2, control area 2 & 3 and control area 1 & 3, respectively. Fig. 3.15(b) represents the tie line power flow for different control areas for bilateral contract and found to be same as calculated values in steady state.

Further, the efficacy of SSA STFOFID controller in terms of the ability to reach a steady-state condition is presented in Fig. 3.16(a) and 3.16(b) for Bilateral and Contract-violation mode, where the SSA STFOFPID controller in the presence of RFB reaches IC region zero (where the rate of error and error will be an order of 1E-5) rapidly in comparison of without RFB and have minimum IC region transition. To get a detailed insight of the SSA STFOFPID controller in the presence of RFB, individual ITAE values of 'Δf' for all three control areas with different contracts with and without RFB using the SSA STFOFPID controller have been calculated and presented in Table 3.6. In this tabulated result, the boldface values represent the best value for each contract scenario and belong to the SSA STFOFPID controller with RFB. From the above simulation studies, we can conclude that the SSA-optimized STFOFPID control structure can provide effective load frequency control performance; further RFB inclusion in IPS proves an excellent LFC solution under sudden load demand. Further, to evaluate the SSA STFOFPID controller's effectiveness in the subsequent subsection system, it has been investigated under random step load perturbation (RSLP) and variation in inherent nonlinearities associated with RTPP, i.e., GRC and GDB.

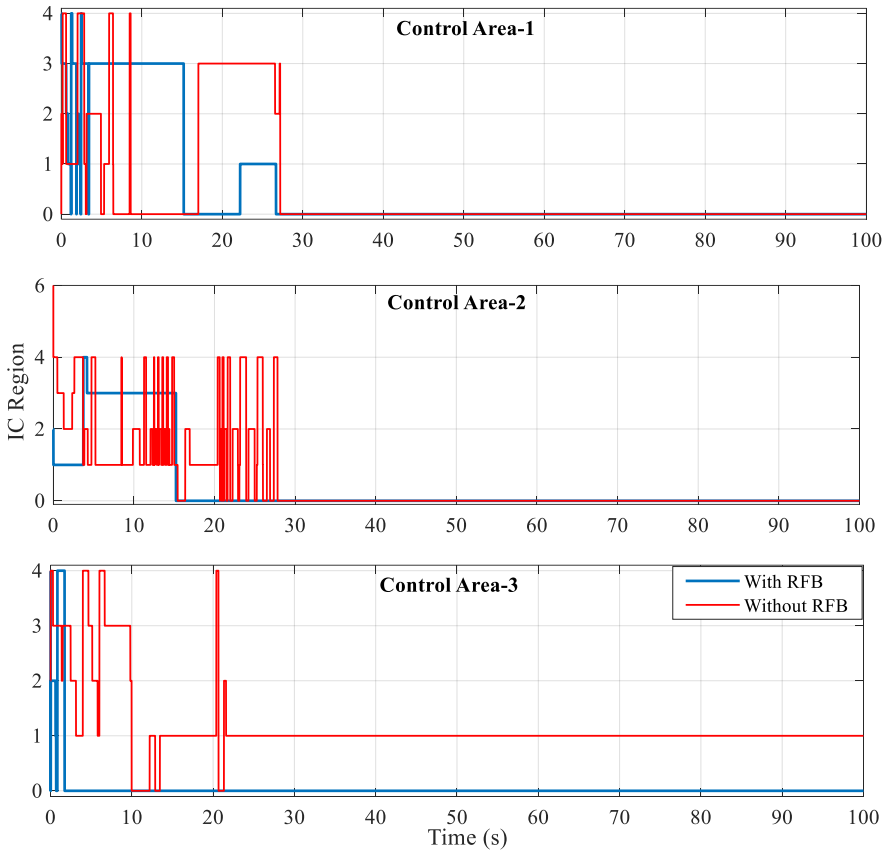

(a)

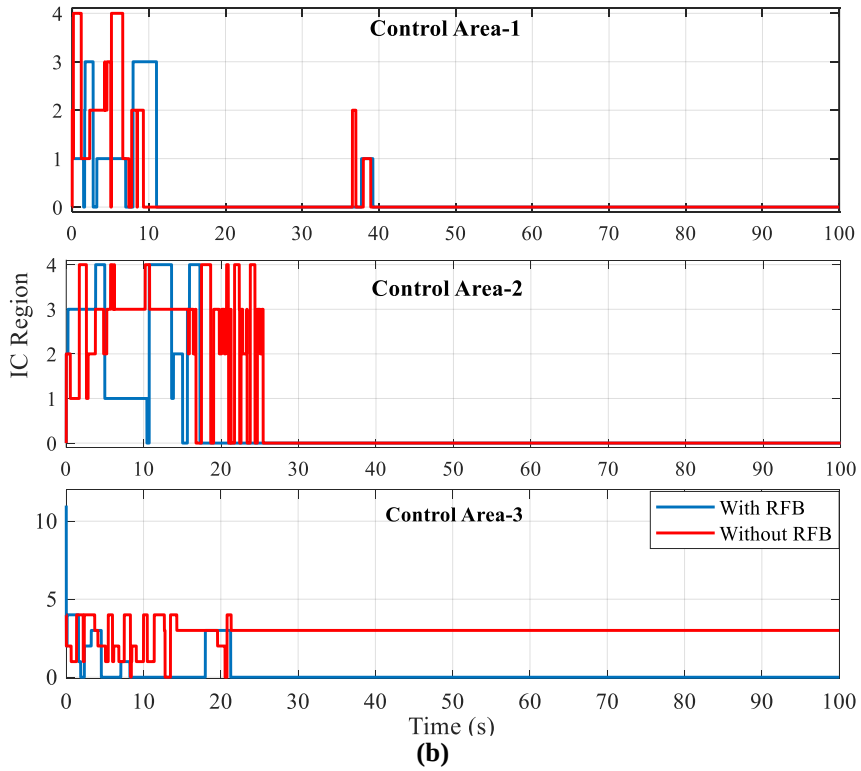

(b)

Fig. 3.16 *Controller IC region for control area-1, 2, and 3 with SSA STFOFPID controller with and without RFB under* ***(a)*** *Bilateral transaction* ***(b)*** *Contract-violation*

3.5.3 LFC performance under random step load perturbation (RSLP):

The load demand in the realistic IPS can change; hence, IPS performance has been investigated under changing load demand conditions. The combined control area load demand has been altered at every 30s in the time span of 150s, as shown in Fig. 3.17. In the present work, the effect of RLSP has been investigated for all three transactions. The nominal DPM, apfs, and optimal controller parameters have been adopted to investigate the RSLP effect on the system's dynamic performance.

The objective function values obtained by considering RSLP under all three contract scenarios by using the SSA STFOFPID controller with and without RFB have been presented in Fig. 3.17(a) as a bar graph. The objective function obtained under Poolco, bilateral, and contract-violation are 129.4, 140.7, and 214.2 for SSA STFOFPID without RFB. The objective function obtained under Poolco, bilateral, and contract-violation are 27.46, 49.78, and 147.6 for SSA STFOFPID with RFB. The SSA STFOFPID controller with RFB proves its superiority in improving *'J'* value by 371.23%, 182.64%, and 45.12% for Poolco, bilateral, and contract-violation, respectively in comparison to SSA STFOFPID without RFB controller.

The SSA STFOFPID controller drives the system to its desired state (IC region zero) in the presence of RFB quickly with minimum transitions in the IC region, as shown in Fig. 3.17(b) for the bilateral transaction scenario. Figure. 3.18 presents the frequency deviations for all control areas under bilateral transaction mode. The maximum deviation in frequency response for control area-3 is 0.02358 Hz with SSA STFOFPID controller without RFB, whereas with RFB, it gets reduced to 0.0095 Hz only. Similarly, for control area-2, the maximum deviation frequency response with the SSA STFOFPID controller without RFB is 0.0468 Hz, whereas, with the inclusion of RFB in the power system, it reduces to a significantly low value, i.e., 0.0123 Hz. Hence from Figs. 3.17 and 3.18, it implies that the system's dynamic performance with SSA STFOFPID controller incorporation with RFB is still satisfactory even under RSLP.

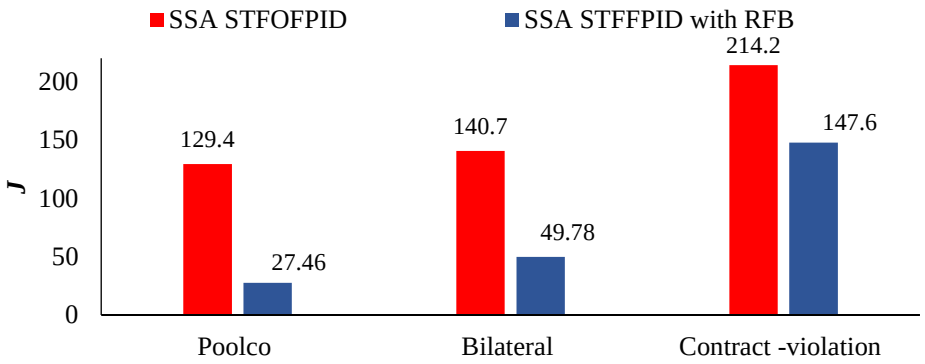

(a)

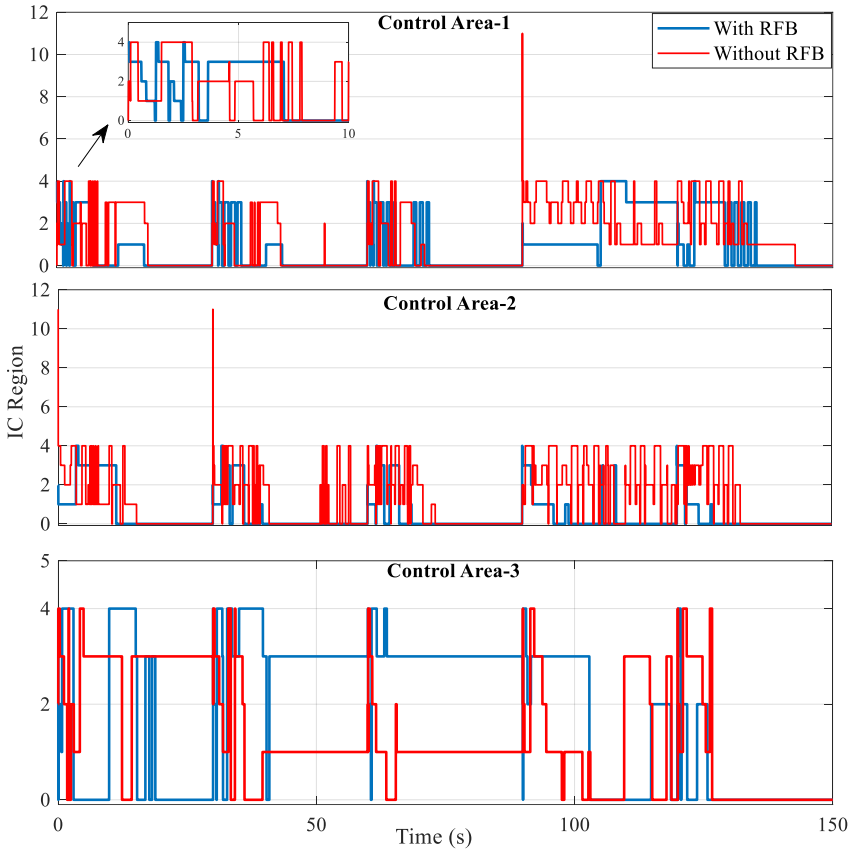

(b)

Fig. 3.17 ***(a)*** *Objective function (J) values under RSLP for Poolco, bilateral and contract-violation mode* ***(b)*** *Controller IC (input-combination) region for control area-1, 2 and 3 under RSLP with SSA optimized controllers for bilateral transaction*

The maximum deviation in frequency response for control area-3 is 0.02358 Hz with SSA STFOFPID controller without RFB, whereas with RFB, it gets reduced to 0.0095 Hz only. Similarly, for control area-2, the maximum deviation frequency response with the SSA STFOFPID controller without RFB is 0.0468 Hz, whereas, with the inclusion of RFB in the power system, it reduces to a significantly low value, i.e., 0.0123 Hz. Hence from Figs. 3.17 and 3.18, it implies that the system's dynamic

performance with SSA STFOFPID controller incorporation with RFB is still satisfactory even under RSLP.

The maximum deviation in frequency response for control area-3 is 0.02358 Hz with SSA STFOFPID controller without RFB, whereas with RFB, it gets reduced to 0.0095 Hz only. Similarly, for control area-2, the maximum deviation frequency response with the SSA STFOFPID controller without RFB is 0.0468 Hz, whereas, with the inclusion of RFB in the power system, it reduces to a significantly low value, i.e., 0.0123 Hz. Hence from Figs. 3.17 and 3.18, it implies that the system's dynamic performance with SSA STFOFPID controller incorporation with RFB is still satisfactory even under RSLP.

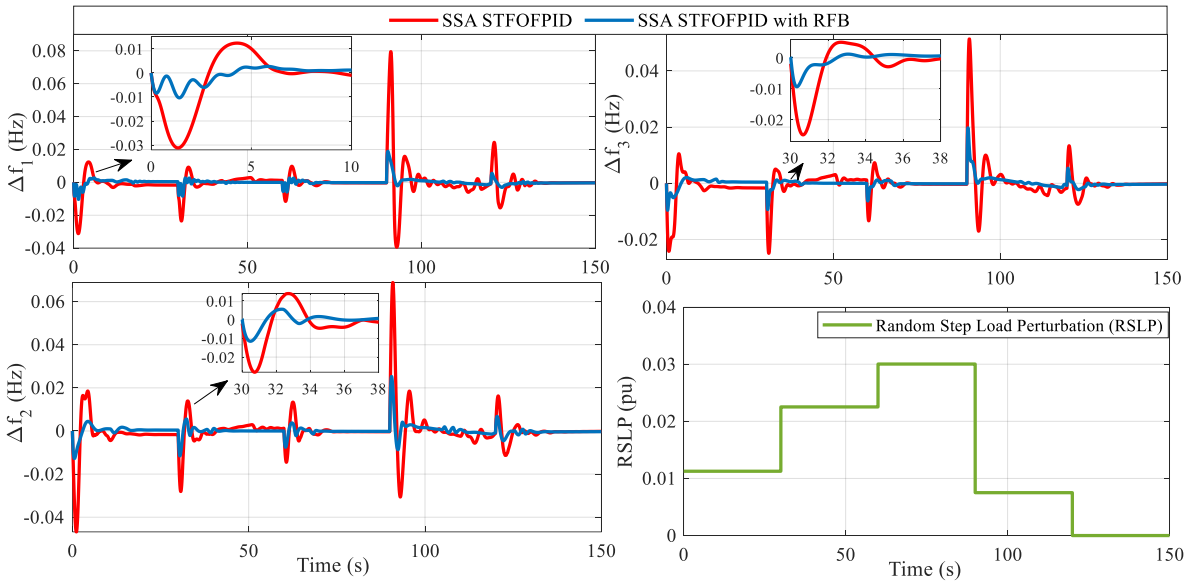

Fig. 3.18 *Deviation in the frequency of area-1, 2and 3 under SLP for bilateral transaction*

3.5.4 Effect of variation in GRC and GDB:

The GRC can significantly deteriorate the LFC dynamic performance, as it restricts sudden compensation for load demand with a restriction of change on the maximum power generation. Therefore, the lower values of the GRC limit increase the settling time as well as the Frequency nadir. The magnitude of the GRC can be uncertain due to various causes, such as measurement error and the aging effect; hence in the present work, the impact of the uncertainty in the magnitude of the GRC has been also presented. The magnitude of the GRC has varied from its nominal value to a decrement of 50% of its nominal value. Figure 3.19 shows the impact of GRC on the frequency response of control-area 2 with an SSA optimized STFOFPID-RFB controller. It is

evident from the response that the decreasing limit of GRC hampers the system response significantly. The quantities, i.e., Frequency nadir, settling time as well steady-state error increase as shown in the different responses. In the case of nominal GRC consideration, the frequency response reaches its desired value within 14 seconds, whereas with a decrement of 50% from its nominal value in GRC, the frequency response settles at 57.5 seconds with a significant steady-state error. The maximum deviation in frequency response under the nominal value of GRC is 0.02407 Hz, whereas under 50% decrement of nominal GRC limit deviations reaches 0.02506 Hz.

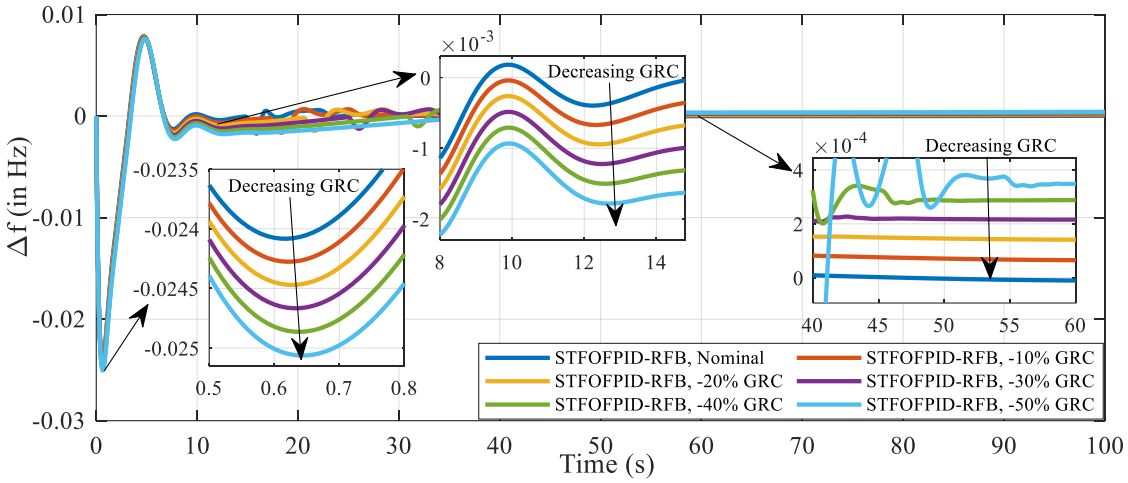

Fig. 3.19 *Deviation in frequency response in control-area 2 under decreasing GRC magnitude with SSA optimized STFOFPID-RFB controllers for bilateral transaction*

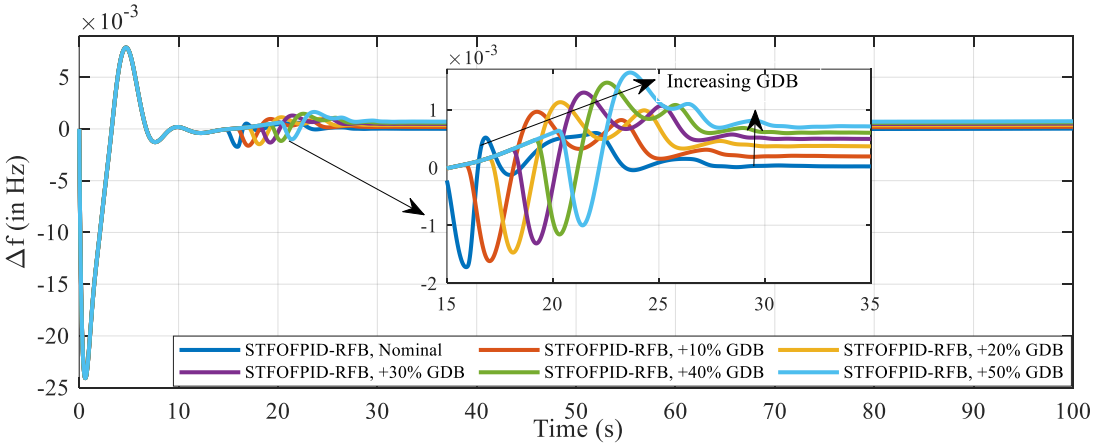

Fig. 3.20 *Deviation in frequency response in control-area 2 under increasing GDB magnitude with SSA optimized STFOFPID-RFB controllers for bilateral transactions*

GDB can produce oscillation in LFC dynamic performance, which is responsible for unnecessary control action and wear and tear in various system equipment. Increased values of GDB can severely affect the system's dynamic performance. We investigated

the impact of uncertainty of the GDB magnitude on the system response by varying the GDB magnitude. The speed governor has no significant change in the output until its input overcomes the governor deadband limit; hence, an increase in GDB causes an increase in oscillatory response. In the present study, the GDB magnitude has been alerted by +50% of its nominal value in the step size of 10% and presented in Fig. 3.20. It is evident from the frequency response that the increased magnitude of GDB causes higher oscillation. The oscillatory measure (OM) for the nominal GDB is found to be 1.175, whereas with a 50% increase in GDB from its nominal value is 1.354.

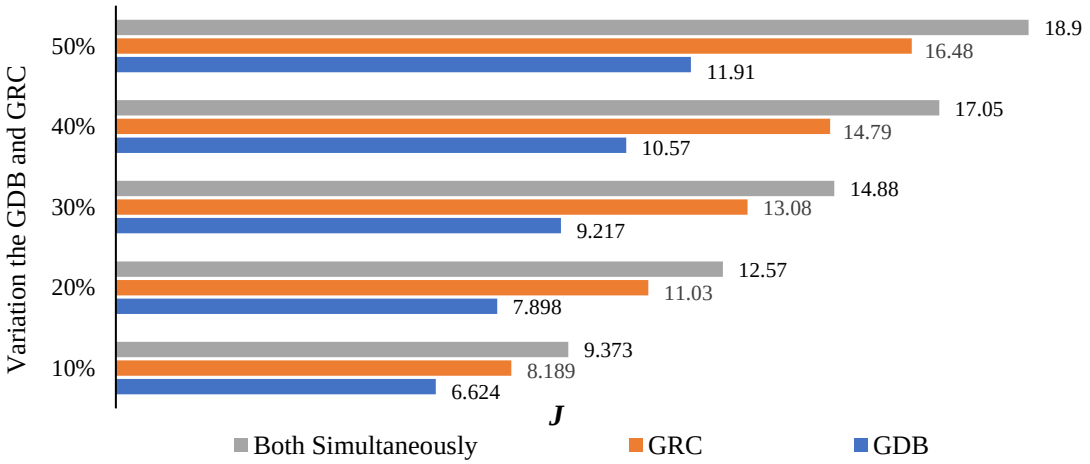

Fig. 3.21 *Objective function 'J' values under variation of inherent nonlinearities for SSA STFOFPID-RFB controllers under Bilateral*

Further, in this work, GRC and GDB have been considered simultaneously for simulating a realistic IPS scenario in deregulated market conditions. A comparative study has been presented for GDB and GRC impact on the considered system performance under bilateral transactions with STFOFPID-RFB controller in terms of the objective function (*J*). Figure 3.21 shows a detailed insight into the impact of uncertainty of system inherent nonlinearities, i.e., GDB and GRC. It is evident from the bar graph shown in Fig. 3.21 that the simultaneous presence of the inherent nonlinearities deteriorates the investigated system performance.

Further, a unique scenario of magnitude variation of nonlinearities, i.e., GRC and GDB, is considered. Investigation of IPS's LFC dynamic performance under deregulated scenario has been performed with different contracts at a 20% increment in GDB, 20% decrement in GRC, and simultaneous change in both from their nominal values. For better visualization of the comparative dynamic performance of the SSA

STFOFPID controller with and without RFB, values of '*J*' for the bilateral and contract-violation scenario are represented as a bar graph in Fig. 3.23. It can be inferred from Fig. 3.22(a) and (b) that even with a wide range variation of GRC and GDB from their nominal values, the SSA STFOFPID controller can provide satisfactory LFC performance.

The frequency deviation for all three control areas of IPS under investigation with considered variation in GRC and GDB for the bilateral contract scenario has been presented in Fig. 3.23(a). The maximum deviation in frequency response for control area-2 with SSA STFOFPID controller without RFB is 0.09052 Hz, whereas with RFB is 0.02319 Hz only. The minimum frequency deviation in control area-3 with the SSA STFOFPID controller without RFB is 0.04689 Hz, which gets reduced to 0.01757 Hz. Fig. 3.23(b) represents the variation of the controller's operating IC region for all three control areas under THE bilateral scenario, and SSA STFOFPID controller response in the presence of RFB reaches IC region zero rapidly with the minimum transition in comparison with SSA STFOOFID controller without RFB.

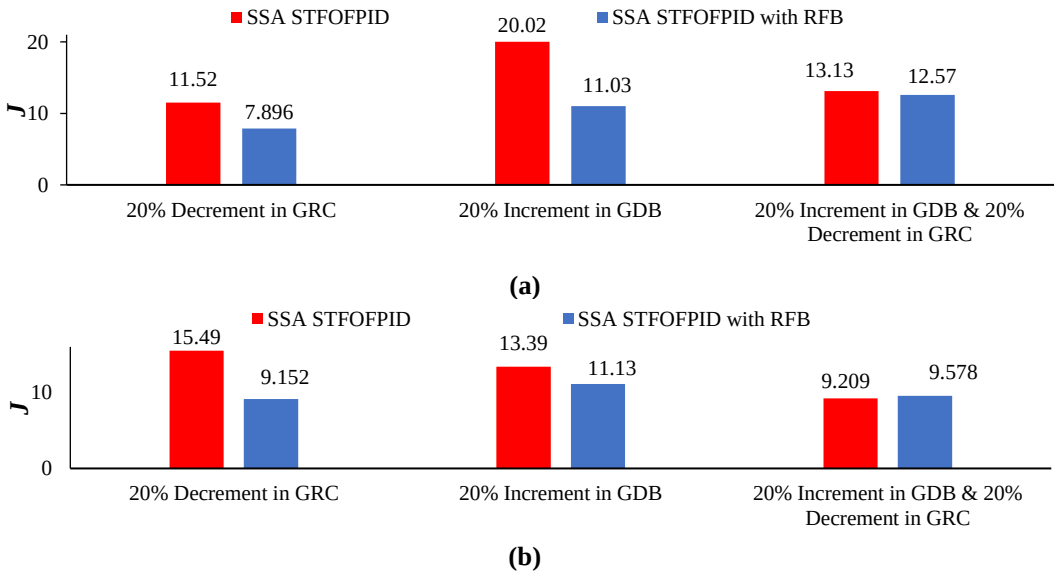

Fig. 3.22 *Objective function (J) with variation in GRC and GDB for* ***(a)*** *bilateral and* ***(b)*** *contract-violation scenario*

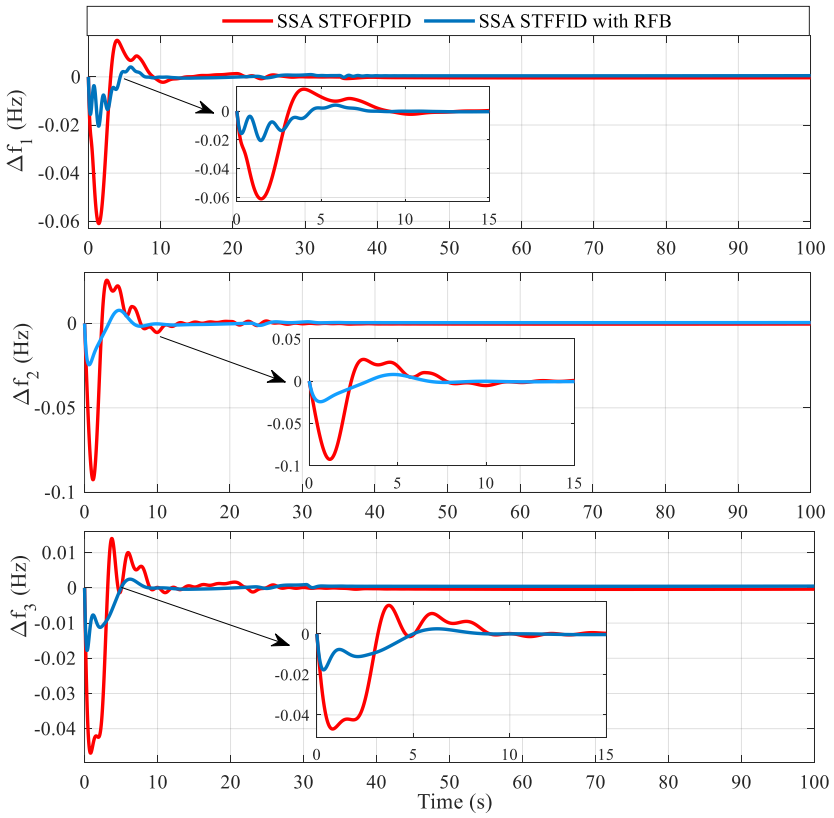

(a)

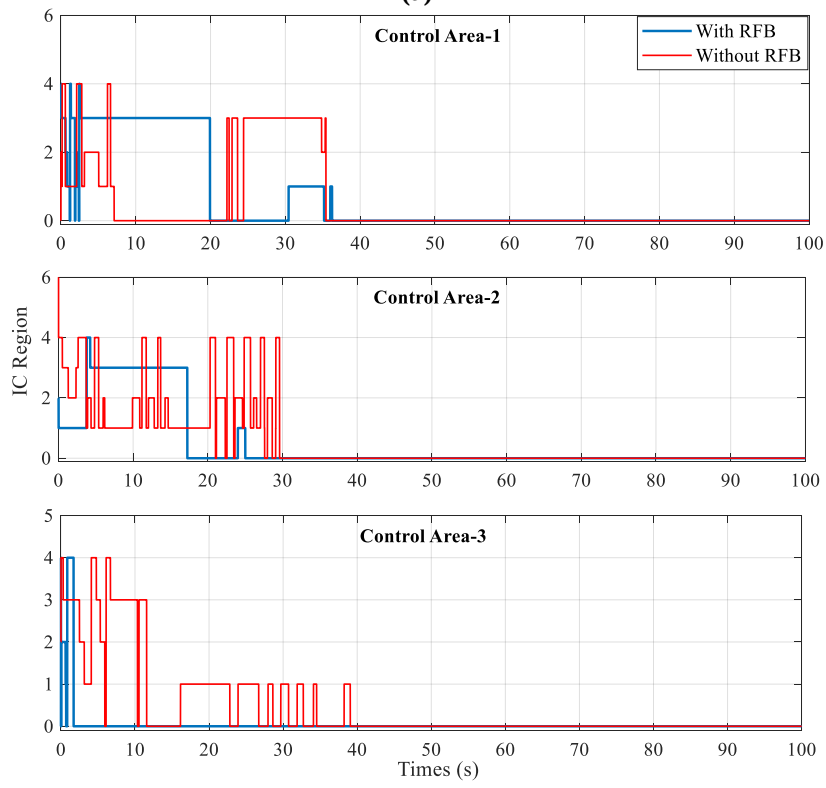

(b)

Fig. 3.23 ***(a)*** *Frequency deviation in area-1, 2 and 3 and* ***(b)*** *Controller IC regions for control area-1, 2, and 3 with the variation of GRC and GDB under bilateral scenario*

3.5.5 Real-time simulation study of the IPS:

It is a recent trend in power system research to evaluate the closed-loop performance on a real-time digital simulation platform (RTDSP). Such analysis reduces the time as well as the cost required in designing, developing, and testing for any plant. The MATLAB/Simulink-based models can be readily converted to a real-time simulation environment, which can be used for conducting real-time analysis on a multiprocessor [19]. In this connection, the OPAL-RT 4510 based on the Xilinx Kintex-7 FPGA board with an INTEL multi-core processor as an RTDSP has been utilized in this study. In this connection, real-time validation of the proposed control configuration has been carried out to assess its computational complexity. To achieve this, various software in loop (SIL) based real-time digital simulations were implemented for the three areas' interconnected power systems in deregulated mode considering various power transaction scenarios and system conditions. To implement, test, and validate different experiment scenarios, the controller, as well as the plant under investigation, were embedded on a single core of the OPAL-RT 4150 using the RT LAB libraries of the SIMULINK.

The systematic procedure for the implementation of the considered experiments is depicted in Fig. 3.24(a). It may be noted from this figure in order to implement and carry out the experiments on the OPAL-RT 4510. Firstly, a Simulink model of the system under study, i.e., three area power systems in deregulated mode, was developed. Then the developed model was made compatible with OPAL-RT, and to attain this compatibility, relevant editing and compilation of the considered model were carried out by utilizing the MATLAB and OPAL-RT Lab libraries. The editing and compilation of the model of the system under investigation requires division into two subsystems, i.e., master (SM) and console (SC), as shown in Fig. 3.24(b). It needs to a mention here that the complete dynamic model of the system is necessarily placed in the master subsystem, whereas display units, i.e., scopes etc., are placed in the console subsystem.

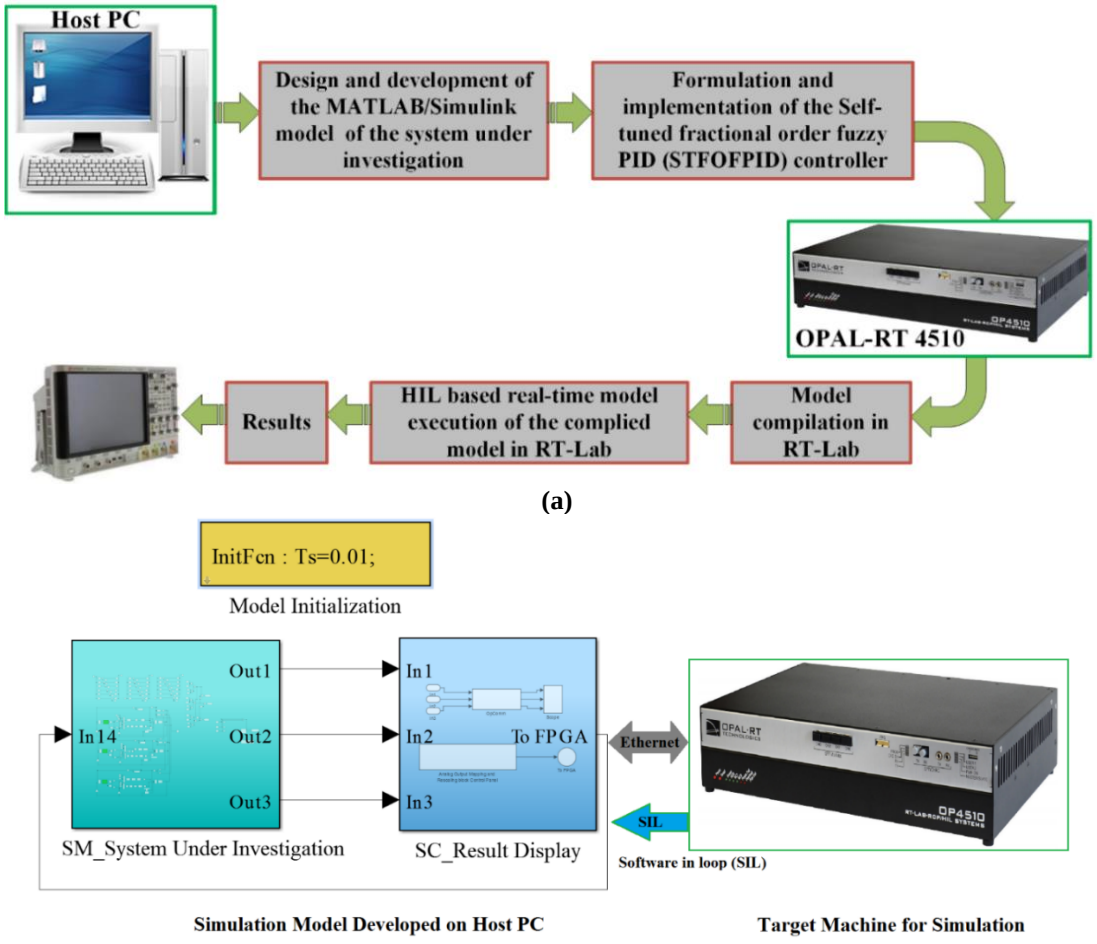

Fig. 3.24 (a) *Flowchart for implementation of real-time digital simulation utilizing OPAL-RT based* **(b)** *Schematic diagram of the system under investigation with OPAL-RT*

Further, these subsystems, i.e., SM and SC, are loaded on the OPAL-RT server for their conversion into equivalent 'C' codes after the successful compilation of the model. Another important point about the implementation of the experiments on the real-time simulator is related to the solver time, which must be considered a fixed step before starting the simulation. One may note that, in a fixed time step, the OPAL-RT processor performs three actions, viz., measurement, computation, and generation of the command signal. If the time step is not taken adequately, corresponding to the system complexity, then these three actions may fail to execute within a specified time and are referred to as overrun. In view of this, the selection of the fixed step becomes an important design element that must be chosen wisely. In the current work, a fixed time step of ten milliseconds has been considered, which is suitable for this class of control problems and the considered control configuration as well. This is an important attribute

of the designed self-tuning fractional order fuzzy controller, as due to its unique formula-based structure of the implementation, the computational time and complexity are greatly reduced. This was further validated by different experimental results, which never encountered an overrun condition for any real-time simulation.

The experimental lab setup for real-time digital simulation has been presented in Fig. 3.25. For the sake of the brevity of the study, the test cases related to the instances, which include (*i*) where the system has its nominal parameters controlled using STFOFPID controller in the presence of RFB under bilateral contract scenario, and (*ii*) where the system has uncertain nonlinear characteristics and is regulated by STFOFPID controller in the presence of RFB under bilateral contract scenario, and (*iii*) where the system is perturbed using random step load perturbation under bilateral contract scenario in the presence of RFB has been presented.

(a) ***(b)***

Fig. 3.25 ***(a)*** *Experimental setup of real-time digital simulation utilizing OPAL-RT* ***(b)*** *Deviation in frequency response under a bilateral transaction by STFOFPID-RFB with the real-time digital simulator on MSO*

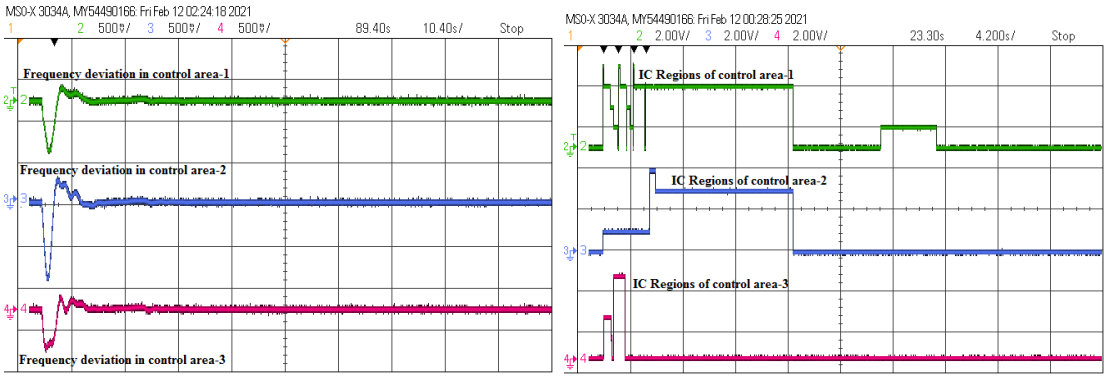

(a)* ***(b)***

Fig. 3.26 *Performance of SSA optimized STFOFPID controller in the presence of RFB under bilateral transaction with nominal system parameters* ***(a)*** *Frequency deviation [Scale: 500mv/div with probe cable gain of 10]* ***(b)*** *Variation in IC regions [Scale: 2V/div with probe cable gain of unity]*

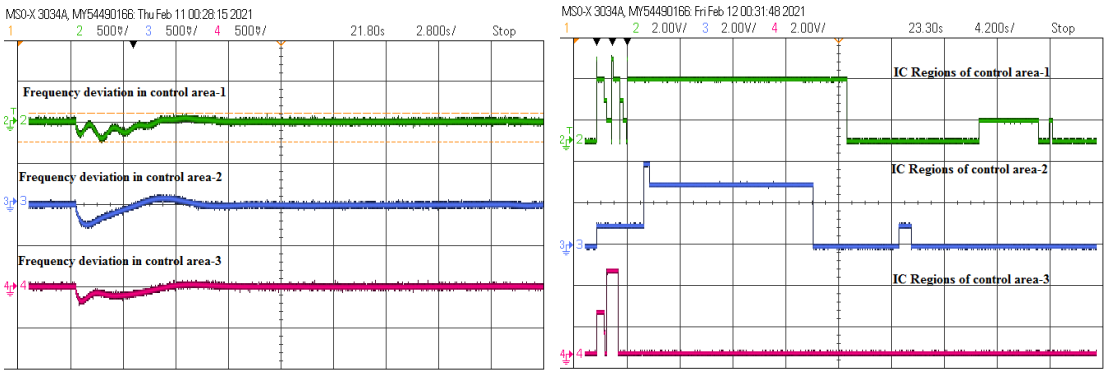

(a) ***(b)***

Fig. 3.27 *Performance of SSA optimized STFOFPID controller in the presence of RFB under bilateral transaction with 20% increase in GDB and 20% decrease in GRC* ***(a)*** *Frequency deviation [Scale: 500mv/div with probe cable gain of unity]* ***(b)*** *Variation in IC regions [Scale: 2V/div with probe cable gain of unity]*

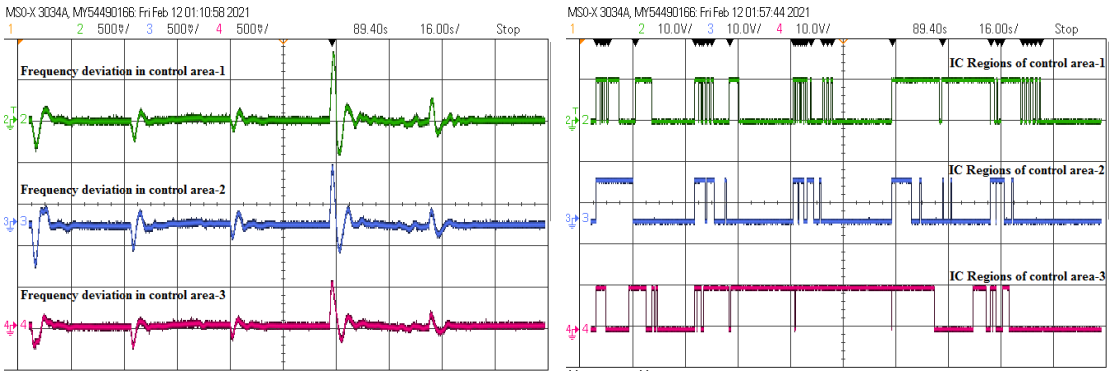

(a) ***(b)***

Fig. 3.28 *Performance of SSA optimized STFOFPID controller in the presence of RFB under bilateral transaction with random load perturbation* ***(a)*** *Frequency deviation [Scale: 500mv/div with probe cable gain of unity]* ***(b)*** *Variation in IC regions [Scale: 2V/div with probe cable gain of unity]*

The variation in frequency deviation and the input combination region variation of the STFOFPID controller for all three control areas with different case studies have been presented. Figures 3.26-3.28 present the frequency deviation response and IC region variation, respectively. The frequency deviation and IC region variation responses have been recorded up to the initial steady-state condition for the sake of clear visibility, as after reaching the steady-state zone, there is no significant variation in both responses.

3.6 Summary:

This chapter explores a self-tuning fractional order fuzzy PID (STFOFPID) control structure as a supplementary controller for the restructured three-area integrated power system (IPS). Optimal controller parameters were obtained using a

salp swarm algorithm (SSA) for all the considered controllers, i.e., conventional PID, fractional order PID, and STFOFPID for a hybrid objective function (J) comprising of integral of time-weighted absolute error (ITAE) and oscillatory measure (OM). The dynamic responses achieved with SSA STFOFPID provided the least oscillations, least steady-state error, and faster settling for deviation in frequency and error in tie-line power exchange. Further, the potential benefits of introducing an energy storage element, i.e., the redox flow battery (RFB), are also shown to provide a quicker response for a short duration under sudden load demand with the existing system for improving dynamic performance. To show the effectiveness of the STFOFPID controller along with RFB, random load perturbation has also been performed. It was found that the combination of the STFOFPID controller and RFB could handle these load variations very effectively, and an improvement of more than 45% was achieved in comparison to the system, which was deprived of RFB. Finally, the effect of parametric uncertainties in associated nonlinearities, i.e., GRC and GDB, has also been investigated. It is worth mentioning that for such parametric uncertainties, the STFOFPID controller performance was exceptionally superior in the presence of RFB. The validation of the proposed control strategy for bilateral transaction scenarios, i.e., the use of STFOFPID in the presence of RFB, has been presented with a real-time digital simulator platform, OPAL-RT 4510.

Further, as we know that the integration RESs in existing grids are occurring at a faster rate to address the increasing power demand as well as carbon emission. The conventional method of electricity generation plays a vital role and is responsible for global warming by producing a significant amount of greenhouse gases in the environment. Hence, in this thesis, a DFIG-based WTG has been considered for its integration with the existing IPS system. The lowered inertia of the electrical system is one of the significant problems with increased penetration from renewable energy sources into the existing power system. The power system's capacity to manage any imbalance between supply and load demand is hampered by the significant reduction in inertia, which might eventually lead to power grid collapse. Therefore, such RES must be integrated with a frequency support mechanism. Moreover, this thesis presents the frequency support schemes for a DFIG-based WTG integrated with existing IPS.

References:

[1] R. D. Christie Member and A. B. Fellow, "Load frequency control issues in power system operations after deregulation," IEEE Trans. Power Syst., vol. 11, pp. 1191–1200, 1996, doi: 10.1109/59.535590.

[2] P. Kundur, Power System Stability and Control. New Delhi: Tata McGraw Hill, 2009.

[3] A. Ibraheem, P. Kumar, and D. P. Kothari, "Recent philosophies of automatic generation control strategies in power systems," IEEE Trans. Power Syst., vol. 20, pp. 346–357, 2005, doi: 10.1109/TPWRS.2004.840438.

[4] V. Donde, M. A. Pai, and I. A. Hiskens, "Simulation and optimization in an AGC system after deregulation," IEEE Trans. Power Syst., vol. 16, pp. 481–489, 2001, doi: 10.1109/59.932285.

[5] S. M. Nosratabadi, M. Bornapour, and M. A. Gharaei, "Grasshopper optimization algorithm for optimal load frequency control considering Predictive Functional Modified PID controller in restructured multi-resource multi-area power system with Redox Flow Battery units," Control Eng. Pract., vol. 89, pp. 204–227, 2019, doi: 10.1016/j.conengprac.2019.06.002.

[6] A. Saha, L. C. Saikia, W. Tasnin, R. Rajbongshi, and D. Saha, "Automatic Generation Control of Multi-Area Multisource System Incorporating Distributed Generation Units and RFB," 2nd Int. Conf. Energy, Power Environ. Towar. Smart Technol. ICEPE 2018, pp. 1–6, 2019, doi: 10.1109/EPETSG.2018.8658980.

[7] W. Tasnin and L. C. Saikia, "Impact of renewables and FACT device on deregulated thermal system having sine cosine algorithm optimised fractional order cascade controller," IET Renew. Power Gener., vol. 13, pp. 1420–1430, 2019, doi: 10.1049/iet-rpg.2018.5638.

[8] V. Kumar, K. P. S. Rana, and D. Kler, "Efficient control of a 3-link planar rigid manipulator using self-regulated fractional-order fuzzy PID controller," Appl. Soft Comput. J., vol. 82, p. 105531, 2019, doi: 10.1016/j.asoc.2019.105531.

[9] S. Mirjalili, A. H. Gandomi, S. Z. Mirjalili, S. Saremi, H. Faris, and S. M. Mirjalili, "Salp Swarm Algorithm: A bio-inspired optimizer for engineering design problems," Adv. Eng. Softw., vol. 114, pp. 163–191, 2017, doi: 10.1016/j.advengsoft.2017.07.002.

[10] D. Guha, P. K. Roy, and S. Banerjee, "Maiden application of SSA-optimised CC-TID controller for load frequency control of power systems," IET Gener. Transm. Distrib., vol. 13, pp. 1110–1120, 2019, doi: 10.1049/iet-gtd.2018.6100.

[11] W. Tasnin, L. C. Saikia, and M. Raju, "Deregulated AGC of multi-area system incorporating dish-Stirling solar thermal and geothermal power plants using fractional order cascade controller," Int. J. Electr. Power Energy Syst., vol. 101, no. December 2017, pp. 60–74, 2018, doi: 10.1016/j.ijepes.2018.03.015.

[12] A. Saha and L. C. Saikia, "Load frequency control of a wind-thermal-split shaft gas turbine-based restructured power system integrating FACTS and energy storage devices," Int. Trans. Electr. Energy Syst., vol. 29, pp. 1–19, 2019, doi: 10.1002/etep.2756.

[13] K. Nithilasaravanan, N. Thakwani, P. Mishra, V. Kumar, and K. P. S. Rana, "Efficient control of integrated power system using self-tuned fractional-order fuzzy PID controller," Neural Comput. Appl., vol. 31, pp. 4137–4155, 2019, doi: 10.1007/s00521-017-3309-9.

[14] Y. Arya, "AGC performance enrichment of multi-source hydrothermal gas power systems using new optimized FOFPID controller and redox flow batteries," Energy, vol. 127, pp. 704–715, 2017, doi: 10.1016/j.energy.2017.03.129.

[15] D. Rerkpreedapong, A. Hasanovic, and A. Feliachi, "Robust load frequency control using genetic algorithms and linear matrix inequalities," IEEE Trans. Power Syst., vol. 18, pp. 855–861, 2003, doi: 10.1109/TPWRS.2003.811005.

[16] H. M. Hasanien and A. A. El-Fergany, "Salp swarm algorithm-based optimal load frequency control of hybrid renewable power systems with communication delay and excitation cross-coupling effect*," Electr. Power Syst. Res., vol. 176, p. 105938, 2019, doi: 10.1016/j.epsr.2019.105938.*

[17] M. V Srikanth and N. Yadaiah, "An AHP based optimized tuning of Modified Active Disturbance Rejection Control : An application to power system load frequency control problem," ISA Trans., vol. 81, pp. 286–305, 2018, doi: 10.1016/j.isatra.2018.07.001.

[18] U. Tamrakar, D. Shrestha, M. Maharjan, B. P. Bhattarai, T. M. Hansen, and R. Tonkoski, "Virtual inertia: Current trends and future directions," Appl. Sci., vol. 7, pp. 1–29, 2017, doi: 10.3390/app7070654.

[19] M. D. O. Faruque *et al.*, "Real-time simulation technologies for power systems design, testing, and analysis," *IEEE Power Energy Technol. Syst. J.*, vol. 2, pp. 63–73, 2015.

Chapter 4: Inertial Control Scheme for Frequency Support from WTG

4.1 Introduction:

According to a recent assessment by the International Renewable Energy Agency (IRENA), conventional energy sources now meet a considerable amount (nearly 75 percent) of the world's electrical energy demand. It is evident that such sources contribute significantly to the increase in carbon footprint and, as a result, global warming. Renewable energy sources, without question, have shown enormous promise in combating these issues. According to the literature, their contribution to meeting the world's electrical energy needs has increased dramatically in the previous two decades, accounting for over 25% of total generation capacity. Wind energy sources are the second most widely used renewable energy source, behind hydropower facilities, and now provide around 18% of all renewable energy generated worldwide. Because of its copious availability and ease of use, wind energy has become a popular choice for generation organizations worldwide [1] [2]. In comparison to other renewable energy sources, wind energy sources have lower maintenance costs due to the utilization of well-established techniques, such as doubly-fed induction generators (DFIG), which are frequently utilized to harvest electrical energy from the wind.

Integration of DFIG-based wind turbines with existing interconnected power systems (IPS) is becoming more common due to the benefits of wind energy sources. However, this might result in major behavioral changes in IPS operation. Various research studies on the impact of integrating DFIG-based wind turbines with IPS have recently been published. These findings point to the fact that when IPS is subjected to load disturbances, variable speed wind turbines (VSWT) do not help to load frequency restoration, owing to the presence of power electronics converters. Increased penetration from DFIG-based wind power plants (WPP) significantly reduces the equivalent inertia of the IPS, making it more difficult to achieve effective load frequency management [3] [4]. This leads to the conclusion that integrating a DFIG-based wind energy conversion system with an existing IPS has many benefits, and it also has a number of drawbacks that must be carefully handled.

It is essential to provide an effective control setup that works in tandem with LFC

while also providing enough frequency support for DFIG-based WPP [5]. However, achieving the same is more difficult than it appears, owing to an increase in control complexity as a result of intrinsic power system nonlinearities as renewable energy sources become more prevalent. Based on the results of the study, it is clear that an effective control plan for such a system must address four important aspects:

i) Nonlinearities in conventional generating units of IPS, i.e., governor dead-band (GDB) and generation rate constraint (GRC),

ii) Parametric uncertainties in the system,

iii) Higher penetration from renewable energy sources results in decreased system inertia, and

iv) Effective frequency support generation specifically for DFIG-based WPP integration in IPS.

Even though the above-mentioned factors are present in the system at the same time, most current control algorithms do not evaluate them simultaneously. As a result, the majority of current strategies, especially when used in conjunction with DFIG-based WPPs, become unsuitable for IPS, which is another reason for doing this investigation. The current study offers a novel control system that combines a fuzzy tilt integral derivative with filter (FTIDN) structure with a fractional order PD (FOPD) as a secondary layer control structure to form a dual-layered control structure. The inertial control strategy for DFIG-based WPP combined with two-area IPS is employed with the proposed dual-layered tilt fuzzy control structure (DLTFCS).

Further, the remaining chapter is structured as follows; Section 4.1 gives a brief description of considered two-area interconnected thermal power systems with associated nonlinearities integrated with DFIG-based WPP. The details of the system under consideration for current work have been presented in section 4.2. In Section 4.3, a description of the proposed DLTFCS, and its tuning using SSA based on the designed hybrid objective function for obtaining optimal controller parameters, has been discussed. Further, Section 4.4 presents detailed simulation results, comparative analysis, and discussion. Finally, the concluding remark and summary of the chapter have been presented in section 4.5.

4.2 System description under investigation:

This chapter considers a two-area interconnected power system with DFIG-based WPP integrated with both control areas. The inertial support scheme has been also incorporated for frequency support provision from WPP. The subsequent subsections present the details of the system under investigation and the inertial control scheme for frequency support from WPP.

4.2.1 Two-area interconnected NRTPU with DFIG-based WPP:

In the present work, a two-area interconnected non-reheated thermal power unit (NRTPU) has been considered in the presence of DFIG-based WPP, as shown in Fig. 4.1. The NRTPU considered in this work has a conventional power source in both areas with an area capacity ratio of unity. The NRTPU and DFIG-based WPP system parameters have been adapted from [5] [6] and are presented in Appendix - II.

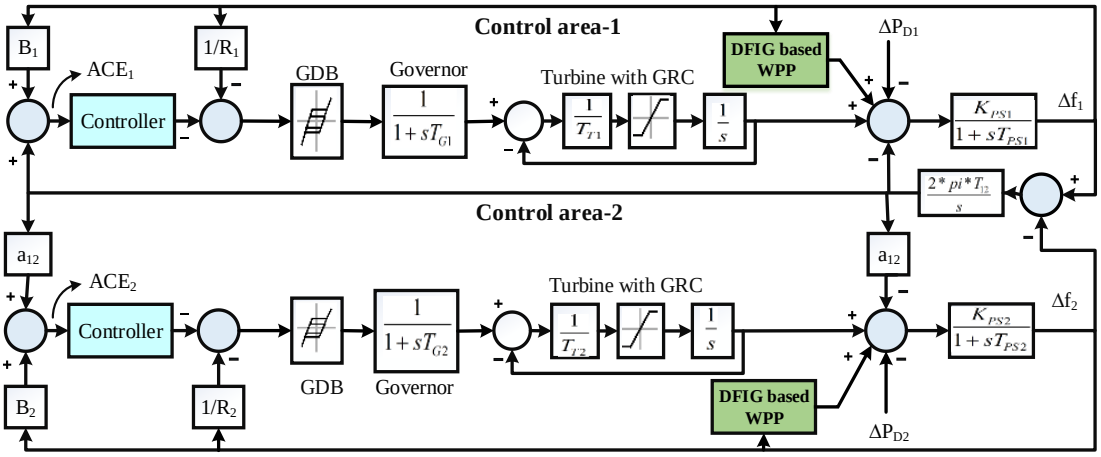

Fig. 4.1 *Block diagram of a realistic NRTPU with DFIG-based WPP*

Both control areas, shown in Fig.4.1, are equipped with their generating unit, speed governing mechanism, and turbine unit along with DFIG-based WPP. Further, the various control schemes regarding the DFIG-based wind turbine generator (WTG) have been presented in the subsequent subsection.

4.2.2 DFIG control schemes:

Unlike conventional thermal power units, the possibility of variable speed wind turbines' participation in load frequency regulation is hugely truncated if they operate at their rated capacity. Hence typically, these wind turbines have a lesser share in the frequency regulation process; however, there exist some methods by which WTG may contribute towards frequency regulation temporarily. Figure 4.2 represents the

schematic diagram of DFIG-based WTG connected with the grid. The capability of real power control in the case of DFIG-based WTG makes them a suitable candidate for participating in load frequency regulation as the wind turbine system has a substantial amount of stored kinetic energy in rotating blades like conventional thermal generating units. The stored energy in the rotating blades of WTG can be released to provide primary frequency control during transient conditions. The various control schemes have been reviewed for DFIG frequency support in [7]; however, thermal power systems integrated with DFIG-based WTG are inertial control, pitch angle control, and speed control via deloading WPP.

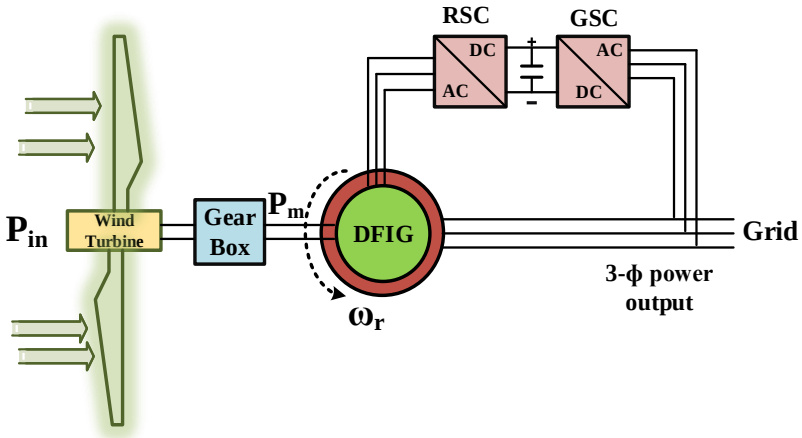

Fig. 4.2 *Block diagram of DFIG-based WTG connected to the grid*

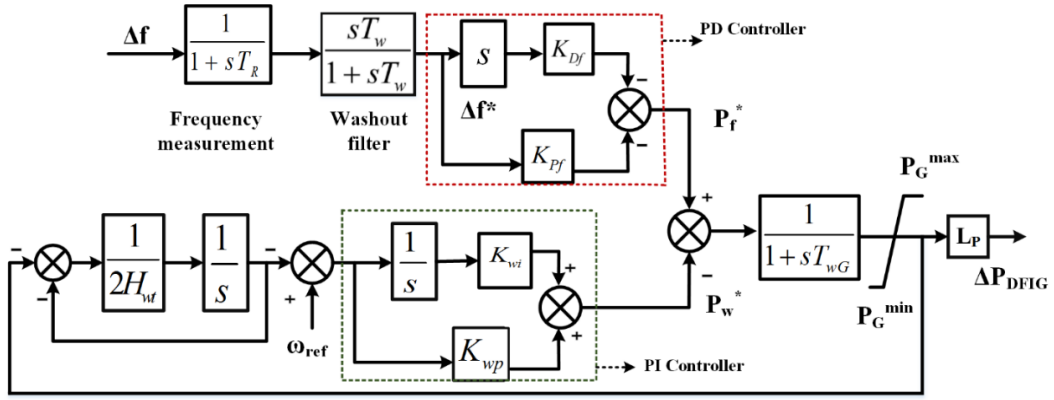

Fig. 4.3 *Block diagram of the inertial control scheme to support frequency regulation from DFIG-based WTG*

The present work focuses only on the inertial control approach to contribute to frequency regulation from the WPP. Figure 4.3 depicts the inertial control scheme for DFIG-based WTG in view of considered IPS. The inertial control scheme essentially has three main components, viz. PD controller, wash out filter, and PI controller. Each component has been briefly described as follows.

4.2.3 PD Controller:

In the case of DFIG-based WTG, the stator winding of DFIG is directly connected with the grid, whereas the rotor circuit connects via a back-to-back converter, as shown in Fig. 4.2. The purpose of the back-to-back converter is to make DFIG-based WTG synchronize with the grid because the angular frequency of the current and voltage in the rotor windings is different from the grid (is equal to the slip times of the grid frequency) and change under different wind speeds. The DFIG structure allows to control of the flow of power from the rotor terminals along with the stator; hence the power handling capability of DFIG-based induction machines increases by approximately 30% of conventional induction machines. The back-to-back converter consists of the rotor side converter (RSC), DC link, and grid-side converter (GSC). The RSC is an AC/DC converter that controls the output power of the stator and rotor to perform MPPT. The variable-speed wind turbine (VSWT) based on DFIG is preferred over the constant speed wind turbine to achieve optimal performance. Under a given wind speed, the maximum power point tracking (MPPT) function makes the active power output of VSWT fixed. Hence, the MPPT function makes the rotating mass of VSWT decoupled from the grid and is responsible for the non-participation in the frequency support from DFIG-based WPP.

The integration of DFIG-based WTG driven by VSWT with the grid does not contribute to the inertia of IPS due to the presence of GSC, which decouples the rotational speed of WPP with the grid frequency. Hence to provide inertial support from WPP, an additional signal has been incorporated, i.e., P_f^* and added with nonconventional generator unit reference power to be continuously tracked, i.e., P_w^* as shown in Fig. 4.3. The additional signal P_f^* can be represented as

$$P_f^* = -K_{Df}\frac{d(\Delta f^*)}{dt} - K_{Pf} \times \Delta f^* \tag{4.1}$$

Where K_{Pf} and K_{Df} are the proportional and derivative gain for the PD controller. When there is an increase in load demand, the system frequency accordingly decreases and is responsible for the activation of the PD controller. The controller provides a control signal, which in turn increases the reference power setting or increases in reference torque setting of WTG'S. To compensate, the required torque setting speed of the rotor eventually starts decreasing with the release of stored kinetic energy in the

rotating mass of WTG.

4.2.4 Washout Filter:

The DFIG-based WTG can provide frequency support only during the transient period by releasing the kinetic energy stored in the rotating mass of the WPP. If frequency support from the WTG is extended beyond the transient period, then the speed of the rotor of the WTG can reach a very low level and causes the stall of the associated generating unit. To avoid such a situation, a high pass filter, commonly known as a washout filter, is utilized in the inertial control scheme, and the frequency deviation signal is passed through it before being applied to the PD controller as input. The washout filter ensures that the PD controller is inactive for permanent frequency deviation, and afterward, only conventional power units keep participating in load frequency control action.

4.2.5 PI Controller:

In the inertial control scheme for providing frequency support, the rotor speed gets reduced from its optimal values to release the stored kinetic energy in the rotating blades of the turbine during the transient period. The speed of the rotor must be restored to its optimal value with the PI controller, as shown in Fig. 4.3, after the transient period, as quickly as possible. The PI controller utilizes a power reference P_w^* to track the required optimal speed ω_{ref}. The power reference P_w^* is given as

$$P_w^* = K_{wp}(\omega_{ref} - \omega_e) + K_{wi}\int(\omega_{ref} - \omega_e)dt \quad (4.2)$$

The PI controller gain must be selected in such a way so that it can provide faster recovery of its optimal speed along with a smaller time frame of transient speed variation. Hence during the transient period of about 2-3 sec, the PI controller acts relatively slower so that DFIG-based WTG can contribute towards mitigation frequency deviation during the transient period. Further, an efficient secondary controller to regulate the load frequency variation must be designed in coordination with the above inertial frequency control scheme for the system under investigation and is presented in detail in the subsequent section.

4.3 LFC structure and its parameters optimization:

4.3.1 Controller structure:

The load frequency controllers are designed with the intention of mitigating the deviations in frequency, generation, and tie-line power exchange to zero in the

minimum possible time with the least under and overshoots, which are caused by any mismatch between electrical power supply and demand. The majority of the power system industry favors the conventional PID controller due to its modest design, robust performance, and low cost. However, with the inherent complexity associated with the integrated large-scale power system, such as nonlinearities, uncertainties, and their simultaneous impacts, the convention control structure fails to provide the anticipated level of resilience and performance in continuously varying operating conditions in large-scale IPS. The fuzzy logic (FL) has proven enhanced flexibility and dynamic performance to accomplish the challenges in IPS; FL in conjunction with PID/PIDN/FOPID control structure has been extensively utilized in the recently appeared LFC literature.

Hence, a dual-layer tilt fuzzy control structure (DLTFCS) viz., fuzzy tilt integral derivative with filter (FTIDN) as the first layer and fractional order proportional derivative (FOPD) controller as a second layer has been utilized in the present work. The proposed controller structure, i.e., DLTFCS utilized as a secondary controller (or LFC), is given in Fig. 4.4, which depicts that the output of the first layer of DLTFCS, i.e., fuzzy TIDN (FTIDN) controller, is used to drive the second layer of DLTFCS, i.e., FOPD. Further, the TID controller offers a better disturbance rejection ratio and is significantly unaffected by system parameter variations in closed-loop response that of the PID controller. The derivative component, which enhances the system stability, offers undesirable magnitude control signal feed to the plant; to resolve this issue, a filter is placed, and the position of its pole is optimized in such a way that it does not produce chattering because of high frequency noise. The transfer function of TID with filter, i.e., TIDN controller transfer function, can be given as,

$$\mathrm{TIDN(s)} = \frac{\mathrm{K_{P1}}}{\frac{1}{\mathrm{s^{\bar{n}}}}} + \frac{\mathrm{K_{I1}}}{\mathrm{s}} + \mathrm{K_{D1}}\left[\frac{\mathrm{N\times s}}{\mathrm{s+N}}\right] \tag{4.3}$$

Where K_{P1}, K_{I1}, and K_{D1} are the TIDN controller gains along with 'N' as the filter coefficient used in the derivative term. The 'n' is a non-zero real number and $\frac{1}{s^{1/n}}$ or $s^{-\left(\frac{1}{n}\right)}$ is referred to as a tilt compensator. When the conventional proportional compensator is replaced by a tilt compensator, the overall closed-loop performance improves by exploiting the value of 'n'. It provides easier tuning, improved disturbance rejection capability, and outstanding robustness against parameter variations. The range

of the 'n' has been taken as 2 to 10 for optimal parameter evaluation in the optimization process. The FTIDN controller provides the input control signal for the second layer of DLTFCS. The combination of these control structures can be effectively used as a secondary controller for mitigating the deviations in control area frequency and tie-line power.

To ensure the protection and endurance of the elements present in the physical control loop, it is essential to generate a balancing control action based on variation originating in controlled output. A typical way to achieve this can be the inclusion of normal derivative action in the controller output to generate suitable control action, which is anticipatory in nature by virtue of derivative control. However, this must be carefully designed since it can also enhance the noise signals present in the measurement of plant outputs and can unnecessarily introduce chattering action in the controller output. This disadvantage can be mitigated with the inclusion of an optimally designed proportional along with fractional-order derivative (FOPD) as the second layer of the proposed DLTFCS. The TIDN structure is driven by an output signal from the fuzzy logic controller, i.e., $\boldsymbol{u}^*_{\boldsymbol{FC}}$, and the final controller output can be represented as

$$\boldsymbol{u_c} = \boldsymbol{u} *_{\boldsymbol{FC}} \times \left[\left(\frac{\mathrm{K_{P1}}}{\mathrm{s}^{1/\mathrm{n}}} + \frac{\mathrm{K_{I1}}}{\mathrm{s}} + \mathrm{K_{D1}}\left[\frac{\mathrm{N}\times\mathrm{s}}{\mathrm{s}+\mathrm{N}}\right]\right) \times \{\mathrm{K}_{P2} + (K_{D2} \times s^{\mu})\}\right] \tag{4.4}$$

To implement the proposed DLTFCS (FTIDN-FOPD), we should decide the suitable values for the controller gains, i.e., K_e, K_r, K_{P1}, K_{I1}, K_{D1}, K_{P2}, K_{D2}, n, N, μ, membership functions, and control rules. Various membership functions, i.e., Trapezoidal, triangular, bell, and Gaussian-shaped, are used due to their more straightforward functional implementation, the lesser memory requirement for storage, and less effort required to be handled by FIS. Further, due to cost-effectiveness and enhanced performance compared with other membership functions, the triangular shape is preferred for FL-based controller implementation. In view of the above, for the present work, five triangular shaped membership functions with five fuzzy linguistic variables, i.e., LN (large negative), SN (small negative), Z (zero), SP (small positive), and LP (large positive) as input and output variables has been considered. The membership for both area control error signals (ACE), the derivative of ACE, and the output of the fuzzy logic controller have been represented in Fig 4.5. The rule base for

the fuzzy controller is presented in Table 4.1. In the present work, the Mamdani fuzzy inference system (FIS) for calculating the firing strength of control laws and the center of gravity method as the defuzzifier has been utilized.

The proposed control structure utilizes the concept of fractional calculus for the implementation of fractional order differential and integral terms [8]. Figure 4.6 represents the complete schematic diagram of the system under investigation, including the supplementary and inertial control structure. Further, in the subsequent subsection, the objective function for the SSA algorithm and optimal controller parameters have been presented.

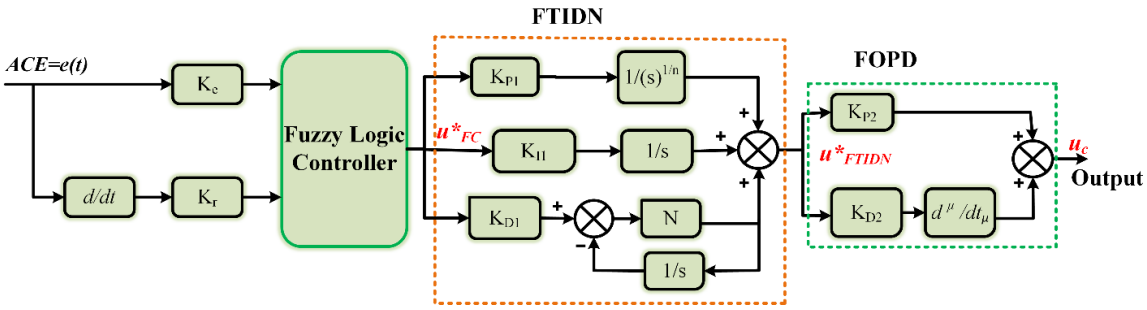

Fig.4.4 *Block diagram of the proposed control structure of DLTFCS (FTIDN-FOPD)*

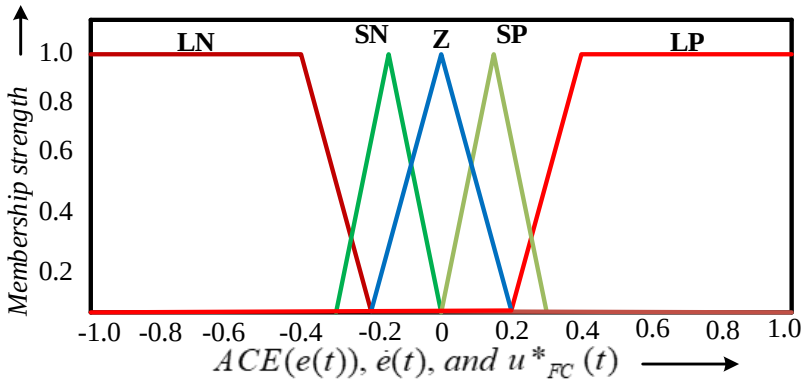

Figure 4.5 *Membership function considered for fuzzy controller*

Table 4.1 Rule base for fuzzy controller

ACE (e)	**Derivative of ACE (ė)**				
	LN	**SN**	**Z**	**SP**	**LP**
LN	LN	LN	LN	SN	Z
SN	LN	SN	SN	Z	SP
Z	LN	SN	Z	SP	LP
SP	SN	Z	SP	SP	LP
LP	Z	SP	LP	LP	LP

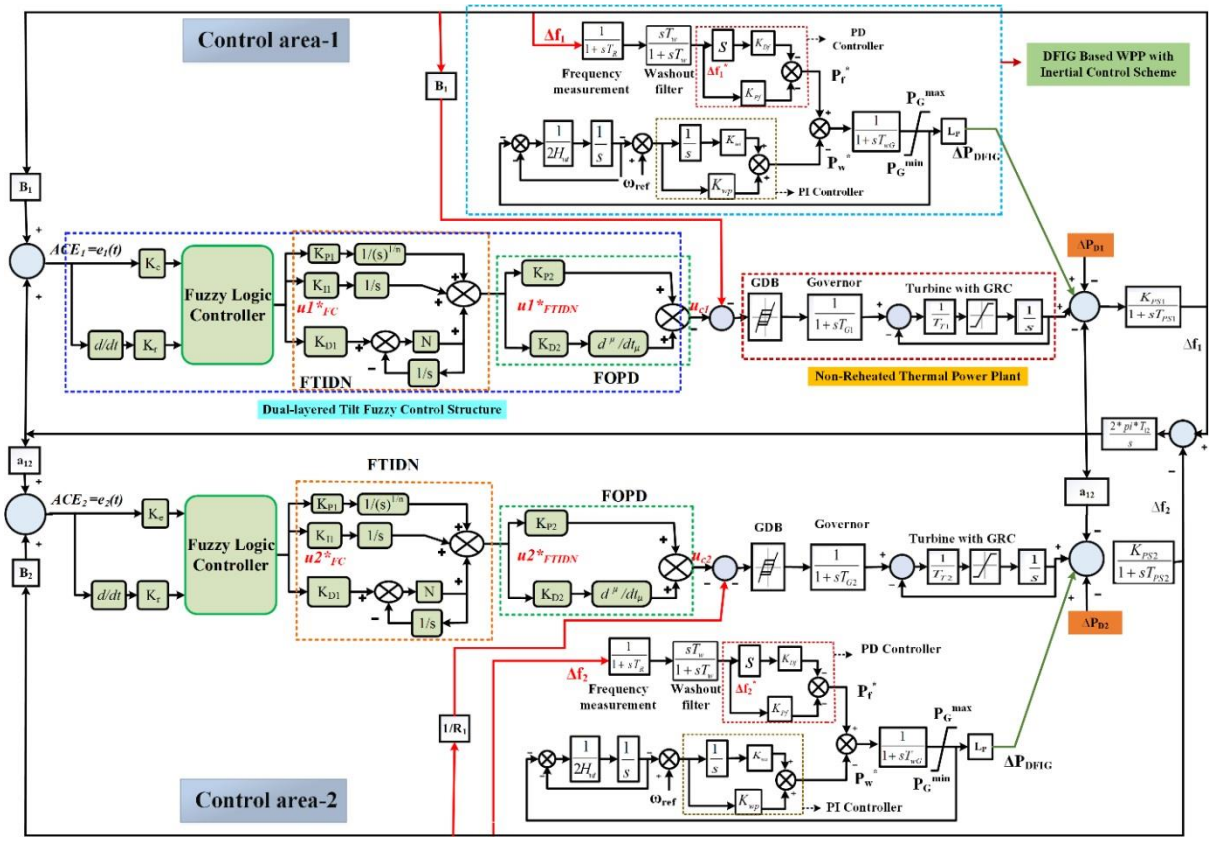

Fig. 4.6 *Schematic representation of the complete system under investigation, including supplementary and inertial control scheme*

4.3.2 Objective function and optimal controller parameters:

In the present work, a hybrid objective function comprising weighted 'ITAE' and 'OM' has been utilized. The 'ITAE' and 'OM' are integral time absolute error and oscillatory measures, respectively. The objective function can be defined as,

Objective function or Performance Index (J) = [w_1×ITAE + w_2×OM] (4.5)

$$\mathrm{OM} = \int_0^t \left(\left| \frac{\mathrm{d}}{\mathrm{dt}} (\Delta f_1) \right| + \left| \frac{\mathrm{d}}{\mathrm{dt}} (\Delta f_2) \right| + \left| \frac{\mathrm{d}}{\mathrm{dt}} (\Delta P_{\mathrm{tie}}) \right| \right) \times t \times \mathrm{dt} \quad (4.6)$$

$$\mathrm{ITAE} = \int_0^t (|\Delta f_1| + |\Delta f_2| + |\Delta P_{\mathrm{tie}}|) \times t \times \mathrm{dt} \quad (4.7)$$

The 'Δf_1', 'Δf_2', and 'ΔP_{tie}' are the deviations in the frequency of area1, area2, and tie-line power exchange between area1 and 2, respectively. The controller gains for FOPID, FFOPID, and DLTFCS (FTIDN-FOPD) have been taken in the range of [-15, 15]. The order of integral and differentials for fractional order controllers has been considered in the range of (0, 2), respectively.

A constrained optimization problem has been formulated to minimize the considered

objective function (J) given in Eq. (4.5) and evaluate the optimal controller parameters via SSA.

$$\left\{\begin{array}{c} K_e^{min} \le K_e \le K_e^{max} \\ K_r^{min} \le K_r \le K_r^{max} \\ K_{P1}^{min} \le K_{P1} \le K_{P1}^{max} \\ K_{I1}^{min} \le K_{I1} \le K_{I1}^{max} \\ K_{D1}^{min} \le K_{D1} \le K_{D1}^{max} \\ K_{P2}^{min} \le K_{P2} \le K_{P2}^{max} \\ K_{D2}^{min} \le K_{D2} \le K_{D2}^{max} \\ n^{min} \le n \le n^{max} \\ N^{min} \le N \le N^{max} \\ \mu^{min} \le \mu \le \mu^{max} \end{array}\right\} \tag{4.8}$$

The minimization of the objective function is subjected to Eq. 4.8. Further, as considered, IPS has an identical capacity as well as energy-generating units in both control areas. Hence to reduce the complexity and cost-effective implementation of the proposed control structure, the same controller has been utilized in both areas. The controller parameter for the three different control structures, i.e., FOPID, FFOPID, and DLTFCS (FTIDN-FOPD) under different system scenarios, have been represented in Table 4.2. The convergence curve of the SSA optimization algorithm for the different utilized controllers has been provided in Fig 4.7. The subsequent section presents an extensive performance analysis of these control structures under different operating conditions.

Table 4.2(a) Optimal controller parameter obtained via SSA for the system without the integration of DFIG-based WPP

Controller Parameters	FOPID	FFOPID	DLTFCS
K_{P1}	10.383	9.0673	2.4718
K_{I1}	0.1546	3.1897	0.0002
K_{D1}	14.828	0.7771	0.4248
K_{P2}	…….	…….	5.9531
K_{D2}	…….	…….	9.9032
N	…….	…….	217.68
λ or n	0.8528	0.00249	9.268
μ	1.2745	1.17288	0.2473
Ke	……	6.38035	8.513
Kr	……	2.03096	1.697

Table 4.2(b) Optimal controller parameter obtained via SSA for a system with integration of DFIG-based WPP

Controllers	Without Frequency Support			With Frequency Support		
	FOPID	**FFOPID**	**DLTFCS**	**FOPID**	**FFOPID**	**DLTFCS**
Kp1	9.9543	0.17993	4.748	6.6147	2.8203	7.797
Ki1	0.5142	3.7385	0.0269	0.61269	1.3514	0.020
Kd1	9.2496	0.26883	4.528	8.3702	1.314	7.138
Kp2	…	…	0.003	…	…	1.046
Kd2	…	…	4.099	…	…	2.270
N	…	…	52.54	…	…	230.81
K_{Df}	…	…	…	9.941	3.3367	4.857
K_{Pf}	…	…	…	1.5066	9.997	9.5249
n	0.56474	0.30058	8.69	0.49326	0.31701	7.32
μ	1.2991	1.3187	0.2326	1.3708	1.2997	0.4485
Ke	…	4.4679	10	…	5.556	9.2805
Kr	…	3.3295	0.2846	…	2.9787	0.2240

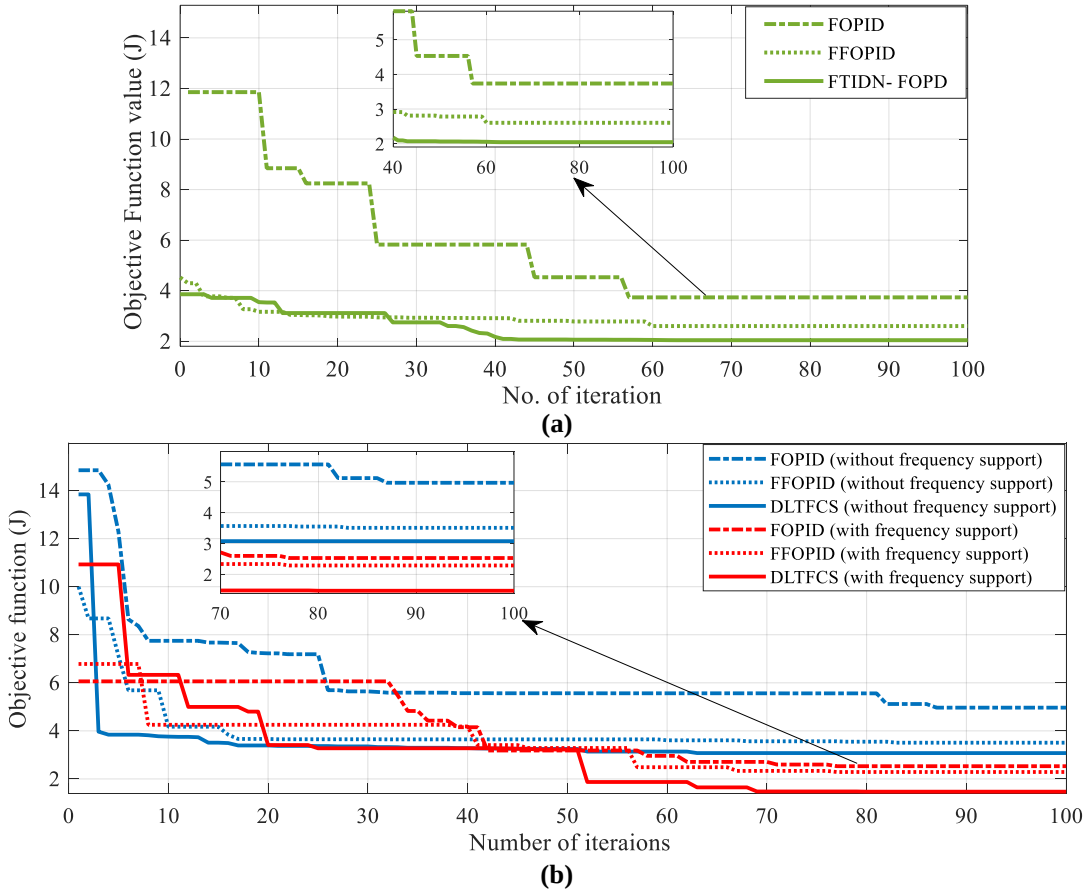

Fig. 4.7 *Convergence curve of SSA for FOPID, FFOPID, and DLTFCS controllers* ***(a)*** *for the system without the integration of DFIG-based WPP* ***(b)*** *for the system with integration of DFIG-based WPP*

4.4 Simulation results and discussion:

The system under investigation has been considered as presented in Fig. 4.1, and its nominal parameters are provided in Appendix II. In this work, the step load perturbation (SLP) of magnitude 0.01 puMW has been applied in control area-1. The system under investigation has been simulated without incorporating the DFIG-based WPP as well as the incorporation of DFIG-based WPP with three control structures viz. FOPID, FFOPID, and DLTFCS. As the system under investigation has an identical both control-area, the same controller parameters are utilized for both area controllers.

Firstly, in this work, the above said control structure, i.e., DLTFCS dynamic performance, has been evaluated under a nominal system scenario without the integration of DFIG-based WPP, with the integration of DFIG-based WPP in the absence and presence of a frequency support scheme. Afterward, the effectiveness of control structures was tested against the system parametric variation (T_T, T_G, and T_{12}) in a range of ±50% from their nominal values. Further, the dynamic performance of the above-said controller has been evaluated under the magnitude variation of inherent system nonlinearities, i.e., GRC and GDB. As the GRC limit decreases, the rejection capability of sudden disturbance reduces, and an increase in GDB causes limit cycles in dynamic performance. Hence, a unique combination of variation in these nonlinearities for our investigation, i.e., an increase in GDB and a decrease in GRC up to 25% of their nominal value in the step of 5%, has been considered. Finally, the impact of variation in penetration level from DFIG-based WPP has been investigated. Further, in subsequent subsection presents the investigation of the LFC dynamic performance of the considered system under nominal system parameters.

4.4.1 LFC under nominal IPS:

The considered IPS in this study for frequency support through an inertial control scheme had been simulated under the nominal system parameter with an investigated controller with an SLP of 0.01 puMW in control area-1. Further, Table 4.3 presents the investigated power system parameters with variations in the wind penetration level. It is needed to mention here that the nominal wind penetration level that has been considered for WPP is 20%. Figure 4.8 represents the objective function *'J'* values obtained via SSA for different control structures under a system without the integration

of DFIG-based WPP and with the integration of DFIG-based WPP in the absence and presence of the inertial frequency support scheme. The '*J*' values obtained with DLTFCS are superior to other control structures for all three conditions.

Table 4. 3 *Variation in the different parameters of equivalent two-area IPS with DFIG-based WPP*

L_P (Wind penetration level)	**Without WPP**	**Without Frequency Support**			**With Frequency Support**		
		10%	20%	30%	10%	20%	30%
$R_{eq}=R/(1-L_p)$	2.4	2.66	3	4.8	2.66	3	4.8
H_{eq} (without frequency support) $= H*(1-L_P)$ H_{eq} (with frequency support) $= H*(1-L_P) + H_{wt}*L_P$	5	4.5	4	3.5	4.85	4.70	4.55
$B_{eq}=(D+1/R_{eq})$	0.425	0.3833	0.3417	0.2999	0.3833	0.3417	0.2999
$T_{PSeq}=(2*H_{eq})/(f*D)$	20	18	16	14	19.40	18.80	18.20

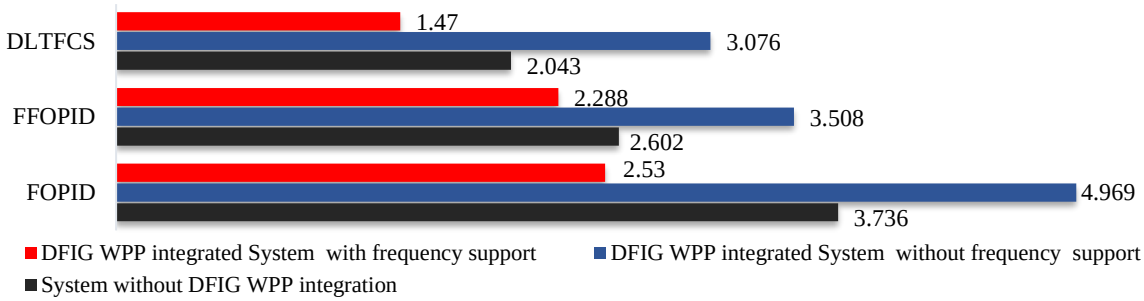

Fig. 4.8 *Objective function values obtained via SSA for different control structures under considered system scenario under nominal system parameters*

DLTFCS improves the LFC performance by 45.31% and 21.48% that of FOPID and FFOPID, respectively, without DFIG based WPP integrated system. A similar response has been achieved for the DLTFCS, where its response has been improved by 38.09% and 12.31% compared to FOPID and FFOPID under the DFIG-based WPP integrated system in the absence of an inertial frequency support scheme. Further, for the DFIG-based WPP integrated system in the presence of an inertial frequency support scheme, the LFC performance has been enhanced by 41.89% and 35.75% with DLTFCS that of FOPID and FFOPID control structure.

The *'J'* value obtained without the frequency support is 3.076, which is degraded by 50.56% than without integration of WPP. After applying for the inertial frequency support, the *'J'* value is 1.47, which improved by 28.05% and 52.21% in comparison with DLTFCS without the integration of DFIG-based WPP and DLTFCS without frequency support. These results advocate the utilization of an inertial frequency support scheme to integrate the DFIG-based WPP with the grid.

Table 4.4 *Frequency nadir, Peak overshoot and settling time of 'Δf_1', 'Δf_2' and 'ΔP_{tie-12}' with the different control structure*

Controllers		System without Integration of DFIG-based WPP			System with Integration of DFIG-based WPP					
					Without Frequency Support			With Frequency Support		
		FOPID	FFOPID	DLTFCS	FOPID	FFOPID	DLTFCS	FOPID	FFOPID	DLTFCS
Frequency nadir ($\times 10^{-2}$)	Δf_1	6.379	6.378	***5.971***	7.573	7.416	***7.569***	5.017	4.875	***4.578***
	Δf_2	6.32	6.01	***5.408***	7.44	7.223	***7.644***	4.631	4.638	***4.357***
	ΔP_{tie-12}	0.8345	0.835	***0.8713***	0.84	0.8502	***0.8403***	0.671	0.7266	***0.6282***
Peak overshoot ($\times 10^{-2}$)	Δf_1	1.188	0.6356	***0.2875***	3.023	0.645	***0.1915***	1.488	0.1902	***0.2748***
	Δf_2	1.296	0.4374	***0.2309***	3.186	0.568	***0.1337***	1.575	0.1691	***0.1277***
	ΔP_{tie-12}	0	0	***0***	0	0	***0***	0.02	0	***0***
Settling time (seconds)	Δf_1	24.9	13.1	***10.77***	14.93	13.71	***10.06***	14.4	9.98	***9.96***
	Δf_2	25.41	11.9	***9.04***	14.96	9.63	***9.05***	17.1	9.63	***9.02***
	ΔP_{tie-12}	12.12	12.62	***10.52***	12.35	13.32	***11.65***	10.54	9.86	***9.92***

Figure 4.9 represents the deviation in frequency of control area-1, area-2, the deviation in the scheduled tie-line power exchange between control area-1 and 2, and the deviation generated power by control area-1 generating unit with different control structures under nominal system parameters. Detailed insight into these responses has been presented in Table 4.4, containing frequency nadir, peak overshoot, and settling time. The boldface values are the best values obtained among the investigated control structure and belong to the DLTFCS in the presence of a frequency support scheme. From these results, it is evident that the DLTFCS provides superior LFC performance than FOPID and FFOPID controllers.

The Dynamic Performance of the FOPID controller is found to be the worst among the three investigated controllers in terms of objective function value *'J'*, frequency nadir, peak overshoot, and settling time represented in Fig 4.9 and Table 4.4. Hence for the brevity of the chapter, FOPID responses have been omitted in further studies. However, its numerical results have been tabulated. Hence it can be inferred that the integration of DFIG-based WPP must be employed with a frequency support scheme; otherwise, it can hamper the LFC performance significantly. Further, to evaluate the effectiveness of the proposed controller, its performance has been investigated under system parametric variation and presented in the subsequent sub-section.

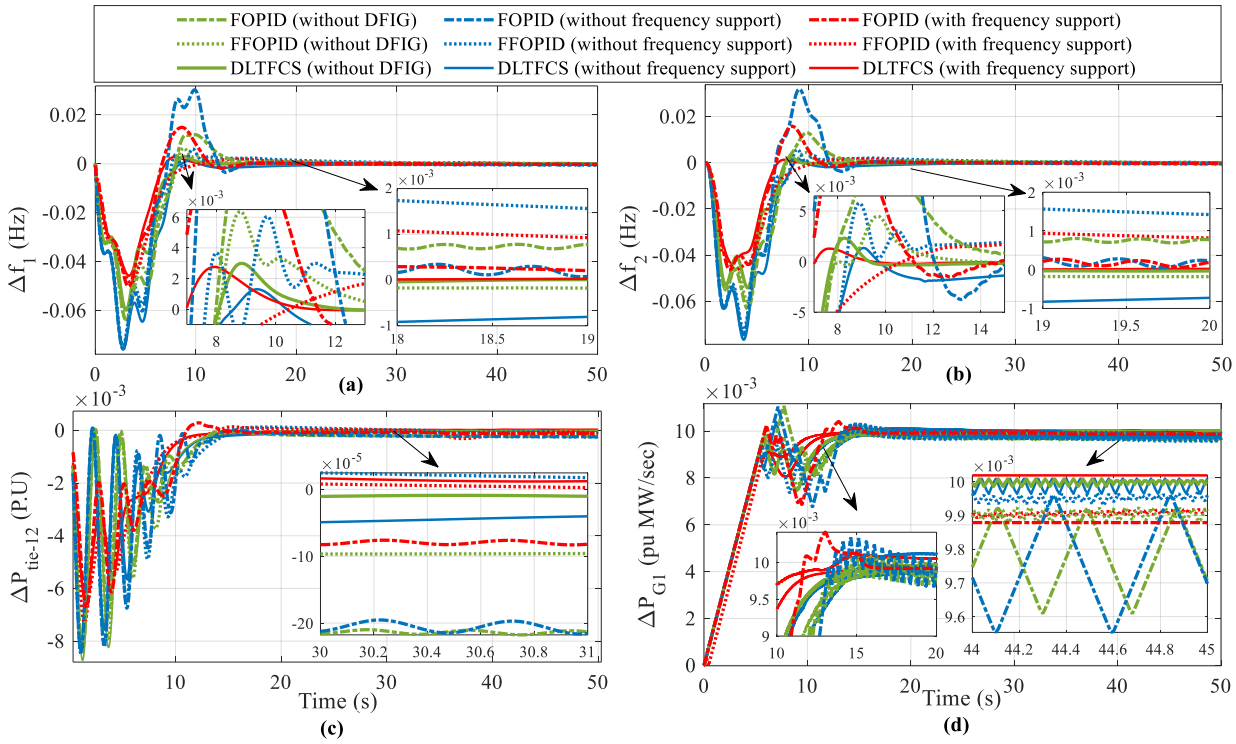

Fig. 4.9 *Deviation in **(a)** frequency of control area-1 **(b)** frequency of control area-2 **(c)** tie-line power exchange **(d)** power generated by control area-1 under nominal system parameters*

4.4.2 LFC performance with uncertainty in time constant of IPS:

A significant amount of uncertainty in the parameters' values for a realistic IPS can be associated with its different components, such as the governor, generator, turbine, and tie-line components. These components are under operation for an extended period and may endure a deviation from their nominal values. The controller performance must be tested for such parametric deviation; to evaluate its robustness; otherwise, sometimes it may lead to system instability. In this sub-section, various parametric settings have been taken in which the time constants of different IPS components have diverged from their nominal values.

In this work, an extreme case has been considered, where the IPS time constants viz. T_G, T_T, and T_{12} are deviated by ±50% from their nominal in various combinations. Table 4.5 presents *'J'* values obtained under various combinations of parametric variation with investigated controllers. The *'J'* value obtained with the DLTFCS under the extreme scenario, i.e., +50% variation in all three-time constants simultaneously, is 2.217, which is improved by 57% and 25.65% for FOPID and FFOPID controller, respectively, with the system without DFIG. This is a decisive investigation to evaluate

the robustness of the controller due to the substantial burden faced by the controller to creditably control the IPS under such parametric variation.

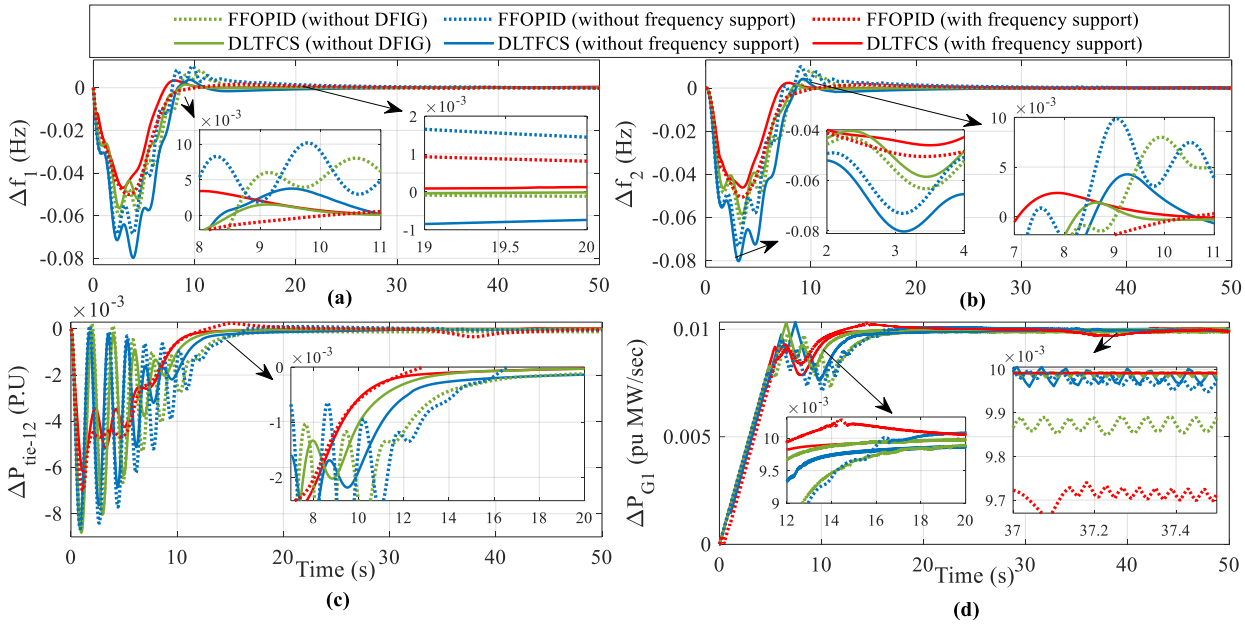

Fig. 4.10 *Deviation in* ***(a)*** *frequency of control area-1* ***(b)*** *frequency of control area-2* ***(c)*** *tie-line power exchange* ***(d)*** *power generated by control area-1 under +50% of* T_T, T_G, *and* T_{12} *simultaneously from their nominal values*

Table 4.5 *'J' values obtained under system parametric variation for FOPID, FFOPID and DLTFCS*

Controllers	System Without Integration of DFIG-Based WPP			DFIG Based on WPP integrated system					
				Without Frequency Support			With Frequency Support		
	FOPID	FFOPID	DLTFCS	FOPID	FFOPID	DLTFCS	FOPID	FFOPID	DLTFCS
Nominal	3.736	2.602	*2.043*	4.967	3.508	*3.076*	2.53	2.288	***1.47***
+50 % (T_G)	3.929	2.818	*2.154*	5.781	4.05	*3.039*	4.356	2.377	***1.412***
-50 % (T_G)	3.554	2.418	*2.24*	4.542	3.242	*3.088*	2.677	2.362	***1.622***
+50 % (T_T)	3.739	2.496	*2.08*	9.664	3.556	*3.083*	2.934	2.296	***1.339***
-50 % (T_T)	3.732	2.582	*2.079*	9.676	3.486	*3.073*	4.05	2.379	***1.368***
+50 % (T_{12})	4.899	2.814	*2.179*	5.855	3.409	*3.621*	4.412	2.469	***1.531***
-50 % (T_{12})	3.394	2.5	*2.324*	6.224	3.692	*2.784*	4.863	2.293	***1.517***
+50 %(T_G, T_T)	3.929	2.772	*2.138*	5.778	3.716	*3.026*	4.346	2.445	***1.345***
-50 %(T_G, T_T)	3.553	2.339	*2.24*	4.544	3.339	*3.084*	2.708	2.428	***1.638***
+50 %(T_G, T_{12})	5.16	3.083	*2.194*	6.929	3.814	*3.539*	4.802	2.27	***1.506***
-50 %(T_G, T_{12})	3.25	2.443	*2.396*	6.698	3.611	*2.773*	5.746	2.615	***1.705***
+50 %(T_T, T_{12})	4.9	2.839	*2.185*	5.857	3.48	*3.624*	2.932	2.299	***1.6***
-50 %(T_T, T_{12})	3.392	2.472	*2.347*	6.226	3.676	*2.771*	4.842	2.316	***1.461***
+50% (T_G, T_T & T_{12})	5.156	2.982	*2.217*	6.927	3.787	*3.538*	4.796	2.301	***1.546***
-50% (T_G, T_T & T_{12})	3.248	2.42	*2.349*	6.704	3.637	*2.773*	4.898	2.69	***1.684***

Figure 4.10 represents the deviation in ''Δf_1', 'Δf_2', 'ΔP_{tie}' and 'ΔP_{G1}' under +50% individual and simultaneous variation in IPS time constants viz. governor time

constant (T_G), turbine time constant (T_T), and tie-line power synchronization constant (T_{12}) with the different investigated controller with SLP of 0.01 puMW in control area-1. It is evident from Fig. 4.10 that the peak overshoot, frequency nadir, settling time, steady-state error, and oscillation are the least with DLTFCS. Table 4.6 presents a detailed insight into Fig. 4. Most of the values obtained via DLTFCS are far superior to its closest competitor, i.e., FFOPID for both control area frequency responses, which proves its efficacy over other investigated control structure under an extreme parametric scenario also.

Table 4.6 *Frequency nadir, Peak overshoot and settling time of 'Δf_1', 'Δf_2' and '$\Delta P_{tie\text{-}12}$' with different control structure2 under +50% of T_T, T_G, and T_{12} simultaneously from their nominal values*

Controllers		System without Integration of DFIG-based WPP		System with Integration of DFIG-based WPP			
				Without Frequency Support		With Frequency Support	
		FFOPID	DLTFCS	FFOPID	DLTFCS	FFOPID	DLTFCS
Frequency nadir ($\times10^{-2}$)	Δf_1	5.765	*5.652*	6.8	*7.961*	5.007	***4.691***
	Δf_2	6.324	*5.856*	7.298	*8.001*	5.056	***4.608***
	$\Delta P_{tie\text{-}12}$	0.8499	*0.8819*	0.8651	*0.8577*	0.698	***0.61***
Peak overshoot ($\times10^{-2}$)	Δf_1	0.7855	*0.1536*	0.9897	*0.374*	*0.1782*	0.3421
	Δf_2	0.8016	*0.1418*	0.9856	*0.4263*	*0.1659*	0.2388
	$\Delta P_{tie\text{-}12}$	0.0213	*0*	0.01162	*0*	0.02395	***0***
Settling time (seconds)	Δf_1	14.18	*8.40*	28.85	*22.6*	10.48	***10.20***
	Δf_2	14.03	*9.14*	29.06	*22.81*	11.22	***9.49***
	$\Delta P_{tie\text{-}12}$	13.06	*11.11*	14.24	*12.16*	10.27	***10.16***

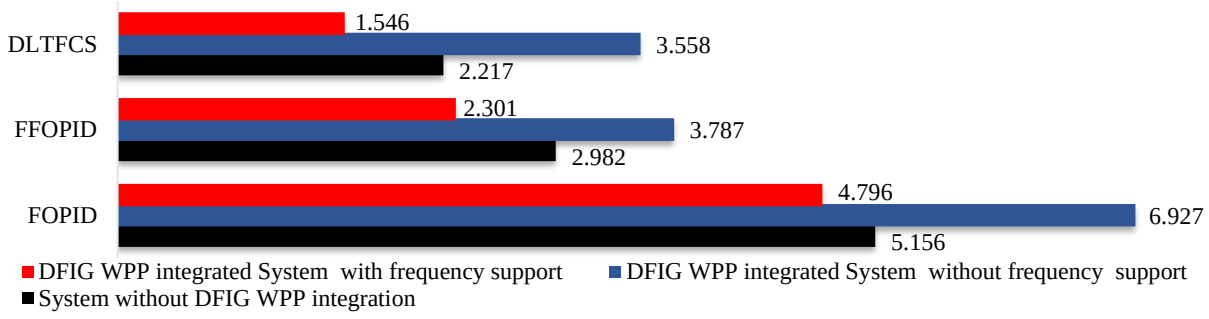

Fig. 4.11 *'J' values with different control structure2 under +50% of T_T, T_G, and T_{12} simultaneously from their nominal values*

Figure 4.11 represents the *'J'* values obtained under +50% simultaneous variation in all three-time constants. It can be inferred from Fig. 4.11 that LFC performance in terms of *'J'* values has been significantly improved with DLTFCS (by 67.76% and 32.81% in comparison to FOPID and FFOPID controller, respectively, in the presence

of frequency support scheme). Further, in the subsequent subsection, the proposed controller performance has been investigated under the magnitude variation of inherent system nonlinearities, i.e., GDB and GRC.

4.4.3 LFC performance with uncertainty in GRC and GDB:

Due to the presence of IPS inherent nonlinearities, i.e., GRC and GDB cause an adverse effect on the dynamic system performance, its incorporation in the IPS model during controller design is essential. The increase in GDB magnitude increases the oscillation content in the system response, whereas decreases in the magnitude of GRC cause a larger settling time. The various aspects, i.e., aging and wear & tear, may lead to considerable variation from their nominal values of the GRC and GDB magnitude. This variation in GDB and GRC magnitude can promote a noteworthy deprivation of dynamic performance or, in some cases, even lead to instability. To deal with such a scenario, the control structure investigated has to be robust enough to cope with these nonlinearities' magnitude variations. This subsection investigates GDB and GRC magnitude variation under an SLP of 0.01 puMW in control area-1.

A unique combination of the increase in GDB and decrease in GRC has been considered for magnitude variation in the step size of 5% up to 25% in this analysis. Table 4.7 and Fig. 4.12 represent the *'J'* values obtained via different investigated controllers under the magnitude variation GRC and GDB simultaneously. It is evident from Table 4.7 that the DLTFCS has the best value for *'J'* in each case.

Further, without the integration of the DFIG-based WPP, the LFC performance has been improved with the DLTFCS by 38.51% and 5.79% in comparison to FOPID and FFOPID controllers, respectively. In the case of integration of the DFIG-based WPP in the absence of a frequency support scheme, the LFC performance has been improved with the DLTFCS by 51.08% and 28.77% compared to FOPID and FFOPID controller, respectively. The LFC performance of all controllers has significantly deteriorated with the integration of the DFIG-based WPP in the absence of frequency support, similar to previous investigations and depicted in Table 4.7. The frequency support scheme enhances the LFC performance with the DLTFCS by 61.9% and 22.1% that of the FOPID and FFOPID controller, respectively, in terms of their *'J'* values.

Table 4.7 *'J' values obtained under simultaneous magnitude variation of GDB and GRC for FOPID, FFOPID, and DLTFCS*

Controllers	System without integrated DFIG-based WPP			*System integrated with DFIG-based WPP*					
				Without Frequency Support			With Frequency Support		
	FOPID	FFOPID	DLTFCS	FOPID	FFOPID	DLTFCS	FOPID	FFOPID	DLTFCS
Nominal	3.736	2.602	*2.043*	4.967	3.508	*3.076*	2.53	2.288	***1.47***
5%	4.225	2.838	2.368	6.134	4.036	*3.355*	3.434	2.535	***1.713***
10%	4.791	3.195	2.653	7.743	4.561	*3.685*	5.37	2.67	***1.815***
15%	5.495	3.576	3.072	8.533	5.377	*4.057*	6.444	3.032	***2.197***
20%	6.295	4.123	3.598	9.085	6.045	*4.48*	7.791	3.322	***2.482***
25%	7.168	4.678	4.407	10.46	7.184	*5.117*	7.751	3.791	***2.953***

Table 4.8 *Frequency nadir, Peak overshoot and settling time of 'Δf_1', 'Δf_2' and 'ΔP_{tie-12}' with different control structures under +25% GDB and -25% GRC simultaneously from their nominal values*

Controllers		System without Integration of DFIG-based WPP		System with Integration of DFIG-based WPP			
				Without Frequency Support		With Frequency Support	
		FFOPID	DLTFCS	FFOPID	DLTFCS	FFOPID	DLTFCS
Frequency nadir ($\times 10^{-2}$)	Δf_1	7.245	***6.928***	8.487	*8.66*	5.579	***5.409***
	Δf_2	7.572	***7.114***	8.923	*9.054*	5.47	***5.189***
	ΔP_{tie-12}	0.8688	*0.8956*	0.8776	***0.8729***	0.7526	***0.653***
Peak overshoot ($\times 10^{-2}$)	Δf_1	1.286	***1.062***	1.974	***1.12***	0.2748	***0.7514***
	Δf_2	1.097	***0.9788***	1.99	***1.2***	0.2480	***0.628***
	ΔP_{tie-12}	0	***0***	0	***0***	0.01782	***0***
Settling Time (seconds)	Δf_1	16.88	***14.92***	35.34	***22.90***	28.85	***13.69***
	Δf_2	16.20	***13.44***	36.14	***23.18***	29.07	***12.71***
	ΔP_{tie-12}	16.18	***14.9***	17.04	***15.81***	12.42	*12.88*

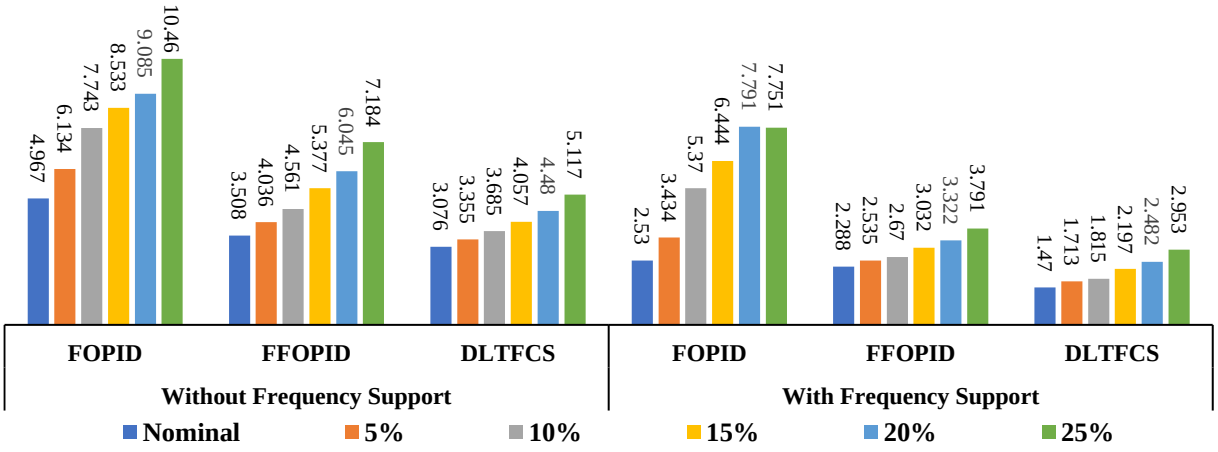

Fig. 4.12 *'J' values obtained under magnitude variation of GDB & GRC for FOPID, FFOPID, and DLTFCS*

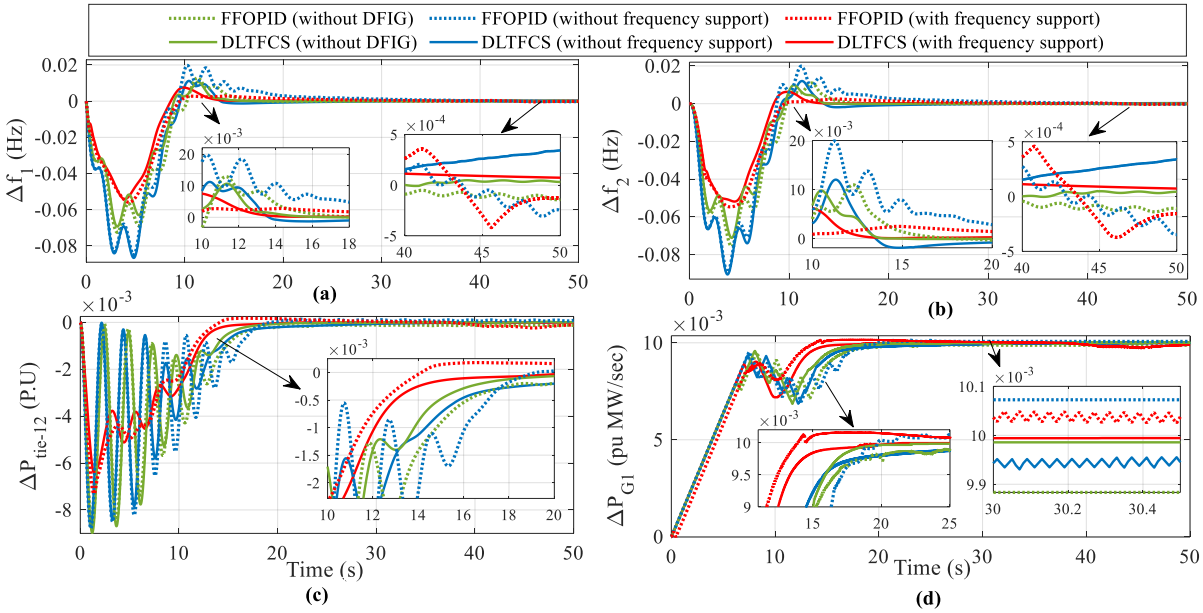

Fig. 4.13 *Deviation in **(a)** frequency of control area-1 **(b)** frequency of control area-2 **(c)** tie-line power exchange **(d)** power generated by control area-1 under +25% GDB and -25% GRC simultaneously from their nominal values*

Figure 4.13 represents the deviation in 'Δf_1', 'Δf_2', and 'ΔPtie' and 'ΔP_{G1}' under 25% increment of GDB and 25% decrement of GRC from their nominal values with SLP of 0.01 puMW in the control area-1 via different controllers. The oscillation magnitude and settling time have been increased significantly from their nominal scenario due to the effect of GRC and GDB. The values of peak overshoot and settling time are the least for the proposed controller, i.e., DLTFCS, and this result is supported by Table 4.8, which contains the peak overshoot, frequency nadir, and settling time of the frequency response for both control area as well tie-line power exchange. Hence DLTFCS is still capable of handling large variations in nonlinearities and provides the best dynamic performance among the investigated controllers.

From the above analysis, it can be concluded that DLTFCS based inertial frequency support scheme is robust enough to provide satisfactory LFC dynamic performance under system parametric variation as well as magnitude variation of system inherent nonlinearities. Further, the LFC performance has been evaluated against an alteration in the level of wind penetration in the subsequent subsection.

4.4.4 Impact of variation in wind penetration level:

Performance evaluation of the proposed controller has also been carried out for the various wind penetration level ranging from 10% to 30% in steps of 10%, 20%

being nominal. Table 4.9 represents objection function values obtained at different wind penetration levels with and without an inertial frequency support scheme. It is clear from these values that even the variation of 'Lp' the DLTFCS in the presence of an inertial frequency control scheme performs efficiently.

Table 4.9 *'J' values under different wind penetration levels*

L_P (level of wind penetration)		**10%**	**20%**	**30%**
Without Frequency Support	FOPID	5.061	4.969	6.078
	FFOPID	3.357	3.508	3.836
	DLTFCS	***2.701***	***3.076***	***3.525***
With Frequency Support	FOPID	2.351	2.53	3.05
	FFOPID	2.573	2.288	2.596
	DLTFCS	***1.54***	***1.47***	***1.505***

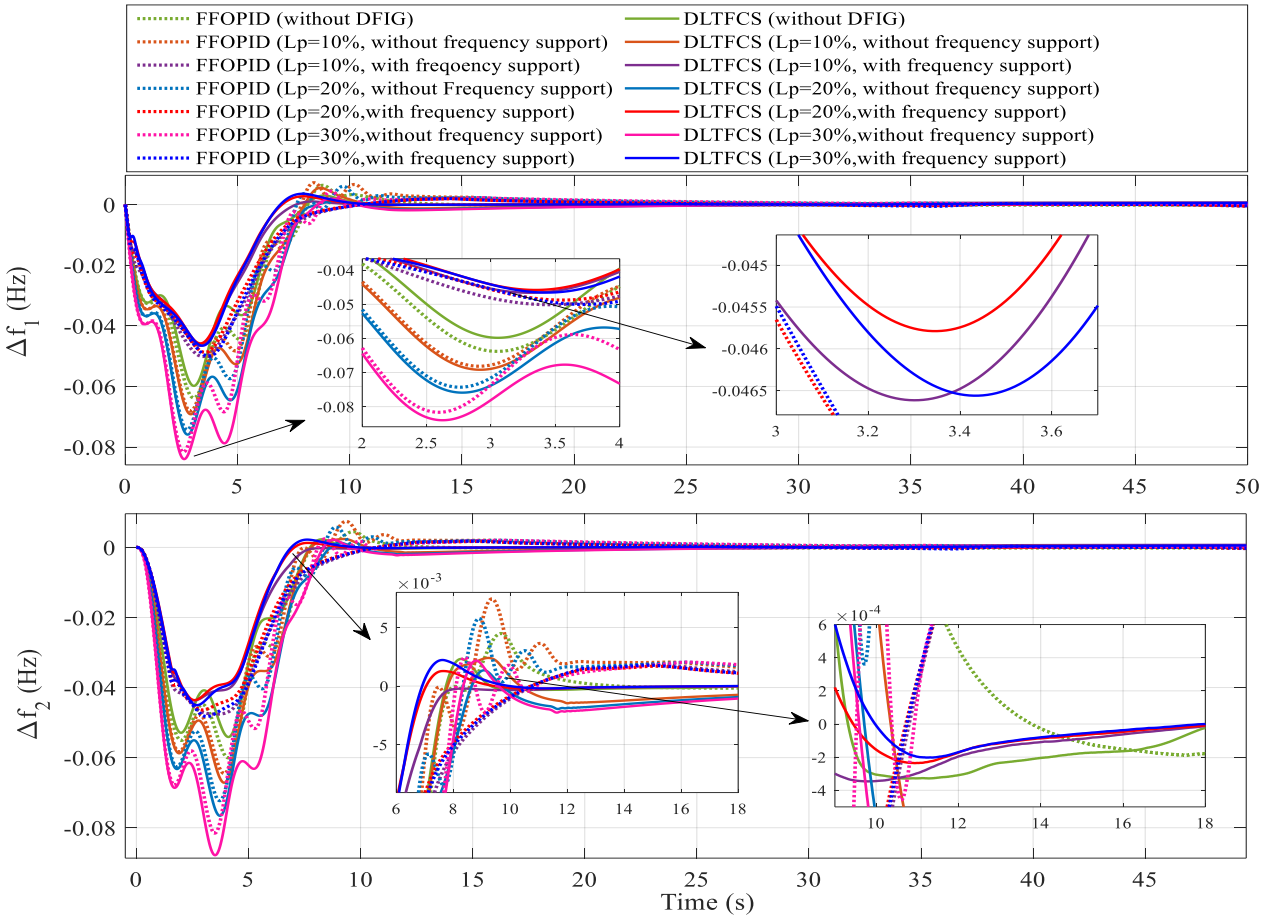

Fig. 4.14 *Deviation of frequency in control area-1 and 2 with the variation of 'Lp' under with and without frequency support*

The maximum variation in *'J'* values obtained with different controllers under frequency support is 20.55%, 13.46%, and 4.76% from the nominal wind penetration for FOPID, FFOPID, and DLTFCS, respectively. The deviation in the frequency of both the control area is presented in Fig. 4.14, and it is evident that for the DLTFCS in

the presence of an inertial frequency control scheme, there is no substantial change under varying 'L_P' as compared with the absence of inertial frequency support scheme. From the above various analyses, it can be inferred that the investigated control structure, i.e., DLTFCS provides an effective solution under variation parametric variation, nonlinearities magnitude variation, and under changing wind penetration level. Further, integrating the DFIG-based WPP with the conventional generating units, an efficient frequency support scheme must be employed; otherwise, LFC performance can be adversely affected. In the subsequent subsection, the summary of the present work has been offered to get a quick insight into the investigations performed.

4.5 Summary:

In the present study, A two-area IPS with an identical non-reheated thermal power unit has been considered for the present study, with its inherent nonlinearities, i.e., governor deadband (GDB) and generation rate constraint (GRC) simultaneously to make the system under investigation more realistic. In the presence of generation rate constraint (a physical limitation on turbine output), the immediate load mitigation capability and load frequency regulation performance of the considered IPS can be significantly hampered. Further, the DFIG-based WPP has been integrated with and without a frequency support scheme (inertial control scheme for DFIG-based WTG) with a conventional generating unit in both control areas to investigate the load frequency regulation.

The *'J'* value obtained without the frequency support is 3.076, which is degraded by 50.56% in the presence of WPP under nominal system parameters. After implementing the inertial frequency support, the *'J'* value is 1.47, which improved by 28.05% and 52.21% in comparison with DLTFCS without the integration of DFIG-based WPP and DLTFCS without frequency support. Further, to evaluate the system performance under varying wind penetration levels with the proposed control structure, the wind penetration level has been altered (10% and 30%) from its nominal value, i.e., 20%. The maximum variation in *'J'* values obtained with different controllers under frequency support is 20.55%, 13.46%, and 4.76% from the nominal wind penetration for FOPID, FFOPID, and DLTFCS, respectively. Hence even under varying wind penetration levels, the proposed controller structure provides exceptionally superior dynamic performance to the rest control structures utilized.

The investigation presented in this chapter focuses on the need for frequency support from the WTGs while integrating with the existing power system. An aggressive approach of installation of renewable energy sources in the global scenario for meeting the sustainable growth world without increasing carbon emission. The share of renewable energy sources is increasing significantly in electrical power generation, causing a remarkable reduction in power system inertia. Hence, long-term frequency support mechanisms are required from renewable energy resources for stable operation of the electrical power system under disparity of generation and load demand. When the WTG operates at a lower rating than its maximum power point of operation, then known as deloading of WTG, a sufficient reserve power margin can be created for power system contingency events through a deloading strategy. In the subsequent chapter, an attempt has been made to incorporate a nonlinear deloading strategy implementation on WTGs for long-term frequency support.

References:

[1] IRENA, "Renewable Energy Capacity Highlights," International Renewable Energy Agency, 2021.https://www.irena.org/publications/2021/March/Renewable-Capacity-Statistics-2021.

[2] S. K. Pandey, S. R. Mohanty, and N. Kishor, "A literature survey on load-frequency control for conventional and distribution generation power systems," Renew. Sustain. Energy Rev., vol. 25, pp. 318–334, 2013, doi: 10.1016/j.rser.2013.04.029.

[3] P. Bhatt, R. Roy, and S. P. Ghoshal, "Dynamic participation of doubly fed induction generator in automatic generation control," Renew. Energy, vol. 36, pp. 1203–1213, 2011, doi: 10.1016/j.renene.2010.08.017.

[4] S. Sondhi and Y. V. Hote, "Fractional order PID controller for load frequency control," Energy Convers. Manag., vol. 85, pp. 343–353, 2014, doi: 10.1016/j.enconman.2014.05.091.

[5] S. P. Singh, T. Prakash, and V. P. Singh, "Coordinated tuning of controller-parameters using symbiotic organisms search algorithm for frequency regulation of multi-area wind integrated power system," Eng. Sci. Technol. an Int. J., vol. 23, pp. 240–252, 2019, doi: 10.1016/j.jestch.2019.03.007.

[6] S. Chaine, M. Tripathy, and S. Satpathy, "NSGA-II based optimal control

scheme of wind thermal power system for improvement of frequency regulation characteristics," Ain Shams Eng. J., vol. 6, pp. 851–863, 2015, doi: 10.1016/j.asej.2015.01.011.

[7] X. Yingcheng and T. Nengling, "Review of contribution to frequency control through variable speed wind turbine," Renew. Energy, vol. 36, pp. 1671–1677, 2011, doi: 10.1016/j.renene.2010.11.009.

[8] I. Podlubny, "Geometric and Physical Interpretation of Fractional Integration and Fractional Differentiation," Fract. Calc. Appl. Anal., vol. 5, pp. 367–386, 2002.

Chapter 5: Nonlinear Deloading Strategy for Frequency Support through WTG

5.1 Introduction:

In continuation of the previous chapter and based on a recent report by the international renewable energy agency (IRENA), one of the most rapidly expanding renewable energy technologies is wind power, and its usage is significantly increasing globally due to lower costs [1]. In this connection, the governments are endorsing the rapid acceleration in wind power development through various means, such as promoting the optimal integration of wind turbine integration with existing grids [1-3]. To achieve this, various power generation companies are using constant speed and variable speed wind turbine generators (WTGs) for their integration with the existing power grid structure [4]. It may be noted that, out of these two WTGs, variable speed wind turbines are recently gaining more popularity due to their superior energy extraction capability from the wind energy conversion system (WECS) at a lower converter cost than fixed-speed wind turbines [5]. However, unlike conventional synchronous machines, variable speed WTGs typically use doubly-fed induction generators (DFIGs), which essentially decouple the rotor speed from the main grid frequency due to its power electronic interface. Hence, it has been observed that the large-scale integration of the wind-based energy sources with the existing power system causes a reduction in equivalent system inertia [6][7]. Therefore, whenever a power system contingency appears, such sources do not participate in frequency regulation, and the operation of such renewable integrated power systems faces severe challenges.

Hence, frequency support is intensely needed from WTGs for optimal power system operation [8]. Moreover, it is customary to run a DFIG-based variable speed wind turbine generator in the maximum power point tracking mode to capture the maximum energy from the wind. However, under such operating mode, WTGs fail to respond against any system frequency change due to a lack of any reserve power, and in the event of any sudden load alteration or generation loss, a significant fluctuation in tie-line power flow along with frequency deviation is observed [9][10]. Few control schemes, such as in [11], have been proposed to address this issue, which enables DFIG-based WTGs to operate dynamically in two different modes, viz. frequency

support mode and maximum power point tracking mode, to handle any power system contingencies.

Further, the reserve power control schemes, also known as the deloading approach, essentially deal with the issue of decrement in system inertia by operating WTGs at a lower power level than their maximum power operating point, so that reserve power can be made available for supporting the grid during the system contingencies [12-14]. Bao and Li presented various deloading approaches for variable speed wind turbines by rotor speed control by operating the WTGs below the MPPT to provide frequency support by considering a distinct output power set point curve [15]. In [16], the authors proposed a control strategy for WTGs to participate in frequency regulation by derating them in consideration of over speeding characteristics of wind turbines in the presence of flywheel. Such operation of WTGs is commonly referred to as the deloading of wind turbines, which can make the WTGs participate in frequency regulation effectively [17]. The other occurrences of frequency support through the deloaded operation of WTGs have been presented in [18-20] with consideration of variable droop and dynamic deloading of wind turbine generators based on a fuzzy approach.

It may be noted that a few works for reserve power creation for long-term frequency support from WTGs based on derating operation have been proposed, considering a linear relationship between rotor measured speed and reserve power to evaluate the reference deloaded power. However, the authors in [21] proposed a quadratic relationship for the rotor measured speed and reserve power to evaluate the reference deloaded power, and through simulation studies, the effectiveness of the nonlinear deloading approach was showcased. Further, the quadratic relationship-based deloading approach should be improved due to their limited operational capability for a narrow wind speed range and inability to handle uncertainties present in the power system dynamics.

In order to overcome the drawbacks related to the existing deloading approaches, which were unaddressed in the earlier literature (e.g. [21]), this work proposes a novel nonlinear deloading approach using a carefully curated blend of higher-order Newton's interpolation polynomial (HNIP) and an intelligent supplementary control technique. The proposed approach uses the HNIP to precisely interpret the relationship between

measured rotor speed and reserve power. The designed fuzzy-based intelligent controller takes care of manipulating the power generation to counteract any load variation or parametric uncertainty present in the system. Further, for effective load frequency control of the system under consideration, supplementary controller parameters have been optimized through SSA.

Additionally, to validate the performance of the proposed approach, a two-area interconnected power system has been considered. Rigorous simulation studies have been carried out with the proposed novel nonlinear HNIP-based deloading approach, and an exhaustive comparative analysis has been drawn. The analysis includes comparing variation in frequency deviation for both control areas, deviation of tie-line power exchange, deviation of wind power, and deviation in thermal power for linear deloading, quadratic deloading, and proposed novel HNIP-based nonlinear deloading technique. Further, the key contributions of this chapter are as follows:

- Design and implement a novel nonlinear deloading approach based on higher-order Newton's interpolation polynomial (HNIP) for WTGs.
- Integration of fractional order fuzzy based FOPID (FFOPID) nonlinear intelligent control structure as a supplementary controller with the proposed deloading strategy for enhancement of frequency support.

The remaining chapter has been organized as follows; the two-area interconnected power system under investigation is briefly presented in Section 5.2. The deloading operation methodology of WTG with the existing approaches is presented in Section 5.3. Further, Section 5.4 presents the proposed novel deloading technique based on HNIP, fuzzy-based intelligent supplementary control structure, and optimal controller parameters. The exhaustive studies have been presented to investigate IPS dynamic performance on MATLAB/Simulink platform under different simulation scenarios in Section 5.5, demonstrating the efficacy of the proposed novel HNIP-based nonlinear deloading technique with FFOPID as a supplementary controller. Section 5.6 presents the summary of the presented work in this chapter.

5.2 Description of the system under investigation:

A two-area interconnected power system (IPS) based on renewable energy sources, namely a doubly fed induction generator (DFIG) based variable speed WTG

in a control area-1, has been explored in this work. As illustrated in Fig. 5.1, the studied IPS consists of a wind energy park with 400 WTGs of identical 1.5MW (with the equivalent of 600 MW capacity wind farm) in control area-1, with a total capacity of 2000MW for each control area. However, control area 2 has only a thermal power unit of 2000MW. The increasing penetration from the renewable energy resources in existing power system is reducing the carbon emission, however reducing the equivalent inertia of the power system. The reduction in the inertia of the power system needs to be urgently addressed for the optimal operation of the electrical power system.

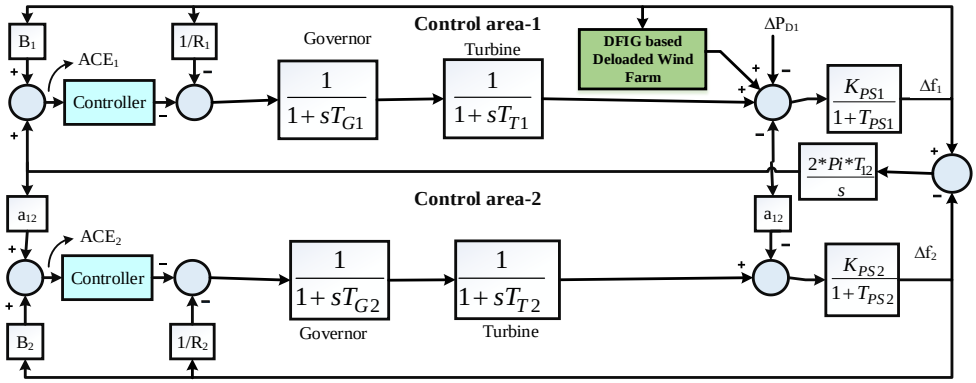

Fig. 5.1 *Schematic block diagram system under investigation (Two-area IPS)*

Hence the present work employs a deloaded WTG in order to provide frequency support from the wind farm as connected in control area-1. In addition, the controller depicted in Fig. 5.1 serves as a supplementary controller. The supplementary controller used in this study is a nonlinear intelligent fractional-order fuzzy-based PID (FFOPID) control structure for effective load frequency regulation. Appendix III lists the different system parameters of the system under consideration. The next section discusses the properties of variable-speed WTGs as well as existing and proposed deloading methodology, i.e., linear, quadratic, and nonlinear deloading strategies to allow the WTG to assist effectively in frequency regulation.

5.3 Deloaded operation of DFIG-based variable speed WTGs:

Deloading is the process in which the variable speed WTGs are supposed to operate at lower power than their maximum power capacity at a given wind speed. Such operation enables the reserve power capacity of a WTG, which in turn can provide active power support during IPS contingencies. This section provides detailed insights into WTGs' power characteristics and deloading operation. The complete schematic

diagram for implementing the deloading techniques in the investigated IPS has been presented in Fig. 5.2. The schematic diagram shows the detailed layout for implementing the deloaded operation of WTGs, including their dynamics in conjunction with Fig. 5.2 for effective load frequency regulation in the IPS under investigation.

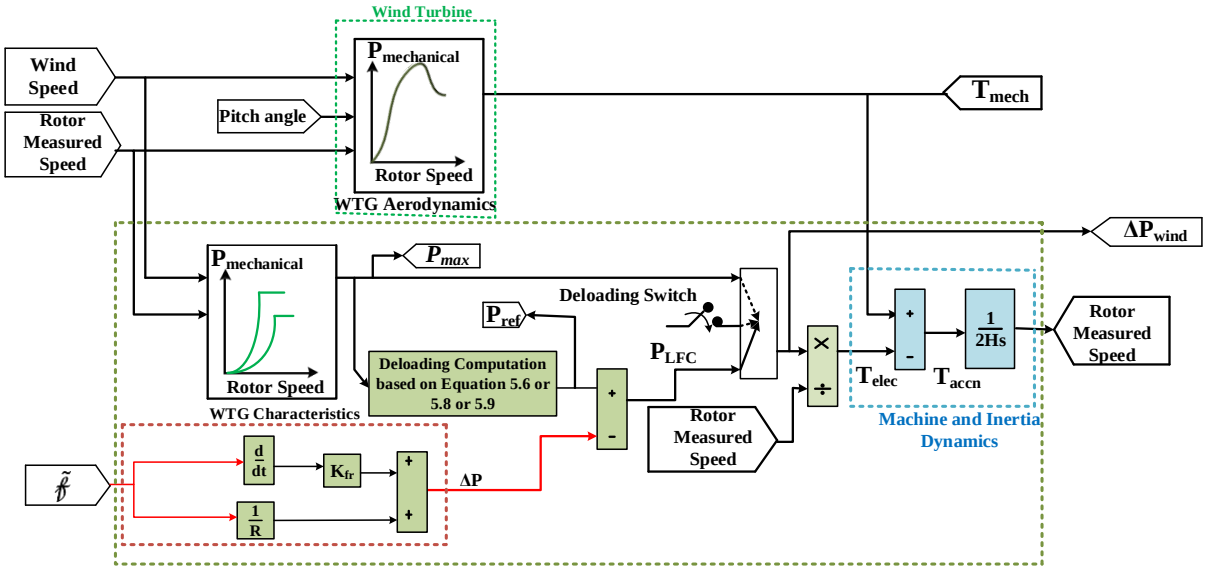

Fig. 5.2 *Schematic block diagram for implementation of deloading operation of DFIG-based WTG*

Further, the frequency support beyond the transient period with an inertial control scheme reduces the rotational speed of WTG and can cause instability of the system. Hence to restrict such events, the WTG can be derated from its maximum power operation and operated at optimal derated or deloaded conditions. This can be performed in two ways, i.e., rotor speed control and pitch angle control. This work solely focuses on rotor speed control methods for deloading activities.

Further, the power versus rotor speed characteristics of WTG plays a significant role during the implementation of the deloading operation. The relation of power versus rotor speed is nonlinear in nature, as shown in Eq. (5.2). The mechanical power developed by a WTG can be given as;

$$P_m = \frac{1}{2}\rho A C_P(\lambda_t, \beta) v^3 \tag{5.2}$$

$$\text{Where, } \lambda_t = \frac{\omega_r * R_{\omega t}}{v}, \text{ and } C_P(\lambda_t, \beta) = \frac{1}{2}\left[\left(\frac{116}{\lambda_c}\right) - 0.4\beta - 5\right] e^{-21/\lambda_c} \tag{5.3}$$

$$\lambda_c = \left[\left(\frac{1}{\lambda_t + 0.08\beta}\right) - \left(\frac{0.035}{\beta^3 + 1}\right)\right]^{-1} \tag{5.4}$$

Where 'v' is the wind speed in m/s, 'ρ' is the air density in Kg/m^3, 'A' is the area swept by the turbine blades in square meters, 'β' is the turbine blade pitch angle in degree, 'λ_t' is the tip speed ratio, 'λ_c' is the tip speed constant, 'ω_r' is the wind turbine rotor speed in rpm, '$R_{\omega t}$' is the rotor radius of the turbine in meters, 'C_P' is known as the power coefficient.

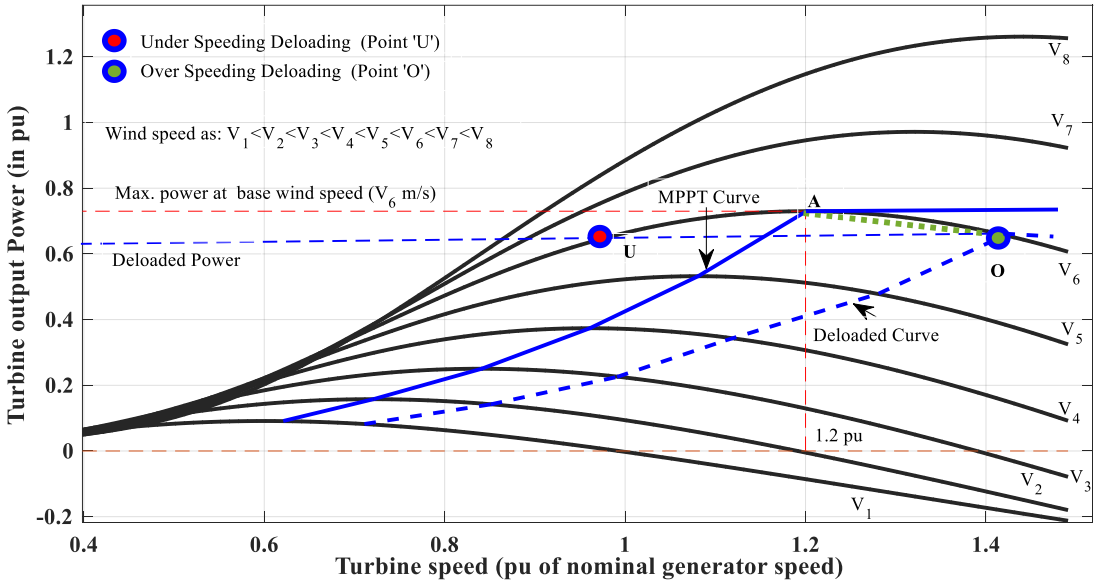

Fig. 5.3 *Wind turbine generator power output versus speed characteristics*

Figure 5.3 shows the power versus speed characteristics of a WTG at different wind speeds. The wind speed of 'V_6' has been considered as a base speed and utilized to implement the deloading operation in which maximum power attains at point 'A' with a rotor speed of 1.2 pu. Further, the solid blue line curve shows the maximum power points trajectory (MPPT) for different wind speeds, and the dashed blue line shows the deloaded power point trajectory for different wind speeds. Hence the reserve power can be achieved by deloading operation and given by Eq. (5.5). Concerning maximum power point operation, the deloading can be performed at two operating points, as shown in Fig. 5.3 by 'O' and 'U' points. The 'U' is for under speeding, and the 'O' is for the overspeeding deloading operation.

$$P_{reserve} = P_{\max(at\ MPPT)} - P_{del} \tag{5.5}$$

It may be noted that an overspeeding deloading operation becomes more effective, as it provides enhanced stability, excess kinetic energy, and improved frequency nadir than under speeding deloaded operation. Hereafter, the present work has utilized a rotor over speeding trajectory (i.e., operate at point 'O' instead of the maximum power point

of operation 'A' as shown in Fig. 5.3) [19][20]. Moreover, frequency support is most appropriately used for a medium wind speed range with overspeeding deloading operation by rotor side control (RSC) from deloaded WTGs. The RSC is utilized to alter the percentage of deloading (in the range of 10-15%) or up to 1.4 per unit rotor speed [20]. Further, in the subsequent subsection, the existing deloading techniques have been briefly presented.

5.3.1 Existing deloading techniques:

In available deloading operations for wind turbine generators in the literature, authors used the concept of linear deloading [19][20]. In the case of linear deloading, a linear function is utilized to define the relationship between maximum power point (P_{max}) and deloaded power point (P_{del}) for calculating system deloaded reference power. The deloaded reference power can be calculated in terms of turbine rotor speed and reserve power (power margin) at the desired wind speed and written as follows,

$$P_{ref} = P_{del} + P_{reserve}\left[\frac{\omega_{del}-\omega_m}{\omega_{del}-\omega_{max}}\right] \quad (5.6)$$

$$P_{reserve} = P_{max} - P_{del} = K * P_{max} \quad (5.7)$$

Where 'P_{max}' is the power obtained at maximum power, 'P_{del}' is the deloaded power, which the system operator can determine, 'ω_{max}', 'ω_{del}' and 'ω_m' are the rotor speed at maximum power, deloaded power-point of operation, and measured rotor speed, respectively (in pu). 'K' is the factor for deloading. Figure 5.4 shows the linearly deloaded WTG power versus rotor speed characteristics (with a dashed black line).

As WTGs have nonlinear power characteristics; therefore, a nonlinear relationship should be used to precisely evaluate the reference deloaded power during the derated operation of WTG as utilized in [21]. The straight-line trajectory for calculating the reference deloading power (P^*_{ref}) has a lesser reserve power margin and reduces the capability of deloaded WTG to participate in primary frequency regulation during power system contingencies.

Figure 5.4 shows the nonlinear trajectory (with bold red line) for evaluating reference deloaded power. It may be inferred from Fig. 5.4 that the nonlinear trajectory considered for evaluating reference deloaded power (P^*_{ref}) has a larger value than the linear trajectory considered in the previous implementation of deloaded operation for

WTGs. The quadratic relationship for calculating the reference deloaded power in [21] has been implemented as follows,

$$P_{ref}^{*} = \frac{A \times B}{\omega_{max}} \omega_m^2 + B(1 - A)\omega_m \tag{5.8}$$

where, $A = \frac{P_{max}}{\omega_{max}}$, $B = \frac{(K_2 - K_1)}{(K_2^2 + 3K_2 + 2)}$, where K_1 is a deloading constant for power, usually in the range of 0 to 0.2, and K_2 is a deloading constant for rotor speed, usually in the range of 0 to 0.1 for stable operation of deloaded WTG [20][21].

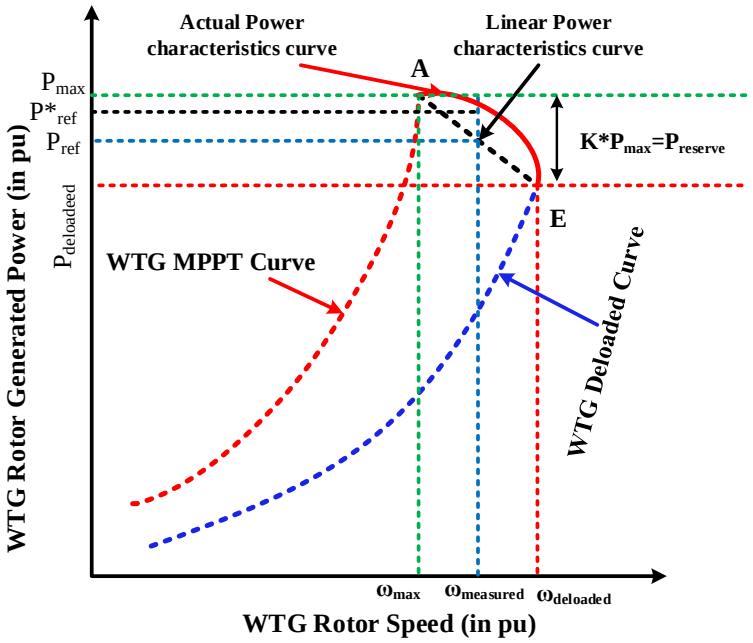

Fig. 5.4 *Wind turbine generator MPPT and deloaded linear and nonlinear characteristics*

The above mentioned quadratic deloading approach has proven to be slightly better than the linear deloading approach up to a certain extent regarding reserve power margin, lesser rotor speed, and frequency response. Hence there is a scope for improvement in dynamic performance, which can be done by replacing the higher-order relationship with a suitable interpolation approach to evaluate 'P_{ref}^{*}' more precisely. Therefore, in this work, an attempt has been made to propose a novel deloading technique based on HNIP, which is presented in detail in the subsequent section.

5.4 Proposed HNIP-based nonlinear deloading of WTG:

As discussed above, the quadratic relationship proposed in [21] fails to precisely represent the nonlinear characteristics of WTGs even utilizing intricate mathematical equations and thereby cannot provide adequate frequency support for certain practical

scenarios. However, in the case of the deloading trajectory devised on the basis of Newton's interpolating polynomial, a more accurate yet easily implementable nonlinear relation is used for calculating the deloaded WTGs reference power. The proposed HNIP-based deloading approach is guaranteed to mitigate any mismatch between generation and load demand satisfactorily due to its higher reference power generation during deloading operation.

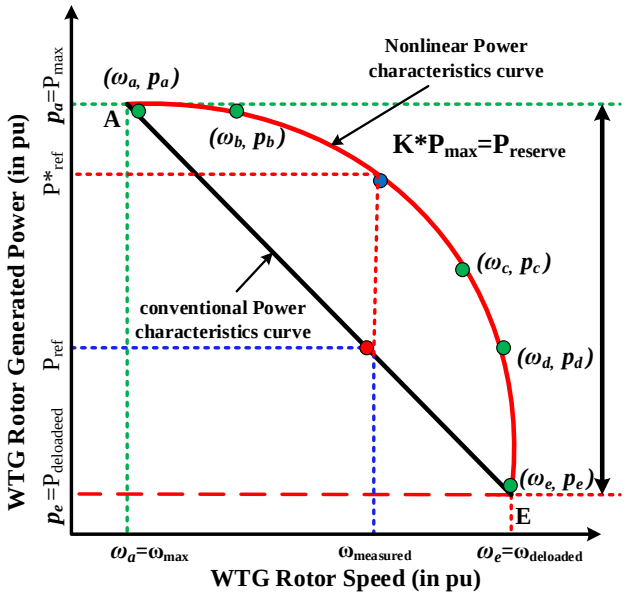

Fig. 5.5 *Deloaded characteristics for calculating 'P^*_{ref}' with Newton's interpolating polynomial*

It may be inferred from Fig. 5.5 that in order to achieve precise and accurate implementation of the deloading operation, the equation representing the nonlinear power characteristic curve must be accurately obtained. In order to achieve this, the present work employs Newton's interpolating polynomial, through which the reference deloaded WTG active power can be precisely calculated as,

$$P_n(\omega_m) = P^*_{ref}(\omega_m) = \sum_{k=0}^{n} b_k * m_k(\omega_m) \tag{5.9}$$

Where, n is the order of the polynomial, $m_k(\omega_m) = \prod_{j=0}^{k-1}(\omega_m - \omega_{m_j})$, coefficients b_k are the divided differences for Newton's interpolation [22], and ω_{m_j} are the considered rotor speed data points for implementing the Newton's interpolating polynomial.

It may be noted that an increase in the order of interpolating polynomials requires extensive information of considered WTG power characteristics and eventually increases the computational complexity without any significant performance improvement. In view of this, the present study uses a fourth-order Newton's

interpolating polynomial for reference deloaded active power calculation. In order to implement the proposed fourth-order interpolating polynomial, five data points for any specific measured rotor speed (ω_m) have been considered, as shown in Fig. 5.5. The maximum power point (P_{max}) and maximum power under deloading condition (P_{del}) are used as upper and lower boundary limits for reference deloaded active power (P_{ref}^*) calculations, which dynamically vary to participate in frequency regulation.

Further, it is essential to utilize the adequate supplementary control structure with the proposed novel HNIP-based nonlinear deloading for investigated IPS to deal with nonlinearity associated with WTG and deloading satisfactorily. In order to accomplish this effectively, a fuzzy-based nonlinear intelligent controller is employed as a supplementary control structure in the considered IPS. The details for the same are presented in the subsequent subsection.

5.4.1 LFC structure and its optimization:

An integral control action has been utilized as the supplementary controller in various instances [15][19][23]. However, the same proves to be ineffective for various practical scenarios. This essentially makes a basis for the need for a nonlinear intelligent control scheme, which has the capability of handling the nonlinear characteristic of WTG, as well as the nonlinear and uncertain behavior of the other power system elements. The detailed design and implementation of the fuzzy-based intelligent controller are presented in the subsequent subsection.

5.4.1.1 Fuzzy logic based nonlinear supplementary control design:

Intelligent control schemes have established their efficacies for various complex control scenarios such as nonlinear and uncertain plant dynamics, imprecise knowledge about the system under consideration, and so on. Because of the above-mentioned advantages of fuzzy control structure, this work utilizes a fuzzy-based intelligent secondary control strategy. The fuzzy control structure can efficiently handle the nonlinearities and uncertainties present in the WTG system and improve the load frequency response of the system under investigation. Figure 5.6 shows the utilized fuzzy-based intelligent supplementary control structure for the IPS under investigation, where deviation in the system input to the controller and its output is used to manipulate the power generation.

This work uses a triangular membership function with five fuzzy linguistic variables as input and output variables, namely LN (large negative), NS (small negative), ZM (zero), SP (small positive), and LP (large positive). The membership function for error signal e(t), the fractional derivative of error, and output has been represented by Fig. 5.7(a). A further surface plot for considered fuzzy based supplementary control structure has been presented in Fig. 5.7(b). The rule base is considered as of the conventional PID controller.

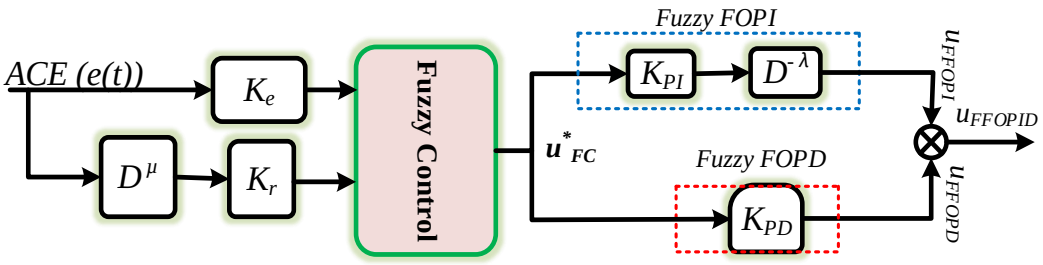

Fig. 5.6 Block diagram of the supplementary control structure with input and output

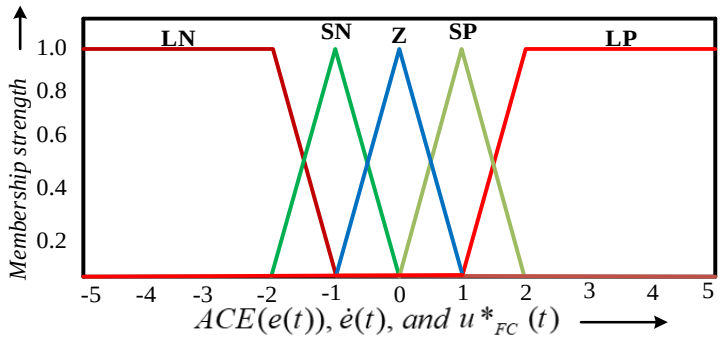

(a)

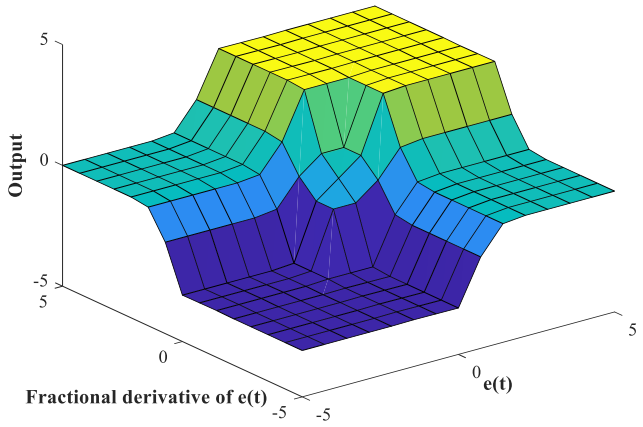

(b)

Fig. 5.7 (a) Rule base for input and output membership function **(b)** three-dimensional surface controller

Further, the optimal values of the controller parameter are found with the help of a global optimization algorithm by minimizing a suitable objective function. The curated hybrid objective function has been considered for obtaining optimal controller parameter values. The subsequent subsection presents the details about the same.

5.4.1.2 Optimal parameters tuning of proposed control approach:

The effective performance of any control structure can only be achieved by the selection of its optimal parameters. The SSA optimization approach has been used for optimal controller parameters, and details for the same can be found in chapter 3.

A tailored hybrid performance measure comprised of weighted 'OM' and 'ITAE' has been used in the investigation. The following is a representation of the objective function or performance index,

Objective function or Performance Index (J) = [w_1×ITAE + w_2×OM] (5.10)

$$\mathrm{OM} = \int_0^{\mathrm{t}} \left(\left| \frac{\mathrm{d}}{\mathrm{dt}} (\Delta \mathrm{f}_1) \right| + \left| \frac{\mathrm{d}}{\mathrm{dt}} (\Delta \mathrm{f}_2) \right| + \left| \frac{\mathrm{d}}{\mathrm{dt}} (\Delta \mathrm{P}_{\mathrm{tie-line}}) \right| \right) \times \mathrm{t} \times \mathrm{dt} \tag{5.11}$$

$$\mathrm{ITAE} = \int_0^{\mathrm{t}} (|\Delta \mathrm{f}_1| + |\Delta \mathrm{f}_2| + |\Delta \mathrm{P}_{\mathrm{tie-line}}|) \times \mathrm{t} \times \mathrm{dt} \tag{5.12}$$

$$\left\{ \begin{array}{c} K_e^{min} \le K_e \le K_e^{max} \\ K_r^{min} \le K_r \le K_r^{max} \\ K_{PI}^{min} \le K_{PI} \le K_{PI}^{max} \\ K_{PD}^{min} \le K_{PD} \le K_{PD}^{max} \\ \mu^{min} \le \mu \le \mu^{max} \\ \lambda^{min} \le \lambda \le \lambda^{max} \end{array} \right\} \tag{5.13}$$

The controller gains that were explored were optimized in the range of [-20, 20]. For fractional order controllers, the order of integrals and differentials has been examined in the range of (0, 2). It's needed to mention here that during the optimization process, the wind speed and a random step load perturbation (RSLP) have been considered in control area-1 as shown in Figs. 5.8 and 5.9. The optimal controller parameters were obtained by SSA for linear constant deloading, and same has been utilized for quadratic deloading and proposed HNIP based nonlinear deloading.

From the convergence curve presented in Fig. 5.10 and Table 5.1, it is evident that the HNIP based nonlinear deloading approach with fuzzy based intelligent controller performs far superior in terms of considered hybrid objective function value than the linear and quadratic deloading approaches. Further, extensive simulation

studies have been carried out to validate the performance of the proposed nonlinear deloading strategy. On the basis of these simulation studies, an exhaustive comparative study is drawn, detailed in the next section.

Table 5.1 *Optimal controller parameters for Fractional-order Fuzzy FOPID control structure along with Objective function*

Parameters		Numerical Values
K_{e1}		12.2209
K_{r1}		0.1215
K_{e2}		14.1914
K_{r2}		1.1325
K_{PI1}		4.9664
K_{PD1}		16.4924
K_{PI2}		0.9264
K_{PD2}		0.2471
K_{fr}		0.2511
λ_1		1.3294
λ_2		0.3387
μ_1		1.4395
μ_2		1.9207
J	**Linear deloading**	22.61
	Quadratic deloading	18.04
	Nonlinear deloading	15.88

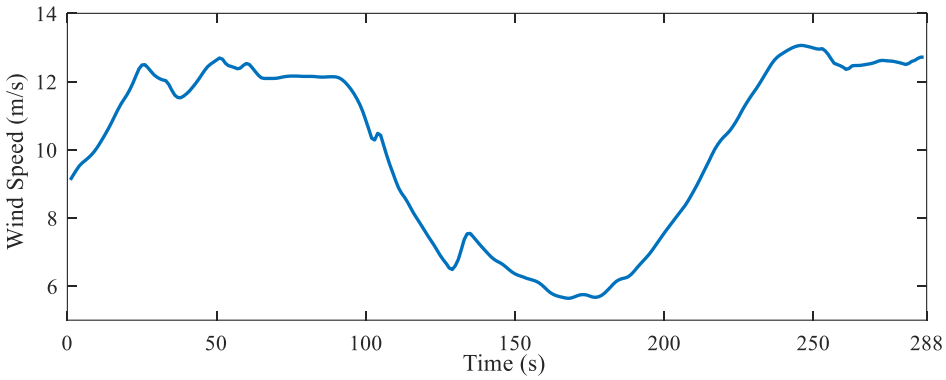

Fig. 5.8 *Wind speed profile*

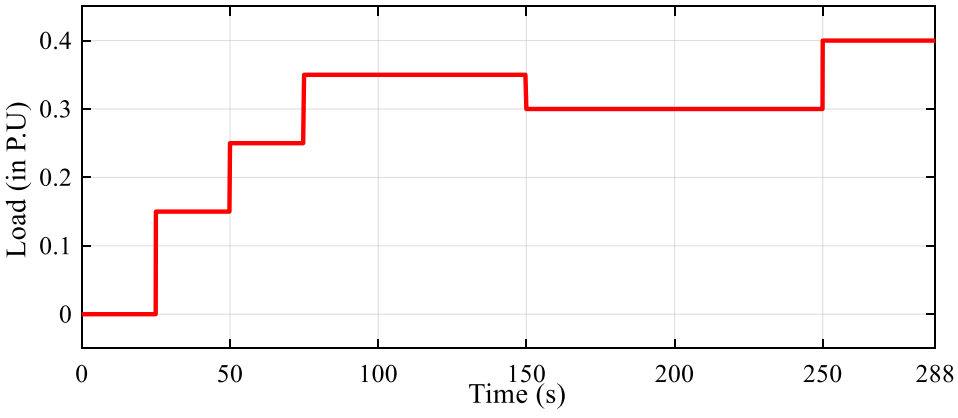

Fig. 5.9 *Random step load perturbation (RSLP) profile*

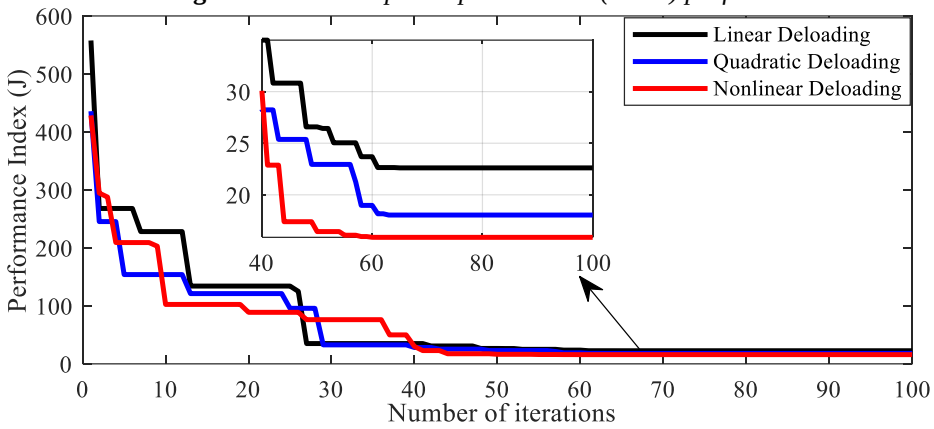

Fig. 5.10 *Comparative convergence curve for linear, quadratic, and nonlinear deloading strategy with FFOPID controller*

5.5 Simulation results and discussion:

As illustrated in Fig. 5.1, the system under consideration was developed in the MATLAB/SIMULINK environment, and its nominal parameters are listed in Appendix-III. In this study, the control area-1 was subjected to a random step load perturbation (RSLP), as shown in Fig 5.9. It should mention that control area-1 has a wind energy park along with a conventional thermal power plant, whereas control area-2 has only a conventional energy source. The system under examination has been simulated with a wind speed profile, i.e., wind speed with measurement block (MBWS). To enhance the frequency support capability from WTG, the present work utilizes the HNIP based nonlinear deloading strategy, and results have been compared with linear and quadratic deloading methodology. It should be noted that a fractional-order fuzzy based PID (FFOPID) control structure has been utilized in both control areas as a supplementary controller, and its optimal parameters were obtained through the salp swarm algorithm. Finally, the proposed nonlinear deloading strategy in the presence of FFOPID has been evaluated against power system parametric variation (K_{PS}, $T_{PS,}$ and T_T) in a range of $\pm$25% from their nominal values, and results were found to be well within stability limits. The assessment of frequency support via the deloaded wind power plant of the studied system through frequency regulation under nominal system parameters is presented in the next subsection.

5.5.1 Investigation with nominal system parameters:

The considered IPS integrated with the wind power plant of control area-1 has been simulated in MATLAB/Simulink environment. The area capacity of both control areas has been considered as 2000MW, and in control area-1, the conventional generation unit of 30% area capacity (i.e., 600MW) has been replaced with the wind power plant. Further, a random step load perturbation, as shown in Fig 5.9, has been applied in control area-1. It's needed to mention here that a measurement block has been considered that continuously receives the wind speed and has measurement dynamics involved for IPS under investigation. In this work, the measurement block dynamics has been considered a first-order system with a time constant of 1.1 seconds and a transport delay of one second. The output of the measurement block can serve as a wind speed input to the wind turbine.

To participate in the frequency regulation process, the wind power plant has been operated in deloaded mode, i.e., the wind turbine operates at a lower point than its maximum power point of operation with increased rotor speed. In this work, the implementation of the existing deloading approaches, i.e., linear and quadratic deloading strategies, has also been employed for performance comparison purposes with the proposed HNIP-based nonlinear deloading strategy. We can infer from Fig. 5.11 that the proposed HNIP-based nonlinear deloading approach is superior to linear and quadratic deloading approaches.

Fig. 5.11 *Objective function 'J' with different deloading strategies*

The quadratic deloading approach improves the objective function by 20.21% compared to the linear deloading approach. In contrast, the nonlinear deloading strategy improves the IPS performance by 29.77% and 12.97% than that of linear and quadratic deloading approaches, as presented in Fig. 5.11.

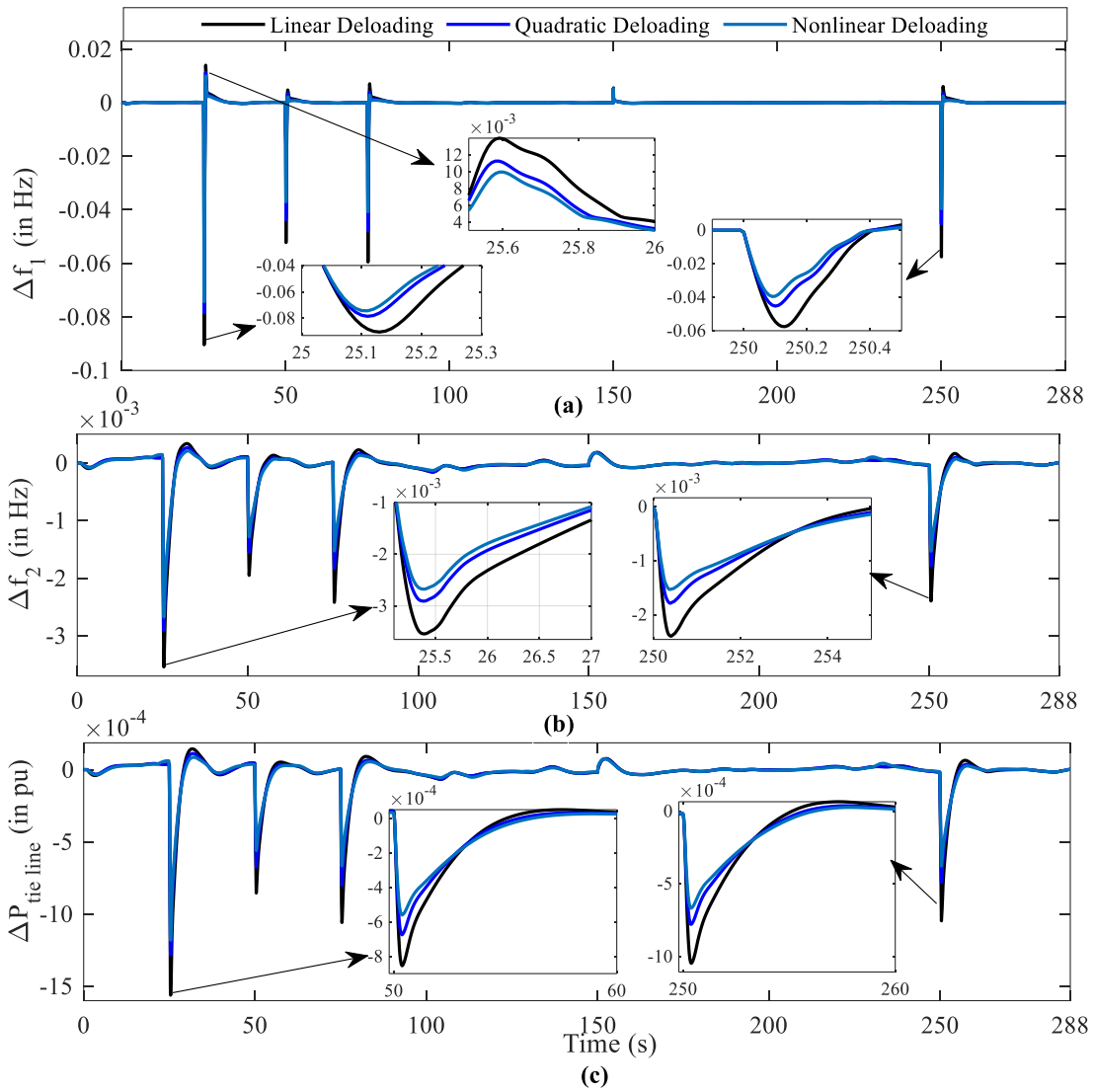

Fig. 5.12 *Variation in* **(a)** *frequency deviation control area-1* **(b)** *frequency deviation control area-2* **(c)** *tie-line power deviation*

Figure 5.12 represents the variation of deviation in frequency and tie-line power exchange between both control areas. It is evident from Fig 5.9 that step load has been applied at 25, 50, 75, 150, and 250 seconds and their impact can be seen in the frequency, wind, and thermal power deviations. The variation of deviation in frequency for control area-1, as shown in Fig. 5.12(a), has been observed with linear deloading approach at 25 and 250 seconds as 0.090398 and 0.05757 Hz, which has been improved with quadratic deloading strategy as 0.07849 and 0.04531Hz. Further, the adaptive nonlinear deloading strategy has significantly improved the frequency support performance compared to linear and quadratic deloading approaches, and frequency deviation was found to be 0.07432 Hz and 0.03941 Hz at 25 and 250 seconds,

respectively. The quadratic deloading approach improves the maximum frequency nadir by 13.21% as of the linear deloading approach. In contrast, the nonlinear deloading strategy improves by 5.21% and 17.78% compared to linear and quadratic deloading approaches.

Similar trends can be seen in Fig 5.12(b) and 5.12(c) for variation in frequency and tie-line deviation, which shows the effectiveness of the proposed nonlinear deloading strategy to that of linear and quadratic deloading approaches.

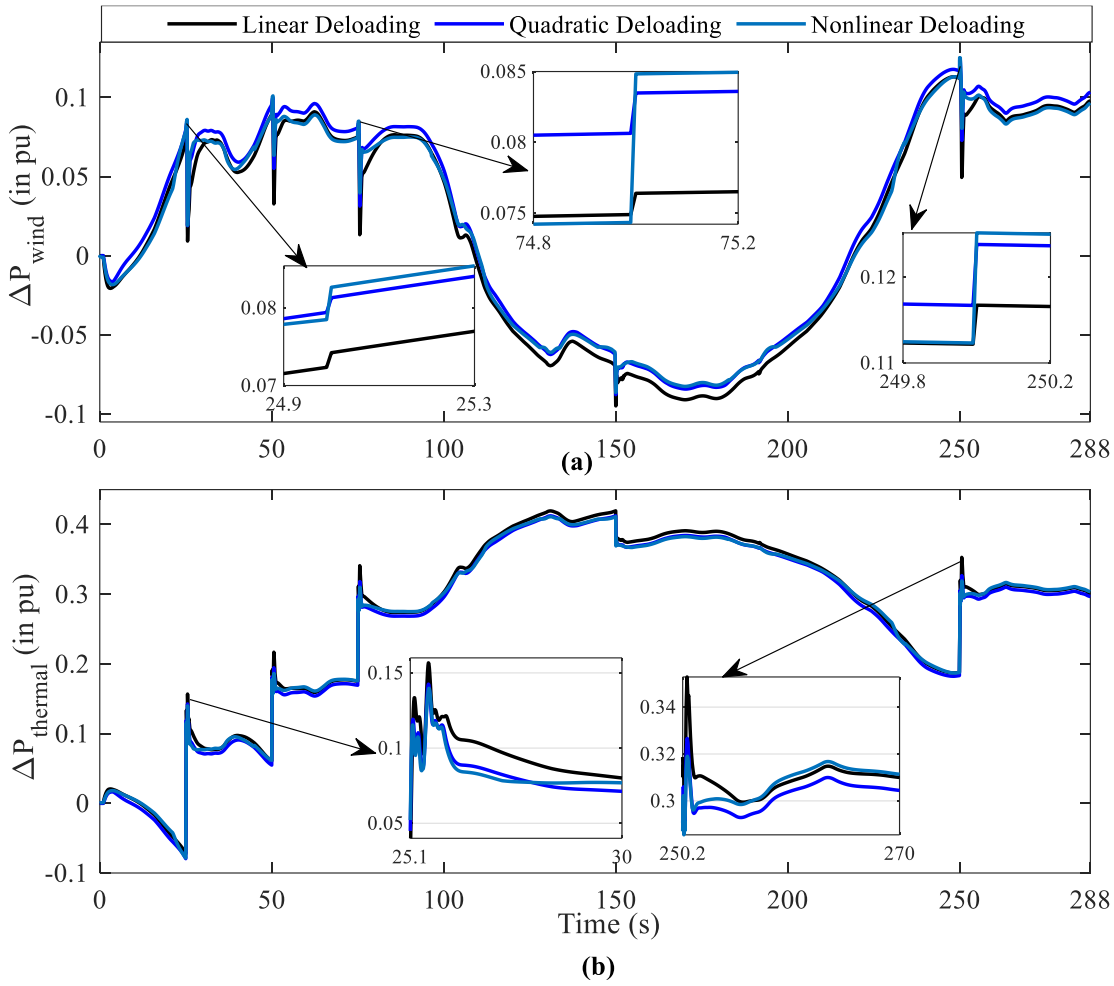

Fig. 5.13 *Variation in* **(a)** *wind power deviation under different deloading strategies* **(b)** *thermal power deviation under different deloading strategies in control area-1*

Figure 5.13(a) and 5.13(b) represent the variation in wind and thermal power in the presence of RSLP with all three deloading approaches. It can be inferred that change in wind power at 25, 75, and 250 seconds is highest for the proposed nonlinear deloading technique than that of others. The change in power of WTG with linear deloading approach at 25, 75, and 250 s instances are 0.0018 pu, 0.0019 pu, and 0.004

pu, whereas with quadratic 0.0019 pu, 0.0029 pu, and 0.007 pu. Further, adaptive nonlinear deloading approaches show the same as 0.00416 pu, 0.0104 pu, and 0.01283 pu, which shows significant improvement in frequency support as with increasing load wind power support has maximum for adaptive nonlinear deloading strategy. In connection with this, thermal power deviation, as shown in Fig 5.13(b), has the least variation for adaptive nonlinear deloading scheme than that of others.

5.5.2 Investigation under parametric variation:

It is necessary to evaluate the efficacy of the proposed nonlinear deloading strategy under a parametric uncertainty scenario. In this work, the variation has been performed in power system parameters, i.e., power system gain (K_{PS}) and time constant (T_{PS}) up to $\pm$25% from the nominal system condition.

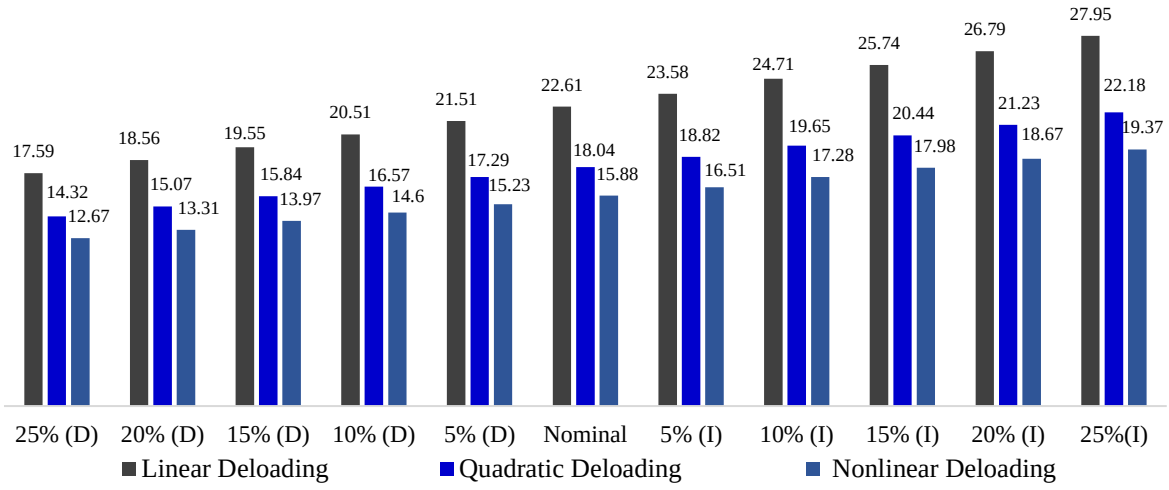

Fig. 5.14 *Variation in Objective function (J) with variation in K_{PS} from -25% to 25% in steps of 5%*

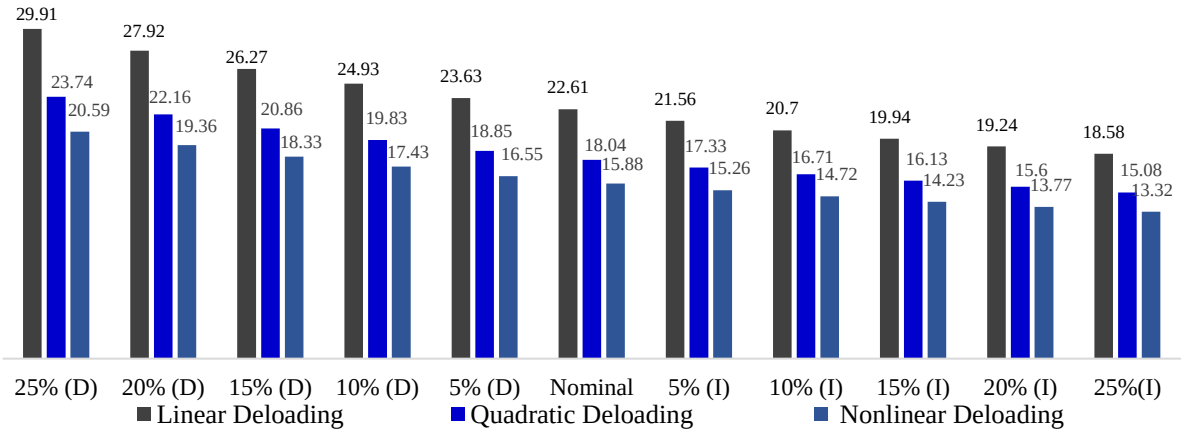

Fig 5.15 *Variation in Objective function (J) with variation in T_{PS} from -25% to 25% in steps of 5%*

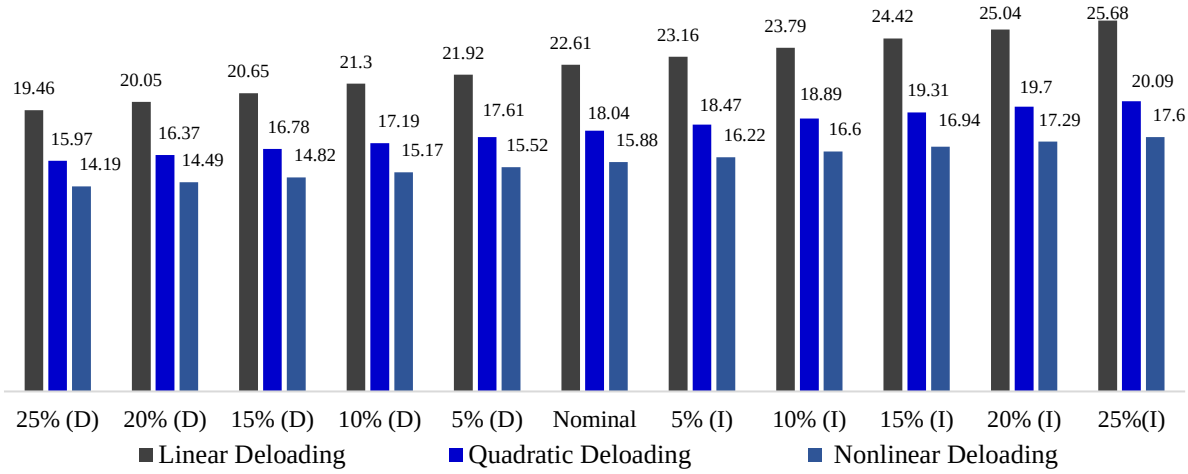

Fig. 5.16 *Variation in Objective function (J) with variation in T_T from -25% to 25% in steps of 5%*

Figures 5.14 and 5.15 show the variation in objective function with variation in power system gain (K_{PS}) and power system time constant (T_{PS}), respectively. It can be inferred from these Figs that with an increase in K_{PS} system performance deteriorates and with a decrease in K_{PS} system performance enhances. Whereas with an increase in T_{PS} system performance enhanced and with a decrease in T_{PS} system performance deteriorates. It should be mentioned here that the 'D' and 'I' represent the increment and decrement, respectively.

Further, it can be inferred from Figs 5.14 and 5.15 that deviations in the objective function have been found maximum with the linear deloading approach and minimum with the proposed nonlinear deloading strategy. The objective function has a change in its value of 23.61%, 22.95%, and 21.98% for linear, quadratic, and proposed nonlinear deloading strategies, respectively, for parametric variation in K_{PS}. While parametric variation in the power system time constant has a change of 32.29%, 31.59%, and 29.66%, respectively. Hence proposed nonlinear deloading strategy has less sensitive against power system parametric variation in comparison to others.

Figure 5.16 shows the turbine time constant (T_T) variation of the thermal power plant for ±25% from their nominal value in the steps of 5%. It can be noted here that the deviation for a 25% increment in turbine time constant causes 14.46%, 11.36%, and 10.83%, respectively, for linear, quadratic, and proposed nonlinear deloading strategies respectively. Whereas with a decrement of 25% causes 13.93%, 11.47%, and 10.64%, respectively. Hence the robustness is highest for the proposed nonlinear deloading

strategy compared with others. Hence, the most critical condition has been presented, i.e., an increase in K_{PS} and a decrease in T_{PS} for evaluating system performance with the proposed nonlinear deloading strategy under FFOPID supplementary control structure in Fig. 5.17.

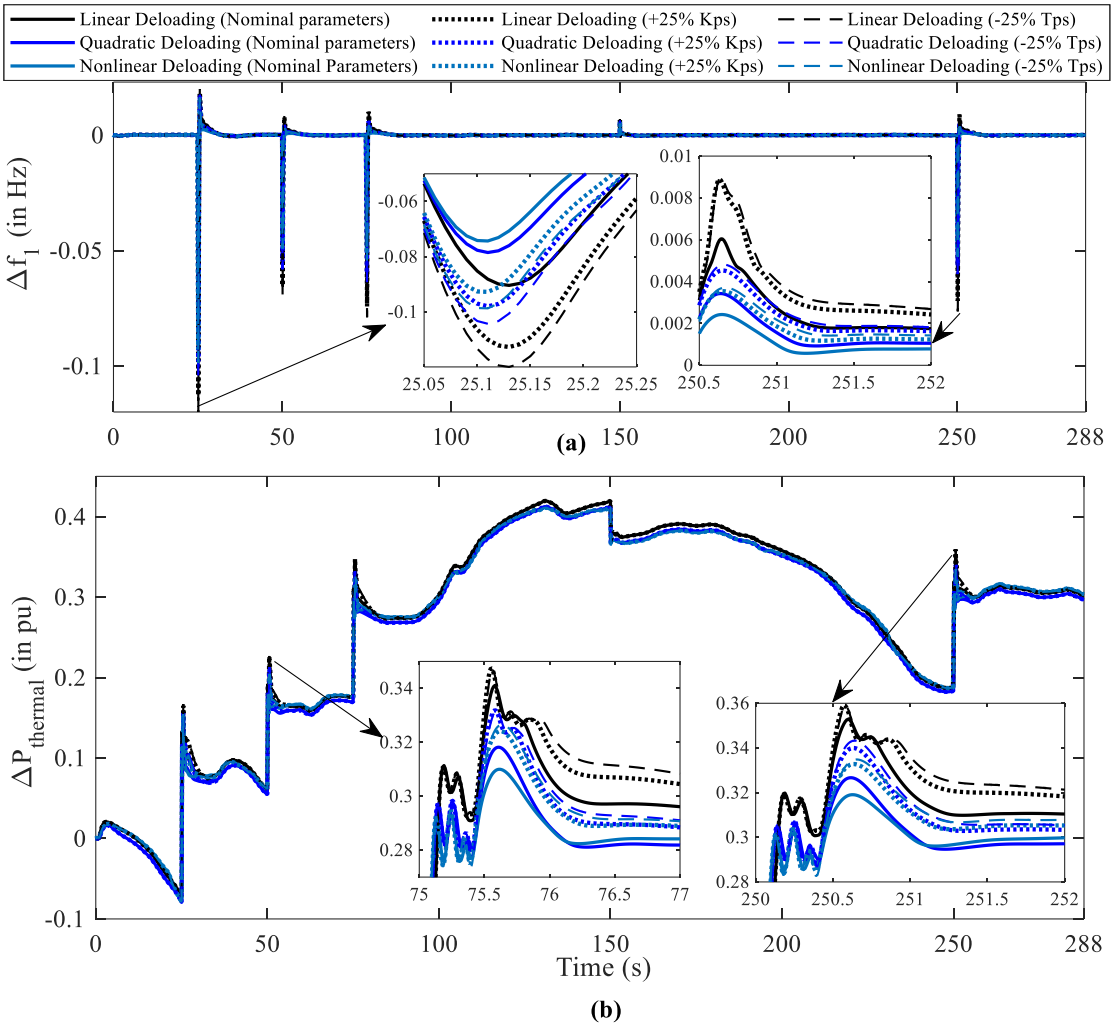

Fig. 5.17 *Variation in* **(a)** *frequency deviation in control area-1* **(b)** *thermal power deviation of investigated IPS with variation of power system parameters in control area-1*

Figure 5.17(a) shows the variation in frequency deviation with nominal system parameters, a 25% increase in $K_{PS,}$ and a 25% decrease in T_{PS}. The maximum frequency deviation is 0.07431, 0.09274, and 0.09871 Hz for nominal, 25% increase in K_{PS} and a 25% decrease in $T_{PS,}$ respectively, with the proposed nonlinear deloading approach, which was found to be the least among all three deloading approaches. Hence a decrease in the power system time constant has a more severe effect on system performance than an increase in power system gain. The variation in thermal power in control area-1 was

found to be the least, as presented in Fig. 5.17(b) for the proposed nonlinear deloading strategy. It needs to be mentioned that other responses have been omitted for the sake of clarity and brevity of the chapter, where all are presented in the bar graph for reference in Figs. 5.14-5.16.

5.6 Summary

The two-area interconnected power system of the identical capacity of 2000MW, consisting of a thermal power plant in both control areas as a conventional energy source, has been considered the system for investigation in the present study. The control area-1 also has a DFIG-based wind farm along with a conventional thermal power plant. The integration of DFIG-based wind farms causes nonparticipation of WTGs in long-term frequency regulation, which can be addressed by an efficiently devised deloading approach. The presented study proposes a novel Newton's interpolating polynomial (HNIP) of fourth-order to address the nonlinear characteristics of WTG. The HNIP deloading has been compared with existing linear and quadratic deloading approaches and was found to be superior in terms of frequency support. Further, 29.77% and 12.97% improvement has been observed in the objective function with the proposed nonlinear deloading strategy as compared with linear and quadratic deloading approaches.

Moreover, the proposed nonlinear deloading in the current chapter uses a constant deloading factor. The deloading factor can be varied instead of considering constant for optimizing the active reserve power present in WPP, which can be utilized during any power system event. In the subsequent chapter, the nonlinear deloading methodology with adaptive deloading factor has been utilized for optimized reserve power margin. The adaptation in the deloading factor has been performed in accordance with wind speed. It is required to have the wind speed in advance to implement the adaptive nonlinear deloading. A forecasting approach has been utilized for having the wind speed in advance. Hence, the next chapter presents the nonlinear adaptive deloading methodology with the help of deep learning for effective frequency support through WPP in an IPS.

References:

[1] J. Lee and F. Zhao, "Global Wind Report 2021," Glob. Wind Energy Counc., pp. 1–80, 2021, [Online]. Available: http://www.gwec.net/global-figures/wind-energy-global-status/.

[2] L. Flint, "Wind energy," S. Afr. Mech. Engr., 2021.

[3] F. Mirzapour, M. Lakzaei, G. Varamini, M. Teimourian, and N. Ghadimi, "A new prediction model of battery and wind-solar output in hybrid power system," J. Ambient Intell. Humaniz. Comput., vol. 10, pp. 77–87, 2019, doi: 10.1007/s12652-017-0600-7.

[4] P. K. Pathak, A. K. Yadav, A. Shastri, and P. A. Alvi, "BWOA assisted PIDF-(1+I) controller for intelligent load frequency management of standalone micro-grid," ISA Trans., 2022, doi: 10.1016/j.isatra.2022.06.010.

[5] M. Dreidy, H. Mokhlis, and S. Mekhilef, "Inertia response and frequency control techniques for renewable energy sources: A review," Renew. Sustain. Energy Rev., vol. 69, pp. 144–155, 2017, doi: 10.1016/j.rser.2016.11.170.

[6] Z. Yang et al., "Robust multi-objective optimal design of islanded hybrid system with renewable and diesel sources/stationary and mobile energy storage systems," Renew. Sustain. Energy Rev., vol. 148, no. May, p. 111295, 2021, doi: 10.1016/j.rser.2021.111295.

[7] H. T. Jadhav and R. Roy, "A critical review on the grid integration issues of DFIG based wind farms," 2011 10th Int. Conf. Environ. Electr. Eng. EEEIC.EU 2011 - Conf. Proc., pp. 11–14, 2011, doi: 10.1109/EEEIC.2011.5874847.

[8] Y. Z. Sun, Z. S. Zhang, G. J. Li, and J. Lin, "Review on frequency control of power systems with wind power penetration," 2010 International Conference on Power System Technology: Technological Innovations Making Power Grid Smarter, POWERCON2010, 2010.

[9] P. Sonkar and O. P. Rahi, "Contribution of wind power plants in grid frequency regulation: Current perspective and future challenges," Wind Eng., vol. 45, pp. 442–456, 2021, doi: 10.1177/0309524X19892899.

[10] M. Debouza and A. Al-Durra, "Grid ancillary services from doubly fed induction generator-based wind energy conversion system: A review," IEEE Access, vol. 7, pp. 7067–7081, 2019, doi: 10.1109/ACCESS.2018.2890168.

[11] R. Ahmadi, A. Sheikholeslami, A. Nabavi Niaki, and A. Ranjbar, "Dynamic participation of doubly fed induction generators in multi-control area load frequency control," Int. Trans. Electr. energy Syst., vol. 20, pp. 1–6, 2014, doi: 10.1002/etep.1891.

[12] K. V. Vidyanandan and N. Senroy, "Frequency regulation in a wind-diesel powered microgrid using flywheels and fuel cells," IET Gener. Transm. Distrib., vol. 10, pp. 780–788, 2016, doi: 10.1049/iet-gtd.2015.0449.

[13] R. C. (ed) Bansal, Handbook of distributed generation: electric power technologies, economics and environmental impacts. Springer, Cham, Switzerland, 2017.

[14] G. Ramtharan, J. B. Ekanayake, and N. Jenkins, "Frequency support from doubly fed induction generator wind turbines," IET Renew. Power Gener., vol. 1, pp. 3–9, 2007, doi: 10.1049/iet-rpg:20060019.

[15] Y. Bao and Y. Li, "On deloading control strategies of wind generators for system frequency regulation," Int. Trans. Electr. energy Syst., vol. 20, no. January 2014, pp. 1–6, 2013, doi: 10.1002/etep.

[16] F. Díaz-González, M. Hau, A. Sumper, and O. Gomis-Bellmunt, "Coordinated operation of wind turbines and flywheel storage for primary frequency control support," Int. J. Electr. Power Energy Syst., vol. 68, pp. 313–326, 2015, doi: 10.1016/j.ijepes.2014.12.062.

[17] R. Prasad and N. P. Padhy, "Coordinated Frequency Controller Operation for DFIG based Wind Turbine Generator Control using Combination Selection Scheme," 2020 IEEE Int. Conf. Power Electron. Smart Grid Renew. Energy, PESGRE 2020, pp. 1–6, 2020, doi: 10.1109/PESGRE45664.2020.9070477.

[18] C. Pradhan and C. Bhende, "Enhancement in Primary Frequency Contribution using Dynamic Deloading of Wind Turbines," IFAC-PapersOnLine, vol. 48, pp. 13–18, 2015, doi: 10.1016/j.ifacol.2015.12.346.

[19] C. Pradhan and C. N. Bhende, "Adaptive deloading of stand-alone wind farm for primary frequency control," Energy Syst., vol. 6, pp. 109–127, Mar. 2015, doi: 10.1007/s12667-014-0131-7.

[20] K. V. Vidyanandan and N. Senroy, "Primary frequency regulation by deloaded wind turbines using variable droop," IEEE Trans. Power Syst., vol. 28, pp. 837–846, 2013, doi: 10.1109/TPWRS.2012.2208233.

[21] D. Kumar, P. Sharma, H. D. Mathur, S. Bhanot, and R. C. Bansal, "Modified Deloading Strategy of Wind Turbine Generators for Primary Frequency Regulation in Micro-Grid," Technol. Econ. Smart Grids Sustain. Energy, vol. 5, no. 1 2020, doi: 10.1007/s40866-020-00083-7.

[22] N. Li, Y. Zhao, Q. Pan, and S. G. Kong, "Demosaicking DoFP images using Newton's polynomial interpolation and polarization difference model," Opt. Express, vol. 27, p. 1376, 2019, doi: 10.1364/oe.27.001376.

[23] M. Ramesh, A. K. Yadav, and P. K. Pathak, "Intelligent adaptive LFC via power flow management of integrated standalone micro-grid system," ISA Trans., vol. 112, pp. 234–250, 2021, doi: 10.1016/j.isatra.2020.12.002.

Chapter 6: DL-Assisted Adaptive Nonlinear Deloading Strategy for WTG

6.1 Introduction:

The frequency support from the variable speed wind turbine for the long term can be efficiently achieved by deloaded operation with creating a sufficient reserve, as presented in the previous chapter for a two-area interconnected power system consisting of a DFIG-based WPP in control area-1. The constant deloading factor, as utilized in the previous chapter for investigated IPS scenario, in which the deloading factor has been considered unchanged irrespective of wind speed. It is evident that for the lower wind speed, the operation of the WTG can be uneconomic due to its overutilization in the frequency support scheme. On the other hand, at higher wind speeds, the ability of the wind to support the grid under any contingency event can be underutilized. These snags of the constant deloading approach used in the previous chapter can be addressed effectively by varying the deloading factor in accordance with the wind speed to optimize the effective available power margin. The work presented in this chapter attempts to address the same issue by proposing a novel adaptive deloading scheme, where the deloading factor is calculated in runtime using an adaptation scheme. Further, in order to address the shortcomings of the quadratic deloading approach presented in [1], this work also uses a nonlinear interpolating method based on Newton's interpolation polynomial for calculating reference deloaded power, as proposed in the previous chapter for IPS. The overall performance of the system under study can be significantly improved with adaptive nonlinear deloading methodology by optimizing the effective available power margin.

Further, to implement a deloading policy, wind speed information is used for the calculation of turbine rotor speed in real time for its effective participation in the frequency regulation process from the wind power plant. However, real-time measurement of wind speed involves the dynamics of the sensing element in the control loop. The inclusion of such dynamics may cause unnecessary lag in the generation of the optimal control action, due to which turbine rotor speed can get significantly affected. This problem can be efficiently handled if one can predict the wind speed well in advance by utilizing forecasted wind speed information. Such wind speed predictions

are often used in modern control systems to compensate for delays. It may be observed that accurate wind speed and power generation forecasting approaches can assist power system operators in reducing the risk of the unreliability of energy supply. These forecasting approaches employ various approaches based on time-series statistical models, which include the autoregressive model [2], autoregressive moving average model (ARMA) [3], and autoregressive integrated moving average model (ARIMA) [4] for the prediction of renewable energy parameters. Researchers are presently adopting AI-based models for forecasting renewable energy sources quantities, i.e., wind speed and solar irradiance [5] Feed Forward Neural Networks (FFNN), Recurrent Neural Networks (RNN), Radial Basis Function Neural Networks (RBFNN), deep learning-based hybrid RNN long-term short-term network [6-9] are being explored by researchers in various domain.

Moreover, deep learning-based forecasting approaches are getting popularity in different domains, i.e., healthcare, manufacturing, agriculture, the stock market, electrical power system, and many more [10-12]. M.N. Akhter *et al.* suggested a deep learning approach for hourly solar system power output forecasting, and its prediction performance was found to be superior to a multilayer perceptron (MLP) and support vector machine (SVM) [13]. According to Chang *et al.* and Zhu *et al.*, long short-term memory (LSTM), an improved variant of RNN, has proven itself superior in processing time series data as well as nonlinear and challenging scenarios, such as electricity price prediction, can be a natural choice for parameter forecasting of renewable energy sources [14] [15]. The problem of vanishing and exploding gradients in recurrent neural networks during training can be significantly handeled by long short-term memory networks. Hence, deep learning-based RNN-LSTM has been employed in the current work for wind speed prediction to implement the proposed adaptive nonlinear deloading technique efficiently.

In this chapter, a novel deep learning-assisted adaptive nonlinear deloading (DL-AND) approach has been proposed for the effective participation of WTGs in long-term frequency support to the electrical grid. The supplementary control structure is essentially required, along with the proposed deloading strategy for efficient load frequency control. The presented study uses a fractional-order-based fuzzy logic intelligent supplementary controller (FFOPID) to handle any load change,

parametric uncertainty, and inherent uncertainties of the DFIG-based WTG and conventional thermal power unit. Furthermore, to achieve efficient LFC control performance of the system under consideration, the optimal controller parameters are essentially required. In the presented study, a metaheuristic optimization, i.e., salp swarm optimizer, has been employed to obtain optimal control parameters.

It needs to mention here that the system under investigation has been considered as described in the previous chapter. Extensive simulation experiments were performed with the proposed novel DL-AND in the presence of an FFOPID control structure, and a comparative analysis has been presented. The analysis compares frequency deviation in both control areas along with thermal and wind power variation for linear, quadratic constant deloading with the proposed novel DL-AND approach. Following are the key contributions of the presented investigation in this chapter:

- Design and implementation of an adaptive nonlinear deloading technique for WTGs integrated with IPS for effective frequency support.
- Implementation of deep learning based RNN-LSTM approach for wind speed forecasting to adaptive nonlinear deloading technique.
- Deep learning assisted adaptive nonlinear adaptive deloading (DL-AND) strategy in the presence of fractional-order fuzzy-based PID controller (FFOPID) for efficient LFC.

The rest of the chapter is structured as follows: In Section 6.2, the proposed novel adaptive nonlinear deloading approach has been presented in detail. Further, the deep learning-based RNN-LSTM technique has been presented for wind speed forecasting in Section 6.3. Section 6.4 includes the details of the fractional-order based fuzzy intelligent supplementary control structure (FFOPID) as well as optimal system and controller parameters with the salp swarm algorithm. In Section 6.5, extensive studies on considered IPS dynamic performance on the MATLAB/Simulink platform under various simulation scenarios (without forecasted wind speed, with forecasted wind speed and parametric variation) have been presented. Finally, section 6.6 presents concluding remarks and a summary of this chapter.

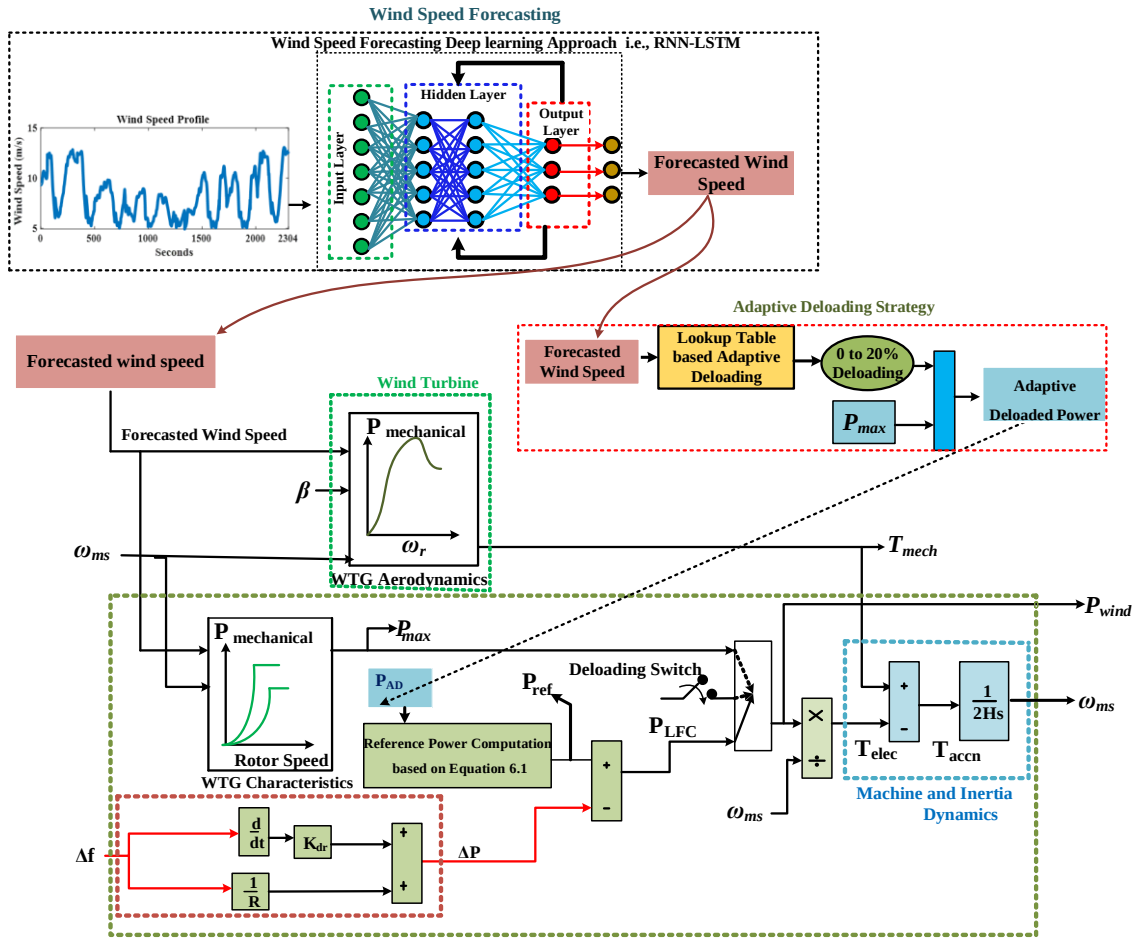

Fig. 6.1 *Schematic block diagram for implementation of Adaptive deloading operation of DFIG-based WTG*

6.2 Adaptive nonlinear deloading of WTG:

Deloading is the process in which variable speed WTGs are designed to run at lesser power than their maximum power capability for a given wind speed. This process allows a WTG to increase its reserve power capacity and offer active power support during IPS emergencies. Figure 6.1 shows the schematic diagram for executing the adaptive nonlinear deloading strategy in the explored IPS. In combination with Fig. 6.1 for effective LFC in the IPS under investigation, the schematic design portrays the exact arrangement for executing the adaptive nonlinear deloading technique of WTGs, including their dynamics. The linear, quadratic, and higher-order Newton's interpolating polynomial-based nonlinear deloading has been presented in the previous chapter. The frequency support from the wind turbine generators is improved with higher order Newton's interpolating polynomial-based deloading methodology with a constant factor. Here the details of linear, quadratic, and nonlinear deloading

methodologies have been omitted for the sake of brevity of the thesis, as they are already presented in the previous chapter in detail.

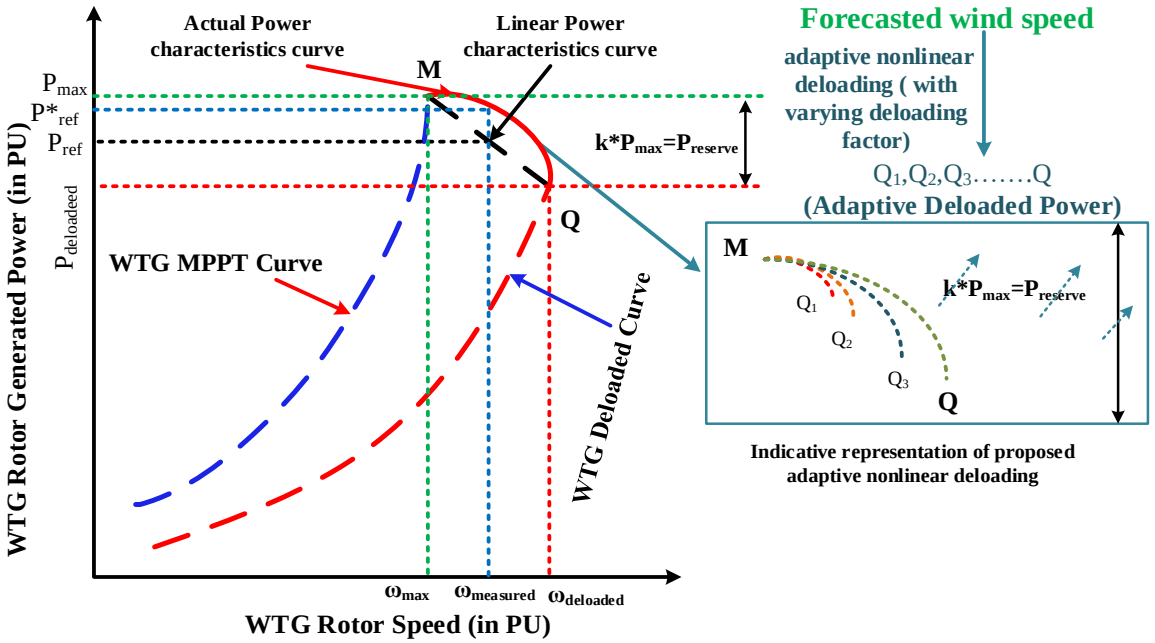

Fig. 6.2 *Wind turbine generator MPPT and deloaded characteristics different deloading scheme*

As WTGs have nonlinear power characteristics, a nonlinear relationship should be employed to correctly estimate the reference deloaded power during the WTG's derated operation, as presented in [1]. The straight-line trajectory for computing the reference deloading power (P_{ref}^{*}) has a smaller reserve power margin and limits deloaded WTG's capacity to involve in primary frequency control during power system outages. The nonlinear trajectory (with bold red line) for measuring reference deloaded power is shown in Fig. 6.2. The nonlinear trajectory used for assessing reference deloaded power (P_{ref}^{*}) has a bigger value than the linear trajectory used in the nonlinear deloading implementation for WTGs, as shown in Fig. 6.2.

Further, in this work, a nonlinear relation with a higher order Newton's interpolation approach has been used as in the previous chapter for the interconnected power system to calculate precisely the P_{ref}^{*} in the previous chapter, which improves the overall dynamic performance of the investigated system. It should be noted here that in the case of constant deloading (for linear and quadratic), the percentage of deloading with respect to maximum power point operation at a specific speed is fixed and, in the present study, considered as 10% (or 0.1 deloading factor). Such a constant

amount of deloading irrespective of wind condition can hamper the frequency support capability of the wind turbine, and efficacy of load frequency control of investigated two areas interconnected power system.

The maximum power point (P_{max}) and maximum power under deloading condition (P_{del}) are used as upper and lower boundary limits for reference deloaded active power (P_{ref}^{*}) calculations, which dynamically vary to participate in frequency regulation. To overcome the issues presented in linear and quadratic deloading with constant deloading factor, causing deterioration in investigated system performance, the current study utilizes an adaptive nonlinear deloading, i.e., varying between 0 to 20% from the maximum power point operation scenario.

From Fig. 6.2 (indicative representation of adaptive deloading), we can infer that adaptive nonlinear deloaded power from the wind turbine can vary according to forecasted wind speed. The deloaded wind power point can be M, Q_1, Q_2, Q_3, or Q (between 0 to 20% of 'P_{max}') depending upon the forecasted wind speed as percentage deloading is adaptive in nature and higher percentage deloading is considered for higher forecasted wind speed. The adaptation in the deloading percentage has been considered based on wind speed, as the captured power by a wind turbine system directly depends on the wind speed. Fig. 6.2 shows that with adaptive nonlinear deloading reserve power margin can be optimized according to wind speed. Also, points 'M' and 'Q' keep changing their position according to the wind speed and, thus, the magnitude of the reserve power margin. The reserve power margin optimizes in adaptive deloading scenarios and hence tends to improve the system's dynamic performance, whereas constant deloading causes an unoptimized reserve power margin.

Further, a lookup table system has been designed to decide the amount of deloading. The lookup table system has been utilized for adaptive deloading, having input as a wind speed in m/s and output as a deloaded factor (0 to 0.2). It needs to be mentioned here that, in the presented study, initially, the current work considers a measurement element (without forecasted wind speed) that provides the continuous wind speed to the wind turbine and converts the wind energy into electrical energy. The measurement block has its dynamics and causes deterioration in the intended operation of the wind power plant. Further, it is necessary to mention that in this study, the initially adaptive nonlinear deloading strategy has been implemented without

forecasting wind speed, i.e., wind speed obtained by considering the dynamics of the measurement block. Implementation of an adaptive nonlinear deloading strategy needs the actual wind speed in advance, which we can obtain through an efficient forecasting technique and presented in a subsequent subsection in detail.

6.3 Time series forecast using deep learning:

Although statistical time series models such as Autoregressive Integrated Moving Average (ARIMA) and Seasonal Autoregressive Integrated Moving Average (SARIMA) produce strong results in forecasting a variable, they are implemented with specific assumptions. These assumptions may collapse in real time when there are asymmetries in data points, unexpected outbreaks at irregular time intervals, and periods of low or high volatility. In such cases, the constant variance assumption in ARMA/SARIMA models may not be valid. Further, with a nonlinear characteristic and sophisticated input-output mapping feature, neural networks are chosen as a popular forecasting tool [16]. To anticipate the output power from renewable energy sources, advanced algorithms are needed in the current scenario. Deep neural network research has gained popularity in recent years. Deep learning networks are layers that learn how to represent data using abstraction layers. The article [17] is a collection of reviews on deep learning approaches. The efficacy of deep learning is studied by creating wind speed forecasting models in the presented work.

LSTM (long short-term memory) networks are used in the suggested technique. Recurrent Neural Networks (RNNs) using LSTM are a type of RNN. Backpropagation or recurrent learning is used to train a basic RNN. The LSTM-RNN compensates for the failure of the RNN model on vanishing/exploding gradient descent. The brief details of the LSTM-RNN network and its training procedure are presented in the subsequent subsection.

6.3.1 Long short-term memory (LSTM) network

The LSTM-RNN network has four main layers: sequence input layer, LSTM layer, fully connected layer, and regression output layer. In contrast to simple RNN, LSTM cells have a memory for each time step. The LSTM-RNN is trained so that with each iteration of the input time step, it gains the ability to predict the value of the upcoming time step. The sequence-to-sequence LSTM-RNN technique produces training sequences with values shifted by one-time steps.

The state of layer consists of the hidden state (also known as the output state) and the cell state. The information from previous time steps is saved in the cell state. At each time step, the layer adds or removes information from the cell state. The layer uses gates to control these changes. A memory cell, input gate, output gate, and forget gate are frequently seen in LSTM blocks, in addition to the hidden state of conventional RNNs.

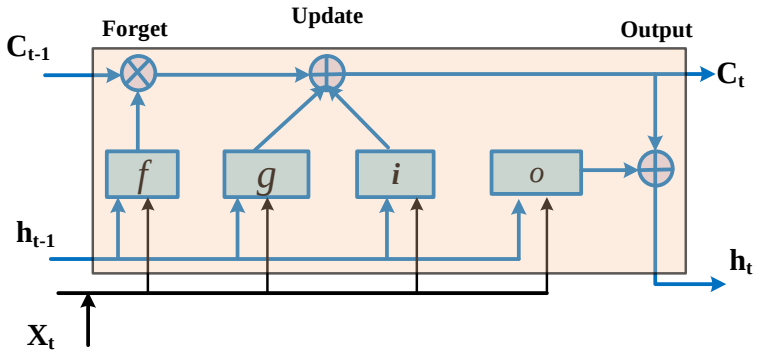

Fig. 6.3 *Schematic diagram of a long short-term memory*

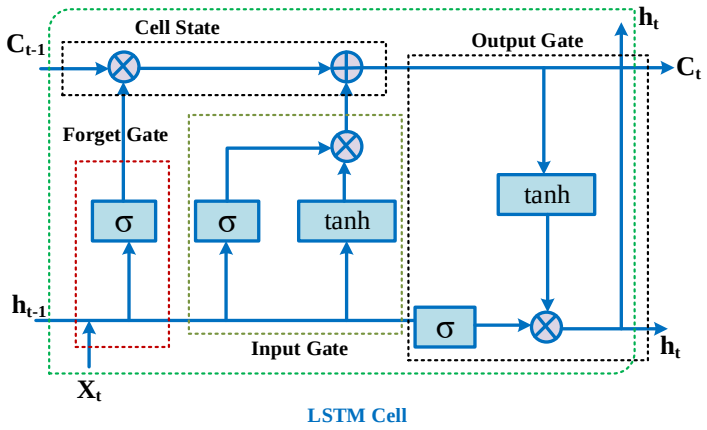

Fig. 6.4 *LSTM cell with activation functions* [5]

In the schematic block diagram of RNN-LSTM, 'h_t' and 'C_t' represent the output (hidden state) and cell state at time step 't', respectively, as represented in Fig. 6.3. The initial LSTM block uses the network's beginning state and the first-time step of the sequence to compute the first output and updated cell state. The LSTM block computes the output and the updated cell state 'C_t' at time step 't' using the previous state of the network (c_{t-1}, h_{t-1}) and the current 'X_t' of the sequence. An LSTM layer's learnable weights are W, R, and bias b. Each component's input weights, recurrent weights, and bias are concatenated into the W, R, and b matrices, respectively.

$$W = \begin{bmatrix} W_i \\ W_f \\ W_g \\ W_o \end{bmatrix}, \qquad R = \begin{bmatrix} R_i \\ R_f \\ R_g \\ R_o \end{bmatrix} \; and \; b = \begin{bmatrix} b_i \\ b_f \\ b_g \\ b_o \end{bmatrix}$$

Where the output gate, input gate, cell candidate, and forget gate are denoted by '*o*', *i*, *g*, and *f*, respectively. The equation represents the cell state at time step t.

$$c_t = f_t \odot c_{t-1} + i_t \odot g_t \tag{6.1}$$

The Hadamard product is denoted by $\odot$ (element-wise multiplication of vectors). Equation (6.1) gives the hidden state at time step 't'.

$$h_t = o_t \odot \sigma_c(c_t) \tag{6.2}$$

The state activation function is denoted by 'σ'. The formula for components (input gate, forget gate, cell candidate, output gate) at time step 't' is described by the equations (6.3) to (6.6).

$$i_t = \sigma_g(W_i X_t + R_i h_{t-1} + b_i) \tag{6.3}$$

$$f_t = \sigma_g(W_f X_t + R_f h_{t-1} + b_f) \tag{6.4}$$

$$g_t = \sigma_g(W_g X_t + R_g h_{t-1} + b_g) \tag{6.5}$$

$$o_t = \sigma_g(W_o X_t + R_o h_{t-1} + b_o) \tag{6.6}$$

The gate activation function is denoted by the letter σ_g in these computations. The gate activation function is computed using the sigmoid function, $\sigma(x) = \frac{1}{(1+ e^{-x})}$. The output state activation function is calculated using *tanh*(*x*) as illustrated in Fig. 6.4.

6.3.2 LSTM network training:

The entire data set is divided into training and test data sets. Starting with the initial data, the network is trained using 87.5% of the full data sets and tested with 12.5 % data present at the end. The backpropagation technique is used to train the weights W, R, and b. The training data series is first normalized to have zero mean and unity variance for better fitting and to prevent the training from diverging. The pseudo-code for training the LSTM network for time series forecasting is as follows.

Pseudo code for RNN-LSTM network training

1. Load the wind speed data set.

   Partition the training data **(**D_{train}**)** and test data **(**D_{test}**).**

2. Training data set standardization

Calculation of variance (σ) and mean (υ) for D_{train}.

Evaluate the standardized dataset D_{std}.

Input the forecasters (X_{train}) and reactions (Y_{train})

3. Define LSTM network architecture with hyper parameters

4. *for* n epochs and i^{th} iteration do

using the supplied training choices, train the network.,

end for

5. Future time steps forecast

using the same parameters as the training data (Eq. 6.10) standardize the test data (Eq. 6.11).

for i= 2: n (n = number of time steps in D_{test}).

state forecasting and update

end

Find the forecasts that aren't standardized using Eq. 6.12 and the standardized prediction using the parameters from step 2.

6. Compute the loss and validation functions

Eqs. 6.7-6.12 were utilized to process data as discussed in the pseudo code for LSTM. They are utilized for data set preparation, network training, prediction, and testing.

$$D_{std} = \frac{D_{train} - \upsilon}{\sigma} \tag{6.7}$$

$$X_{train} = D_{std}(1: end - 1) \tag{6.8}$$

$$Y_{train} = D_{std}(2: end) \tag{6.9}$$

$$D_{test_{std}} = \frac{D_{test} - \upsilon}{\sigma} \tag{6.10}$$

$$X_{train} = D_{test_{std}}(1: end - 1) \tag{6.11}$$

$$Y_{pred} = \sigma * Y_{pred}^{-} + \upsilon \tag{6.12}$$

The total amount of data points is 2304, representing wind speed at different times, as shown in Fig. 6.5. The MATLAB function 'predictAndUpdateState' is used to calculate the future values of many time steps. This works by predicting the values at each time step one by one and then updating the network state for each forecast. As a result, previous predictions are used as input to the function for each prediction step. In Fig. 6.6, the RMSE is determined, and the training data is shown against the projected

data without updating the states. We can infer from Fig. 6.6 that without updates in the state, the prediction and observed values have significant errors, as the root mean square error (RSME) is found to be 4.1683.

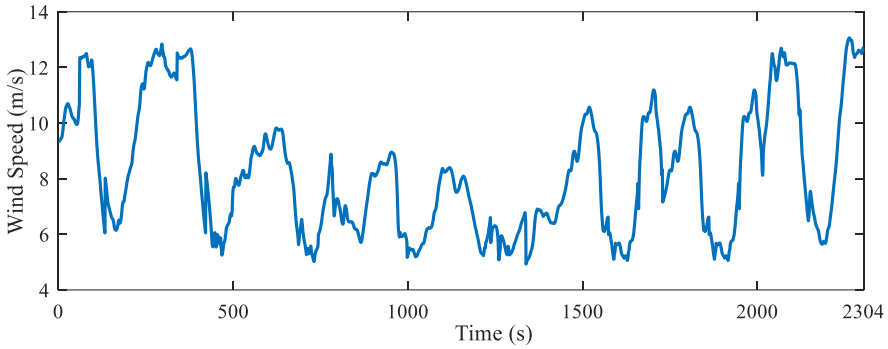

Fig. 6.5 *Wind speed profile*

The RSME get improved significantly by using 'predictAndUpdateState' strategy, which shows a close match between predicted and observed wind speed as represented in Fig. 6.7 and RSME was found to be exceptionally improved to 0.10158 in comparison to without updates the states. Further, the solver used for RNN-LSTM has been taken as 'adam'. The number of hidden units, maximum epochs, gradient threshold, initial learning rate, learn rate drop period, learn rate drop factor, and iteration per epoch are 300, 300, 1, 0.05, 50, 0.2, and 1, respectively.

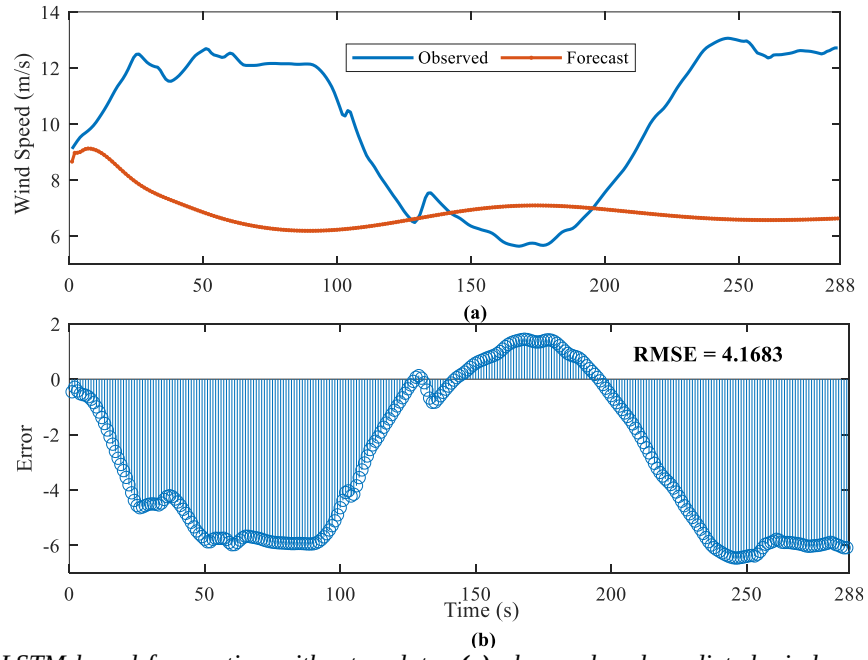

Fig. 6.6 *RNN-LSTM based forecasting without updates* ***(a)*** *observed and predicted wind speed* ***(b)*** *Root mean square error*

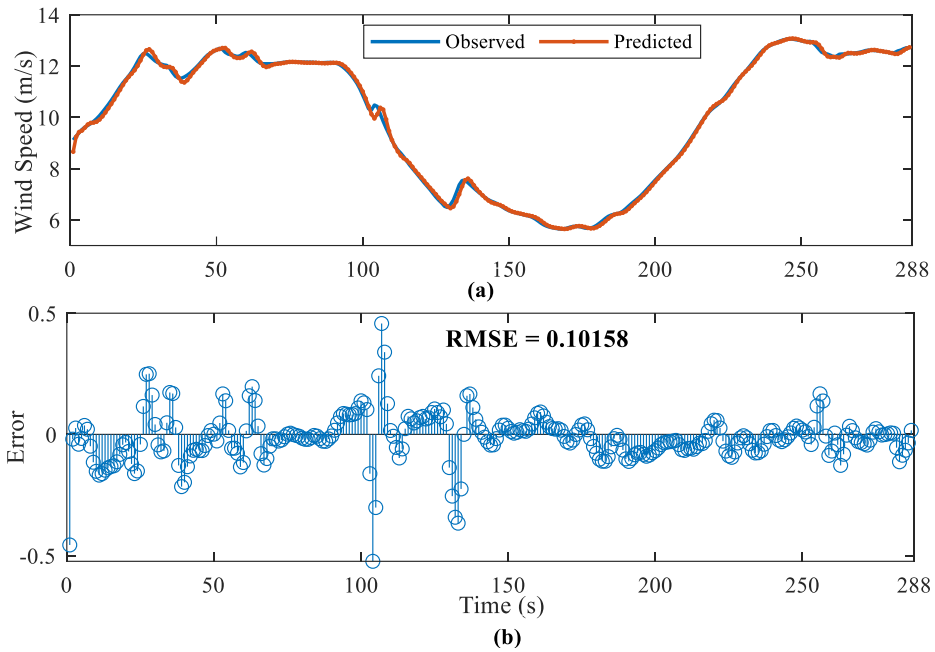

Fig. 6.7 *RNN-LSTM based forecasting with updates* ***(a)*** *observed and predicted wind speed* ***(b)*** *Root mean square error*

Further, Fig. 6.8(a) represents the comparative rotor speed without deloading, with constant deloading and adaptive deloading. The rotor speed increases with deloading as overspeeding deloading is preferred for long-term frequency. For adaptive deloading, the deloading factor is lesser in low wind speed, due to which rotor speed is less than constant deloading, whereas, for higher wind speed, the rotor wind speed is higher. In connection with the previous discussion, Fig. 6.8(b) represents the forecasted wind speed versus the adaptive deloading factor. It can be observed in Fig. 6.8(b) that with adaptive deloading factor keep on changing in accordance with wind speed, while for constant deloading is constant (10%) irrespective of wind speed. To improve the performance of adaptive nonlinear deloading methodology, in this study, a forecasted wind speed has been used for precisely implementing the adaptive nonlinear deloading strategy. Hence, as discussed above, the deep learning-assisted adaptive nonlinear deloading approach has been utilized for enhanced frequency support from the WTG. Further, to deal adequately with nonlinearity associated with WTG and adaptive nonlinear deloading, it is also necessary to use the appropriate supplementary control structure with the proposed novel deep learning-assisted adaptive nonlinear deloading (DL-AND) strategy for effective load frequency control. Hence, a fractional-order fuzzy PID (FFOPID) intelligent controller is used as a supplementary control structure

in the considered IPS. The next subsection contains the optimal controller parameters regarding the incorporated FFOPID control structure as a supplementary controller for effective LFC. It should be noted that the details of the controller have been omitted here as it has already been presented in the previous chapter.

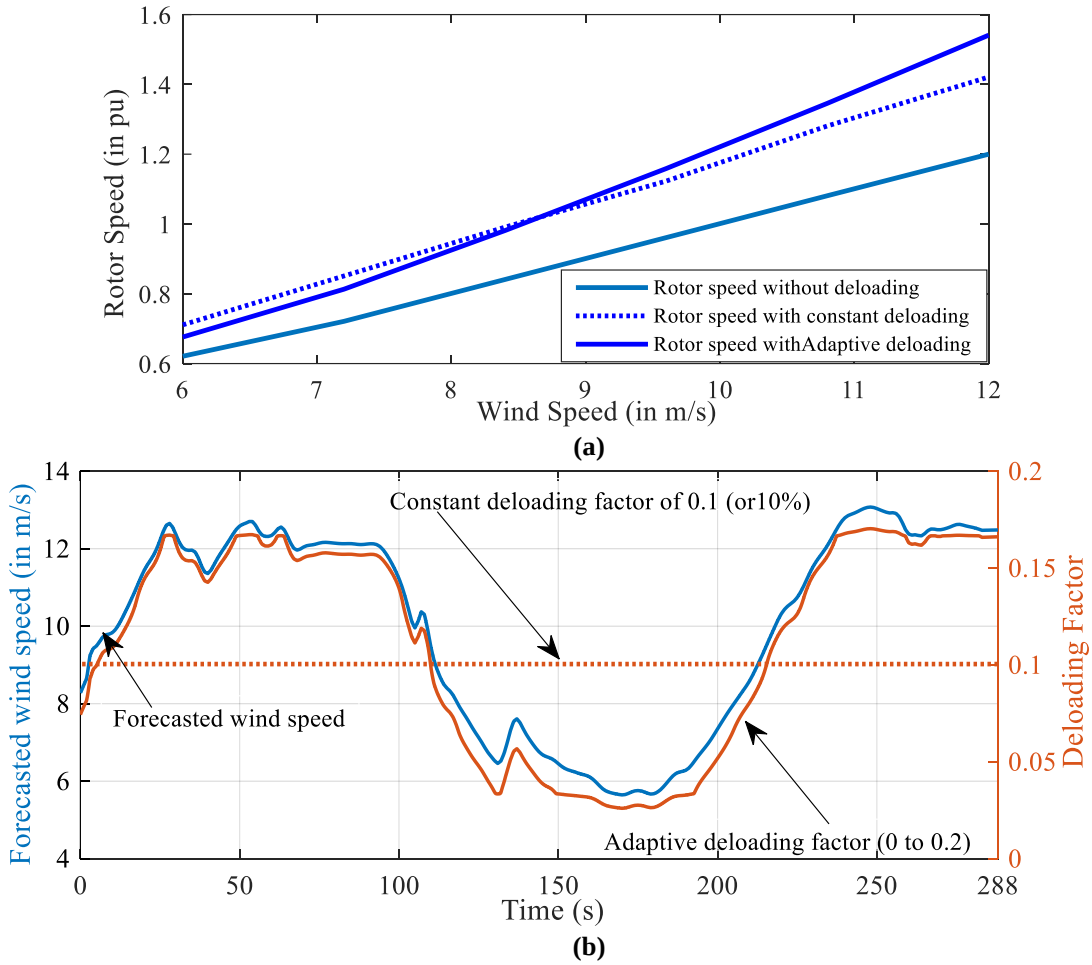

Fig. 6.8 ***(a)*** *Rotor speed with constant and adaptive deloading* ***(b)*** *Forecasted wind speed and adaptive deloading factor*

6.4 Optimal parameters tuning of LFC structure:

The current study utilizes the fuzzy controller, i.e., fractional-order fuzzy FOPID, as presented in the previous chapter, and the controller parameters have been obtained through SSA. The optimal controller parameters obtained by SSA for the nonlinear deloading approach have been utilized for the adaptive nonlinear deloading approach. During the optimization process, a random step load perturbation (RSLP) has been considered in control area-1 as shown in Fig. 6.9. The convergence curve for the optimization process has been presented in Fig. 6.10 for nonlinear deloading, adaptive

nonlinear deloading, and the proposed novel DL-AND methodology FFOPID controller.

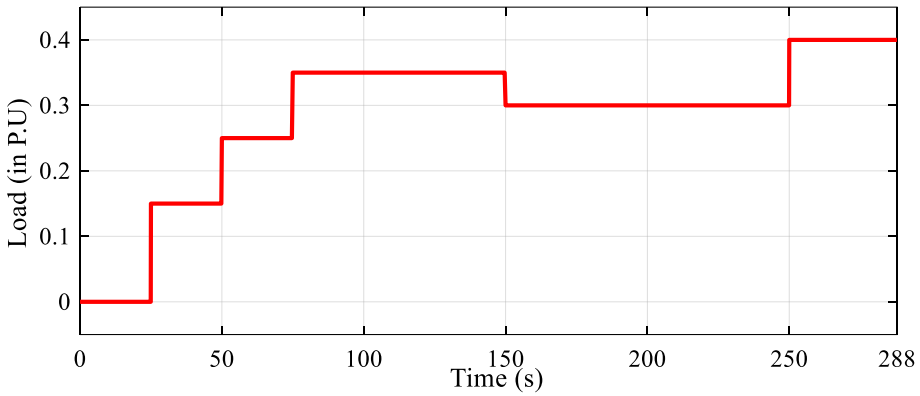

Fig. 6.9 *Random step load perturbation (RSLP) profile*

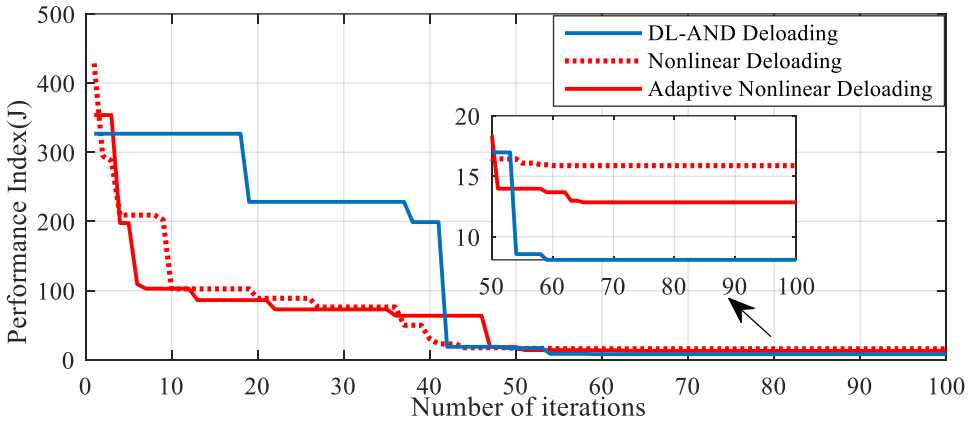

Fig. 6.10 *Comparative convergence curve for nonlinear deloading, adaptive nonlinear deloading and proposed novel DL-AND strategy with FFOPID controller*

Table 6.1 *Optimal controller parameters for Fractional-order Fuzzy PID (FFOPID) control structure along with J values*

Control Structure / Parameters	**Nonlinear deloading and Nonlinear adaptive deloading strategy**	**DL-AND Strategy**
$\mathbf{K_{e1}}$	12.2209	14.0021
$\mathbf{K_{r1}}$	0.1215	0.0612
$\mathbf{K_{e2}}$	14.1914	13.3614
$\mathbf{K_{r2}}$	1.1325	2.4327
$\mathbf{K_{PI1}}$	4.9664	10.0734
$\mathbf{K_{PD1}}$	16.4924	18.0602
$\mathbf{K_{PI2}}$	0.9264	1.6035
$\mathbf{K_{PD2}}$	0.2471	0.4580
$\mathbf{K_{fr}}$	0.2511	0.1452
$\boldsymbol{\lambda_1}$	1.3294	1.1373
$\boldsymbol{\lambda_2}$	0.3387	0.6013
$\boldsymbol{\mu_1}$	1.4395	1.4364
$\boldsymbol{\mu_2}$	1.9207	1.2276
J	**[15.88, 12.85]**	**8.099**

Further, optimal control parameters have been presented in Table 6.1. From the convergence curve and Table 6.1, it is evident that the proposed novel DL-AND approach with FFOPID controller performs far superior in terms of considered objective function value than the nonlinear and adaptive nonlinear deloading approach. The 'J' values for nonlinear deloading, adaptive nonlinear deloading, and the proposed DL-AND strategy are 15.88, 12.85, and 8.099, respectively, as represented in Table 6.1. Further, in order to validate the performance of the investigated control strategy with the proposed novel DL-AND approach, extensive simulation studies are carried out. On the basis of these simulation studies, an exhaustive comparative study is drawn, which is presented in detail in the subsequent section.

6.5 Simulation results and discussion:

In this work, the system under investigation has been considered a two-area IPS, as discussed in the previous chapter. Further, the control area-1 was subjected to a random step load perturbation (RSLP), as shown in Fig 6.10. To enhance the frequency support capability as compared with nonlinear deloading as presented in previous chapter, the present work utilizes an adaptive nonlinear deloading strategy. The system under examination has been simulated without forecasted wind speed, i.e., wind speed with measurement block (MBWS) scenario for nonlinear deloading and adaptive nonlinear deloading approach.

Forecasting techniques are used nowadays in power systems for their effective and economic operation. Hence to mitigate the deteriorating effects of measurement block on the performance of considered IPS, in this work, the deep learning-based RNN-LSTM forecasting technique has been utilized for wind speed forecasting. Hence in the present work, the novel deep learning-assisted adaptive nonlinear deloading (DL-AND) strategy has been implemented for investigated IPS, and its performance was found to be exceptionally superior to that of rest. It should be noted that a fractional-order fuzzy-based FOPID (FFOPID) control structure has been utilized in both control areas as a supplementary controller, and its optimal parameters were obtained through the salp swarm algorithm. Finally, the supplementary control structure has been evaluated against power system parametric variation (K_{PS}, $T_{PS,}$ and T_T) in a range of $\pm$25% from their nominal values, and results were found to be well within stability limits. The assessment of frequency support via the deloaded wind power plant of the

studied system through frequency regulation under nominal system parameters is presented in the next subsection.

6.5.1 Investigation with proposed DL-AND strategy:

Figure 6.11 represents the objective function 'J' for different applied deloading strategies. We can infer from Fig. 6.11 that the adaptive nonlinear deloading approach is superior to the nonlinear deloading approach, which uses a constant deloading of 10% (or 0.1 deloading factor). It should mention here that in adaptive nonlinear deloading, the deloading factor depends on the wind speed at the instant and varies in the range of 0-0.2. Further, in the above investigation, a measurement block has been considered which provides continuous wind speed to the wind turbine, which converts the wind energy into electrical energy. It can be noted that the measurement block has its dynamics and cause for deterioration in the wind power plant's intended operation. As we are utilizing an adaptive deloading strategy, we should have the actual wind speed in advance, which we can obtain through an efficient forecasting technique, i.e., as discussed previously in a detailed manner in section 6.3. Hence the proposed DL-AND strategy has been utilized to improve the performance of the investigated system with the FFOPID controller structure.

Fig. 6.11 *Objective function 'J' with nonlinear deloading, nonlinear adaptive deloading and DL-AND strategy under FFOPID control structure*

The adaptive nonlinear deloading strategy improves the IPS performance by 19.08% in comparison to the nonlinear deloading approach. In contrast, the proposed DL-AND technique improves the performance in terms of 'J' values by 48.99% and 36.97% than that of nonlinear and adaptive nonlinear deloading approaches, as represented in Fig. 6.11.

Fig. 6.12(a) and 6.12(b) represent the variation in frequency deviation in control areas 1 and 2, respectively. It is evident from Fig 6.10 that step load has been applied at 25, 50, 75, 150, and 250 seconds and their impact can be seen in the frequency, wind, and thermal power deviations. The deviation in frequency for control area -1 as shown

in Fig. 6.12(a) has been observed with the nonlinear deloading approach at 25 and 250 seconds as 0.07432 and 0.03941Hz, which has been improved with adaptive nonlinear deloading strategy as 0.06924 and 0.033277Hz. Further DL-AND deloading strategy has significantly improved the frequency support performance compared to nonlinear and adaptive nonlinear deloading approaches, and frequency deviation was found to be 0.053847 Hz and 0.01811 Hz at 25 and 250 seconds. Similar trends can be seen in Figs 6.12(b) and 6.14(c) for variation in the frequency of control area-2 and tie-line deviation, which shows the effectiveness of the DL-AND strategy.

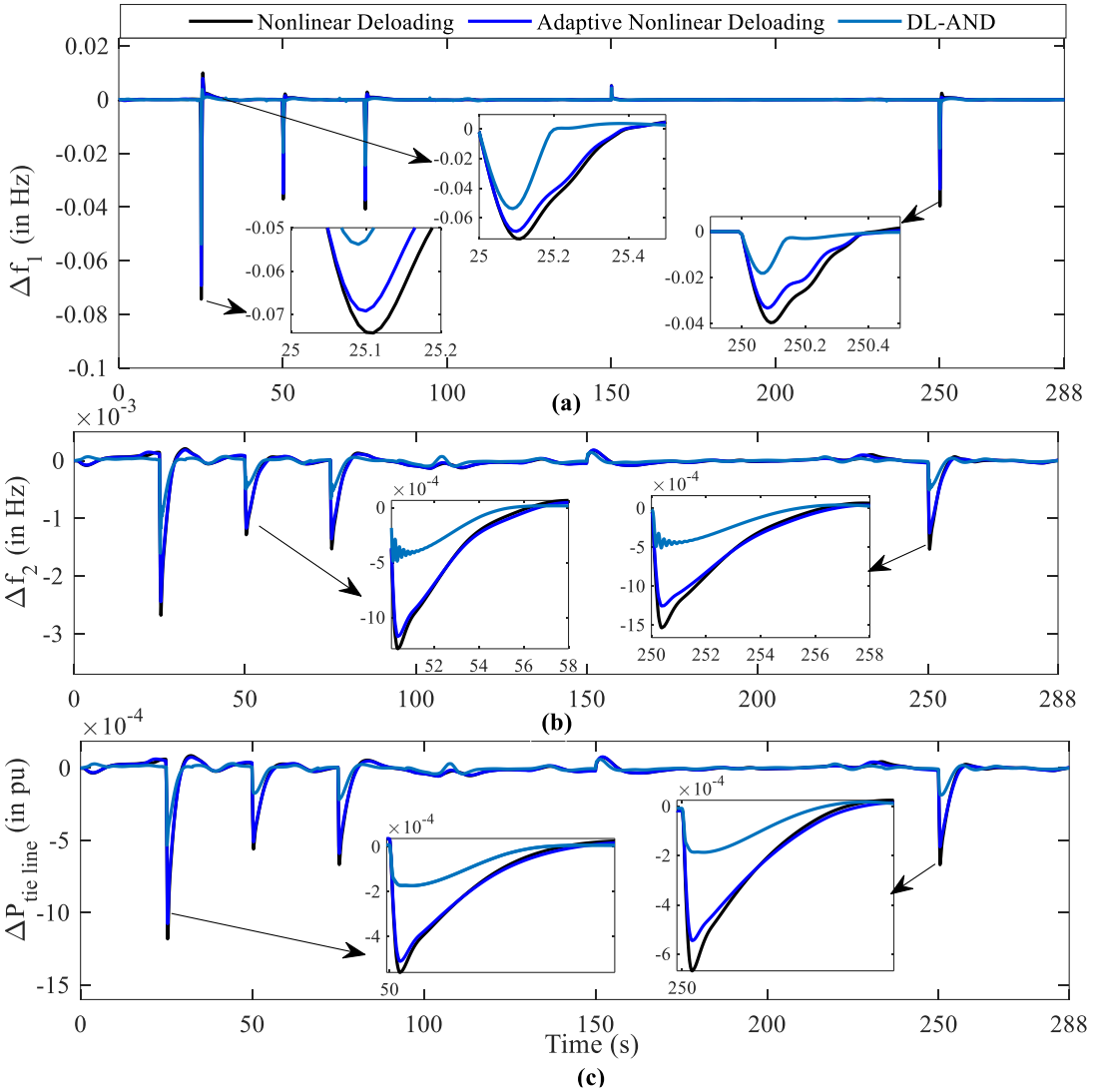

Fig. 6.12 *Variation in* **(a)** *frequency deviation control area-1* **(b)** *frequency deviation control area-2* **(c)** *tie-line power deviation*

Figure 6.13 represents the variation in wind and thermal power in the presence of RSLP with all three deloading approaches. It can be inferred that change in wind power

at 25, 75, and 250 seconds is highest for the DL-AND technique than that of others. The change in power of WTG with nonlinear deloading approach at 25, 75, and 250s instances are 0.00416 pu, 0.0104 pu, and 0.01283 pu, whereas with adaptive nonlinear deloading values are 0.0079 pu, 0.01436 pu, and 0.02634 pu. Further, DL-AND deloading approach shows the same as 0.0275 pu, 0.0329 pu, and 0.0473 pu. Which shows significant improvement in frequency support with the proposed deloading methodology.

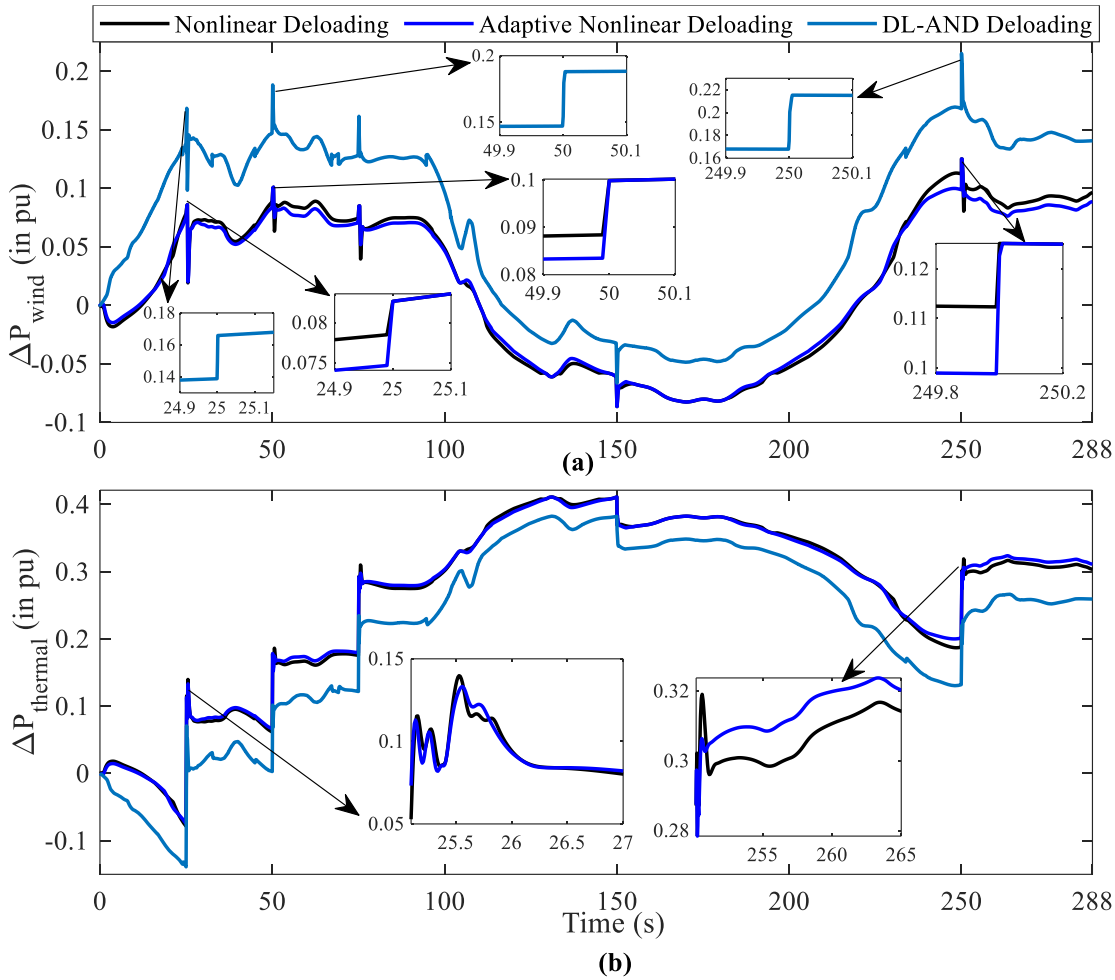

Fig. 6.13 *Variation in* **(a)** *wind power deviation* **(b)** *thermal power deviation of investigated IPS using different deloading strategies in control area-1*

It can be inferred from the results that the DL-AND strategy performs superior in terms of objective function, frequency, and tie-line power deviation. The variation in frequency and wind power was found to be the least and most, respectively for the proposed approach, which indicates effective participation in the frequency regulation process compared to nonlinear and adaptive nonlinear approaches.

The proposed novel DL-AND strategy has performed exceptionally well compared to previously existing deloading methodologies for frequency support from the wind power plant. In the subsequent subsection, the efficacy of the proposed novel DL-AND strategy under the FFOPID control structure as a supplementary controller has been evaluated through power system parametric variation.

6.5.2 Investigation under parametric variation:

It is necessary to evaluate the efficacy of the proposed novel DL-AND strategy in the presence of FFOPID, i.e., supplementary control structure for investigated IPS under a parametric uncertainty scenario. In this work, the variation has been performed in power system parameters, i.e., power system gain (K_{PS}) and time constant (T_{PS}) up to $\pm$25% from the nominal system condition.

Figures 6.14 and 6.15 show the variation in objective function with variation in power system gain (K_{PS}) and power system time constant (T_{PS}), respectively. It can be inferred from these Figs that with the increase in $K_{PS,}$ system performance deteriorates, and with a decrease in $K_{PS,}$ system performance enhances. Whereas an increase in T_{PS} system performance enhances and a decrease in T_{PS} system performance deteriorates.

Further, it can be inferred from Figs 6.14-6.17 that deviations in objective function have been found maximum with the nonlinear deloading approach and minimum with the proposed novel DL-AND strategy. The objective function has a change in its value of 23.61%, 21.16%, and 12.79% for nonlinear, adaptive nonlinear deloading strategy and with proposed novel DL-AND strategy, respectively, for parametric variation in power system gain. While parametric variation in the power system time constant has a change of 29.65%, 27.23%, and 17.73%, respectively. Hence the proposed novel DL-AND strategy has significantly less sensitivity than others with power system parametric variation. Further, it can be noted here that the deviation for a 25% increment in turbine time constant causes 10.83%, 8.79 %, and 7.55%, respectively, for nonlinear deloading, adaptive nonlinear deloading strategy and with proposed novel DL-AND strategy, respectively.

Moreover, the robustness is highest for the proposed novel DL-AND strategy compared with others. In connection with this, the most critical condition has been presented, i.e., an increase in K_{PS} and a decrease in T_{PS} for evaluating system

performance with the proposed novel DL-AND strategy under FFOPID supplementary control structure in Fig. 6.17.

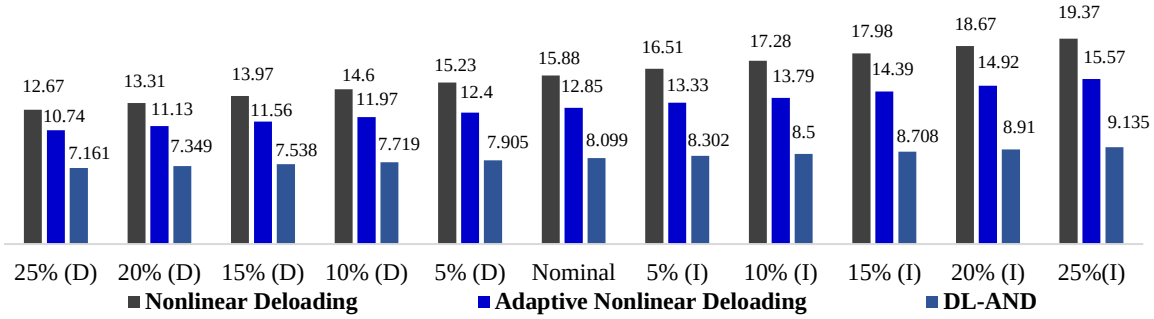

Fig. 6.14 *Variation in objective function (J) with variation in K_{PS} from -25% to 25% in steps of 5%*

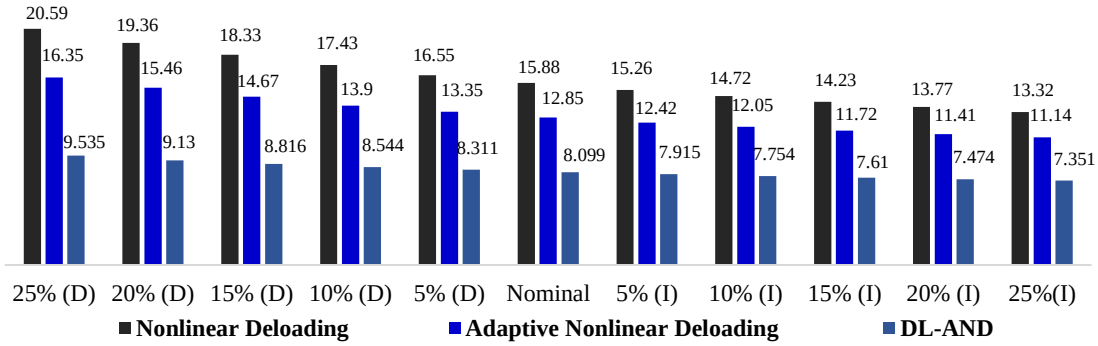

Fig 6.15 *Variation in objective function (J) with variation in T_{PS} from -25% to 25% in steps of 5%*

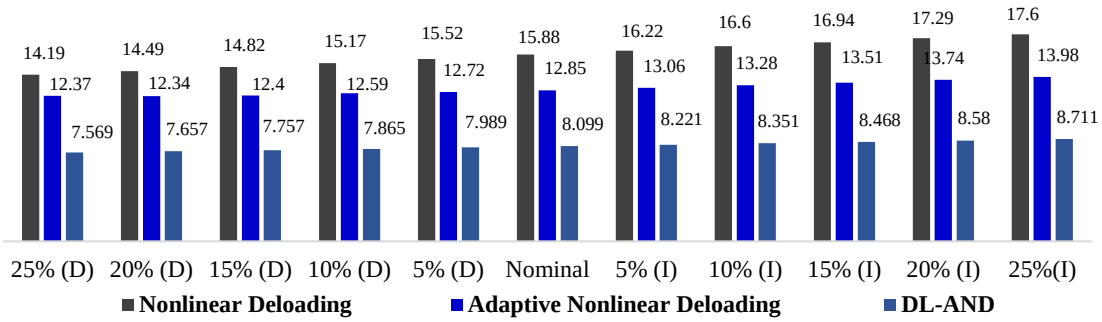

Fig. 6.16 *Variation in objective function (J) with variation in T_T from -25% to 25% in steps of 5%*

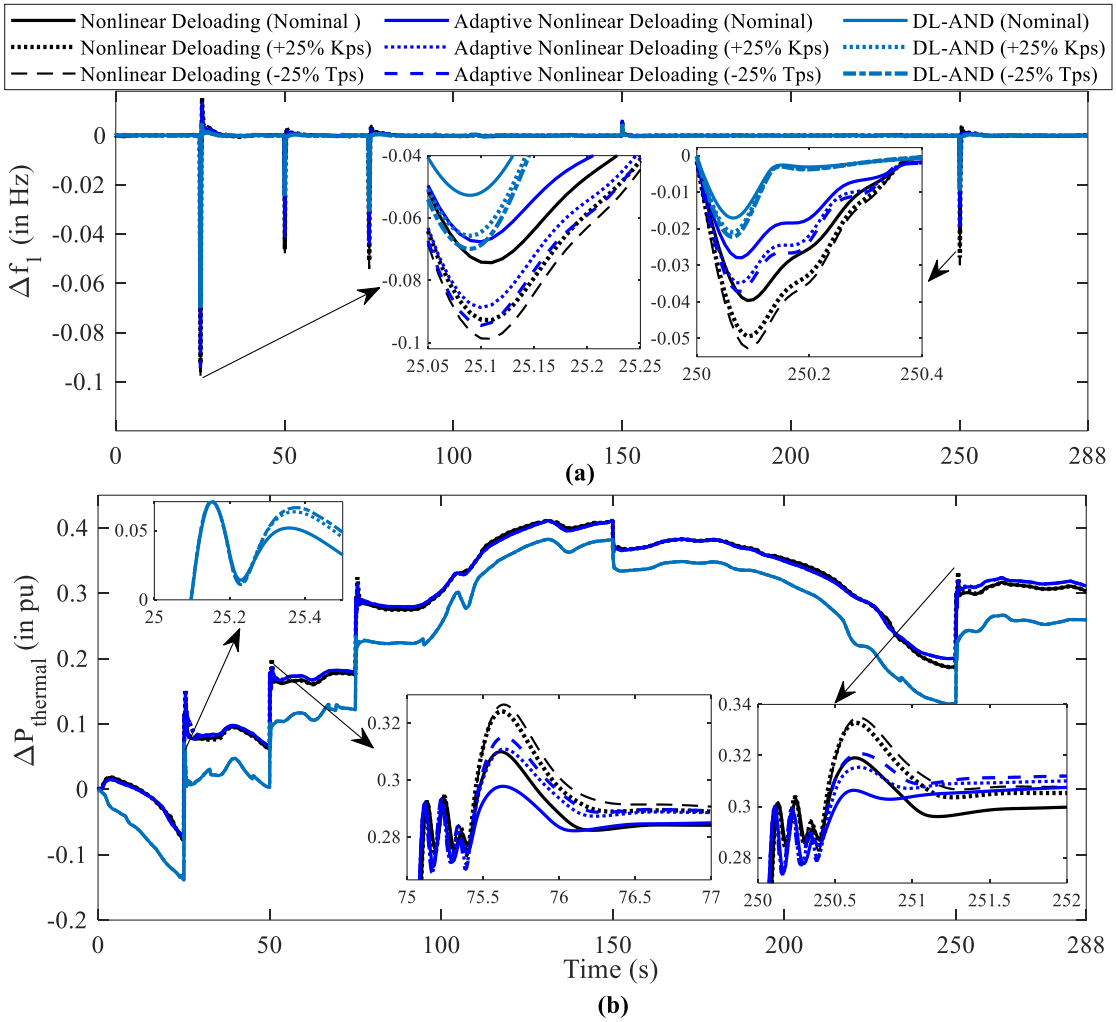

Fig. 6.17 *Variation in* **(a)** *frequency deviation* **(b)** *thermal power deviation of investigated IPS with a variation of power system parameters in control area-1*

Figure 6.17(a) shows the variation in frequency deviation with nominal system parameters, a 25% increase in $K_{PS,}$ and a 25% decrease in T_{PS}. The maximum frequency deviation with the proposed DL-AND strategy is 0.05271, 0.06567, and 0.06984Hz for nominal, 25% increase in K_{PS} and a 25% decrease in $T_{PS,}$ respectively, at 25 seconds, which was found to be the least among all three deloading strategies employed. The frequency nadir has been improved with the proposed DL-AND strategy by 22.87%, 25.97%, and 26.06%, respectively, compared with adaptive nonlinear deloading. The inference can be drawn from these results that a decrease in the power system time constant has a more severe impact on system performance than an increase in power system gain. The variation in thermal power in control area-1 was found to be the least, as presented in Fig. 6.17(b) for the proposed novel DL-AND strategy. It needs to be

mentioned that other responses have been omitted for the sake of clarity and brevity of the chapter, where all are presented in the bar graph for reference in Figs. 6.14-6.16.

6.5.3 Validation of the proposed scheme on a real-time digital simulation platform

The proposed DL-AND strategy with FFOPID control structure as load frequency controller performance has been validated through the OPAL-RT 4510. The details of the implementation of real-time digital simulation have been omitted here and can be found in chapter 3 in detail. For the chapter's brevity, the test case for the novel DL-AND in the presence of FFOPID as a supplementary control structure with forecasted wind speed under nominal system parameters has been presented. Figure 6.18(a), (b), and (c) presents the variation in frequency deviation, wind power deviation, and thermal power deviation, respectively, in control area-1, with the proposed deloading technique on OPAL-RT platform, which matches the MATLAB simulation results. Further, it has been observed that the outcomes on the OPAL-RT 4510 platforms are perfectly congruent. This demonstrated unequivocally that the proposed scheme could be applied to real-world situations and that computations could be easily performed without running afoul of any time-sensitive constraints.

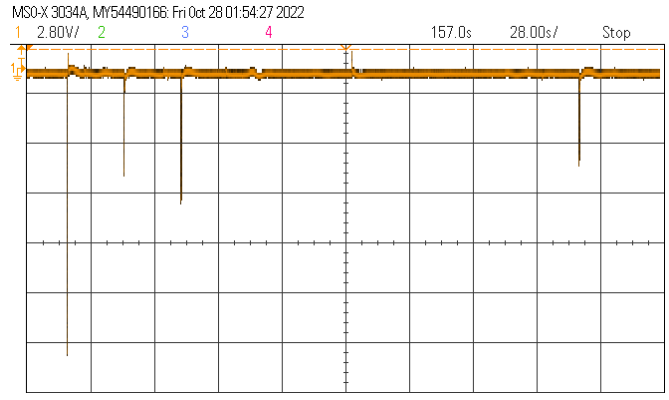

(a)

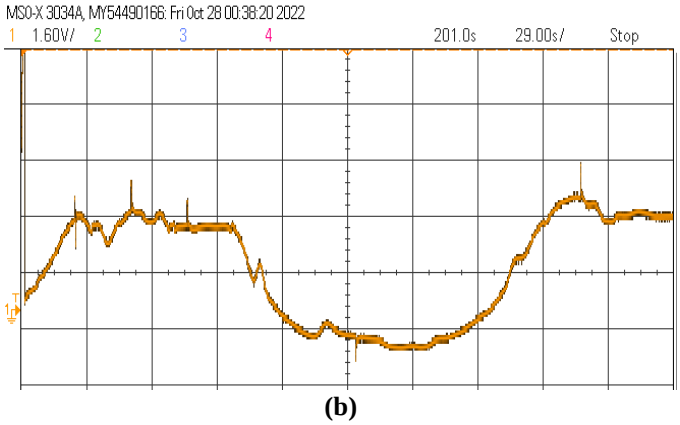

(b)

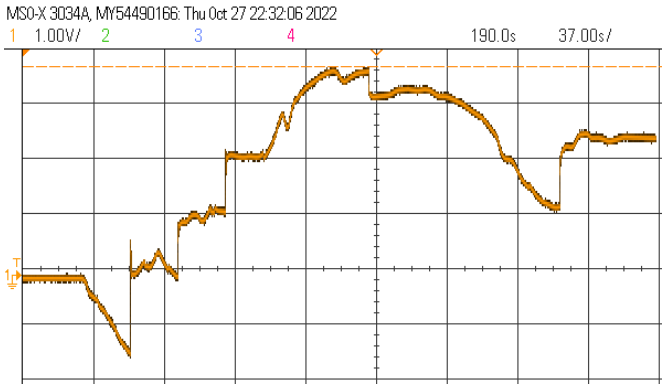

(c)

Fig. 6.18 *Performance of proposed novel DL-AND with forecasted wind speed in the presence of FFOPID for control area-1* ***(a)*** *Variation in frequency deviation [Scale: 2.8V/div with probe cable gain of 10]* ***(b)*** *Variation in wind power deviation [Scale: 1.6V/div with probe cable gain of 10]* ***(c)*** *Variation in thermal power deviation [Scale: 1V/div with probe cable gain of 10]*

6.6 Summary

The two-area interconnected power system with wind power plant (IPS-WPP) in control area-1 has been investigated in this study. The integration of doubly field induction generator-based WPP does not participate in frequency regulation inherently and can be achieved by a deloading strategy. To address the nonlinear properties of WTG and enhance the frequency support capability of linear and quadratic constant deloading techniques, the present work proposes an adaptive nonlinear deloading strategy. The reserve power margin can be optimized with adaptation in deloading amount, and the study utilizes wind speed for adaptation purposes. The real-time wind speed measurement causes deterioration of investigated system load frequency control performance due to the inclusion of measurement device dynamics. The proposed work focuses on the need for wind forecasting techniques to implement the adaptive nonlinear deloading strategy effectively.

Further, the deep learning-based hybrid forecasting approach, i.e., recurrent neural network combined with long-term short term (RNN-LSTM), has been employed for wind speed forecasting. The problem of vanishing/exploding gradient, which can arise with RNN forecasting, is not present with RNN-LSTM forecasting. An intelligent nonlinear fractional-order fuzzy logic-based supplementary control structure (FFOPID) has been adopted for all deloading strategies. To demonstrate the efficiency of the proposed deep learning-assisted adaptive nonlinear deloading (DL-AND) strategy in presence of FFOPID control structure as supplementary controller, the investigated IPS

performance was evaluated under random step load perturbation with nominal system parameters. The adaptive deloading without wind speed forecasting enhanced the objective function by 19.08% that of nonlinear deloading presented in the previous chapter. Moreover, when the novel DL-AND approach is compared with adaptive deloading without wind speed forecasting, the objective function improves by 36.97%.

Further, the current study includes a ±25% parametric alteration and the related effect on system performance to evaluate the efficiency of the proposed novel DL-AND approach. The results of parametric variation demonstrate that the devised approach is resilient, with the least variance in objective function when compared to the others. The proposed deloading strategy for effective frequency support from WTG in investigated two-area interconnected IPS has been validated on the OPAL-RT 4510.

References:

[1] D. Kumar, P. Sharma, H. D. Mathur, S. Bhanot, and R. C. Bansal, "Modified Deloading Strategy of Wind Turbine Generators for Primary Frequency Regulation in Micro-Grid," Technol. Econ. Smart Grids Sustain. Energy, vol. 5, no. 1, 2020, doi: 10.1007/s40866-020-00083-7.

[2] U. Firat, S. N. Engin, M. Saraclar, and A. B. Ertuzun, "Wind speed forecasting based on second order blind identification and autoregressive model," in 2010 Ninth International Conference on Machine Learning and Applications, 2010, pp. 686–691.

[3] E. Erdem and J. Shi, "ARMA based approaches for forecasting the tuple of wind speed and direction," Appl. Energy, vol. 88, pp. 1405–1414, 2011.

[4] J. C. Palomares-Salas, J. J. G. De La Rosa, J. G. Ramiro, J. Melgar, A. Aguera, and A. Moreno, "ARIMA vs. Neural networks for wind speed forecasting," in 2009 IEEE International Conference on Computational Intelligence for Measurement Systems and Applications, 2009, pp. 129–133.

[5] D. Kumar, H. D. Mathur, S. Bhanot, and R. C. Bansal, "Frequency regulation in islanded microgrid considering stochastic model of wind and PV," Int. Trans. Electr. Energy Syst., vol. 29, no. 9, p. e12049, 2019.

[6] G. Kumar and H. Malik, "Generalized regression neural network based wind speed prediction model for western region of India," Procedia Comput. Sci., vol. 93, pp. 26–32, 2016.

[7] H. Acikgoz, C. Yildiz, and M. Sekkeli, "An extreme learning machine based very short-term wind power forecasting method for complex terrain," Energy Sources, Part A Recover. Util. Environ. Eff., vol. 42, no. 22, pp. 2715–2730, 2020.

[8] Shivani, K. S. Sandhu, and A. R. Nair, "A Comparative Study of ARIMA and RNN for Short Term Wind Speed Forecasting," in 2019 10th International Conference on Computing, Communication and Networking Technologies (ICCCNT), 2019, pp. 1–7, doi: 10.1109/ICCCNT45670.2019.8944466.

[9] M. Elsaraiti and A. Merabet, "Application of Long-Short-Term-Memory Recurrent Neural Networks to Forecast Wind Speed," Applied Sciences, vol. 11, no. 5. 2021, doi: 10.3390/app11052387.

[10] A. Kamilaris and F. X. Prenafeta-Boldú, "Deep learning in agriculture: A survey," Comput. Electron. Agric., vol. 147, pp. 70–90, 2018, doi: https://doi.org/10.1016/j.compag.2018.02.016.

[11] C. Shorten, T. M. Khoshgoftaar, and B. Furht, "Deep Learning applications for COVID-19," J. Big Data, vol. 8, no. 1, p. 18, 2021, doi: 10.1186/s40537-020-00392-9.

[12] A. Esteva *et al.*, "A guide to deep learning in healthcare," Nat. Med., vol. 25, no. 1, pp. 24–29, 2019, doi: 10.1038/s41591-018-0316-z.

[13] M. N. Akhter *et al.*, "A hybrid deep learning method for an hour ahead power output forecasting of three different photovoltaic systems," Appl. Energy, vol. 307, p. 118185, 2022, doi: https://doi.org/10.1016/j.apenergy.2021.118185.

[14] Z. Chang, Y. Zhang, and W. Chen, "Electricity price prediction based on hybrid model of adam optimized LSTM neural network and wavelet transform," Energy, vol. 187, p. 115804, 2019, doi: https://doi.org/10.1016/j.energy.2019.07.134.

[15] Y. Zhu, R. Dai, G. Liu, Z. Wang, and S. Lu, "Power Market Price Forecasting via Deep Learning," in IECON 2018 - 44th Annual Conference of the IEEE Industrial Electronics Society, 2018, pp. 4935–4939, doi: 10.1109/IECON.2018.8591581.

[16] F. Gokgoz and F. Filiz, "Electricity price forecasting in Turkey with artificial neural network models," Invest. Manag. Financ. Innov., vol. 13, no. 3 (contin. 1), pp. 150–158, 2016.

[17] Y. LeCun, Y. Bengio, and G. Hinton, "Deep learning," *Nature*, vol. 521, pp. 436–444, 2015.

Chapter 7: Closure

The research work carried out in this thesis focuses on the design and implementation of a fuzzy-based intelligent load frequency control structure for the interconnected power system. Global energy requirements are increasing exponentially, and conventional sources of electrical energy generation are depleting very fast. Also, conventional energy sources are responsible for increasing global warming due to significant carbon emissions. Hence, renewable energy-based sources, i.e., wind and solar, are integrated with the existing power system. The wind power plant normally does not participate in the frequency regulation process due to decoupling from the grid in the presence of grid and rotor side converters.

Moreover, such operation of renewable energy sources effectively decreases the inertia of power system and make them vulnerable to any power system contingency events. The present research work focuses on the challenges of integrating wind power plants with the existing grid. The main contribution of the present work is a fuzzy-based intelligent load frequency controller and frequency support strategies with the wind power plant.

7.1 Conclusion:

This thesis presents the enhanced load frequency control approaches for an interconnected power system with conventional and renewable energy sources. The fuzzy-based intelligent control structure as a load frequency controller has been utilized for effective load frequency control to deal with inherent nonlinearities, uncertainties, and unmodeled system dynamics. Further, the redox flow battery as an energy storage unit has been used for improving the load frequency controller performance. As, the integration of DFIG-based wind power plants with the existing grid is an increasing trend to meet the ever-increasing power demand. However, due to such integration, overall power system inertia has been significantly reduced and hence the power system stability. Further, to deal with this issue, the thesis proposes inertial and nonlinear deloading methodologies with efficient load frequency control structures for providing frequency support from DFIG-based WPP to the integrating grid. The proposed inertial and nonlinear deloading methodologies provide frequency support from the WPP during power system contingency events and hence improve the frequency regulation

and reliability of the investigated system. Moreover, the efficacy of the proposed load frequency control structure has been validated through the OPAL-RT digital simulator. The key finding of the presented work in thesis has been presented as follows:

- The performance of investigated three-area restructured interconnected power system with utilized self-tuned fractional order fuzzy PID (STFOFPID) control structure as load frequency controller improves by 67.42%, 19.28%, and 24.22% for Poolco, a bilateral and contract-violation transaction in comparison of FOPID. Further, incorporating redox flow battery (RFB) with STFOFPID control structure enhances the performance by 59.01%, 30.3%, and 17.78% for Poolco, bilateral and contract-violation transactions than that of without RFB. Further, the load frequency controller's performance has also been validated through OPAL-RT 4510, a real-time digital simulator.
- Inertial control strategy implementation in a two-area interconnected power system integrated with DFIG-based WPP for efficient load frequency control. The objective function (*J*) value obtained without the frequency support is 3.076, degraded by 50.56% in the presence of WPP under nominal system parameters. After implementing the inertial frequency support, the *'J'* value is 1.47, which improved by 52.21% compared to the without-frequency support mechanism.
- The Higher order Newton's interpolation polynomial (HNIP) based nonlinear deloading strategy for long-term frequency support has been designed for WPP and implemented in interconnected power systems. The performance has been improved with the proposed deloading compared to existing linear and quadratic deloading approaches. The objective function improves by 29.77% and 12.97% compared to linear and quadratic deloading approaches, respectively, showing the superiority of the proposed deloading approach.
- Further, a nonlinear adaptive deloading strategy for long-term frequency support for the WPP has been designed and implemented in an interconnected power system. The deep learning technique, i.e., RNN-LSTM, has been used for wind speed forecasting. The adaptive deloading without wind speed forecasting improves the objective function by 19.08% as compared with the nonlinear deloading approach. Further, an improvement of 36.97% has been

observed with the proposed deep learning-assisted adaptive nonlinear deloading approach compared to adaptive nonlinear deloading without wind speed forecasting.

7.2 Future Scope:

This thesis establishes a new direction for research frequency support from renewable energy sources integrated with existing interconnected power systems. The various investigations and associated findings presented in this thesis provide future research direction in electrical power systems, which can be summarized as follows:

- ✓ Electricity generation must be shifted from conventional methods to renewable energy-based resources to mitigate climate change issues and deplete conventional energy resources. The current electricity generation is about 25% from renewable energy resources, which tends to increase significantly in upcoming years. Most renewable energy resources are intermittent and pose very less inertia or do not pose any inertia. Hence the load frequency control problem tends to be more complex with decreasing conventional energy units and increased uncertainty in the load and generation (renewable). Hence, different frequency support schemes must be developed for those renewable energy sources which inherently do not participate in frequency regulation before integrating them with the existing grid.
- ✓ The proposed deep learning assisted adaptive nonlinear deloading methodology uses RNN-LSTM for wind speed forecasting. This forecasting approach has minute prediction errors, which can still cause deterioration in the frequency support. The energy storage unit can be used for handling forecasting errors.
- ✓ The pitch angle control of wind turbines can be performed along with a deloading strategy for efficient frequency support.
- ✓ The frequency support strategies can be designed and implemented for other renewable energy sources, i.e., solar energy-based power plants.
- ✓ Further, the deregulated and multi-area power system can be explored for frequency support strategies.

List of Publications

Journal Publications:

The following works included in this thesis have been published/ communicated in the following journals:

1. A. K. Mishra, P. Mishra, and H.D. Mathur, "Enhancing the performance of a deregulated nonlinear integrated power system utilizing a redox flow battery with a self-tuning fractional-order fuzzy controller," ISA Transactions, vol. 121, 2022, pp. 284-305. (SCIE Journal, Publisher- Elsevier, Impact factor: 5.911, DOI: 10.1016/j.isatra.2021.04.002)
2. A. K. Mishra, P. Mishra, and H.D. Mathur, "Design of a dual-layered tilt fuzzy control structure for interconnected power system integrated with DFIG," International Transactions on Electrical Energy Systems, vol. 31, no. 9, 2021, pp. 1–24. (SCIE Journal, Publisher- Wiley, Impact factor: 2.693, DOI:10.1002/2050-7038.13015)
3. A. K. Mishra, P. Mishra, and H. D. Mathur, "A deep learning assisted adaptive nonlinear deloading strategy for wind turbine generator integrated with an interconnected power system for enhanced load frequency control," Electric Power System Research, vol. 214, p. 108960, 2023. (SCIE Journal, Publisher- Elsevier, Impact factor: 3.818, DOI: 10.1016/j.epsr.2022.108960)
4. A. K. Mishra, P. Mishra, and H.D. Mathur, "A Novel Nonlinear Deloading Approach for a Wind Turbine Generator in an Islanded Microgrid utilizing an Intelligent Supplementary Controller," *ISA Transactions (Status - under review after second revision).*

Book Chapter Publications:

The following works included in this thesis have been published in the following book chapters:

1. A. K. Mishra, P. Mishra and H.D. Mathur, "Fractional Order Load Frequency control of a Two-Area Interconnected Power System with Uncertain Actuator

Nonlinearities," Lecture Notes in Networks and Systems, vol. 192, pp. 211-222, Springer, Singapore, 2021.

2. A. K. Mishra, P. Mishra and H.D. Mathur, "Robust Non-integer Control of a Nonlinear Two-Area Interconnected Power System Subjected to Large Parametric Variations," Lecture Notes in Networks and Systems, vol. 192, pp. 223-234, Springer, Singapore, 2021.

Conferences Publications:

The following works included in this thesis have been presented in the following conferences:

1. A. K. Mishra and P. Mishra, "Improved Fractional Order Control of a Nonlinear Interconnected Power System using Salp Swarm Algorithm," 2019 IEEE 16th India Council International Conference (INDICON), 2019, pp. 1-4, doi: 10.1109/INDICON47234.2019.9029023.

2. A. K. Mishra and P. Mishra, "Analysis of a Nested Control Configuration for a Nonlinear Interconnected Power System," TENCON 2019 - 2019 IEEE Region 10 Conference (TENCON), 2019, pp. 2123-2128, doi: 10.1109/TENCON.2019.8929375.

3. A. K. Mishra, P. Mishra, and H. D. Mathur, "Load Frequency Control of a Nonlinear Power System via Demand Response Control Strategy Based Fractional Order Fuzzy Controller," 2020 21st National Power Systems Conference (NPSC), 2020, pp. 1-6, doi: 10.1109/NPSC49263.2020.9331919.

4. A. K. Mishra, P. Sharma, H. Siguerdidjane, P. Mishra, and H. D. Mathur, "Maiden Application of Integral-Tilt Integral Derivative with Filter (I-TDN) Control Structure for Load Frequency Control," IFAC-PapersOnLine, vol. 55, pp. 72–77, 2022, doi: https://doi.org/10.1016/j.ifacol.2022.11.310.

Appendix -I: Three-area IPS nominal parameters in deregulated scenario [1-3]

T_{grti}=0.08s; T_{trti}=0.3s; T_{ri}=10s; K_{ri}=5; T_{gst}=1s; T_{tst}=3s; T_{st}=1.8s; K_{st}=1.8; T_{ggt}=0.2s; T_{tgt}=0.3; K_{wp1}=1.25; K_{wp2}=1.4; T_D=1s; T_{wp1}=0.041s; T_{wp2}=0.6s; K_{PC}=0.8; K_{RFB} =0.67; T_{RFB} =0s; K_{Pi} =120Hz/P.UMW (power system transfer function gain); T_{Pi} =20s (power system transfer function time constant); T_{12}=T_{23}=T_{13}=0.086 puMW/rad (Tie-line power synchronization coefficient); H_i =5s (inertia constant); D_i=8.33×10^{-3} P.UMW/Hz (area damping coefficient); R_i =2.4 P.U MW/Hz (speed governor parameter); B_i = 0.425 P.U MW/Hz (frequency bias constant); Governor dead-band=0.06 P.U. and Generation rate constraint = 3% P.U MW/min; K_1=0.85; K_2=0.095; K_3=0.92; T_d=0s; T_F=10s; C_B=200; K_{IB}=0.03; T_{IB}=26; T_{RB}=69.

The capacity of control areas 1, 2, and 3 are 2000MW, 4000MW, and 8000MW, respectively.

Where, *i*=1, 2, and 3 represent the control area-1, 2, and 3, respectively.

References:

[1] W. Tasnin and L. C. Saikia, “Impact of renewables and FACT device on deregulated thermal system having sine cosine algorithm optimized fractional order cascade controller,” IET Renew. Power Gener., vol. 13, pp. 1420–1430, 2019, doi: 10.1049/iet-rpg.2018.5638.

[2] W. Tasnin, L. C. Saikia, and M. Raju, “Deregulated AGC of multi-area system incorporating dish-Stirling solar thermal and geothermal power plants using fractional order cascade controller,” Int. J. Electr. Power Energy Syst., vol. 101, pp. 60–74, 2018, doi: 10.1016/j.ijepes.2018.03.015.

[3] S. M. Nosratabadi, M. Bornapour, and M. A. Gharaei, “Grasshopper optimization algorithm for optimal load frequency control considering Predictive Functional Modified PID controller in restructured multi-resource multi-area power system with Redox Flow Battery units,” Control Eng. Pract., vol. 89, pp. 204–227, 2019, doi: 10.1016/j.conengprac.2019.06.002.

Appendix-II: Two-area IPS with DFIG based WPP integrated in both control area [1-3]

$P_{R1} = P_{R2}$ =2000 MW (rating); $PL_1 = PL_2$ = 1000 MW (nominal loading); f = 60Hz; $T_{PS1} = T_{PS2}$ = 20 s; $T_{T1} = T_{T2}$ = 0.3 s; 2*pi*T_{12} = 0.545 P.U. MW/Hz; $T_{G1} = T_{G2}$ = 0.08 s; $K_{PS1} = K_{PS2}$ =120 Hz/pu MW; a_{12} = -1; $R_1 = R_2$ = 2.4 Hz/P.U MW; $B_1 = B_2$ =0.425 P.U. MW/Hz; Governor dead-band=0.06 P.U; Generation rate constraint = 3% P.U MW/min; H_{wt}=3.5s; T_w=6s; T_R=0.1s; T_{WG}=0.2s; K_{wp}=1.5; K_{wi}=0.15; $P_G^{min} = 0$; P_G^{max} =1.2 P.U.

References:

[1] S. P. Singh, T. Prakash, and V. P. Singh, "Coordinated tuning of controller-parameters using symbiotic organisms search algorithm for frequency regulation of multi-area wind integrated power system," Eng. Sci. Technol. an Int. J., vol. 23, pp. 240–252, 2019, doi: 10.1016/j.jestch.2019.03.007.

[2] S. Chaine, M. Tripathy, and S. Satpathy, "NSGA-II based optimal control scheme of wind thermal power system for improvement of frequency regulation characteristics," Ain Shams Eng. J., vol. 6, pp. 851–863, 2015, doi: 10.1016/j.asej.2015.01.011.

[3] E. S. Ali and S. M. Abd-Elazim, "BFOA based design of PID controller for two area Load Frequency Control with nonlinearities," Int. J. Electr. Power Energy Syst., vol. 51, pp. 224–231, 2013, doi: 10.1016/j.ijepes.2013.02.030.

Appendix-III: Two-area IPS with DFIG-based WPP integrated with control area-1 [1-3]

P_{R1} = P_{R2} =2000 MW (rating); PL_1 = PL_2 = 1000 MW (nominal loading); f = 60Hz; K_{PS1} = K_{PS2} =120 Hz/pu MW; T_{PS1} = 15.82; T_{PS2} = 20 s; T_{T1} = T_{T2} = 0.3 s; T_{12} = 0.086 puMW/rad; T_{G1} = T_{G2} = 0.08 s; a_{12} = -1; R_1 = 3.429; R_2 = 2.4 Hz/P.U.MW; B_1 = B_2 =0.425 P.U. MW/Hz; WTG rating=1.5MW; Inertia constant of WTG=5.024s.

References:

[1] E. S. Ali and S. M. Abd-Elazim, "BFOA based design of PID controller for two area Load Frequency Control with nonlinearities," Int. J. Electr. Power Energy Syst., vol. 51, pp. 224–231, 2013, doi: 10.1016/j.ijepes.2013.02.030.

[2] K. V. Vidyanandan and N. Senroy, "Primary frequency regulation by deloaded wind turbines using variable droop," in IEEE Transactions on Power Systems, vol. 28, pp. 837-846, May 2013, doi: 10.1109/TPWRS.2012.2208233.

[3] D. Kumar, P. Sharma, H. D. Mathur, S. Bhanot, and R. C. Bansal, "Modified Deloading Strategy of Wind Turbine Generators for Primary Frequency Regulation in Micro-Grid," Technol. Econ. Smart Grids Sustain. Energy, vol. 5, no. 1 2020, doi: 10.1007/s40866-020-00083-7.

Brief Biography of the Candidate

Akhilesh Kumar Mishra received the B.Tech. (Electrical and Electronics Engineering) degree from Uttar Pradesh Technical University, Lucknow, India, in 2008, and M.Tech. (Control and Instrumentation) degree from Motilal Nehru National Institute of Technology (MNNIT), Prayagraj, in 2013. He is currently a full-time research scholar and pursuing Ph.D. degree at the department of Electrical and Electronics Engineering, Birla Institute of Technology and Science, Pilani-Rajasthan, India. His research interests include load frequency control (LFC), renewable energy integration to the grid. He has authored 5 research articles in peer-reviewed international journals of repute, and his 7 papers have been published in IEEE sponsored international and top national conferences.

Brief Biography of the Supervisor

Dr. Puneet Mishra has completed his PhD in Instrumentation and Control engineering from Netaji Subhas Institute of Technology, University of Delhi, India in 2017, and M.E. in Control and Instrumentation Engineering from Delhi College of Engineering, University of Delhi, India, in the year 2011. He is currently serving as an Assistant Professor in the Department of Electrical and Electronics Engineering at Birla Institute of Technology and Science, Pilani, since December 2017. Prior to this, he served at GLA University, Mathura and BIT Mesra as Assistant Professor. He has published more than 55 papers in national/international journals and conference proceedings. His current research interests include Intelligent Control, Fuzzy Adaptive Control, Fractional order control and related fields.

Brief Biography of the Co-Supervisor

Prof. Hitesh Datt Mathur received B.E. degree from Nagpur University, Nagpur, India, in 1998; M.E. degree from Malaviya Regional Engineering College, Jaipur, India, in 2000; and the Ph.D. degree from Birla Institute of Technology and Science (BITS) Pilani, India in 2007 and He was Post-Doctoral Fellow in Supelec, Paris, France in 2013. He was also invited as visiting scientist to Centralesupelec, France in May- June of 2015 and May- June of 2019.

Currently, He is Professor in the Department of Electrical and Electronics Engineering, Birla Institute of Technology and Science, Pilani. He has teaching and research experience of more than 22 years. Prof. Mathur is Associate Editor of IET Renewable Power Generation as well as in editorial board and reviewer of various journals mainly in field of electrical power system, renewable energy.

He is a senior member IEEE, Fellow of Institution of Engineers (India), Chartered Engineer and life member of Indian Society of Technical Education. He has published more than 90 papers in national/international journals and conference proceedings. His research interests include power system control of isolated and interconnected power systems, power system optimization, automatic generation control and artificial intelligence techniques applications in power systems and distributed generation (DG) with grid interconnection issues. He is handling research projects of various government and non-government organizations such as Dept. of Science and Technology, Ministry of Power, Ministry of Human Resource and Development, Department of Biotechnology etc. The projects are related to the area of Energy management through IoT, Renewable source integration, microgrids and Electric vehicle penetration challenges.